Femtosecond and Two-Dimensional Spectroscopy of Lead Chalcogenide Quantum Dots

Samuel D. Park
B.S., University of California at Berkeley, 2010

A thesis submitted to the
Faculty of the Graduate School of the
University of Colorado in partial fulfillment
of the requirement for the degree of
Doctor of Philosophy
Department of Chemistry and Biochemistry
2015

This thesis entitled:
Femtosecond and Two-Dimensional Spectroscopy of Lead Chalcogenide Quantum Dots
written by Samuel D. Park
has been approved for the Department of Chemistry and Biochemistry

David M. Jonas

Robert P. Parson

Date:

The final copy of this thesis has been examined by the signatories, and we find that both the content and the form meet acceptable presentation standards of scholarly work in the above mentioned discipline.

Park, Samuel D. (Ph. D., Chemistry and Biochemistry)

Femtosecond and Two-Dimensional Spectroscopy of Lead Chalcogenide Quantum Dots

Thesis directed by Professor David M. Jonas

Quantum dots have applications in lighting displays and in biomedical imaging, and potential applications in next generation photovoltaics. The fine structure, optical inhomogeneity, coupling between excitons, and exciton dephasing rates are important to quantify because they affect the optical properties of quantum dots. These observables are encrypted in linear absorption lineshapes but can be measured with nonlinear spectroscopy.

The first two-dimensional (2D) Fourier transform spectra of lead chalcogenide quantum dots in the short-wave infrared are presented. With the additional dimension afforded by 2D spectra, linewidths from homogeneous and inhomogeneous broadening can be separated. Simulations to model the experimental 2D spectra are performed at long relaxation times to extract the optical inhomogeneity of a PbSe quantum dot ensemble. Additional information can be determined more accurately from 2D spectra than from transient absorption measurements. Specifically, the simulation of experimental 2D spectra shows that the excited state absorption redshift, which has been attributed to the bi-exciton binding energy, is larger than previously reported results, suggesting new interpretations.

Pump-probe polarization anisotropy measurements with 15 fs pulse durations are employed to investigate the electronic structure of chlorine-passivated PbS quantum dots at the bandgap. The measurement of the initial anisotropy required the removal of unwanted signal contribution from cross-phase modulation. The presence of cross-phase modulation motivated the calculation, simulation, and measurement of this signal for spectrally resolved pump-probe transients and two-dimensional Fourier transform spectroscopy. The initial anisotropy contains information about both bi-exciton states and some hot single exciton states, and the time dependence quantifies the timescale of intervalley scattering. Our results for PbS quantum dots indicate a lower initial anisotropy than expected from the effective mass approximations for PbS quantum dots with a rapid loss of any anisotropy in less than 20 fs.

To my grandfather

Acknowledgments

First and foremost, I thank my advisor, David M. Jonas, who welcomed me into his group and had confidence in me with my research. To me, Dave was more than an advisor; he was a father and a friend. Dave has been very patient with me and always treated me with kindness and respect. I can not imagine how many times he was asked the same questions about science and spectroscopy throughout his career, but always took the time and effort to explain many concepts. Dave taught me the importance of fundamentals and having a strong foundation for understanding more complicated concepts. I will cherish all of the enlightening discussions we had in his office. I will never forget all the time we spent together from surviving a typhoon in Japan, playing catch with him in the quad, and to talking (arguing) about baseball. Thanks, Dave, for everything. I could not have asked for a better advisor.

I am nothing without the help from many of the Jonas group members during my time in the group. I had the privilege to work with Trevor L. Courtney in my first two years in the group, who taught me all I know about optics and interferometry. It was a blast working with him in the short-wave infrared two-dimensional spectroscopy project and we had a lot of fun with all of the late night data collection (especially the night we were suspected as burglars by the police). Byungmoon Cho helped a lot with the quantum dot project. Byung really taught me how to run and tweak the laser for optimal performance for experiments. Byung brought a lot of enthusiasm to the project and had a lot of humility that I will always respect. Thanks to Robert Hill, who was very good at machining materials necessary for the project. To Bill Peters, who had a lot of literature knowledge and provided good discussions about research.

I would like to thank Dmitry Baranov, my battery mate in the quantum dot project, for his knowledge and expertise in materials and synthesis. Dmitry synthesized, characterized, and prepared all of the quantum dots for our project. He also finished the construction of the sample cell for the perfect experiment. Dmitry answered many of my stupid "chemistry" questions and he really kept me going throughout the project. Jisu Ryu was also very helpful with the project and brought new perspectives into the research. Jisu asked many questions about spectroscopy, which also helped me in my understanding of the topic. He was the only one who completed all of my exercises in fast Fourier transforms and spectral interferometry. Jisu also helped a lot in making figures for this thesis, which would have taken me a long time to complete otherwise. Dmitry and Jisu made all of the late night data collection easier and more fun with paper airplane competitions in the hallways and playing old school video games.

I also appreciated a lot of fun conversations and experiences with many of the other group members. To Jordan Corbman, who came from the same city of brotherly love as me. Danielle Buckley in always competing for the best parking spot. Vivek Tiwari for fun discussions about research and Rock 'n' Roll music. Austin Spencer, who is a fun guy to talk about electronics and video games. Anna Curtis, a ninja, startling me when she speaks when I do not notice her presence. Peter Foster with his random trivia knowledge. Alexa Carollo with her love of goats (too bad she is from New Jersey). Alina Mateo with her very distinct and contagious laughter. Adriana Huerta Viga, a new postdoc, who is a fun person to talk with and has a really cute hamster. I was and still am blessed with a great group of people.

There is also a very long list of professors, friends, colleagues, and staff members that I would like to thank. Mostly everyone I met always greeted me with kindness, even the people I only encountered in hallways. I enjoyed all of the small talk I had with them and appreciated all of their support.

Lastly, I would like to thank my family for their unconditional love and support throughout my entire life and in always helping me become a better person. My mother, who always reminds me to stay humble. My father, who reminds me not to worry about the small things in life. My sister, who is a good listener and always gives me helpful advice. I am eternally grateful and forever indebted to them.

Contents

List of Figures

List of Tables

Chapter 1

Introduction

1.1 Quantum Dots

When a crystalline semiconductor is reduced to a size comparable to the Bohr exciton radius of the material, it begins to exhibit interesting optical properties [1]. More specifically, either the electron or hole (or both) no longer "fits" inside the crystal so that the bulk band structure is restricted from continuous to discrete standing waves, which results in a quantum mechanical blueshift of the bandgap. Because of the quantum confinement in all three directions, these nanocrystals are also called quantum dots (QDs). With confinement energies given approximately by particle in a sphere energies, the QD size affects the energy bandgap, thus changing both absorption and luminescence spectra. The tunable luminescence spectrum of quantum dots has been exploited for light emitting applications such as lighting for displays [2][3] and biomedical imaging [4]. For these applications, information about the fine structure at the bandgap is important because it may affect both the quantum yield, which is essential for maximizing light emission efficiency in all applications, and the luminescence linewidth, where narrower spectral widths are desired for pure saturation colors [3].

Another reason for studying QDs is for their potential use in next generation photovoltaics to surpass the efficiency of single-junction photovoltaics. In single-junction photovoltaics, a photon must have energy of at least the bandgap to be absorbed. However, any absorbed photon yields only one charge carrier at the bandgap because the excess energy of a hot carrier is lost as heat. For these reasons, single-junction photovoltaics have a fundamental efficiency limit of ∼30% [5]. In order to recover some of this dissipated energy, harvesting multiple electron-hole pairs (excitons) from the absorption of a single high-energy photon has been proposed (multiple exciton generation). In addition to having a tunable bandgap, QDs have been attractive candidates as photovoltaics due to predictions of slower carrier cooling and increased coupling between excitons that mediate the process of multiple exciton generation [6][7]. To exploit carrier multiplication for increased efficiency, next generation photovoltaics must have their bandgap in the shortwave infrared, so that the peak of the solar spectrum can be used for multiple exciton generation and the short-wave infrared can be used to generate additional single charge carriers from light that would not be absorbed with the optimal bandgap of a single-junction photovoltaic. For this reason, lead chalcogenides QDs are particularly interesting because of their strong quantum confinement effects. However, the quantities that determine the the multiple exciton generation yield, such as the amount of exciton-exciton coupling and exciton-phonon dephasing, are not well known and critical in establishing whether lead chalcogenide QDs can be used in viable next generation photovoltaics. Information about the electronic structure at the bandgap is also important in understanding the accessible states, which are important for understanding the generation of excess carriers at threshold.

This thesis probes the underlying physics of excitons in QDs at the bandgap: how do excitons interact with other excitons and how are the excitons coupled to the nuclear degrees of freedom (phonons)? What is the electronic structure of lead chalcogenide QDs at the bandgap? To answer these questions, nonlinear spectroscopic techniques such as two-dimensional Fourier transform (2DFT) spectroscopy and femtosecond pump-probe polarization anisotropy are employed. The additional dimension of 2DFT spectroscopy decongests information that is convoluted by inhomogeneity due to the static size distribution of the QDs; this is an advantage over other nonlinear spectroscopy techniques such as pump-probe and spectrally resolved pump-probe (transient absorption). Information such as the exciton-phonon coupling that is encrypted inside the linear absorption spectrum can also be extracted using 2DFT spectroscopy. Given the reported hot carrier dynamics faster than ∼15 fs [8][9] present in QDs, 2DFT spectroscopy is a powerful technique because it does not compromise time and frequency resolution. If there is fine structure under the bandgap transition, when dynamics are expected to be slower, 2D spectroscopy should be able to resolve it. The pump-probe polarization anisotropy can reveal structural information on the angles between transition dipoles; this will be insightful because direct bandgap excitation of bulk lead chalcogenide semiconductors reaches a conduction band that is 4-fold degenerate at the equilibrium rock salt structure of the ground state. Thus, it would be enlightening to learn how the degeneracy is modified in a QD and how any remaining initial degeneracy is lifted after excitation. Understanding the nature of excitons inside QDs could be useful to engineer them for optimal efficiency.

1.2 Two-Dimensional Fourier Transform Spectroscopy: Basic Principles and Methods

1.2.1 Basic Principles

2DFT optical spectroscopy gives the ability to resolve inter- and intra- molecular interactions that determine the behavioral dynamics of complex systems. Such techniques can be considered as optical analogs of the early 2D Fourier transform nuclear magnetic resonance (2DFT NMR) experiments known as Nuclear Overhauser Effect Spectroscopy (NOESY) and Corre-

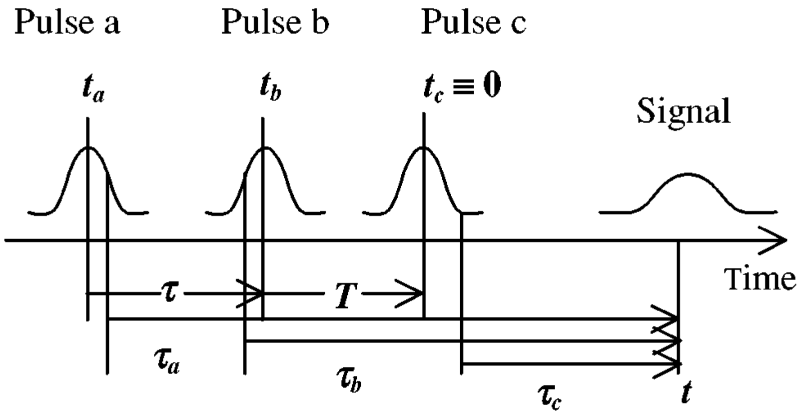

Figure 1.1: Pulse scheme for 2DFT spectroscopy. In the 2DFT experiments presented here, three pulses excite the sample and generate a signal in the phase matched direction ($\vec{k_s} = \mp\vec{k_a} \pm \vec{k_b} + \vec{k_c}$). Pulses a and b are collinear so that the difference between their wave vectors, $k_a - k_b \sim 0$, and the signal is collinear with pulse c. The time delays between the pulses are labeled τ, T, and t, for evolution, relaxation (or waiting), and detection time, respectively. (Figure from ref. [12])

lation Spectroscopy (COSY) 2D NMR, which revolutionized the application of NMR to study structural and imaging problems [10]. The extension of the 2DFT NMR techniques to the optical domain opened up exciting possibilities [11], because dynamics on the femtosecond timescale can be resolved with large spectral bandwidths to probe coupling between chromophores. This technique offers the highest possible frequency and time resolution, limited only by the molecular response.

2DFT spectroscopy is a four-wave mixing nonlinear spectroscopic technique. In four-wave mixing, three fields (which can be from one, two, or three pulses) excite the sample and generate a signal as the fourth field. The signal is radiated as a nonlinear optical free induction decay (Figure 1.1) [12]. The time delay between the first two pulses, τ, is Fourier transformed to resolve the excitation frequency axis, ω_τ, and the detection frequency, ω_t, can be directly resolved with a spectrograph. A 2D spectrum shows the correlation between the excitation and detection frequencies at a given waiting time, T. In other words, the experiment measures the correlation between the dipole oscillations during the time periods τ and t.

The capabilities of 2DFT spectroscopy can be illustrated by considering a system with two coupled absorbers. Figure 1.2 shows an energy level diagram and the corresponding 2D spectrum with two energy levels for each absorber. The coupled system has four energy levels: in the level (0,0), both absorbers are in their ground state; in the level (α,0), the first absorber is excited and the second is not; in the level (0,β), the second absorber is excited and the first is not; in the level (α,β), both absorbers are excited. An excitation with the frequency $\omega_\tau = \omega_\alpha$ will cause a decrease in absorption (positive signal) at $\omega_t = \omega_\alpha$ due to stimulated emission from the excited state population (excited state emission (ESE)) and a reduction in absorption from the reduction in the population of the ground state (ground state bleach (GSB)). Similarly, there will be a peak at $\omega_\tau = \omega_\beta$ and $\omega_t = \omega_\beta$. Since the two absorbers share a common ground state, excitation at either absorption frequency will reduce the population of the ground state for both, so cross peaks will arise from the ground state bleach contribution at (ω_β,ω_α) and (ω_α,ω_β). Furthermore, electronic coupling can alter the transitions to the doubly excited state (α, β), such that the excited state absorption (ESA) is detected at a different frequency at ($\omega_{\alpha'}$,ω_β) and ($\omega_{\beta'}$,ω_α); this increase in absorption is a negative signal. The negative off-diagonal peaks at ($\omega_{\alpha'}$,ω_α) and ($\omega_{\beta'}$,ω_β) arise from the coherent contributions that must be understood at the electromagnetic field/quantum wavefunction level. In generating these peaks, the first field excites quantum amplitude on one absorber and the second field excites quantum amplitude on the second absorber; these features will not appear in a non-FT experiment. The magnitude of the excited state absorption shift reflects the strength of coupling between transitions.

The projection of the 2D spectrum onto the detection axis, ω_t, calculated by the integration over ω_τ, yields the same information as the spectrally resolved pump-probe. From the previous example, the additional excitation frequency dimension helps separate the in-

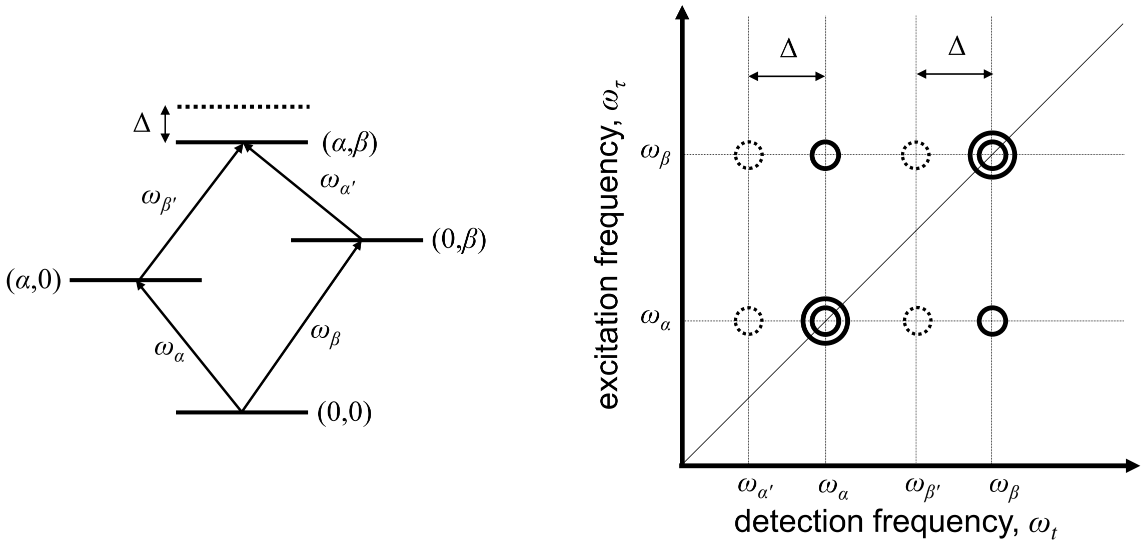

Figure 1.2: Energy level diagram (left) and corresponding 2D spectrum (right) for a coupled system of two absorbers. In a coupled system with transitions ω_α and ω_β arising from the same molecule (i.e. common ground state), excited state emission and ground state bleach occur along the diagonal in the 2D spectrum (positive, solid lines). In addition, cross peaks also appear $(\omega_\alpha, \omega_\beta)$ and $(\omega_\beta, \omega_\alpha)$ due to the two transitions having a common ground state. Furthermore, electronic coupling reduces the energy of the doubly excited state (α, β) such that excited state absorptions (negative, dotted lines) are detected at lower frequencies.

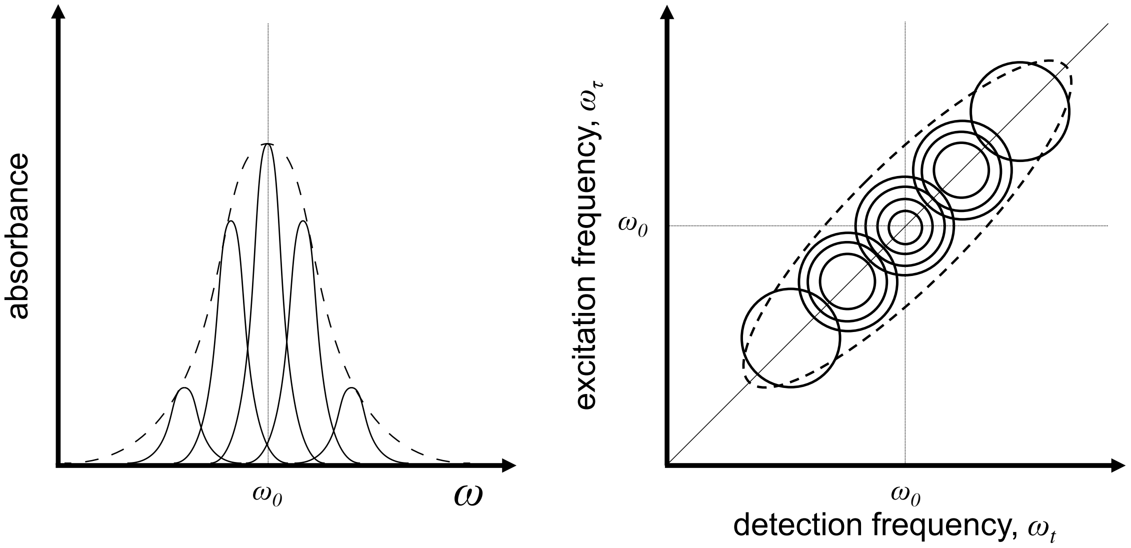

Figure 1.3: Separation of inhomogeneity in a 2D spectrum. The absorption spectrum on the left shows an inhomogeneously broadened lineshape (dashed) along with several homogeneous contributions. The 2D spectrum on the right shows how the inhomogeneity is spread along the diagonal. Each oscillator, with its own frequency, contributes linearly in a 2D spectrum.

formation between the peaks along the diagonal and off the diagonal in an otherwise congested spectrum. The additional dimension also alleviates the problem of an inhomogeneously broadened spectrum; since a Fourier transform is a linear operation, the total 2D spectrum is a sum of homogeneous 2D spectra (Fig. 1.3). For a single inhomogeneously broadened peak, each homogeneously broadened transition will contribute at its frequency so that the 2D spectrum is inhomogeneously broadened along the diagonal, but not the anti-diagonal. In addition, the 2D signal measurement is at the field level, where the signal strength is proportional to the number of molecules. This feature in particular is very useful for the sample we are interested in and key for determining linewidths, which will be discussed in the later chapters.

Polar solvation dynamics are also shown in 2DFT spectra, which is important for studying charge transfer reactions in solution [13]. This also applies to QDs where the excitons are perturbed by phonons from both inside the dot and from the complex environment. Upon initial optical excitation, the pre-existing velocity distribution from the nuclear coordinates continues inertial motion [13] even though a new charge distribution has been formed. As this motion and equilibrium distribution are gradually modified by the new forces, stabilization of the new charge distribution reduces the optical frequency, a phenomenon known as the dynamic Stokes' shift [14]. After this relaxation, the steady-state Stokes' shift, or red-shift of fluorescence relative to absorption is seen. These effects of inertial solvation are shown in 2DFT spectra by the following signatures: at $T = 0$, the positive peak is shifted above the diagonal, which indicates a red-shift in frequency as the signal is emitting; at $T = 0$, a negative region appears above the diagonal; the 2D spectrum shows a red-shift along the detection frequency as the waiting time increases [14]. The most intuitive reasoning for the negative region above the diagonal is explained through the projection-slice theorem [14]. At early times after electronic excitation, the signal is dominated by pre-existing velocity distributions. The echo-slice ($\tau = t$) at early times has a form in which the lowest power in the Taylor series expansion of the signal decays is t^4 [15]. This t^4 decay has a very flat top with a sudden drop, which causes ringing after a Fourier transform; this appears in 2D spectra as an off-diagonal negative region. The signatures of inertial solvation in 2D spectra are a "memory effect" of the type treated by Kubo [16] in nuclear magnetic resonance.

In 2DFT spectroscopy, time and frequency resolution are not compromised when peak-shape analysis is used to probe the interaction with the solvent [12]. On the femtosecond timescale, molecules are essentially "frozen" which can result in different instantaneous frequencies from their interaction with the environment. 2DFT can separate this distribution of instantaneous frequencies as dynamic inhomogeneous broadening. This example is illustrated in Fig. 1.4. As a function of waiting time, T, and allowing spectral diffusion, the system can evolve and lose correlation between excitation and detection frequencies. In other words, at some time after the excitation, the system excited at one frequency can be observed at any other frequency within the limits of the homogeneous lineshape and pulse bandwidth.

The time scale of losing correlation between excitation and detection frequencies is often represented as the correlation time, τ_c, for a particular system.

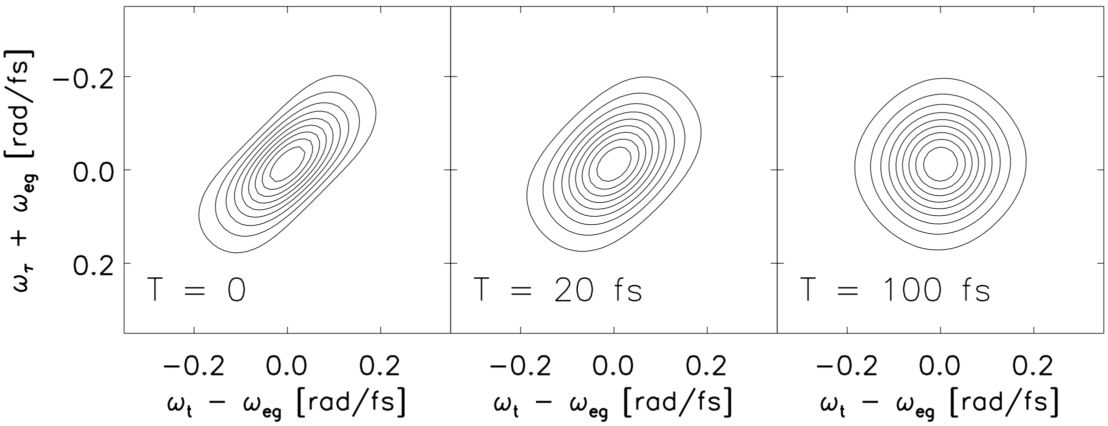

Figure 1.4: Instantaneous frequency and spectral diffusion in 2D spectra for a homogeneous system. Kubo stochastic spectral diffusion model in the slow modulation limit ($\Delta\tau_c = 3 > 1$), which has a Gaussian absorption lineshape (variance Δ^2) and an exponential decay of frequency correlation with decay time τ_c.

1.2.2 Experimental Designs

The most common types of geometry used in 2DFT spectroscopy are the fully non-collinear and the partially collinear (pump-probe). Each of these geometries have its own advantages and disadvantages.

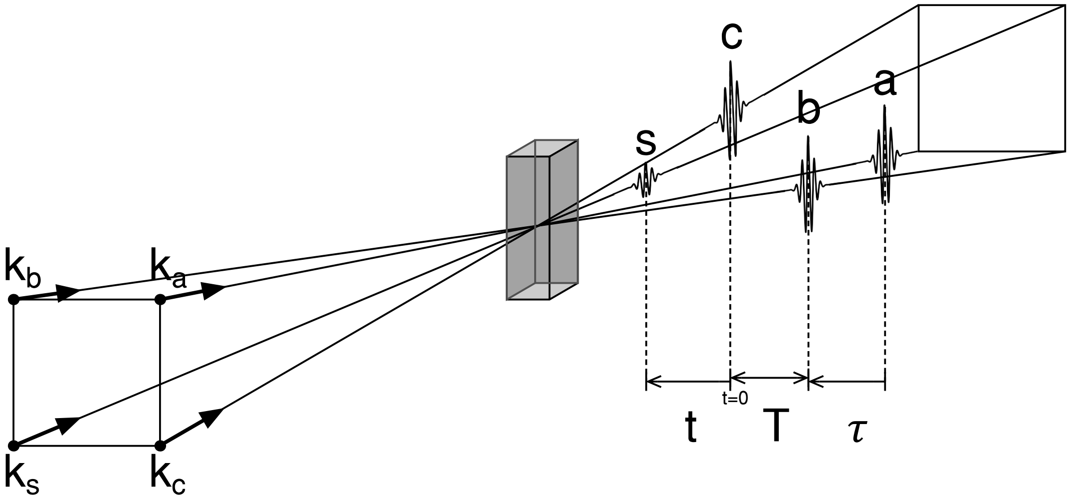

Figure 1.5: 2DFT spectroscopy measured in the BOXCARS geometry. The series of pulses are all non-collinear and the signal radiates in the background free phase matched direction, $\vec{k}_s = -\vec{k}_a + \vec{k}_b + \vec{k}_c$. A strongly attenuated fourth pulse, called the local oscillator, is used to both amplify the signal and retrieve the phase of the signal.

In the EASY (Echo Argument SpectroscopY) fully non-collinear geometry (Fig. 1.5), the phase modulation of the signal field is detected in a stimulated photon echo geometry [12]. The fully non-collinear geometry separates out the p-type (non-rephasing) and n-type (rephasing) signals; both of these signals are required to obtain the purely absorptive line shape, which is needed for analyzing lineshapes. This square BOXCARS geometry was used for the first 2D FT optical spectroscopy experiments by Hybl *et al.* [17]. In the fully non-collinear geometry, three pulses excite the sample, and the background-free signal is detected in the phase matched direction, $\vec{k}_s = -\vec{k}_a + \vec{k}_b + \vec{k}_c$. The first two pulses create a spatial excitation grating off of which pulse c diffracts [12], under a Bragg diffraction condition. In this geometry, pulses *a* and *b* create both an absorptive and refractive grating [18]. For this reason, the signal field contains both absorptive (real) and refractive (imaginary) information, which are extracted by interferometric detection with a local oscillator. A key advantage of the non-collinear geometry is the background free signal, which allows the time delay and amplitude of the local oscillator to be adjusted for optimal interference detection [19]. Although the 2D spectra must be phased to separate absorption from refraction, the fully non-collinear geometry offers a high signal-to-noise interferometric detection.

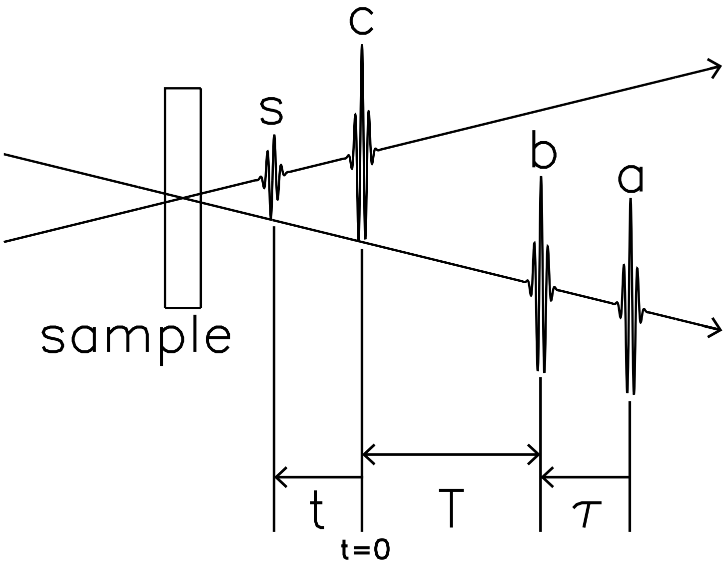

Figure 1.6: 2DFT spectroscopy in the pump-probe geometry. In the pump-probe geometry, pulses *a* and *b* travel collinearly and the radiated signal travels collinearly with pulse *c*; the signal is intrinsically heterodyned. The radiated signal is amplitude modulated, which results in a purely absorptive lineshape.

In the HARD (Homotime Absorptive Response Detection) partially collinear geometry, pulses *a* and *b* travel collinearly and the signal is detected in the pump-probe geometry (Fig. 1.6). In this geometry, pulses *a* and *b* do not create a spatial molecular excitation grating but only a spatially uniform absorptive frequency dependent excitation. The signal field is detected through interference with the temporally overlapping last excitation pulse *c*, which results in purely absorptive 2D spectra. In other words, only the change in absorption prepared by pulses a and b is detected. The signal is modulated only in amplitude, which results in purely absorptive 2D spectra. 2DFT spectroscopy in the pump-probe geometry has been demonstrated by several groups using an interferometer [20], spatial light modulator (SLM) [21], and acousto-optic modulator [22][23] to generate the pump-pulse pairs. In the pump-probe geometry, the signal radiates in the same wave vector as pulse c ($\vec{k}_s \sim \vec{k}_c$ because $\vec{k}_a \sim \vec{k}_b$ with equality holding for equal frequencies). The third pulse acts as an excitation pulse and a fixed local oscillator; the signal is intrinsically detected by interference with the third pulse. This causes the main disadvantage of the pump-probe geometry because the signal is weak compared to the excitation pulses, so their noise can overwhelm the interference. For this reason, the signal-to-noise ratio is at a premium in the pump-probe geometry. Polarization techniques [24] and phase cycling schemes [23] have been used to improve the signal detection. We also made efforts to circumvent this disadvantage using a Sagnac interferometer, which worked very well with our initial pulse bandwidth [25][26]. However, phase problems existed for the larger bandwidths used here in the short-wave infrared spectral region for studying lead chalcogenide QDs, which will be discussed later. One advantage in the partially collinear geometry is that the intrinsic heterodyne detection eliminates the need for absolute phase [20][27]; only the phase difference between pulses a and b is necessary. This quantity can be easily measured in parallel with the experiment using an integrated photodiode; a no adjustable parameter phasing of the 2D spectra is achieved. Another motivation for using the partially collinear geometry is the minimization of the directional filtering effect [28][29]. When two beams cross at an angle, the time delay between them has a spatial variation that increases with beam diameter [28]. This smearing of the time delay is called “crossing-angle smearing”. The crossing-angle smearing between noncollinear beams limits the off-diagonal range of 2D spectra. Since new and useful cross-peak information in molecular and solid-state systems may lie well off the diagonal in 2D spectra, the partially collinear geometry may become more widely useful.

1.3 Pump-probe Polarization Anisotropy

Pump-probe polarization anisotropy can provide structural information by measuring the angles between transition dipoles in an orientationally isotropic ensemble of molecules [30][31][32]. In this experiment, a linearly polarized pump pulse selectively excites molecules with transition dipoles aligned in a distribution parallel to the pump polarization, and a subsequent linearly polarized probe pulse detects the change in transmission. Due to the selective excitation of aligned transition dipoles, the linearly polarized probe pulse experiences an anisotropic absorption depending on the probe polarization angle with respect to the pump polarization. For dipolar excitation transition in isotropic media, the signals with probe polarized parallel and perpendicular to the pump fully characterize this anisotropic absorption. The polarization anisotropy is obtained by taking the difference between parallel and perpendicular signals, and dividing by the isotropic signal. The division by the isotropic signal removes common factors, such as lifetime decay, so that the anisotropy purely reflects the changes in dipole alignment. As a result, the anisotropy quantifies the fractional difference between the relative change in transmission with the linearly polarized probe pulse parallel and perpendicular to the pump polarization. As a function of the time delay between the pump and probe pulses, a time dependent anisotropy can occur and has been used to quantify molecular rotation times [30], dephasing times of electronic levels [33], electron transfer [34], and energy transfer processes to reveal how multiple pigments are coupled [31][35].

The anisotropic signal from the sample is a sum of nonlinear signals from individual molecules, which are randomly oriented in an isotropic sample. To understand the effects, it is helpful to begin by considering a single molecule. Figure 1.7 shows an example of the pump-probe polarization anisotropy for coupled perpendicularly oriented transition dipoles of a single molecule. The combined system has four levels: $g_x g_y$ is the ground electronic state; $e_x g_y$ and $g_x e_y$ are the two singly excited basis states reached by transition dipoles $\mu\hat{x}$ and $\mu\hat{y}$, respectively; and $e_x e_y$ is the common doubly excited state reached by transition dipoles $\mu\hat{y}$ and $\mu\hat{x}$ from the singly excited basis states, $e_x g_y$ and $g_x e_y$, respectively. The basis states are coupled, so that they are not eigenstates of the Hamiltonian, and a wavefunction that is excited to one singly excited basis state (for example, $e_x g_y$) will evolve into the other ($g_x e_y$ for this example) with time. In this example, the molecule is aligned in the laboratory frame and the transition dipole $\mu\hat{x}$ ($\mu\hat{y}$) is aligned parallel (perpendicular) to the pump polarization. After the pump pulse with polarization $\hat{x}$ excites an electron to the singly excited state $e_x g_y$, the parallel pump-probe signal will have contributions only from GSB and ESE, because the doubly excited state can only be reached from $e_x g_y$ with the perpendicular transition dipole moment $\mu\hat{y}$. As a function of time, the excitation is gradually transferred from the basis state $e_x g_y$ to the basis state $g_x e_y$ because they are coupled. After this excitation transfer, the excited state $g_x e_y$ can absorb light polarized parallel to the pump, but can no longer emit light polarized parallel to the pump. The pump-probe signal strength for each contribution is shown by the projection of the black arrow on to the red and blue axes which indicate the polarization geometries parallel and perpendicular with respect to the pump pulse. The corresponding total signal strength is shown in the bottom, which is the sum of all the separate contributions. With unit dipole strengths, the parallel pump-probe signal strength is initially 2 because the positive GSB and positive ESE contributions add, in contrast, the perpendicular pump-probe signal is initially 0 because the positive GSB and negative ESA contributions cancel. After the excitation is completely transferred from the basis state $e_x g_y$ to the basis state $g_x e_y$, the parallel pump-probe signal is 0 because the positive GSB and negative ESA contributions cancel and the perpendicular pump-probe signal is 2 because the positive GSB and positive ESE contributions add.

In an isotropic sample, with randomly oriented molecules and one transition dipole, a linearly polarized light generates an anisotropic $\cos^2(\theta)$ angular distribution of excited molecules, where θ is the angle between the transition dipole and the excitation electric field [36][37]. Calculation of the signal involves averaging the signal explained above over the isotropic angular distribution of molecules that exists before excitation.

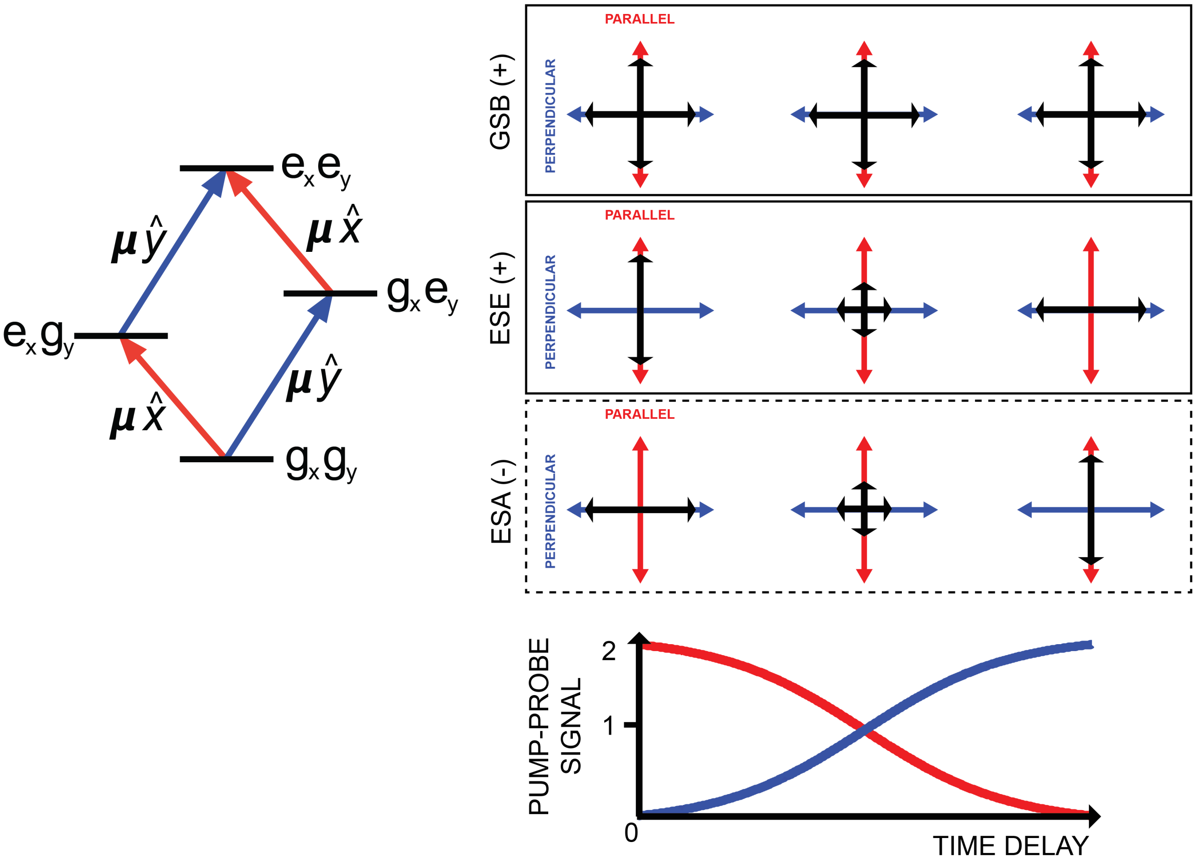

Figure 1.7: Polarized pump-probe signals for a single molecule with coupled, perpendicularly oriented, transition dipoles. The molecule is aligned in the laboratory frame and the transition dipole $\mu\hat{x}$ ($\mu\hat{y}$) is aligned parallel (perpendicular) to the pump polarization. The energy level diagram with the corresponding transition dipole moments is shown on the left. The right shows the separate contributions from GSB, ESE, and ESA. The projection of the black arrows on to the red and blue axes indicates the signal strength for parallel and perpendicular polarization geometries with respect to the pump polarization with unit dipole strengths. As a function of time, the excitation is gradually transferred between the perpendicular transition dipoles because they are coupled. The bottom figure shows the corresponding total pump-probe signal when probing with parallel (red) and perpendicular (blue) polarizations with respect to the pump pulse.

1.4 Cross-phase Modulation (XPM)

Cross-phase modulation (XPM) occurs when one pulse affects a different pulse while they are temporally and spatially overlapped in a transparent and nonlinear medium [38] and results in temporal and spectral changes to the pulses [39]. This phenomena is caused by the same underlying physics as the optical Kerr effect [40][41], which arises because the refractive index is intensity dependent,

$$n = n_0 + n_2 \cdot I, \tag{1.1}$$

where n_0 is the linear refractive index and n_2 is the non-linear refractive index that is proportional to the intensity. The temporal envelope of one ultrafast pulse causes the refractive index to be time dependent. This time varying refractive index produces a shift in the instantaneous phase of the second pulse, which results in a frequency shift up or down, depending on the time derivative of the refractive index. As a result, the second pulse experiences a spectral red-shift or blue-shift when temporally overlapped with the rising or falling edge of the first pulse's temporal envelope, respectively. This same principle applies to self-phase modulation (SPM) of a single pulse, in which the time-dependent refractive index change is due to the time varying envelope of the pulse itself. SPM has been exploited for continuum generation in optical fibers and nonlinear pulse compression [42][43]. XPM is usually attributed to a nonlinearity in the refractive index arising from a non-resonant two-photon absorption, which explains the positive sign of n_2. The additional intensity dependent absorption at frequencies above the laser frequency causes two-photon refraction.

Unfortunately, the XPM signal radiates with the same wave vector as resonant third-order spectroscopic techniques. For this reason, XPM has been mislabeled as "coherent artifacts" or "coherent spikes" [44][45] because it contributes to the signal during pulse overlap with improper pulse orderings and complicates the analysis of the resonant signal. This becomes a larger problem for samples that radiate weak resonant signals and for shorter pulses because the XPM signal is proportional to the square of the peak intensity.

1.5 Femtosecond and 2D Spectroscopy on Lead Chalcogenide Quantum Dots

Lead chalcogenide QDs have potential for proposed next generation photovoltaics. For this reason, many spectroscopic studies have been done on lead chalcogenide QDs to determine quantities such as exciton dephasing rates [8][46], exciton-exciton coupling [47], and exciton-phonon coupling, all of which are important to understand the mechanism of carrier multiplication. However, these quantities remain uncertain and result in different proposed lifetimes for the creation of a multiple excitons ranging from 50 – 200 fs [7][48]. In addition, no calculations indicate multiple exciton generation faster than 100 fs, and none includes the interaction with phonons or a realistic treatment of the surface [49][50][51]. A previous report from our group [8] suggests that any formation of multiple excitons must be faster than 10 fs, which implies either a stronger Coulombic coupling than previously reported [7][51] between excitons or that the QD surface has a greater role in multiple exciton generation. This discrepancy between multiple exciton generation timescales measured by integrated pump-probe signals and exciton-exciton couplings measured by spectrally-resolved pump-probe signals motivates a closer look at exciton-exciton and exciton-phonon coupling as well as exciton dephasing using 2D FT spectroscopy, which offers the highest possible time and frequency resolution.

For a homogeneously broadened system, the 2D spectrum approaches a product lineshape at sufficiently long relaxation times because there is no correlation between the excitation and detection frequencies [18][17]. The static size distribution of the QDs will result in an inhomogeneous distribution of energy bandgaps similar to an ensemble of quantum particles in different diameter spheres as shown in Fig. 1.8. As a result, the linear absorption spectrum is the sum of all the individual QDs' absorption spectra. The complex-valued 2D spectrum including inhomogeneity is the sum of all the complex-valued 2D spectra for each individual QD. The total real-valued absorptive 2D spectrum is the sum of all the real-valued absorptive 2D spectra because no nonlinear operations are used in processing the 2D data; in particular, Fourier transformation is a linear operation. The above statements about additivity do not apply to absolute value 2D spectra. Because each QD has its respective bandgap, the change in absorption will also appear at the respective excitation and detection frequencies and the inhomogeneity will be spread along the diagonal. Although there are methods to more directly measure nanoparticle size and size distribution, such as transmission electron microscopy, the optical bandgap inhomogeneity is still in question for QDs because different dots have different shapes, facets, and symmetries, which can affect the energy bandgap transitions and the underlying fine structure [52][53]. In other words, size inhomogeneity may not be directly indicative of optical bandgap inhomogeneity. For this reason, 2DFT spectroscopy is advantageous because it directly measures the optical transition(s) and can be used as an additional tool in determining the bandgap inhomogeneity of a QD sample.

Femtosecond pump-probe polarization anisotropy can probe the electronic structure of QDs by providing structural information on the angles between transition dipoles. Bulk lead chalcogenides have a rock salt structure. They have an interesting electronic structure, with their bandgap at the 4-fold degenerate (8-fold including spin) L-point of the first Brillouin zone, shown in Fig. 1.9. The electronic structure near the bandgap of their QDs is more complicated than suggested by the particle in a sphere model used to explain quantum confinement and critical for generation of excess carriers at threshold [54]. Depending on QD symmetry and stoichiometry, the 4-fold valley degeneracy may be lifted in near-spherical QDs [53]. Furthermore, the electronic structure of lead chalcogenide QDs is important for understanding the electronic envelope function, which has been reported to be important to understand the coupling to the optical phonons [55], which affect dephasing rates. To

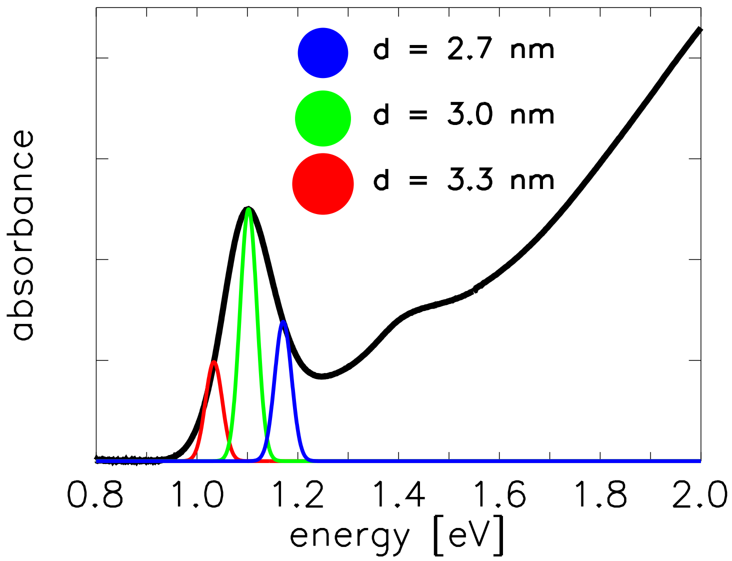

Figure 1.8: Linear absorption spectrum of a quantum dot ensemble. The blue, red, and green peaks inside the bandgap transition illustrate that different sizes, shown in the figure, affect the energy bandgap and appear as a static inhomogeneous distribution.

this end, pump-probe anisotropy measurements with sufficient time resolution can reveal the interaction between different valleys. The initial anisotropy can also elucidate the biexciton states. Coupling between valleys from the degenerate L-point and a distribution of energy gaps between these states in non-spherical QDs can lead to a time dependence of the anisotropy. The dephasing of the anisotropy essentially quantifies the timescale of the polarization "memory" of the excited electron, that is, how long the transition dipole is conserved before the individual transition dipoles rotate so that the ensemble of transition dipoles is no longer aligned. For lead chalcogenide QDs, this should directly probe the intervalley scattering at the bandgap.

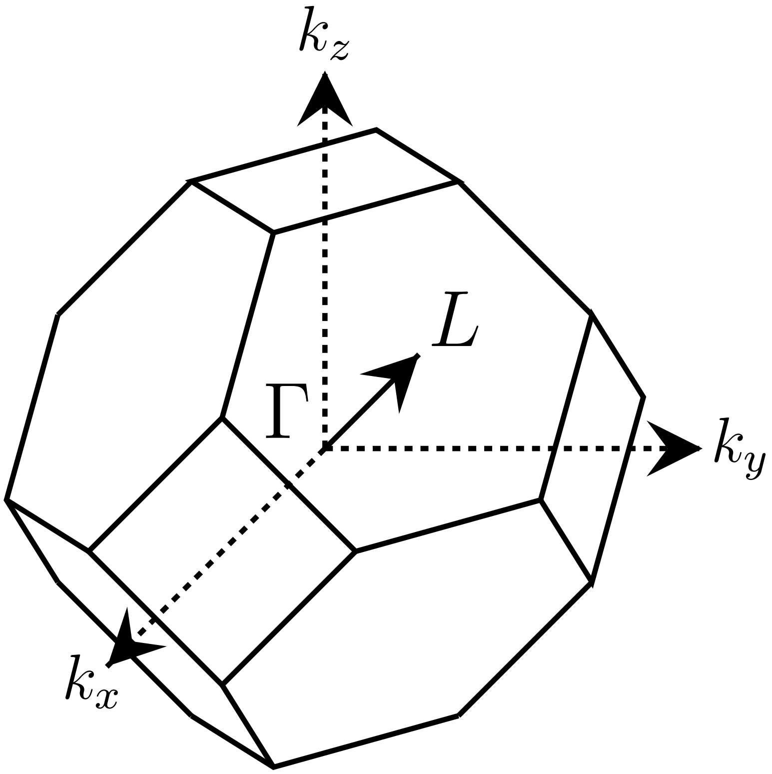

Figure 1.9: First Brillouin zone for the rock salt crystal structure. The direct energy bandgaps for bulk lead chalcogenides lie along the L points of the Brillouin zone with $\vec{k} = (\pm\pi/a, \pm\pi/a, \pm\pi/a)$, which is 4-fold degenerate. The degeneracy is 4-fold rather than 8-fold because opposite L points represent the same physical wave vector.

1.6 Organization of Thesis

Chapter 2 of this thesis is a continuation of T. L. Courtney's work implementing a Sagnac interferometer for 2D spectroscopy in the pump-probe geometry. The Sagnac interferometer was used to enhance the interferometric detection of the third-order signal with an attenuated local oscillator constructed by destructively interfering pulse c with a reference, thus improving the signal-to-noise. Because the beam-splitter used to combine pulse c and the reference has a complex refractive index, further calculations of phase errors in the 2D spectra are needed. This chapter presents and corrects for these phase errors and addresses considerations for using a Sagnac interferometer for 2D spectroscopy.

Chapter 3 shows the implementation of 2D spectroscopy to retrieve the optical inhomogeneity of lead selenide quantum dots. Because quantum dots are synthesized, there is a static distribution of sizes that affect the energy bandgap; this should result in a static optical inhomogeneity. A standard method for determining the static size distribution uses transmission electron microscopy images, in which each quantum dot size is measured. Although TEM offers a direct method for measuring the sizes of quantum dots, it is shown that literature procedures may lead to an over estimation in the size dispersity of the quantum dot sample that is inconsistent with the linear absorption spectrum. 2D spectroscopy and simple simulations are used to determine the optical inhomogeneity in a sample of quantum dots.

Chapter 4 of this thesis shows theoretical and experimental results for 2D spectra of XPM. The XPM signal is present during pulse overlap. The strength of the XPM signal is proportional to the square of the intensity and therefore becomes more apparent and more important for shorter pulses. This makes the interpretation of the data during pulse overlap difficult. Furthermore, the XPM in 2D spectra is more complicated and can be misinterpreted as transient positive and negative signal. The XPM signal is simulated and measured in 2D spectroscopy. Propagation effects in an absorbing sample are also simulated for implementing an XPM subtraction scheme in resonant pump-probe and 2D experiments.

Chapter 5 describes spectrally resolved pump-probe polarization anisotropy measurements on lead sulfide quantum dots. It presents an intriguing result, where the initial anisotropy with 15 fs pulses does not have the value of $2/5$ expected for a dipolar transition. Theoretical calculation of the initial anisotropy illustrated using a particle in a 3D box filled with two electrons, which has an initial anisotropy of $2/5$ when excited state absorption to both two-electron and one-electron states is included. The initial anisotropy is then calculated for PbS quantum dots in an effective mass approximation (rigorous derivations of the effective mass approximation is strictly justified only for semiconductors with a bandgap at the Γ point, $k = 0$), including 4 valleys each filled with two electrons. This calculation, which does not include one-electron states in excited state absorption, also yields an initial anisotropy of $2/5$ with each valley being an independent, uncoupled absorber. The measured initial anisotropy is less than 0.1, and the anisotropy is zero within error after 10 fs. The departure from the expected anisotropy of $2/5$ raises possibilities such as strong one-electron contributions to the excited state absorption contribution, strong spin-orbit interactions generating splittings outside the 1S-1S exciton absorption, or intervalley coupling generating splittings outside the 1S-1S exciton absorption.

References

[1] L. E. Brus, “Electron-electron and electron-hole interactions in small semiconductor crystallites: The size dependence of the lowest excited electronic state,” J. Chem. Phys. 80(9), 4403-4409 (1984).

[2] Y. Shirasaki, G. J. Supran, M. G. Bawendi, and V. Bulovic, “Emergence of colloidal quantum-dot light-emitting technologies,” Nature Photon. 7, 13-23 (2013).

[3] J. S. Steckel, R. Colby, W. Liu, K. Hutchinson, C. Breen, J. Ritter, and S. Coe-Sullivan, “Quantum Dot Manufacturing Requirements for the High Volume LCD Market,” SID Symp. Dig. Tech. Pap. 44, 943-945 (2013).

[4] W. C. W. Chan, D. J. Maxwell, X. Gao, R. E. Bailey, M. Han, and S. Nie, “Luminescent quantum dots for multiplexed biological detection and imaging,” Current Opinion in Biotechnology 13, 40-46 (2002).

[5] W. Shockley and H. J. Queisser, “Detailed Balance Limit of Efficiency of p-n Junction Solar Cells,” J. App. Phys. 32, 510-519 (1961).

[6] A. J. Nozik, “Quantum dot solar cells,” Physica E 14, 115-120 (2002).

[7] R. D. Schaller, V. M. Agranovich, and V. I. Klimov, “High-efficiency carrier multiplication through direct photogeneration of multi-excitons via virtual single-exciton states,” Nat. Phys. 1, 189-194 (2005).

[8] B. Cho, W. K. Peters, R. J. Hill, T. L. Courtney, and D. M. Jonas, “Bulklike Hot Carrier Dynamics in Lead Sulfide Quantum Dots,” Nano Lett. 10, 2498-2505 (2010).

[9] H. Kamisaka, S. V. Kilina, K. Yamashita, and O. V. Prezhdo, “Ultrafast Vibrationally-Induced Dephasing of Electronic Excitations in PbSe Quantum Dots,” Nano Lett. 6(10), 2295-2300 (2006).

[10] R. R. Ernst, G. Bodenhausen, and A. Wokaun, *Principles of Nuclear Magnetic Resonance in One and Two Dimensions* (Oxford Univ. Press, 1987).

[11] J. D. Hybl, A. A. Ferro, and D. M. Jonas, “Two-dimensional Fourier transform electronic spectroscopy,” J. Chem. Phys. 115(14), 6606-6621 (2001).

[12] D. M. Jonas, “Two-Dimensional Femtosecond Spectroscopy,” Annu. Rev. Phys. Chem. 54, 425-463 (2003).

[13] E. A. Carter and J. T. Hynes, “Solvation dynamics for an ion pair in a polar solvent: Time-dependent fluorescence and photochemical charge transfer,” J. Chem. Phys. 94(9), 5961-5979 (1991).

[14] J. D. Hybl, Y. Christophe, and D. M. Jonas, “Peak shapes in femtosecond 2D correlation spectroscopy,” Chem. Phys. 266, 295-309 (2001).

[15] A. M. Walsh and R. F. Loring, “Photon echoes in a nonpolar fluid,” Chem. Phys. Lett. 186(1), 77-83 (1991).

[16] R. Kubo, “Note on the Stochastic Theory of Resonance Absorption,” J. Phys. Soc. Jpn. 9(6), 935-944 (1954).

[17] J. D. Hybl, A. W. Albrecht, S. M. G. Faeder, and D. M. Jonas, “Two-dimensional electronic spectroscopy,” Chem. Phys. Lett. 297, 307-313 (1998).

[18] K. A. Nelson, R. Casalegno, R. J. D. Miller, and M. D. Fayer, “Laser-induced excited state and ultrasonic wave gratings: Amplitude and phase grating contributions to diffraction,” J. Chem. Phys. 77(3), 1144-1152 (1985).

[19] M. Levenson and G. Eesley, “Polarization selective optical heterodyne detection for dramatically improved sensitivity in laser spectroscopy,” Appl. Phys. A 19, 1-17 (1979).

[20] L. P. DeFlores, R. A. Nicodemus, and A. Tokmakoff, “Two dimensonal Fourier transform spectroscopy in the pump-probe geometry,” Opt. Lett. 32, 2966-2968 (2007).

[21] E. M. Grumstrup, S. H. Shim, M. A. Montgomery, N. H. Damrauer, and M. T. Zanni, “Facile collection of two-dimensional electronic spectra using femtosecond pulse-shaping technology,” Opt. Express 15, 16681-16689 (2007).

[22] J. A. Myers, K. L. M. Lewis, P. F. Tekavec, and J. P. Ogilvie, “Two-color two-dimensional Fourier transform electronic spectroscopy with a pulse-shaper,” Opt. Express 16, 17420-17428 (2008).

[23] S. X. Yan and H. S. Tan, “Phase cycling schemes for two-dimensional optical spectroscopy with a pump-probe beam geometry,” J. Chem. Phys. 360, 110-115 (2009).

[24] W. Xiong and M. T. Zanni, “Signal enhancement and background cancellation in collinear two-dimensional spectroscopies,” Opt. Lett. 33, 1371-1373 (2008).

[25] T. L. Courtney, S. D. Park, R. J. Hill, B. Cho, and D. M. Jonas, “Enhanced interferometric detection in two-dimensional spectroscopy with a Sagnac interferometer,” Opt. Lett. 39, 513- 516 (2014).

[26] S. D. Park, T. L. Courtney, D. Baranov, B. Cho, and D. M. Jonas, "Sagnac Interferometer for Two-Dimensional Spectroscopy in the Pump-Probe Geometry," Ultrafast Phenomena XIX, edited by K. Yamanouchi, S. Cundiff, R. Vivie-Riedle, M. Kuwata-Gonokami, and L. DiMauro (Springer, New York, 2015), p. 428.

[27] S. M. G. Faeder and D. M. Jonas, "Two-dimensional electronic correlation and relaxation spectra: Theory and model calculations," J. Phys. Chem. A 103, 10489-10505 (1999).

[28] N. Belabas and D. M. Jonas, "Three-dimensional view of signal propagation in femtosecond four-wave mixing with application to the boxcars geometry," J. Opt. Soc. Am. B 22, 655-674 (2005).

[29] M. K. Yetzbacher, N. Belabas, K. A. Kitney, and D. M. Jonas, "Propagation, beam geometry, and detection distortions of peak shapes in two-dimensional Fourier transform spectra," J. Chem. Phys. 126, 044511 (2007).

[30] G. R. Fleming, *Chemical Applications of Ultrafast Spectroscopy* (Clarendon Press: Oxford, U. K., 1986).

[31] D. M. Jonas, M. J. Lang, Y. Nagasawa, T. Joo, and G. R. Fleming, "Pump-Probe Polarization Anisotropy Study of Femtosecond Energy Transfer within the Photosynthetic Reaction Center of *Rhodobacter sphaeroides* R26," J. Phys. Chem. 100, 12660-12673 (1996).

[32] E. R. Smith and D. M. Jonas, "Alignment, Vibronic Level Splitting, and Coherent Coupling Effects on the Pump-Probe Polarization Anisotropy," J. Phys. Chem. A 115, 4101-4113 (2011).

[33] C. Galli, K. Wynne, S. M. LeCours, M. J. Therien, and R. M. Hochstrasser, "Direct measurement of electronic dephasing using anisotropy," Chem. Phys. Lett. 206, 493-499 (1993).

[34] A. T. Yeh, C. V. Shank, J. K. McCusker, "Ultrafast Electron Localization Dynamics Following Photo-Induced Charge Transfer," Science 289, 935-938 (2000).

[35] D. A. Farrow, W. Qian, E. R. Smith, A. A. Ferro, and D. M. Jonas, "Polarized pump-probe measurements of electronic motion via a conical intersection," J. Chem. Phys. 128, 144510 (2008).

[36] R. N. Zare, *Angular Momentum: Understanding Spatial Aspects in Physics and Chemistry* (Wiley-Interscience, New York, 1988).

[37] W. Qian and D. M. Jonas, "Role of cyclic sets of transition dipoles in the pump-probe polarization anisotropy: Application to square symmetric molecules and perpendicular chromophore pairs," J. Chem. Phys. 119(3), 1611-1622 (2003).

[38] G. P. Agrawal, "Modulation Instability Induced by Cross-Phase Modulation," Phys. Rev. Lett. 59(8), 880-883 (1987).

[39] R. R. Alfano, P. L. Baldeck, P. P. Ho, and G. P. Agrawal, "Cross-phase modulation and induced focusing due to optical nonlinearities in optical fibers and bulk materials," J. Opt. Soc. Am. B 6(4), 824-829 (1989).

[40] G. Mayer and R. Gires, "The effect of an intense light beam on the index of refraction of liquids," C. R. Acad. Sci. 258, 2039 (1963).

[41] P. D. Maker, R. W. Terhune, and C. M. Savage, "Intensity-dependent changes in the refractive index of liquids," Phys. Rev. Lett. 12(18), 507-509 (1964).

[42] M. N. Islam, L. F. Mollenauer, R. H. Stolen, J. R. Simpson, and H. T. Shang, "Cross-phase modulation in optical fibers," Opt. Lett. 12(8), 625-627 (1987).

[43] G. P. Agrawal, P. L. Baldeck, and R. R. Alfano, "Modulation instability induced by cross-phase modulation in optical fibers," Phys. Rev. A 39(7), 3406-3413 (1989).

[44] M. W. Balk and G. R. Fleming, "Dependence of the coherence spike on the material dephasing time in pump-probe experiments," J. Chem. Phys. 83(9), 4300-4307 (1985).

[45] M. Lorenc, M. Ziolek, R. Naskrecki, J. Karolczak, J. Kubicki, and A. Maciejewski, "Artifacts in femtosecond transient absorption spectroscopy," Appl. Phys. B 74, 19-27 (2002).

[46] C. V. Shank and P. Becker, "Femtosecond Processes in Semiconductors. In *Spectroscopy of Nonequilibrium Electrons and Phonons*," C. V. Shank and B. P. Zakharchenya Eds. Elsivier: Amsterdamn, p. 215 (1992).

[47] L. A. Yurs, S. B. Block, A. V. Pakoulev, R. S. Selinsky, S. Jin, and J. Wright, "Multiresonant Coherent Multidimensional Electronic Spectroscopy of Colloidal PbSe Quantum Dots," J. Phys. Chem. C 115, 22833-22844 (2011).

[48] A. O. El-Ballouli, E. Alarousu, A. Usman, J. Pan, O. M. Bakr, and O. F. Mohammed, "Real-Time Observation of Ultrafast Intraband Relaxation and Exciton Multiplication in PbS Quantum Dots," ACS Photonics 1, 285-292 (2014).

[49] A. Franceschetti, J. M. An, and A. Zunger, "Impact Ionization Can Explain Carrier Multiplication in PbSe Quantum Dots," Nano Lett. 6(10), 2191-2195 (2006).

[50] R. Baer and E. Rabani, "Expeditious Stochastic Calculation of Multiexciton Generation Rates in Semiconductor Nanocrystals," Nano Lett. 12, 2123-2128 (2012).

[51] R. J. Ellingson, M. C. Bear, J. C. Johnson, P. Yu, O. I. Micic, A. J. Nozik, A. Shabaev, and A. L. Efros, "Highly Efficient Multiple Exciton Generation in Colloidal PbSe and PbS Quantum Dots," Nano Lett. 5(5), 865-871 (2005).

[52] D. Segets, J. M. Lucas, R. N. Klupp Taylor, M. Scheele, H. Zheng, A. P. Alivisatos, and W. Peukert, "Determination of the Quantum Dot Band Gap Dependence on Particle Size from Optical Absorbance and Transmission Electron Microscopy Measurements," ACS Nano 6(10), 9021-9032 (2012).

[53] A. N. Poddubny, M. O. Nestoklon, and S. V. Goupalov, "Anomalous suppression of valley splittings in lead salt nanocrystals without inversion center," Phys. Rev. B 86, 035324 (2012)

[54] J. M. An, A. Franceschetti, S. V. Dudiy, and A. Zunger, "The peculiar electronic structure of PbSe quantum dots," Nano Letters 6(12), 2728-2735 (2006).

[55] S. Nomura and T. Kobayashi, "Exciton-LO-phonon couplings in spherical semiconductor microcrystallites," Phys. Rev. B 45(3), 1305-1316 (1992).

Chapter 2

Sagnac Interferometer for Two-Dimensional Spectroscopy in the Pump-Probe Geometry

An intrinsically phase-stable Sagnac interferometer is introduced for optimized interferometric detection in partially collinear two-dimensional (2D) spectroscopy. With a pump-pulse pair from an actively stabilized Mach-Zehnder interferometer, the Sagnac scheme is demonstrated in broadband, short-wave IR (1-2 μm), 2D electronic spectroscopy of IR-26 dye.

This chapter is adapted from the paper "Enhanced interferometric detection in two-dimensional spectroscopy with a Sagnac interferometer" published in February, 2014 in *Optics Letters* [30]. This chapter contains the introduction and experimental methods sections from this article and my contributions to the data analysis and results that go beyond the work discussed in Trevor L. Courtney's Ph.D. thesis. The extension of calculating the local oscillator phase error, correcting the 2D spectra, and Sagnac beam splitter properties to be used for early waiting times (coherent regime) for two-dimensional Fourier Transform (2DFT) experiments are also beyond the scope of this article. These results were published in *Ultrafast Phenomena XIX Conference Proceedings* [31].

2.1 Introduction

Two-dimensional Fourier transform (2D FT) spectra show how a nonlinear signal field, as a function of radiated frequency, depends on an excitation frequency, revealing coupling between excitations [1]. Except for a gap in the 1-2 μm short-wave IR region, 2D FT spectra are used from the THz [2] to the deep UV [3]. Pulses in the short-wave IR [4] access low energy electronic processes and next-generation photovoltaics, motivating extension to this region, where sensitivity is at a premium. 2D FT beam geometries range from fully noncollinear to fully collinear, with advantages and disadvantages for each. In all, three short pulses excite a sample, generating a nonlinear signal field that decays after the last pulse. The fully noncollinear 2D geometry produces a background-free signal field measured through optimized interference with a delayed local oscillator (LO) to sensitively detect both real absorptive and imaginary refractive parts of the 2D spectrum [1]. The LO must be strong enough to raise interference with the signal above detector noise but not so strong that it swamps the signal with LO shot noise [5]. In contrast, a limitation of partially collinear 2D spectroscopy is that the last pulse and nonlinear signal co-propagate [6], which can make their interference more difficult to detect. Several groups have demonstrated the partially collinear pump-probe geometry [7][8][9][10], which selectively detects the real part of the 2D spectrum [6]. The new method presented here combines the advantages of both geometries in a relatively compact and simple design: a partially collinear 2D spectrometer with a Sagnac interferometer creates a nearly background-free signal and selectively detects the absorptive 2D spectrum.

In a common-path Sagnac interferometer, the output that returns light to the source has a symmetrical path (one beam splitter reflection with Fresnel coefficient $\hat{r}$, and one

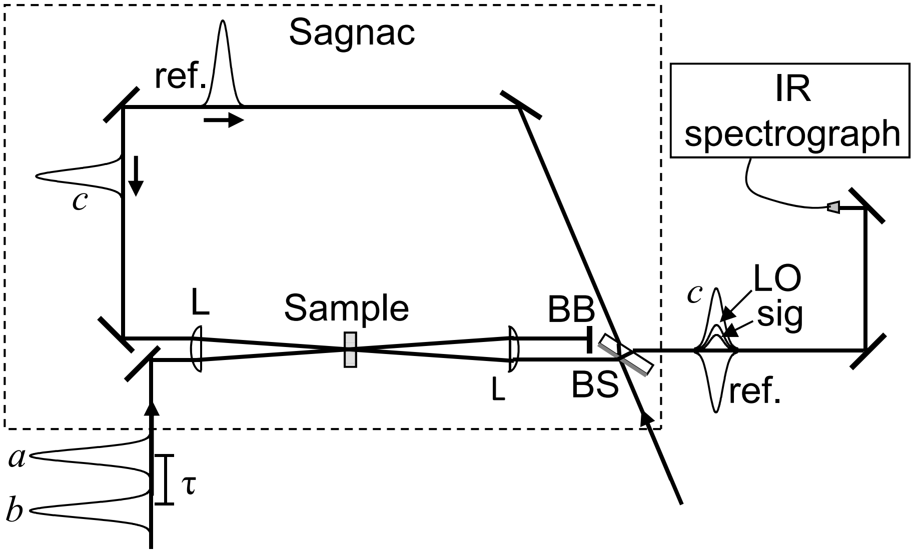

Figure 2.1: Partially collinear 2D spectrometer with Brewster's angle interferometer. Pulses a and b, separated by delay τ, from the Mach-Zehnder impinge on the sample, followed by pulse c at delay T. The signal co-propagates with pulse c in the Sagnac; pulses c and reference destructively interfere to become the attenuated local oscillator (LO) in the Sagnac dark output. BS: gold-coated beam splitter, BB: beam block, L: plano-convex lens, f = 7.5 cm. Protected silver mirrors are unlabeled.

transmission with Fresnel coefficient $\hat{t}$, for each beam), which makes it the bright output [11]. The more accessible, dark output of a lossless Sagnac has a π phase shift ($\Delta\phi(\omega) = \pi$) between a beam with two reflections (first- and second-surface, or $\hat{r}$ and $\hat{r}'$) and one with two transmissions. The intrinsic stability and ease of alignment of a Sagnac interferometer are appealing for ultrafast phase spectroscopy and optical background suppression in pump-probe spectroscopies [12][13]. In such experiments, an external pump pulse crosses a sample inserted in the interferometer; the signal is detected via perturbation of the dark output [14]. This chapter outlines the adaptation of such a Sagnac interferometer to a Brewster's angle design [15] and its introduction for 2D spectroscopy. With a slight $\hat{r}/\hat{t}$ amplitude imbalance of the Sagnac beam splitter, destructive interference between probe and reference pulses forms an attenuated LO, which co-propagates with the 2D signal field (Fig. 2.1).

2.2 Experimental Design

In this experiment, pulses from a 1 kHz Ti:Sapphire regenerative amplifier pump a single-pass, short-wave IR noncollinear optical parametric amplifier (NOPA) with a PPSLT crystal [4]. The wavelength-tunable NOPA generates 1-2.5 μJ pulses that enter a grating compressor; compression with a deformable mirror uses second-harmonic generation (SHG) feedback in a genetic algorithm [16]. After the compressor, the beam is spatially filtered with a 150 μm pinhole to remove any frequency-dependent angular deviations from the deformable mirror. Pulse durations of 30 fs are determined by zero-additional-phase spectral phase interferometry of direct electric-field reconstruction (ZAP-SPIDER) [17] and SHG frequency-resolved optical gating (FROG) [18]. All spectral infrared detection uses single-mode fiber coupling (ThorLabs 1060XP, NA = 0.14) to a 0.15-m Czerny-Turner spectrograph (Princeton Instruments SP-2150i) with a liquid nitrogen cooled 1024x1 pixel InGaAs array (Princeton Instruments OMAV:1024-2.2).

The 2D spectrometer consists of an actively stabilized Mach-Zehnder interferometer and a Sagnac interferometer. A broadband, inconel-coated, glass window [15][19] splits the spectrometer input beam into pump and Sagnac-incident beams. All beam splitters in this apparatus exploit the air-glass interface Brewster's angle to prevent additional surface reflections and their interference. The Brewster's angle Mach-Zehnder interferometer with inconel beam splitters creates a pump-pulse pair (pulses a and b) from the bright output with a delay, τ, roughly controlled by computerized translation stages. Interferometric feedback from a red HeNe laser is used to drive a piezoelectric transducer in one arm to lock τ with 0.6-nm stability during the 1 s collection of one interferogram. Actively stabilized steps in τ are taken at an integer plus a quarter cycle of the red HeNe wavelength [20]; a yellow HeNe laser is used to measure lock stability and track τ during a 2D scan.

The beam path entering the Sagnac interferometer is split into counter-propagating probe

(c, transmitted) and reference (*ref.*, reflected) pulses by a gold-coated Sagnac beam splitter at the air-glass Brewster's angle (Fig. 2.1). Thus, three pulses (a, b, and c) pass through two metallic beam splitters (inconel- or gold-coated, 1-mm thick glass) at oppositely signed Brewster's angles for matched dispersion and spatial compensation before the sample. The counter-propagating reference pulse passes through the sample $t_r \approx 1.5$ ns before the other three pulses. The off-axis collinear pump pulse pair with delay $\tau = t_b - t_a$ impinges on the sample, followed by pulse c at the computer-controlled delay T, thus generating various nonlinear signals.

For Sagnac interferometers with planar beam paths and flat mirrors, several properties depend on whether the number of mirrors is even or odd [11]. An even number of flat mirrors creates a common-path interferometer, in which clockwise and counter-clockwise rays retrace each other exactly for all rays parallel to the central ray. In contrast, for an odd number of flat mirrors, the central ray follows a common path, while parallel rays follow cyclic paths that are vulnerable to differential phase distortions between counter-propagating paths. Sagnac interferometers for ultrafast phase spectroscopy and background suppression have employed two flat mirrors [12], two flat mirrors plus a telescope [13][14], and three flat mirrors plus a telescope [21]. Inserting a telescope in order to generate a larger nonlinear signal introduces an additional inversion, altering the standard analysis. Figure 2.2a traces rays in the horizontal interferometer plane containing the telescope symmetry axis. The common-path property of Sagnac interferometers with an even number of mirrors arises here because the interferometer beams undergo an even number (4) of left-right reversals within the Sagnac: one from each of the three mirrors plus one from the telescope. However, Fig. 2.2b shows how the telescope also introduces one top-bottom reversal for beams above and below the interferometer symmetry plane. Inside the Sagnac interferometer, the clockwise and counter-clockwise propagating images at each point along the beam path are always upside down relative to each other. Relative to the input, all output images (bright and dark) are upside down. Thus, spatial phase imperfections in the input beam cancel, but rays above and below the symmetry plane follow cyclic paths that differ for clockwise and counter-clockwise propagating rays. The resulting differential phase shifts are antisymmetric with respect to the symmetry plane, and so have negligible effect for collimated 3 mm diameter beams in this plane. For comparison, a Sagnac interferometer with two mirrors and a telescope has two-dimensionally inverted outputs and a common path only through the telescope axis.

The gold-coated beam splitter recombines the out-of-phase probe, $\hat{E}_c = \hat{t}\hat{E}_i$, and reference, $\hat{E}_r = \hat{r}\hat{E}_i$, where $\hat{E}_i$ is the field incident on the Sagnac beam splitter, to produce an attenuated LO, $\hat{E}_{LO}(\omega_t) = (\hat{t}\hat{t} + \hat{r}'\hat{r})\hat{E}_i(\omega_t)$. For maximal interference, the Sagnac uses 3 mirror reflections plus 1 telescope inversion to superpose two fully inverted beams in the dark output. The 2D signal co-propagates with the LO and background terms, given by

$$\begin{aligned} I_{2D}(t_a, t_b, \omega_t) \;=\; & \Big| \hat{r}'\hat{r}[(\hat{E}_i + \hat{E}^{(1)}) + \hat{r}\hat{r}^* \hat{E}^{(3)}_{rrr}] + \hat{t}\hat{t}\hat{r}\hat{r}^* \hat{E}^{(3)}_{crr} \\ & + \hat{t}\hat{t}[(\hat{E}_i + \hat{E}^{(1)}) + (\hat{t}\hat{t}^* \hat{E}^{(3)}_{ccc} + \hat{E}^{(3)}_{caa} + \hat{E}^{(3)}_{cbb}) + (\hat{E}^{(3)}_{cba} + \hat{E}^{(3)}_{cab})] \Big|^2 . \end{aligned} \tag{2.1}$$

The amplitude-modulated 2D signal, $\hat{E}^{(3)}_{2D} = \hat{E}^{(3)}_{cba} + \hat{E}^{(3)}_{cab}$ is the sum of rephasing (cba) and nonrephasing (cab) terms that are oppositely phase modulated with τ (Subscripts are time-ordered right to left). If the spectral phases of pulses a and b differ only by the delay, $\phi_b(\omega) = \phi_a(\omega) + \omega\tau$, then the two phase-modulated signals add to produce a purely amplitude-modulated signal without phase shifting the underlying $\chi^{(3)}$ response. $\hat{E}^{(3)}_{2D}$ co-propagates with the following fields: the τ-independent free induction decays $\hat{t}\hat{t}\hat{E}^{(1)}(\omega_t)$ (pulse c) and $\hat{r}'\hat{r}\hat{E}^{(1)}(\omega_t)$ (reference); third-order saturated absorption signals from three interactions each with pulse c, $\hat{t}\hat{t}^*\hat{E}^{(3)}_{ccc}$, and the reference, $\hat{r}\hat{r}^*\hat{E}^{(3)}_{rrr}$; the third-order pump-probe signals from pumps a, $\hat{E}^{(3)}_{caa}$, b, $\hat{E}^{(3)}_{cbb}$, and the reference, $\hat{E}^{(3)}_{crr}$. Except for differences arising from phase matching, third-order fields in Eq. 2.1 are of the form $\hat{E}^{(3)}_{\gamma\beta\alpha} = i\omega_t\chi^{(3)}\vdots\hat{E}_\gamma\hat{E}_\beta\hat{E}_\alpha$

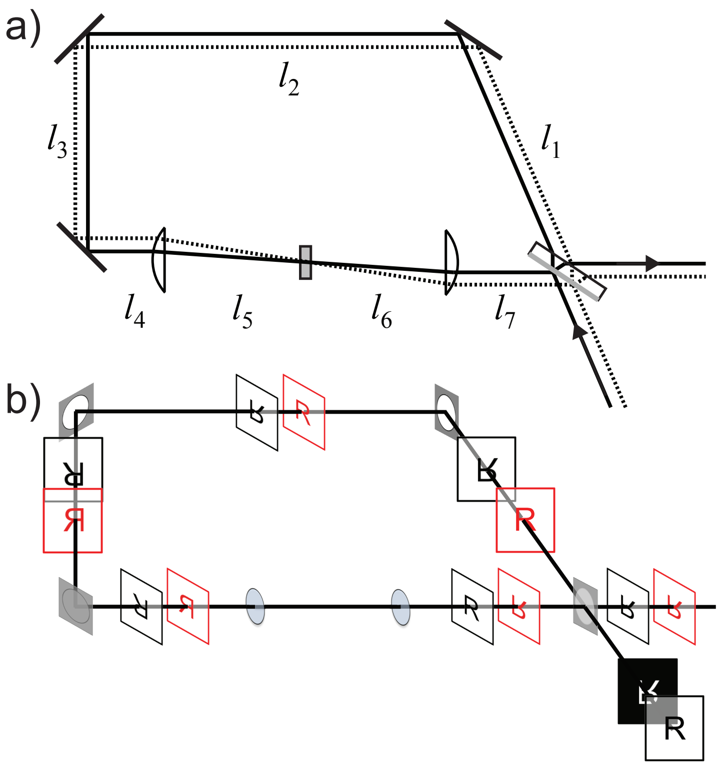

Figure 2.2: (a) Parallel beam paths in the Sagnac interferometer demonstrate the common-path property of counter-propagating beams in the horizontal interferometer plane that contains the symmetry axis of the telescope. Both the dotted and solid beam paths in this plane are precisely the same for beams propagating clockwise and counter-clockwise. At beam center, the interferometer path distances are l1 = 15.5 cm, l2 = 21.0 cm, l3 = 13.5 cm, l4 = 6.5 cm, l5 = l6 = 7.5 cm, and l7 = 4.9 cm; the total path length from the beam splitter to the single mode fiber coupler is 30.8 cm. (b) Perspective showing image propagation through the Sagnac interferometer. The input is a single black letter R at lower right. Clockwise propagating images reflected from the beam splitter are in black. Counter-clockwise propagating images transmitted through the beam splitter are in red (color online). The black R is always positioned behind or to the left of the red R. Dark output images leave the interferometer to the right. Bright output images are shown together as a white R on a black background.

with wavevectors $\vec{k}_s = \vec{k}_\gamma + \vec{k}_\beta - \vec{k}_\alpha = \vec{k}_c$. For $\tau > 0$, $t_a = -T - |\tau|$ and $t_b = -T$; for $\tau < 0$, $t_a = -T$ and $t_b = -T - |\tau|$. The only terms with a τ dependence are one pump-probe field with pulse a or b as pump, $\hat{E}^{(3)}_{PP}(T + |\tau|, \omega_t)$, and the sum of 2D fields, $\hat{E}^{(3)}_{2D}$ [6].

2.3 Results and Discussions

The Sagnac interferometer beam splitter requires careful attention to assure a π phase shift between dark outputs $\hat{t}\hat{t}$ and $\hat{r}'\hat{r}$ while avoiding dispersion. The Brewster's angle beam splitter (Fig. 2.1) has an ∼8-nm thin film of gold deposited on a 1-mm thick BK7 substrate. The refractive index, $\hat{n} = n + ik$, of amorphous gold has $k \approx 25 \times n$ [22] to assure a nearly π phase shift (170-171°, compared to ∼30° with inconel) between dark output pulses ($\hat{t}\hat{t}$ vs. $\hat{r}'\hat{r}$). Destructive interference in the dark output suppresses the in-phase component of the reference pulse, and increases the phase error of the LO as the LO is attenuated. Near 1100 nm wavelength, the beam splitter absorbs 7%, reflects 37%, and transmits 56% of the incident pulse energy, yielding an LO phase error of 15° after accounting for six-fold attenuation.

2D spectra of readily available cyanine dyes were used to test the first femtosecond 2D FT spectrometer [23] and have been replicated in testing new approaches to 2D FT spectroscopy in the visible [24]. Because of this work, the form of the 2D spectrum is known for cyanine dyes, making them suitable for this first demonstration of 2D FT spectroscopy in the short-wave IR. The heptamethine cyanine infrared dye IR-26 has been previously characterized with steady-state absorption and photoluminescence [25][26]. Here, a 30-fs pulse centered at 1100 nm is used to excite and probe dynamics at the red edge of the IR-26 spectrum in dichloroethane using degenerate, partially collinear 2D spectroscopy (flowing sample, 200-μm path length, maximum O.D. $\approx$ 0.7). IR-26 has an excited-state lifetime of 22 ps, which is two orders of magnitude less than the 1.5 ns reference delay in the Sagnac; thus, $\hat{E}^{(3)}_{crr}$ vanishes in Eq. 2.1. Following background subtraction of the τ-dependent pump-probe signals, $\hat{E}^{(3)}_{caa}$

and $\hat{E}^{(3)}_{cbb}$ in Eq. 2.1, a Fourier transform with respect to τ isolates the interference term $\hat{E}^{(3)}_{2D}(\omega_t, \omega_\tau, T) \cdot \hat{E}^{*}_{LO}(\omega_t) + c.c.$; division by $|\hat{E}_{LO}(\omega_t)|$ yields $\hat{S}^{raw}_{2D}(\omega_t, \omega_\tau, T)$.

The phase corrections of 2D spectra are simplified in the partially collinear geometry, because the third pulse also acts as the LO. The only required phase correction in ω_τ arises from the spectral phase difference, $\Delta\phi_{ba}(\omega_\tau)$, between pulses b and a. Characterization of the Mach-Zehnder [15] yields a near-linear $\Delta\phi_{ba}(\omega_\tau)$ that corresponds to the lack of a $\tau = 0$ sampling point in the PZT locking scheme; specifically, $\Delta\phi_{ba}(\omega_\tau) = \omega_\tau\tau_{min}$, where τ_{min} is the τ delay closest to zero. Phase shifting the raw 2D spectrum

$$\hat{S}_{2D}(\omega_t, \omega_\tau, T) = \hat{S}^{raw}_{2D}(\omega_t, \omega_\tau, T) \exp\left[-i\Delta\phi_{ba}(\omega_\tau)\right] \tag{2.2}$$

creates the 2D spectrum that would be generated by sampling at and symmetrically about $\tau = 0$.

In addition, there is also a phase error in the LO due to the complex index of refraction of the Sagnac beam splitter. The detected 2D spectrum, when the LO has a phase ϕ_{LO}, is $Real[S_{2D} \times \exp(i\phi_{LO})]$, which is expressed by Eqn. 2.3. For the ∼8-nm thick gold beam splitter, the determined phase error is ∼0.28 rad from the measurements of the interference (Fig. 2.3). The phase error is assumed to be constant over the bandwidth used in the experiment. To correct for this error, the $\frac{\pi}{2}$ shifted quadrature using the Kramers-Kronig relations was calculated (Fig. 2.4), which is expressed by Eqn. 2.4 [27]. The LO phase error was corrected by multiplying Eqn. 2.4 by $\tan(\phi_{LO})$ and subtracting it from Eqn. 2.3 to eliminate the refractive contribution.

$$S_{2D}(\phi_{LO}) = \cos(\phi_{LO})Real[\hat{S}_{2D}] + \sin(\phi_{LO})Imag[\hat{S}_{2D}] \tag{2.3}$$

$$S_{2D}(\phi_{LO} + \frac{\pi}{2}) = \sin(\phi_{LO})Real[\hat{S}_{2D}] + \cos(\phi_{LO})Imag[\hat{S}_{2D}] \tag{2.4}$$

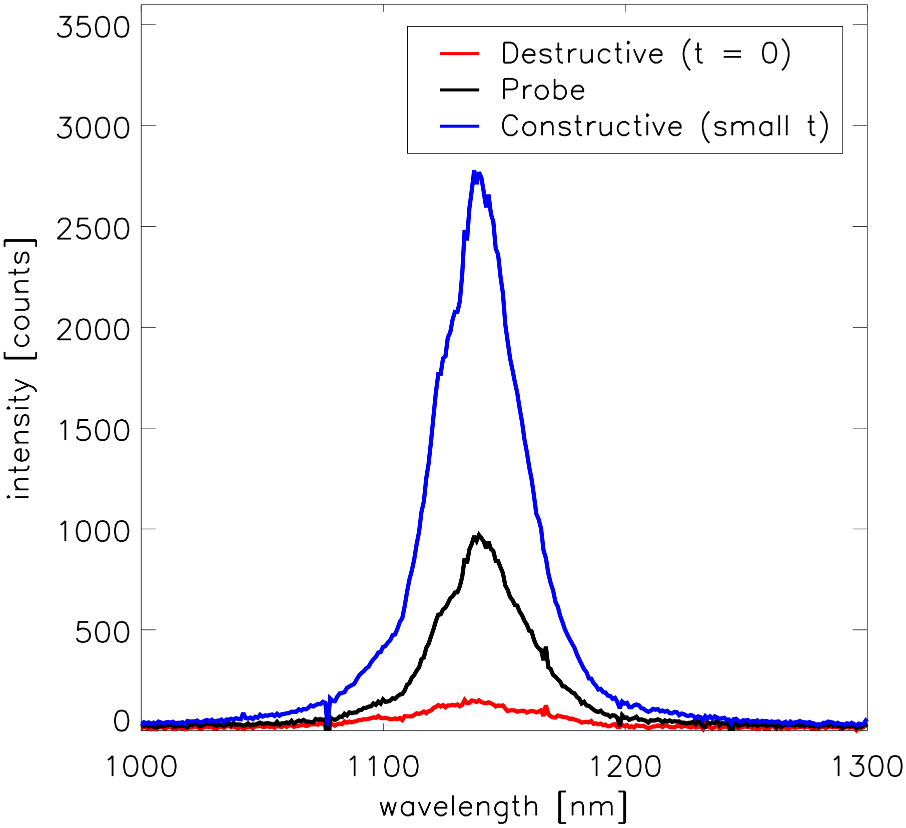

Figure 2.3: Interference of probe (pulse *c*) and reference with the gold beam-splitter used in the Sagnac interferometer. The black curve is the probe without any interference with the reference, obtained by angular misalignment so that the output beams do not overlap. The red curve shows the destructive interference, when the Sagnac interferometer is properly aligned, between the probe and the reference, which results in the attenuated local oscillator used for interfering with the 2D signal. The blue curve is the constructive interference between the two pulses by a small misalignment of the gold beam-splitter in the Sagnac interferometer.

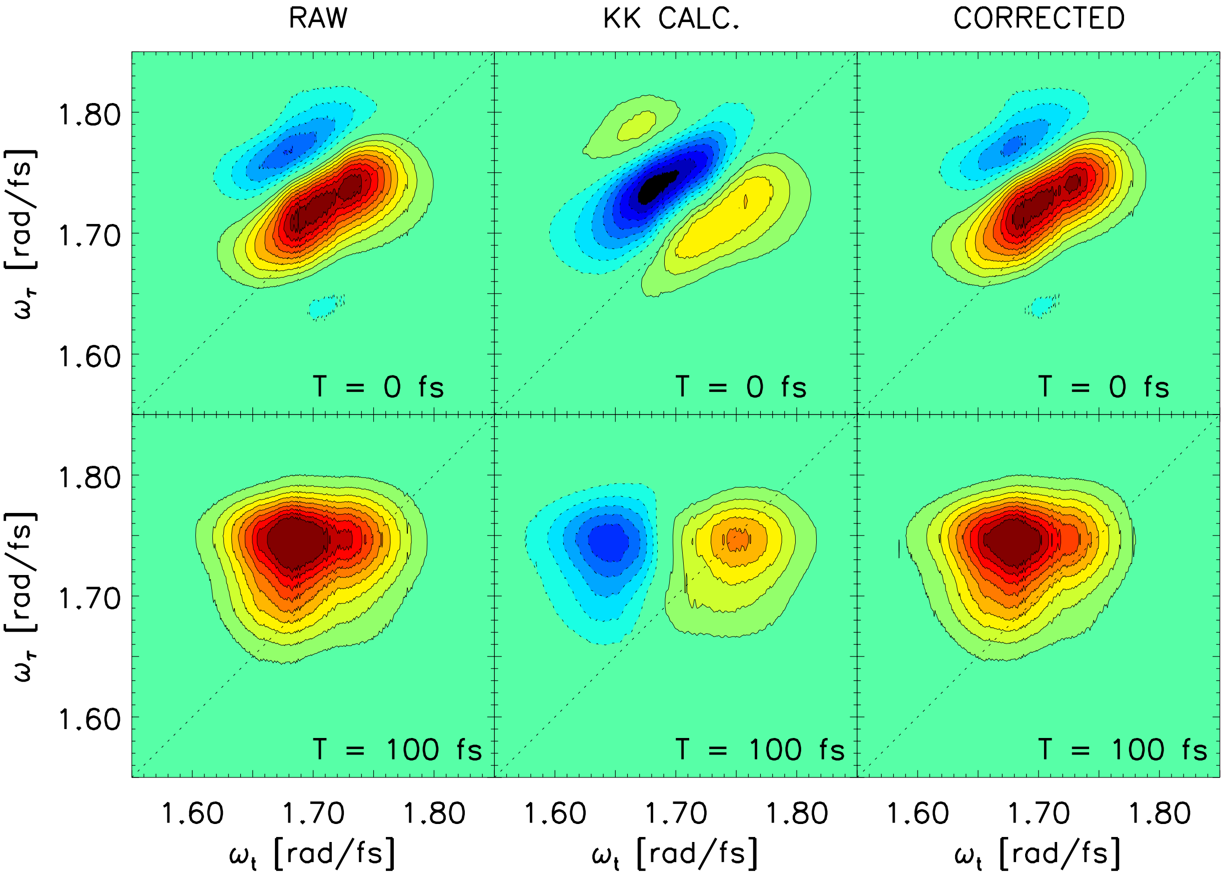

Figure 2.4: LO phase corrected 2D spectra of IR-26. The first column shows the measured, raw, 2D spectra ($Real[S_{2D} \times \exp{(i\phi_{LO})}]$). The second column is the dispersive (imaginary) component of the raw 2D spectra calculated using 2D Kramers-Kronig relations ($Imag[S_{2D} \times \exp{(i\phi_{LO})}]$). The third column is the LO phase corrected 2D spectra. The LO phase corrected T = 0 spectrum shows the peak elongated more on the diagonal, and lessens the negative region above the diagonal. The LO phase correction amounts to less than 5% rms.

The LO phase correction in ω_t using 2D Kramers-Kronig relations amounts to less than 5% rms.

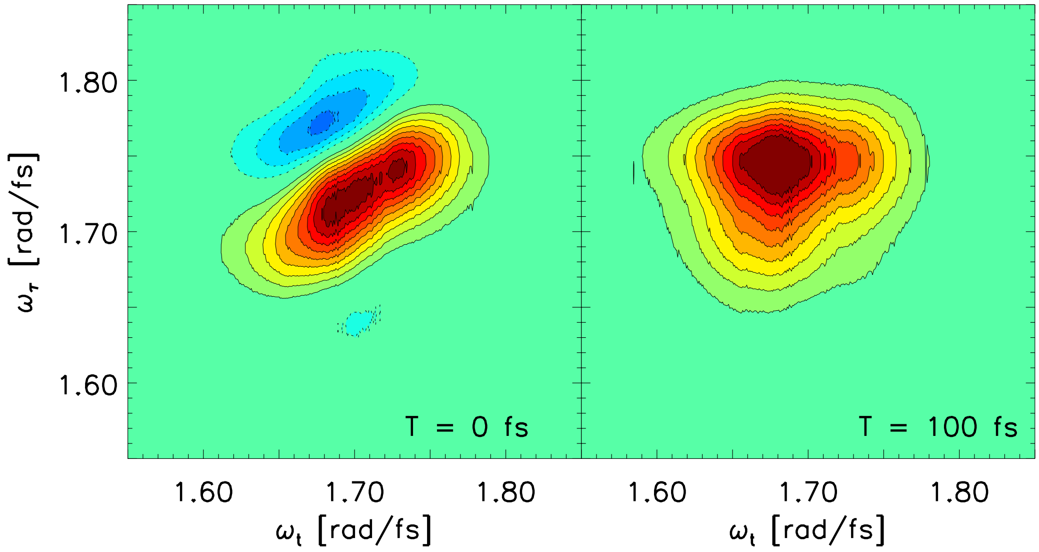

Figure 2.5: Real, T = 0 fs (left) and T = 100 fs (right) 2D correlation spectra of IR-26 in dichloroethane with 30-fs pulses. At zero waiting time, the diagonally elongated positive peak (red 10% contours, solid lines) reflects the strong correlation between the excitation frequency, ω_τ, and signal frequency, ω_t. A negative region (blue 10% contours, dotted lines) indicates vibrational and solvent frequency memory. Only the positive peak remains at 100 fs waiting time; this peak approaches a product line shape after a rapid loss of correlation between ω_τ and ω_t.

The resulting real 2D correlation spectra of IR-26 are shown in Fig. 2.5. In the $T = 0$ spectrum (left panel, Fig. 2.5), the diagonally elongated positive peak reflects the strong correlation between excitation frequency, ω_τ, and detection frequency, ω_t. Also, a slight shift above the diagonal and the off-diagonal, negative (blue) region are indicative of vibrational and solvent frequency memory [6]. By $T = 100$ fs relaxation time, nearly all correlation between ω_τ and ω_t is lost: the peak is purely positive, approaches a product lineshape, and is shifted above the diagonal by the Stokes' shift (right panel, Fig. 2.5). The performance of the 2D spectrometer is verified by agreement between experimental 2D spectra and predicted spectra at large T calculated with absorption line shapes, emission line shapes, and propagation-corrected pulse spectra [23].

The 2D spectra in Fig. 2.5 measure nonlinear response tensor element R_{XXXX}. Although the probe polarization is fixed, the pump pulse polarizations can be varied, for example to measure R_{XXZZ}. Complementary to the Sagnac approach developed here, 2D spectra for tensor elements R_{XZXZ}. and R_{XZZX} have been measured using a polarizer for background suppression [28].

For evaluating whether a beam splitter is useful for 2DFT, one must consider a signal frequency different from that of pulse c (probe). Such contributions to the signal are important in the coherent transient regime (small waiting time, T) and can lead to a 2D phase distortion if the phase of the signal transmitted through the Sagnac varies relative to the phase of the reference. For this reason, we need to compare the signal phase for each contribution to the signal at frequency ω_{sig} generated by ω_c to the LO phase at the signal frequency that it interferes with. This requires a 2D phase map of the following equation.

$$\Delta\phi_{c-sig}(\omega_c, \omega_{sig}) = arg[t(\omega_{sig})t(\omega_{sig}) + r(\omega_{sig})r'(\omega_{sig})] - arg[t(\omega_c)t(\omega_{sig})] \tag{2.5}$$

Figure 2.6 shows the 2D phase map correlating the signal frequency generated by pulse c and the frequency of pulse c. The 2D phase map shows that the error is less than 0.2 rad in the upper right region used for our experiments.

2.4 Conclusion

The optimization of signal detection with a Sagnac interferometer is a useful feature of this 2D spectrometer design. The ∼8-nm thin-film gold Sagnac beam splitter increases the ratio of third-order signal to LO by up to a factor of six compared to the pump-probe geometry. This factor can be reduced (in the case of a large signal) by a slight misalignment of the

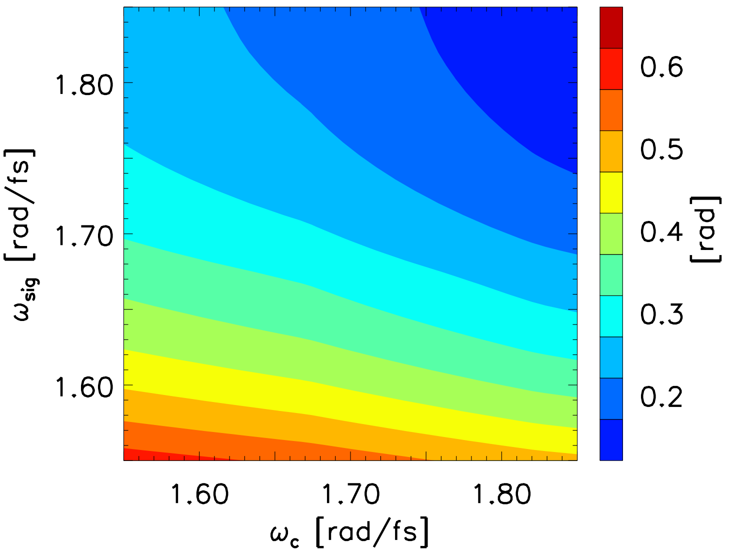

Figure 2.6: 2D phase distortion map for ∼8-nm thick gold beam splitter (Eqn. 2.5). The range of the phase error for the experiment amounts to less than 0.2 radians, which causes minimal phase distortions of the signal in the coherent transient regime.

Sagnac interferometer or increased (for a small signal) by using a beam-splitter coating with more even splitting in a desired frequency range (which requires a more accurate π phase shift in the dark output, obtainable with thin films of Germanium). With suitable beam splitters, extension to 2D spectroscopy with a supercontinuum probe may be possible [29]. While the final transmission through the Sagnac beam splitter attenuates the signal, the LO is effectively attenuated even more: the destructive interference in the Sagnac creates a LO with 1/6 of both the intensity and laser power fluctuations of the original LO (pulse c). The ability to control and reduce the LO intensity would be especially useful in experiments on systems with weak 2D signals. The signal detection improvement, stability, and simplicity of this geometry have opened up a new wavelength region for 2D FT spectroscopy.

2.5 Acknowledgments

We thank Octavi Semonin (NREL) for coating the gold beam splitter and Giulio Cerullo for helpful discussions about the IR NOPA. This material is based upon work supported by the National Science Foundation under Grant No. CHE-1112365.

References

[1] D. M. Jonas, “Two-dimensional femtosecond spectroscopy,” Annu. Rev. Phys. Chem. 54, 425-463 (2003).

[2] W. Kuehn, K. Reimann, M. Woerner, and T. Elsaesser, “Phase-resolved two-dimensional spectroscopy based on collinear n-wave mixing in the ultrafast time domain,” J. Chem. Phys. 130, 164503 (2009).

[3] C. H. Tseng, S. Matsika, and T. C. Weinacht, “Two-Dimensional Ultrafast Fourier Transform Spectroscopy in the Deep Ultraviolet,” Opt. Express 17, 18788-18793 (2009).

[4] D. Brida, S. Bonora, C. Manzoni, M. Marangoni, P. Villoresi, S. De Silvestri, and G. Cerullo, “Generation of 8.5-fs pulses at 1.3 μm for ultrabroadband pump-probe spectroscopy,” Opt. Express 17, 12510-12515 (2009).

[5] M. Levenson and G. Eesley, “Polarization selective optical heterodyne detection for dramatically improved sensitivity in laser spectroscopy,” Appl. Phys. A 19, 1-17 (1979).

[6] S. M. Gallagher Faeder and D. M. Jonas, “Two-dimensional electronic correlation and relaxation spectra: theory and model calculations,” J. Phys. Chem. A 103, 10489-10505 (1999).

[7] E. M. Grumstrup, S. H. Shim, M. A. Montgomery, N. H. Damrauer, and M. T. Zanni, “Facile collection of two-dimensional electronic spectra using femtosecond pulse-shaping technology,” Opt. Express 15, 16681-16689 (2007).

[8] J. A. Myers, K. L. M. Lewis, P. F. Tekavec, and J. P. Ogilvie, “Two-color two-dimensional Fourier transform electronic spectroscopy with a pulse-shaper,” Opt. Express 16, 17420-17428 (2008).

[9] L. P. DeFlores, R. A. Nicodemus, and A. Tokmakoff, “Two-dimensional Fourier transform spectroscopy in the pump-probe geometry,” Opt. Lett. 32, 2966-2968 (2007).

[10] J. Helbing, and P. Hamm, “Compact implementation of Fourier transform two-dimensional IR spectroscopy without phase ambiguity,” J. Opt. Soc. Am. B 28, 171-178 (2011).

[11] W. H. Steel, *Interferometry* (Cambridge University Press, 1967).

[12] R. Trebino and C. C. Hayden, “Antiresonant-ring transient spectroscopy,” Opt. Lett. 16, 493-495 (1991).

[13] S. Dobner, C. Cleff, C. Fallnich, and P. Gross, “Interferometric background reduction for femtosecond stimulated Raman scattering loss spectroscopy,” J. Chem. Phys. 137, 174201 (2012).

[14] K. Misawa and T. Kobayashi, “Femtosecond Sagnac interferometer for phase spectroscopy,” Opt. Lett. 20, 1550-1552 (1995).

[15] T. L. Courtney, S. D. Park, R. J. Hill, and D. M. Jonas, “Broadband, low-dispersion, Brewster’s angle interferometers,” (in preparation).

[16] E. Zeek, K. Maginnis, S. Backus, U. Russek, M. Murnane, G. Mourou, H. Kapteyn, and G. Vdovin, “Pulse compression by use of deformable mirrors,” Opt. Lett. 24, 493-495 (1999).

[17] P. Baum and E. Riedle, “Design and calibration of zero-additional-phase SPIDER,” J. Opt. Soc. Am. B 22, 1875-1883 (2005).

[18] R. Trebino and D. J. Kane, “Using phase retrieval to measure the intensity and phase of ultrashort pulses - frequency-resolved optical gating,” J. Opt. Soc. Am. A 10, 1101-1111 (1993).

[19] M. Zavelani-Rossi, G. Cerullo, S. De Silvestri, L. Gallmann, N. Matuschek, G. Steinmeyer, U. Keller, G. Angelow, V. Scheuer, and T. Tschudi, “Pulse compression over a 170-THz bandwidth in the visible by use of only chirped mirrors,” Opt. Lett. 26, 1155-1157 (2001).

[20] M. K. Yetzbacher, T. L. Courtney, W. K. Peters, K. A. Kitney, E. R. Smith, and D. M. Jonas, “Spectral restoration for femtosecond spectral interferometry with attosecond accuracy,” J. Opt. Soc. Am. B 27, 1104-1117 (2010).

[21] Q. Zhong, X. Zhu, and J. T. Fourkas, “Antiresonant-ring Kerr spectroscopy,” Opt. Express 15, 6561-6568 (2007).

[22] E. D. Palik, *Handbook of Optical Constants of Solids* (Academic Press, 1985).

[23] J. D. Hybl, A. Albrecht Ferro, and D. M. Jonas, “Two dimensional Fourier transform electronic spectroscopy,” J. Chem. Phys. 115, 6606-6622 (2001).

[24] E. Harel, A. F. Fidler, and G. S. Engel, “Real-time mapping of electronic structure with single-shot two-dimensional electronic spectroscopy,” Proceedings of the Natl. Acad. Sci. USA 107, 16444-16447 (2010).

[25] B. Kopainsky, P. Qiu, W. Kaiser, B. Sens, and K. H. Drexhage, “Lifetime, photostability, and chemical-structure of IR heptamethine cyanine dyes absorbing beyond 1 μm,” Appl. Phys. B 29, 15-18 (1982).

[26] O. E. Semonin, J. C. Johnson, J. M. Luther, A. G. Midgett, A. J. Nozik, and M. C. Beard, “Absolute photoluminescence quantum yields of IR-26 dye, PbS, and PbSe quantum dots,” J. Phys. Chem. Lett. 1, 2445-2450 (2010).

[27] The two Kramers-Kronig relations between real and imaginary parts can be written as a single complex relation such as Eq. 1.6.7 of H. M. Nussenzveig, *Causality and Dispersion Relations* (Academic, New York, 1972).

[28] W. Xiong, and M. T. Zanni, “Signal enhancement and background cancellation in collinear two-dimensional spectroscopies,” Opt. Lett. 33, 1371-1373 (2008).

[29] P. E. Tekavec, J. A. Myers, K. L. M. Lewis, and J. P. Ogilvie, “Two-dimensional electronic spectroscopy with a continuum probe,” Opt. Lett. 34, 1390-1392 (2009).

[30] T. L. Courtney, S. D. Park, R. J. Hill, B. Cho, and D. M. Jonas, “Enhanced interferometric detection in two-dimensional spectroscopy with a Sagnac interferometer,” Opt. Lett. 39, 513-516 (2014).

[31] S. D. Park, T. L. Courtney, D. Baranov, B. Cho, and D. M. Jonas, “Sagnac Interferometer for Two-Dimensional Spectroscopy in the Pump-Probe Geometry,” *Ultrafast Phenomena XIX*, edited by K. Yamanouchi, S. Cundiff, R. Vivie-Riedle, M. Kuwata-Gonokami, and L. DiMauro (Springer, New York, 2015), p. 428.

Chapter 3

Optical Inhomogeneity of a PbSe Quantum Dot Ensemble Determined by Two-Dimensional Spectroscopy

3.1 Introduction

Lead chalcogenide semiconductors have low bandgaps in the short-wave infrared, which makes their quantum dots (QDs) particularly interesting for proposed next generation photovoltaics [1][2]. For this reason, many spectroscopic studies have been done on lead chalcogenide QDs to determine quantities such as exciton dephasing rates [3][4], exciton-exciton coupling [5], and hot electron transfer times [6]. In parallel, the synthesis has been developed to achieve QDs with narrow particle size distributions and probe the effect of different surface passivations on the carriers [7][8]. QDs are different from molecules in that different sizes, symmetries, and geometries of QDs occur within a single synthesis batch. All of these properties affect the energy bandgap and fine structure [9][10]. Although it may be subtle, size dispersion is an important parameter in understanding the fundamental dynamics because optical inhomogeneity broadens linewidths through the size dependent bandgap. In applications relying on carrier transport in QD arrays, QD size dispersity results in localized carrier traps from QDs with smaller bandgaps [11] and a decrease in conductivity through the array [12]. Size dispersion is also detrimental in applications utilizing light-emitting properties of QDs [13], such as displays [14], where narrow emission is needed for pure saturated colors.

The quality of a QD batch is customarily judged by the linewidth of the first exciton ($1S_e$-$1S_h$) absorption peak in the linear absorption spectrum and/or the band edge emission peak [13], where narrow linewidths indicate low size-dispersion QD batches. Because of the size dependent QD bandgap, size dispersity is a factor in these optically measured linewidths. The linear absorption spectrum of a QD ensemble is the sum of all the individual QD homogeneous absorption linewidths. One contribution to these linewidths is called fine structure, which conventionally includes all splitting of the bandgap transition, not just the spin-orbit splitting that gives rise to "fine structure" in atoms and molecules. Relaxation of the fine structure levels typically takes place before emission. As a result, ensemble emission linewidths contain different contributions from fine structure than absorption [15].

Particle size distributions are typically determined from transmission electron microscopy (TEM) images. Conventional (low resolution) TEM allows a more or less direct measurement of the QD size, as opposed to optical methods, and the size distribution of a QD ensemble is usually represented by the statistics obtained from TEM measurements [16]. Other techniques for determining the size distribution include dynamic light scattering, small-angle X-ray scattering, field-flow fractionation, and analytical ultracentrifugation [16]. A natural set of questions arises: How does the size inhomogeneity contribute to the ensemble optical linewidths? Can optical inhomogeneity be directly measured and separated from the absorption and emission linewidths? To what extent is optical inhomogeneity represented by the QD size distribution?

Two-dimensional (2D) spectroscopy offers a powerful technique in determining the optical inhomogeneity. 2D spectroscopy is a four-wave mixing technique that is frequency resolved in both excitation and detection. Since 2D spectra are detected at the field level, where contributions from different molecules are additive, a 2D spectrum is a sum over molecular correlation maps between the excitation and detection frequencies at a given relaxation time. In Fourier transform 2D spectroscopy, time and frequency resolution are not experimentally compromised, but both are set by sample properties so that peakshape analysis can be used to probe the interactions between an absorber and all motions that affect the absorption lineshape and relaxation to thermal quasi-equilibrium [17][18]. On the femtosecond timescale, solvent and vibrational configurations can be "frozen" so that they appear as inhomogeneous broadening at short relaxation times and as homogeneous broadening at long relaxation times. In NMR, homogeneous and inhomogeneous broadening are time dependent when "spectral diffusion" arises from spatial diffusion in an inhomogeneous magnetic field [19][20]. The key difference for electronic spectral diffusion is that solvent and vibrational line broadening are *intrinsic* to a single QD/solvent system and can have inertial aspects of time dependent inhomogeneity. Methods of analyzing the relaxation time evolution of dynamically inhomogeneous 2D peaks, such as the center line slope (CLS) method [21] and the peakshape ellipticity method [22], have been developed to extract quantities such as the rate of spectral diffusion at early relaxation times.

At sufficiently long relaxation times, the homogeneous 2D spectrum of a single QD approaches the product lineshape for a homogeneously broadened system because correlation between the excitation and detection frequencies is lost [17][18]. The static size distribution of the QDs will result in an inhomogeneous distribution of energy bandgaps and 2D spectra that persists as inhomogeneity throughout the life of the QD structure. As a result, the 2D spectra always have an inhomogeneous component and never reach a product lineshape.

For lineshape analysis, the absorptive 2D spectrum is required and corresponds to the real part of the complex-valued 2D spectrum. The 2D spectrum of the ensemble is complex-valued and is the inhomogeneous sum over the complex-valued homogeneous 2D spectra for each individual QD. The total real-valued absorptive 2D spectrum is the sum of all the real-valued absorptive 2D spectra because no nonlinear operations are used in processing the absorptive 2D data. Figure 3.1 shows a cartoon 2D spectrum at long relaxation times with a static inhomogeneity. Only real-valued absorptive 2D spectra allow an experimental separation of homogeneous and inhomogeneous broadening. The above statements about additivity do not apply to absolute value 2D spectra, such as those in references [23] and [24], because taking the absolute value is a nonlinear operation.

In this chapter, we determine the optical inhomogeneity of a sample of PbSe QDs using femtosecond 2D Fourier transform spectroscopy by exploiting the additional dimension to separate homogeneous and inhomogeneous broadening contributions to the total ensemble absorption lineshape. Using a deconvolution procedure, we vary the inhomogeneity to find the homogeneous linewidth that simulates the experimental 2D spectrum at long relaxation times.

3.2 Experimental Methods

3.2.1 Sample Synthesis and Preparation

The sample of lead selenide (PbSe) QDs with a bandgap of 1.108 eV and a 145 meV FWHM of the first absorption peak was synthesized from lead (II) oleate and tri-n-octylphosphine selenide (TOPSe) in octadecene-1. The synthesis procedure follows the hot injection procedure reported by the Colvin group [25] with a modification. The modification consists of adding a small amount of diphenylphosphine (DPP) to the selenium precursor before injection, thus adapting the findings of the groups of Bawendi [26] and Krauss [27] who showed that secondary phosphines are responsible for the nucleation of nanocrystals and improve the precursor conversion yields. The details of the synthesis procedure are explained in the

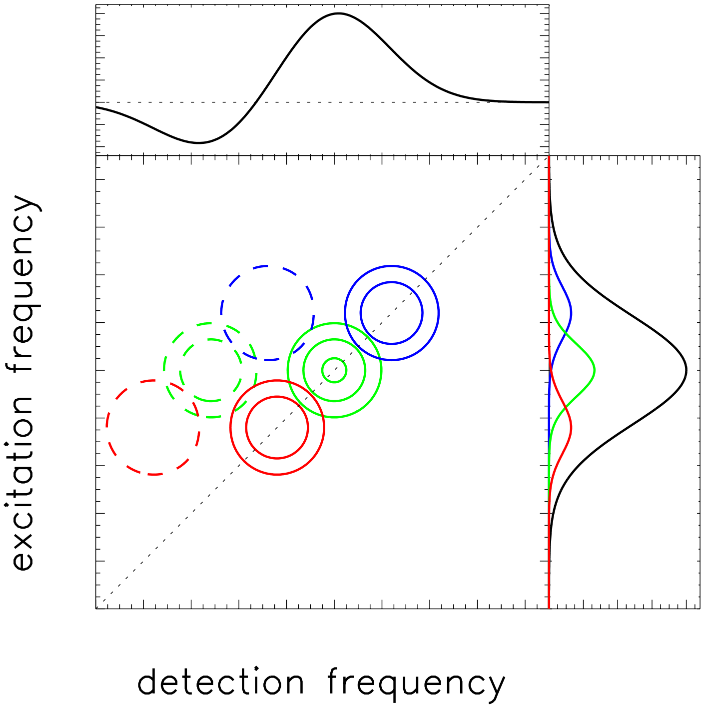

Figure 3.1: Separation of inhomogeneity in 2D spectra. The middle figure shows an example of a 2D spectrum separating out the inhomogeneity. The solid and dashed contours represent the positive and negative peaks, respectively. The figure above the 2D spectrum is the projection onto the detection frequency axis, which is equivalent to the spectrally resolved pump-probe spectrum. The figure on the right of the 2D spectrum is the projection onto the excitation frequency axis to illustrate the separation of the inhomogeneity. The three sets of peaks on the 2D spectrum represent three different transitions arising from QDs with three different sizes. Each of three colored 2D spectra is a homogeneous 2D spectrum. The 2D spectrum including inhomogeneity is the sum of all the 2D spectra for each individual QD. In the limit where the negative peaks are much closer to the positive peaks, the inhomogeneous distribution will increase the partial cancelation of positive and negative peaks in the projection of the 2D spectrum and give an inaccurate determination of the frequency separation between the positive and negative signals.

Appendix. The diameter and size distribution of the PbSe QDs are approximately 3.62 ± 0.40 nm as calculated from TEM images by measuring the area of individual particles and assuming that the particles cast circular shadows. The TEM resolution for the images were approximately 0.135 nm and 0.1 nm per pixel. This nominal single diameter is reported here only because it is determined by the same method used for the sizing curve of references [28], [29], and [30]. Reference [30] used the same PbSe QD synthesis as ours, while a different lead source (lead (II) acetate trihydrate) and solvent (diphenyl ether) were both used for the synthesis described in references [28] and [29]. For the particles used here, the shapes in the TEM images are apparently irregular. Analyzing the TEM shadow distribution assuming the particles cast ellipsoidal shadows yields measured major and minor projections of 4.15 ± 0.52 nm and 3.13 ± 0.42 nm, respectively. For ellipsoidal particles with three unequal principal axes, these measured shadow projection distributions would be larger than the principal axis length distribution of the particles.

Stationary PbSe QDs in tetrachloroethylene (TCE) were prepared with an optical density of 0.3 at the bandgap for an optical path length of 200-microns. A commercial 200 μm pathlength Starna flow cell (48-Q-0.2) was modified with air-tight valves at the ends of each flow tube to minimize the exposure of the sample to air during data collection. This experiment on a stationary sample probably has repetitive excitation artifacts from a long-lived photoproduct that is usually attributed to “charging” quantum dots [31]. Since charged dots also have bandgaps with the same size dependence, they are expected to increase the optical inhomogeneity. Another systematic error is expected to increase the measured optical inhomogeneity (see below) so this 2D measurement is expected to give an upper bound.

The excitation pulse energies at the sample position were too low to measure with the joule meter (Molectron J5-09-2k). Based on the energy measured before entering the 2D spectrometer (∼500 nJ) and the reflective and transmissive properties of the inconel-coated beam splitters in the 2D spectrometer, the excitation pulse energies at the sample position were estimated to have an upper bound of ∼10 nJ. The beam size before the focusing lens was measured to have a $1/e^2$ diameter of ∼1.5 mm. With a beam diameter of 1.5 mm, a focal length of 75 mm, and a pulse center wavelength of 1.15 μm, the diffraction limited FWHM beam waist was calculated to be ∼90 μm. Using the estimated beam spot size, estimated pulse energy, measured pulse spectrum, and the determined frequency dependent extinction coefficient, the excitation probability was calculated to be less than 0.10. This means that $\lesssim 1/10$ of the excited quantum dots are doubly excited, so that (if the signal is proportional to the number of excitations) $\gtrsim$ 80% of the signal arises from singly excited quantum dots.

3.2.2 Experimental Apparatus

In this experiment, pulses from a 1 kHz Ti:Sapphire regenerative amplifier pump a single-pass, short-wave infrared (IR) noncollinear optical parametric amplifier (NOPA) with a PP-SLT crystal [32]. The pulses used for this experiment have energies of 2.6 μJ with a stability better than 0.5% directly out of the NOPA. The pulse then enters a deformable mirror grating compressor. After the compressor, the beam is spatially filtered with a 150 μm pinhole that acts to suppress frequency-dependent angular deviations from the deformable mirror during adaptive pulse compression. Pulse compression is accomplished by optimizing second harmonic generation (SHG) at the sample position with the deformable mirror using a genetic algorithm [32][33]. The pulse energy measured after the pinhole is about 650 nJ with stabilities better than 1%. Pulse durations of ∼25 fs are determined by autocorrelation and SHG frequency-resolved optical gating (FROG) [34]. All measurements of infrared spectra used single-mode fiber coupling (Thorlabs 1060 XP, NA = 0.14) in to a 0.15-m Czerny-Turner spectrograph (Princeton Instruments SP-2150i) with a liquid nitrogen cooled 1024x1 pixel InGaAs array (Princeton Instruments OMAV:1024-2.2).

The 2D spectrometer consists of an actively stabilized Mach-Zehnder interferometer and a Sagnac interferometer [35][36][37]. The Mach-Zehnder interferometer is described in Chapter

4 of this thesis, which remained unmodified in the new 2D apparatus. In the Mach-Zehnder interferometer, broadband, inconel-coated, glass windows [38][39] are used as beam splitters that exploit the air-glass interface Brewster's angle to prevent additional surface reflections and their interference. The bright output of the Mach-Zehnder interferometer creates a pump-pulse pair (pulses a and b) with a delay, τ, that is roughly controlled by computerized translation stages. Interferometric feedback from a red helium-neon (HeNe) laser is used to drive a piezoelectric transducer in one interferometer arm to lock τ with 0.7-nm stability during the 1 s integration time for collection of one interferogram. Actively stabilized steps in τ are taken by locking at each successive integer plus a quarter cycle of the red HeNe wavelength [35]; a co-propagating yellow HeNe laser is used to measure lock stability and track τ during a 2D scan. The yellow HeNe interference is a sensitive indicator used to prevent any skipped or redundant steps in the τ sampling in the LabVIEW data acquisition program.

The Sagnac interferometer is the same one described in Ref. [36], and was not modified for this experiment. The beam entering the Sagnac interferometer is split into counterpropagating probe (c, transmitted) and reference (ref., reflected) pulses in a Brewster's angle Sagnac interferometer with a gold-coated beam splitter. The off-axis collinear pump-pulse pair with delay $\tau = t_b - t_a$ impinges on the sample, followed by pulse c at the computer-controlled relaxation time, T, thus generating various nonlinear signals. The reference pulse recombines with pulse c (and the nonlinear signals) at the gold-coated beam splitter and destructively interferes to yield an attenuated local oscillator for enhanced interferometric detection [36][37]. At a given T, τ is scanned symmetrically and a spectrum is acquired at every τ delay [38]. The spectra are directly measured through the spectrograph to give the detection frequency axis and the 2D spectrum is generated by Fourier transforming the symmetric τ scan for the excitation frequency axis.

3.3 Calculations

The QD sample studied here has a static inhomogeneity from the size distribution, which broadens the absorption lineshape. In a 2D spectrum, the inhomogeneity causes peakshape elongation along the diagonal because the 2D spectra are additive and proportional to the number of molecules [17]. For a homogeneously broadened system, the 2D spectrum would become a product lineshape at relaxation times sufficiently long that no correlation remains between the excitation and detection frequencies. In this limit, the homogeneous 2D spectrum can be calculated using the experimental pulse spectrum, absorption lineshape, and emission lineshape [18]. The simulation of the 2D spectrum for the QD sample at a sufficiently long relaxation time requires a deconvolution of the inhomogeneity in the absorption lineshape from the measured linear absorption spectrum, a calculation of the homogeneous 2D spectrum for many members of the ensemble, and a sum over the individual homogeneously broadened 2D spectra. The inhomogeneity used for deconvolution and 2D summation is varied to match the experimental 2D spectrum. Simulations show that the absolute quantities of a few parameters do not alter the 2D nodal line slope signature of inhomogeneity, which supports this new method of determining the inhomogeneous static size distribution and the homogeneous linewidth.

3.3.1 Deconvolution Procedure

The experimentally measured linear absorption spectrum of QDs is broadened by the homogeneous linewidth of individual QDs and the inhomogeneous static size distribution. The most general form for the absorption lineshape including inhomogeneity can be represented as

$$g_{abs}^{tot}(\omega) = \sum_{i}^{N} g_{abs}^{i}(\omega), \tag{3.1}$$

where g_{abs}^{tot} is the total absorption lineshape of the inhomogeneously broadened ensemble, $g_{abs}^{i}(\omega)$ is the homogeneous absorption lineshape of the i^{th} QD, and N is the total number of QDs. Eqn. 3.1 allows each QD to have a homogeneous spectrum that depends on its detailed molecular structure and not just on its bandgap; a dependence of the homogeneous fine structure on lead salt QDs has been calculated from semi-empirical tight-binding methods by Goupalov and co-workers [9]. A simpler model, motivated by the effective mass approximation, assumes that the 1S$_e$-1S$_h$ bandgap uniquely determines the spectrum [10]. Assuming that the bandgap uniquely determines the spectrum, the total absorption lineshape can be expressed as

$$g_{abs}^{tot}(\omega) \approx \int_{-\infty}^{\infty} p(\omega_{eg}) g_{abs}^{homo}(\omega_{eg}, \omega)\, d\omega_{eg}, \tag{3.2}$$

where $p(\omega_{eg})$ is the inhomogeneous probability distribution (normalized so that $\int_{-\infty}^{\infty} p(\omega_{eg})\ d\omega_{eg} = 1$) of the QD 1S$_e$-1S$_h$ bandgap ω_{eg}, and $g_{abs}^{homo}(\omega_{eg}, \omega)$ is the homogeneous absorption lineshape of a QD with 1S$_e$-1S$_h$ bandgap of ω_{eg}. Eqn. 3.2 allows for exciton bandgaps to scale differently with size at different points of the Brillouin zone [4][40]. The stronger assumption that will be used in this chapter is that QDs with different 1S$_e$-1S$_h$ bandgaps all have exactly the same homogeneous absorption lineshape. In this case, Eqn. 3.2 can be further simplified to a convolution of the homogeneous lineshape with the inhomogeneous distribution, $p(\omega_{eg})$, expressed as:

$$g_{abs}^{tot}(\omega) \approx \int_{-\infty}^{\infty} p(\omega_{eg}) g_{abs}^{homo}(\omega - \omega_{eg})\, d\omega_{eg}, \tag{3.3}$$

where $g_{abs}^{homo}(\omega - \omega_{eg})$ is the absorption lineshape of a single QD with a bandgap of ω_{eg}. If all QDs in the ensemble have the same fine structure, the convolution assumption in Eqn. 3.3 would be a reasonable approximation for this experiment because the pulse spectrum probes only the first exciton (1S$_e$-1S$_h$) absorption peak for a small range of QD sizes. We regard the convolution assumption as justified more by the need to start somewhere, but note it could be justified if the probability distribution for the different fine structures were the same for all bandgaps in the ensemble.

To simulate the 2D spectrum at long relaxation times, a deconvolution procedure is used to obtain a homogeneously broadened absorption lineshape for the PbSe QDs, $g_{abs}^{homo}(\omega)$ (Eqn. 3.3). We assume a Gaussian distribution of QD bandgaps. Figure 3.2 shows the homogeneous absorption lineshape of a single QD assuming a Gaussian bandgap inhomogeneity with a standard deviation of 36 meV. The details of the deconvolution procedure are explained in the Appendix (Section 3.7.3).

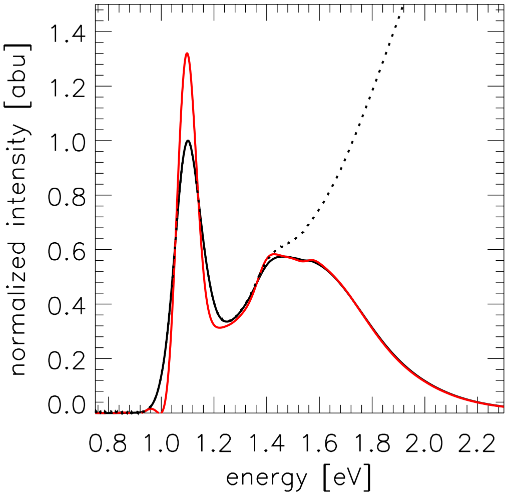

Figure 3.2: Deconvolved absorption lineshape used for simulating the 2D spectrum at long relaxation time. The dotted black line shows the measured absorption lineshape, including the monotonic rise of bulk-like absorption at high photon energy. The black solid line shows the area normalized total absorption lineshape after filtering to remove the high energy absorption so that the bandgap transition can be deconvolved. The red line shows the deconvolved area normalized absorption lineshape, which is only valid in the bandgap region where the measured (dotted black) and filtered (black) lineshapes agree.

3.3.2 Long T 2D Spectrum Simulation

For a homogeneously broadened system at long relaxation times, the 2D spectrum has a product lineshape, in which the excitation and detection frequencies are no longer correlated. In this limit, the 2D spectrum can be calculated from the projections onto the excitation and detection frequency axes. Using the homogeneous absorption lineshape retrieved from the previous section, the total 2D spectrum is an inhomogeneous sum of the uncorrelated homogeneous 2D spectra. For each QD size, the ω_τ projection $A(\omega_\tau)$, accounting for the gradual (and frequency dependent) attenuation of the exciton pulses throughout the sample, is constructed from

$$A_i(\omega_\tau) = g_{abs}^{homo,i}(\omega_\tau) I_{ab}(\omega_\tau) \frac{1-\exp[-2\omega_\tau \kappa(\omega_\tau) l/c]}{2\omega_\tau \kappa(\omega_\tau) l/c}, \tag{3.4}$$

where $g_{abs}^{homo,i}(\omega - \omega_{eg})$ is the homogeneous absorption lineshape for the i^{th} sized QD determined by deconvolving the measured linear absorption spectrum from equation 3.3; the absorption lineshapes only differ by the bandgap, ω_{eg}. $I_{ab}(\omega_\tau)$ is the excitation pulse intensity spectrum at the sample entrance, κ is the imaginary part of the complex-valued refractive index, l is the sample pathlength, and c is the speed of light in vacuum. The ω_t projection, $B(\omega_t)$, accounting for attenuation through sample absorption is:

$$B_i(\omega_t) = [\mathrm{w}_{abs} \cdot g_{abs}^{homo,i}(\omega_t) + \mathrm{w}_{ems} \cdot g_{ems}^{homo,i}(\omega_t) - \mathrm{w}_{esa} \cdot g_{esa}^{homo,i}(\omega_t)] I_c(\omega_t) \exp[-2\omega_t \kappa(\omega_t) l/c], \tag{3.5}$$

where $g_{ems}^{homo,i}(\omega)$ is the homogeneous emission lineshape as deconvoluted from the measured photoluminescence spectrum (PL), $g_{esa}^{homo,i}(\omega)$ is the homogeneous excited state absorption (ESA) lineshape (assumed to be a red-shifted homogeneous absorption lineshape), and w_{abs}, w_{ems}, and w_{esa} are the weights for the corresponding lineshapes. It is assumed that the homogeneous emission redshift for each member of the ensemble is the same as the redshift between absorption and PL. Another assumption is made that the absorption from the first excitation to the second exciton has the absorption lineshape, but redshifted,

$$g_{esa}^{homo,i}(\omega_t) = g_{abs}^{homo,i}(\omega_t + \Delta), \tag{3.6}$$

where Δ is the ESA redshift. The real part of the 2D spectrum is then obtained by summing over the outer products of the two projections:

$$\hat{S}_{2D}(\omega_t, \omega_\tau) = \sum_i^N A_i(\omega_\tau) \times B_i(\omega_t). \tag{3.7}$$

where N is the total number of QDs. The 2D spectrum including inhomogeneity is the sum of all the homogeneous 2D spectra for each individual QD.

3.4 Results and Discussions

3.4.1 TEM Analysis

TEM images were collected for our sample of PbSe QDs for size distribution analysis and high resolution TEM (HRTEM) images were collected to visualize the facets, lattices, and shapes of individual QDs. Figure 3.3 shows sample HRTEM images of the PbSe QDs used in this analysis. The particles are not spherical, but faceted and irregular, which makes the analysis with a single diameter wrong for these samples. For comparison with prior work, the size distribution of $N = 1512$ particles is calculated by assuming the particles to be spherical to estimate the bandgap distribution. The procedure for analyzing the TEM image is explained in detail in the Appendix but closely follows the methods reported by Tisdale and co-workers [41] and Segets *et al.* [42].

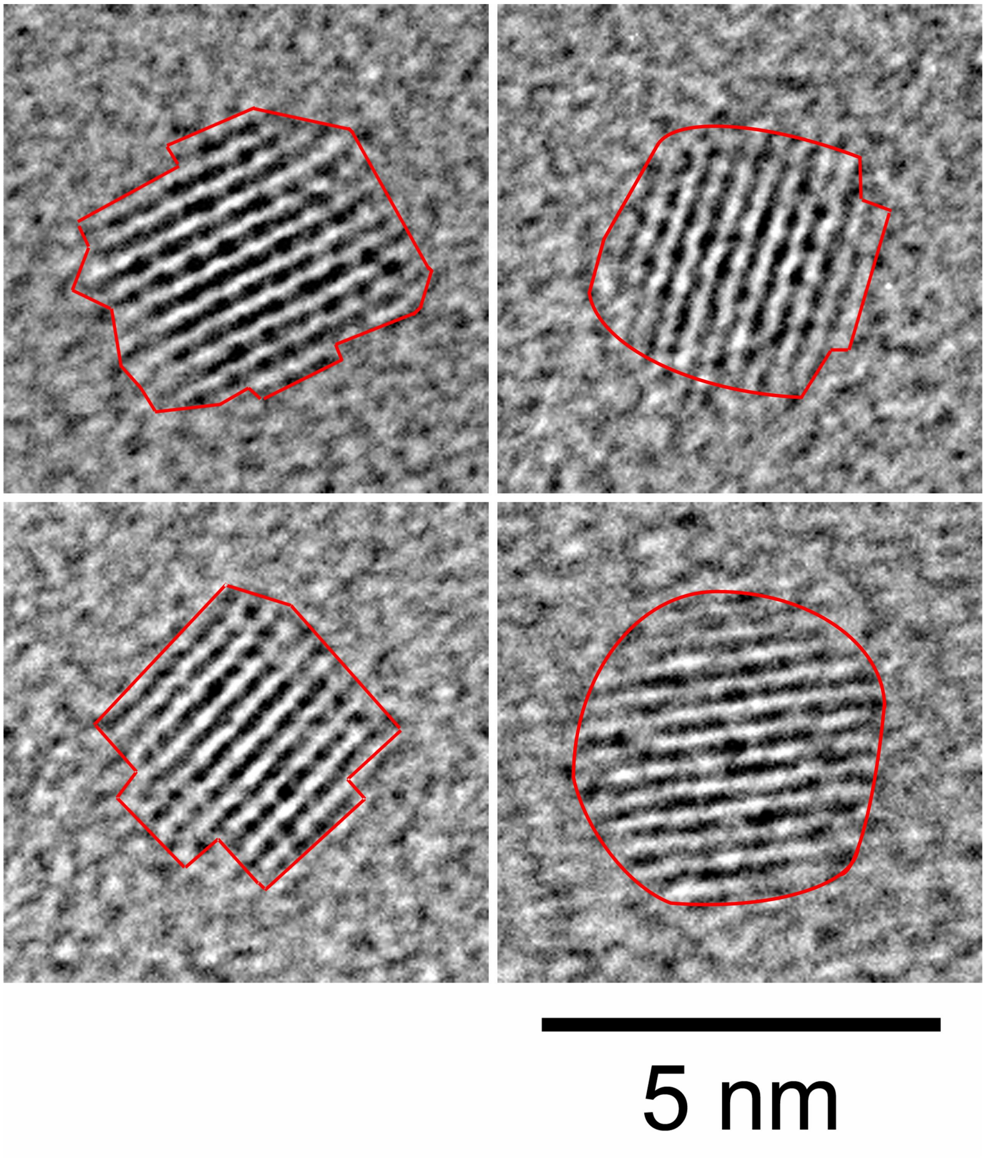

Figure 3.3: Four HRTEM images of nominal 3.62 ± 0.4 nm diameter PbSe QDs. The top two and lower left images appear to show nanocrystals with irregular facets or surface layers. The nanocrystal at lower right appears to be roughly spherical. The image resolution is 0.028 nm per pixel. (Ellipsoidal measured major and minor projection distributions are 4.15 ± 0.52 nm and 3.13 ± 0.42 nm, respectively).

Given the mean particle diameter of 3.62 nm and a standard deviation of 0.40 nm, multiple sizing curves for PbSe QDs [28][29][30][43] that relate the particle size to the energy bandgaps were used to determine the bandgap energy distribution. Even assuming a delta function homogeneous lineshape for each size QD, all the sizing curves yield a bandgap energy distribution wider than the measured linear absorption spectrum as shown in Fig. 3.4. The sizing curve from Ref. [29] yields the closest agreement, with a calculated linewidth of ∼153 meV compared to our measured linear absorption spectrum of ∼145 meV. Furthermore, measured single-molecule linewidths of 85 meV at room temperature for 3 nm diameter PbS QDs [44], enlarge the disagreement between the absorption lineshape calculated using the size distribution inhomogeneity determined from TEM images. Including the homogeneous linewidth and ignoring its size dependence, the calculated total absorption linewidth would have a FWHM of ∼175 meV. Assuming ellipsoidal particles, and using the minor diameter to calculate the bandgap, the minor diameter distribution results in a slightly larger energy bandgap distribution. This is an overestimate because the bandgap depends on all three principal axes and because, for ellipsoids with three unequal principal axes, the measured minor axis projection will have a larger distribution than the true minor axis distribution. Still, the discrepancy is large enough that this likely indicates a problem with the TEM images or analysis.

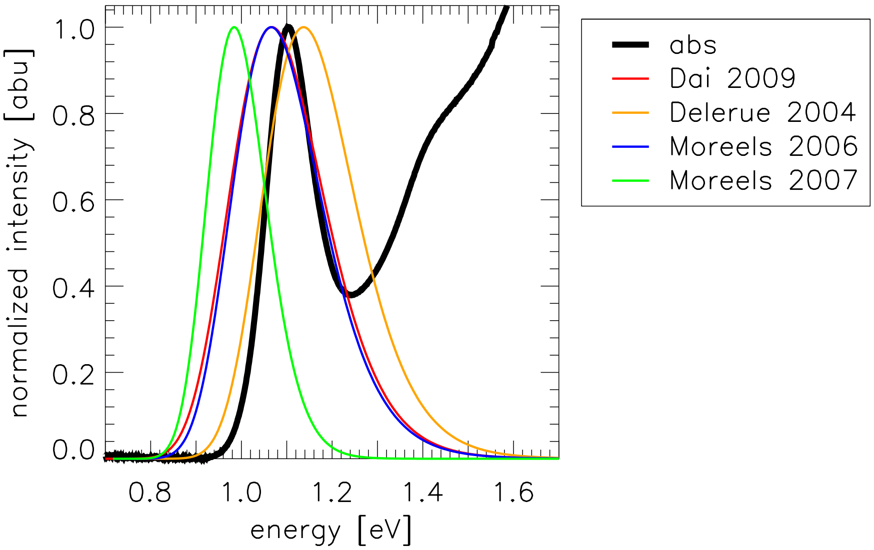

Figure 3.4: Inhomogeneous energy bandgap distribution calculated using multiple sizing curves for PbSe QDs and assuming a spherical shape. The black solid line shows the linear absorption spectrum and the colored lines show calculated energy bandgap distributions. All the energy bandgap distributions from the inhomogeneous spherical particle fit to TEM images are wider than the linear absorption spectrum. The closest width is the green curve (Moreels *et al.* [29]), which has a FWHM of ∼153 meV compared to the experimental FWHM of ∼145 meV.

Assuming the particles cast ellipsoidal shadows, the major and minor projections were measured to be 4.15 ± 0.52 nm and 3.13 ± 0.42 nm, respectively, from TEM images. Using these values for the principal axes of an ellipsoid, we simulate the 2D shadow projection distribution for an ensemble of ellipsoids by uniformly sampling the particle orientation using the algorithm of references [45] and [46] (see Appendix). This simulation of the projection distribution double counts the projection effect because the projection distribution is used as a principal axis distribution and then projected. The simulations show good agreement with the experimental 2D minor and major diameter correlation map assuming a prolate ellipsoid, but not an oblate ellipsoid. For a particle in a 3D box with unequal sides a, b, and c, the zero-point (quantum confinement) energies correspond to cubic box energies with an effective size D_{eff} given by

$$\frac{3}{D_{eff}^2} = \frac{1}{a^2} + \frac{1}{b^2} + \frac{1}{c^2} \tag{3.8}$$

assuming $a = 4.15 \pm 0.52$ nm, $b = 3.13 \pm 0.42$ nm, and $c = 3.13 \pm 0.42$ gives $D_{eff} = 3.38 \pm 0.27$ nm. With this assumption, the effective (average) diameter of an ellipsoidal or rectangular box was calculated to be 3.38 ± 0.27 nm. The main reason for the smaller error in the effective diameter is that all three dimensions of the box are assumed to have independent errors. Using this as the spherical diameter and distribution in the sizing curves generates the energy bandgap distribution in Fig. 3.5. The effective diameter and standard deviation which are justified as giving confinement energies for a particle in a 3D box, show a better agreement with the measured linear absorption spectrum. The narrowest energy gap distribution is that of Moreels *et al.* [29] with a FWHM of ∼110 meV, corresponding to a standard deviation of ∼47 meV. This is narrower than the absorption linewidth of ∼145 meV FWHM.

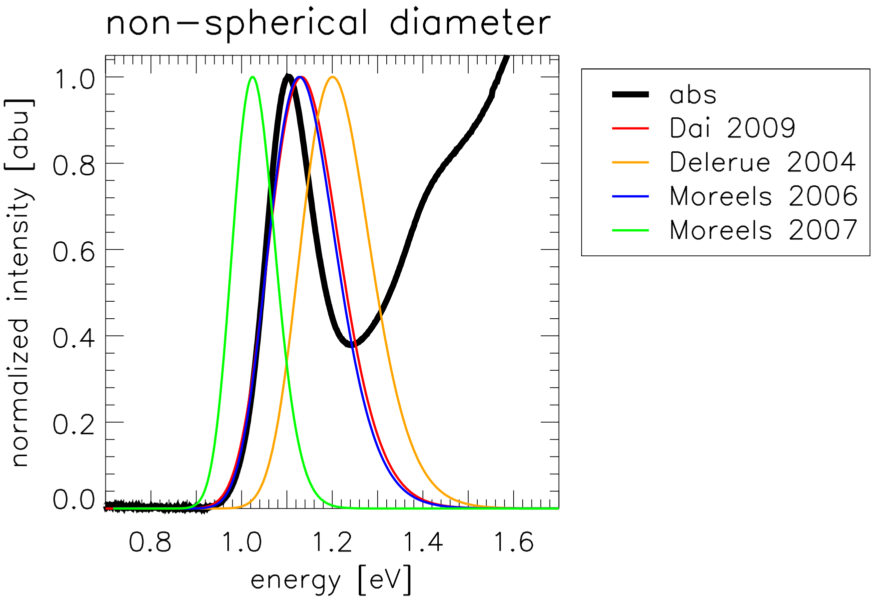

Figure 3.5: Inhomogeneous energy bandgap distribution calculated using multiple sizing curves for PbSe QDs and assuming non-spherical shapes. The black solid line shows the linear absorption spectrum and the colored lines show calculated energy bandgap distributions.

3.4.2 Long T 2D Spectrum of PbSe QDs

The second panel of Fig. 3.6 shows the experimental 2D spectrum of the PbSe QDs at a relaxation time at $T = 1$ ps. The origin of the negative peak to the left of the diagonal shown in Fig. 3.8 is not certain. Several reports attribute negative peaks in spectrally resolved pump-probe (SRPP) to excited state absorption, which is red-shifted from the single exciton transition energy by the bi-exciton binding energy, Δ_{XX} (i.e. Δ in Eqn. 3.6 $= \Delta_{XX}$). The projection of the 2D spectrum onto the detection axis (ω_t) results in the SRPP signal and is shown in the third panel of Fig. 3.6. The bottom panel of 3.6 shows the SRPP divided by the pulse intensity spectrum with the ground state bleach (GSB - increased transmission) positive signal and excited state absorption (ESA - decreased transmission) negative signal peak maxima both captured. The SRPP signal, obtained from the 2D spectrum, when divided by the pulse spectrum at $T = 1$ ps yields a separation between the positive and negative peaks of approximately 0.1 eV and a measured signal extremum ratio a little less than 2:-1, which agree with previously reported transient absorption measurement by Ruhman and co-workers at a time delay, $T = 1$ ps [47]. The excited state absorption has also been attributed to absorption from trap states [31][48][49][50][51][52]. As in these prior experiments, our samples were stationary during the experiment, which may lead to photo-charge accumulation that alter the interactions inside QDs [53][54][55]. However for this study, the negative peak and the positive peak combine to conveniently create a straight nodal line that can be used to precisely measure the tilt of the 2D lineshape. The tilt helps determine the amount of inhomogeneity that is convoluted in the linear absorption spectrum.

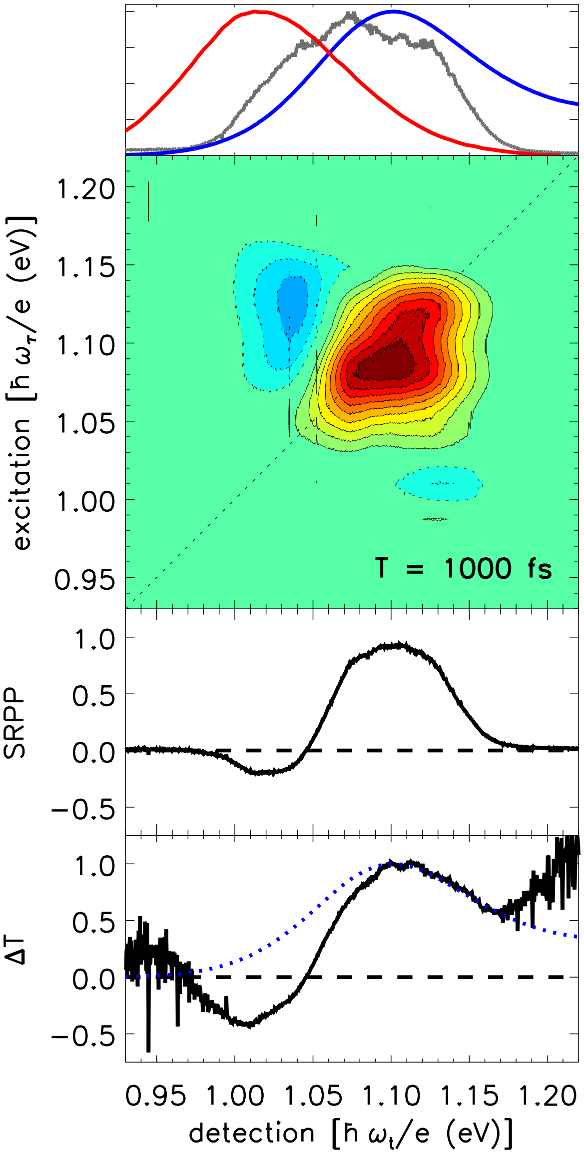

Figure 3.6: 2D spectrum of PbSe QDs with projection onto ω_t at a relaxation time of $T = 1$ ps. (First panel) Pulse spectrum (grey) and the linear absorption (blue) and PL (red) of PbSe QDs (3.62 ± 0.40 nm diameter). (Second panel) Experimental 2D spectrum with ±10% contour levels. The red (solid) contours show positive amplitudes and blue (dashed) contours show negative amplitudes. (Third panel) Normalized spectrally resolved pump-probe signal calculated by projecting the 2D spectrum onto ω_t (i. e. integrating over ω_τ). (Fourth panel) Normalized ΔT obtained by dividing the SRPP signal at $T = 1$ ps by the pulse intensity spectrum. The dotted blue line shows the linear absorption spectrum of the PbSe QDs normalized to the first exciton peak.

3.4.3 Long T 2D Spectrum Simulations of PbSe QDs

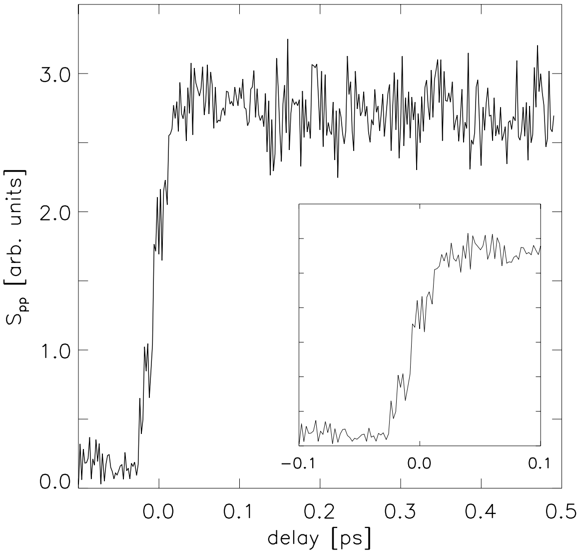

Figure 3.7: Integrated pump-probe signal for PbSe QDs acquired on the same day of the 2D experiment. The inset zooms in on the early rise of the pump-probe signal. The pump-probe signal does not show any decay in the first 500 fs, indicating that all dynamics will have relaxed by 1 ps.

At a relaxation time of 1 ps, Johnson *et al.* [56] reported that fine structure relaxation was experimentally complete for 5 nm diameter PbSe QDs. Their reported trend is that fine structure relaxation becomes faster as size decreases [56]. The following analysis assumes complete fine structure relaxation, which is consistent with our measured integrated pump-probe signal shown in Fig. 3.7. In our measured integrated pump-probe signal on the same day and on the same sample as our 2D experiment, there is no decay or dynamics in the first 500 fs. This indicates that all dynamics will have relaxed by 1 ps, which justifies our analysis of the 2D spectrum at $T = 1$ ps to be sufficiently relaxed. Furthermore, previous reports using transient absorption measurements [47] do not yield a negative peak at delays longer than 1 ps. 2D spectra without a negative peak will not have a nodal line between the positive and negative peaks, so the analysis of static inhomogeneity will be more difficult. For an incomplete fine structure relaxation, the inhomogeneity determined through our analysis can only be an over estimate, that is an upper bound on the optical inhomogeneity that would agree better with the TEM size distribution than the smaller, true inhomogeneity.

Assuming that the increased absorption is due to bi-excitons, the weights for each of the lineshapes used in the simulation are conventionally considered to be 1, 49/64, and 1/64 for w_{abs}, w_{esa}, and w_{ems}, respectively. The considerations justifying these weights below have been used by Trinh *et al.* [57] and Nair *et al.* [58]. These weights are conventionally determined by the following assumptions: (1) There are 4 equivalent L-point valleys for the rock-salt structure, which results in 4-fold degenerate molecular orbitals for the HOMO and LUMO. Thus, the HOMO and LUMO are each 8-fold degenerate including spin, making a total of 64 possible singly excited states. (2) Complete fine structure relaxation leads to thermal quasi-equilibrium, in which all fine structure states are equally populated. (3) The strengths are, on average, unaffected by the coupling that gives rise to energetic shifts such as the bi-exciton binding energy. Assumptions (1) - (3) determine the following weights. (i) There are 8 bright states in one-photon absorption and emission that have electrons and holes in corresponding valleys with the same spin (signal strength = 8). (ii) After excitation and fine structure relaxation, there is a 1/8 probability that any of the 7 unexcited electrons can be promoted by ESA (signal strength = 7) and a 7/8 probability that Pauli blocking allows only 6 of the 7 unexcited electrons to be promoted by ESA (signal strength = 6). Dividing by the GSB signal strength of 8, the weighted average signal for these two leads to a net relative ESA strength of 49/64. (iii) After fine structure relaxation, there is a 1/8 probability for bright excited state emission (signal strength = 1). Dividing by the GSB signal strength of 8 gives a weighted net relative ESE strength of 1/64. These weights for the separate transitions were used by Zhu and co-workers [57] to extract the bi-exciton binding energy from spectrally resolved experiments. For comparison, the weight ratio before any relaxation depends on orientational factors not included above (see Chapter 5) and gives larger weights to ESE and ESA.

Figure 3.8 compares the experimental 2D spectrum to simulations with 3 different inhomogeneities for an ESA redshift of 140 meV. As the inhomogeneity is increased, the simulated 2D spectrum approaches the static inhomogeneous broadening limit, in which the nodal line becomes parallel to the diagonal at 45°. In the absence of inhomogeneity, the 2D spectrum approaches the homogeneous limit, in which the simulated 2D spectrum becomes a product line shape with a vertical nodal line slope of 90°. The intermediate nodal line slope of 68.18° ± 0.92° indicates that this PbSe QD sample lies between these two limits. The nodal line slope in the experimental 2D spectrum was determined using a least squares fit to the positive 10% contour over the range 1.044 eV to 1.068 eV along the excitation axis and used to determine the amount of inhomogeneity in the total absorption lineshape for deconvolution.

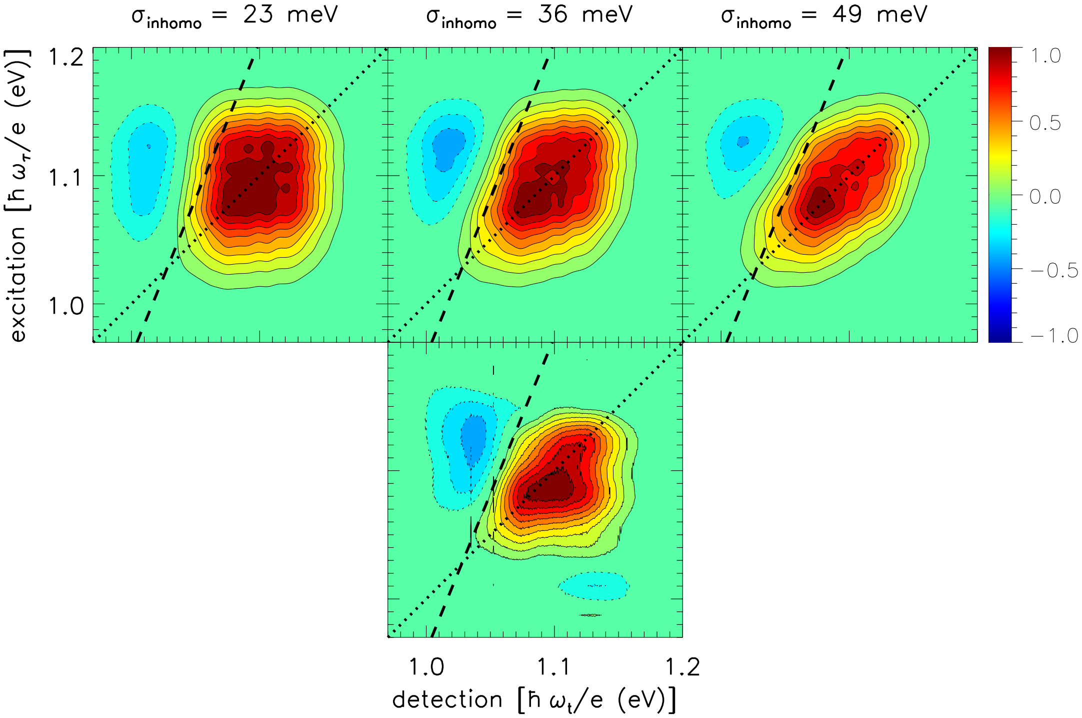

Figure 3.8: Simulated (top row) PbSe 2D spectra for three values of the inhomogeneity compared to the experimental (bottom row) 2D spectrum. The top row shows the simulated results for the inhomogeneous linewidth standard deviations labeled on the top of the spectra, all for an ESA redshift of $\Delta = 140$ meV. The dotted line shows the diagonal and the dashed line shows the slope of the nodal line from the experimental 2D spectrum for comparison. The weights are 1:(49/64):(1/64) for GSB:ESA:ESE.

The simulated 2D spectrum at long T showed the best agreement with an ESA redshift of Δ = 140 meV for the fully relaxed signal weights justified above. Figure 3.9 shows the calculated 2D spectra around Δ = 140 meV. Δ = 140 meV best captures the depth of the negative peak. However, there is another range near Δ = 20 meV, which also has a similar agreement in the relative peak heights, shown in Fig. 3.10. This leads to an ambiguity in the analysis of the magnitude of the ESA redshift, Δ, but the nodal line slope does not change. In simulations, changing Δ over the range of 15 - 180 meV and the relative ratio of w_{gsb}:w_{esa} from 1:(1/10) to 1:1 does not change the nodal line slope, so the nodal line slope can be used to determine the inhomogeneous broadening without having determined the the redshift and weights precisely. The standard deviation of the optical inhomogeneous linewidth for this particular sample is determined to be $\sim$36 $\pm$ 2 meV ($\sim$85 $\pm$ 5 meV FWHM) with a homogeneous linewidth of $\sim$34 $\mp$ 2 meV ($\sim$80 $\mp$ 5 meV FWHM). The reversal of the $\pm$ signs in the uncertainties is meant to indicate how an increase in one must be compensated by a decrease in the other to reproduce the absorption linewidth. This 85 $\pm$ 5 meV FWHM upper bound on the inhomogeneous linewidth from the 2D spectra is still smaller than the smallest bandgap distribution of $\sim$110 meV.

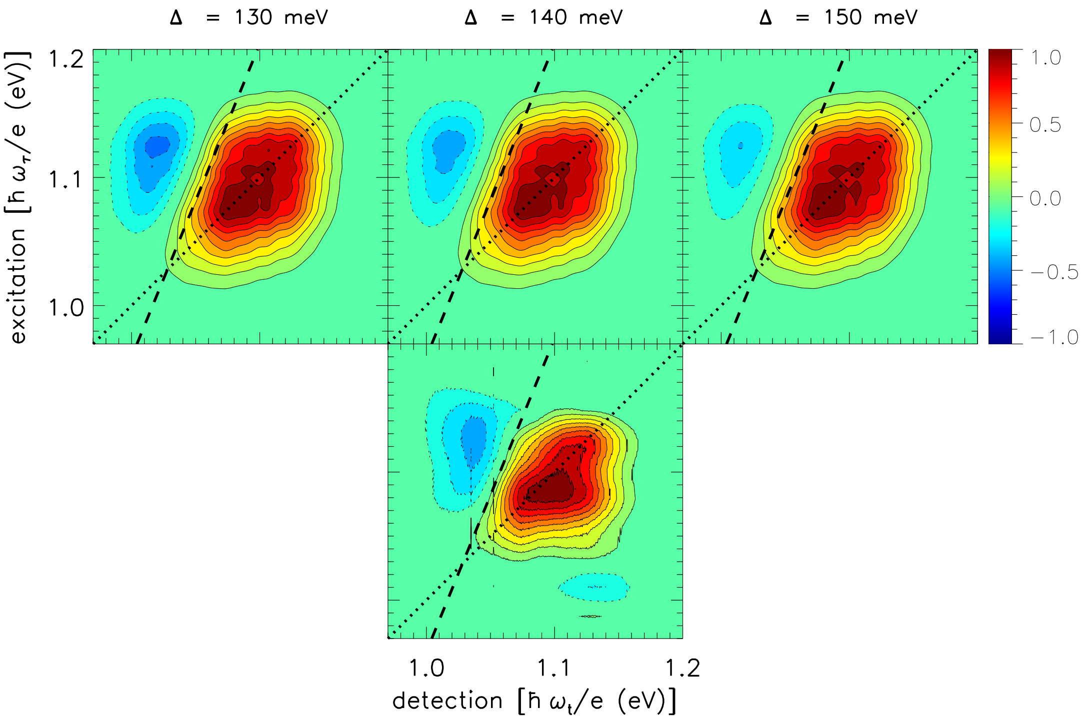

Figure 3.9: Simulated (top row) PbSe 2D spectra for three values of Δ near 140 meV compared to the experimental (bottom row) 2D spectrum. The top row shows the simulated results with Δ labeled on the top of each spectrum, all with an inhomogeneous standard deviation of 36 meV. The dotted line shows the diagonal and the dashed line shows the slope of the nodal line from the experimental 2D spectrum for comparison. The weights are 1:(49/64):(1/64) for GSB:ESA:ESE.

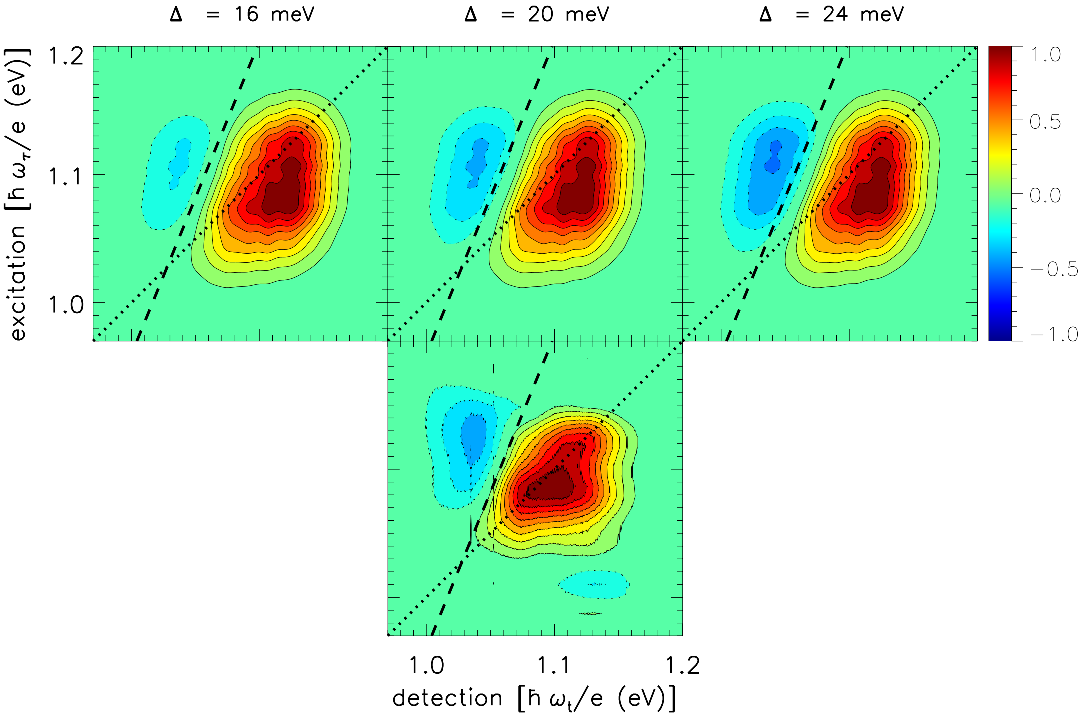

Figure 3.10: Simulated (top row) PbSe 2D spectra for three values of Δ near 20 meV compared to the experimental (bottom row) 2D spectrum. The top row shows the simulated results with Δ labeled on the top of the spectra, all for an inhomogeneous standard deviation of 36 meV. The dotted line shows the diagonal and the dashed line shows the slope of the nodal line from the experimental 2D spectrum for comparison. Varying Δ does not affect the nodal line slope. The weights are 1:(49/64):(1/64) for GSB:ESA:ESE.

The homogeneous linewidth of QDs has been reported to be size dependent [41][59]. Theoretical studies of CdSe and CuCl nanocrystals by Takagahara suggested that an increase in the nanocrystal size weakens the coupling between the exciton and acoustic phonons, thus decreasing the homogeneous linewidth [59]. Fernée *et al.* [60] reported a homogeneous linewidth of 125 meV FWHM for 2.5 nm diameter PbS QDs using size-selective photoluminescence excitation spectroscopy. Peterson *et al.* [44] reported a homogeneous linewidth of 85 meV FWHM for 3 nm diameter PbS QDs by measuring the photoluminescence spectrum for a single QD. Comparing to these results, the homogeneous linewidth of $\sim$80 ± 5 meV FWHM we obtained for $\sim$3.6 nm diameter PbSe QDs is reasonable and in agreement with the theoretically predicted trend. In addition, the nodal line slope method of determining the homogeneous linewidth probes ground state and excited state absorption at the bandgap and does not rely much emission because it has a low weight. It is known that photoluminescence might have additional line broadening contributions from fine structure [15], so an alternate method in which any additional line broadening might come from fine structure in excited state absorption provides a useful check on both methods.

The agreement between the experimental and simulated 2D spectra shown in figures 3.8, 3.9, and 3.10 is not sufficient in the magnitude and position of the peaks. These quantities heavily depend on the ESA redshift and the relative weights of w_{abs}, w_{esa}, and w_{ems} in Eqn. 3.5. For example, it is possible to make an *ad hoc* alteration of w_{esa} and adjust the ESA redshift to obtain a closer agreement with the experimental 2D spectrum. Figure 3.11 shows simulated long relaxation time with the ESA weight to be half of the GSB weight, which yields best fits near $\Delta = 70$ meV. With the new weights and Δ, the simulation shows a better agreement in both relative amplitudes and positions of the positive and negative peaks.

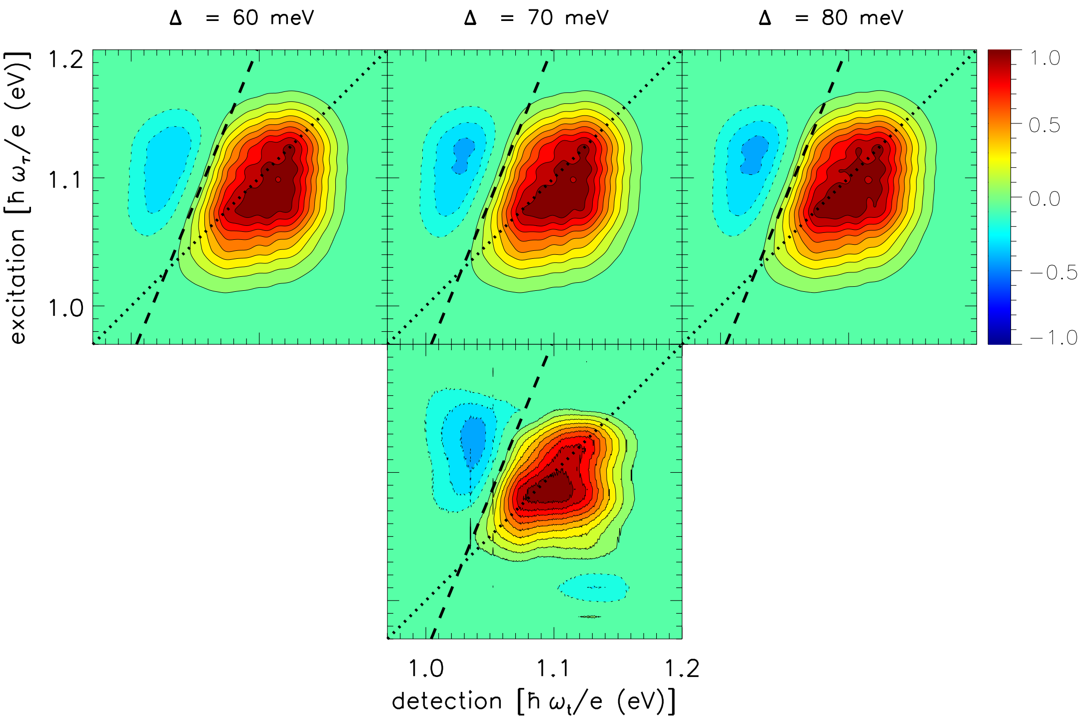

Figure 3.11: Simulated (top row) long relaxation time PbSe 2D spectra with an *ad hoc* change in ESA strength for three ESA redshifts compared to the experimental (bottom row) 2D spectrum. The net ESA strength is set to half of the GSB strength, so the weights are 1:(1/2):(1/64) for GSB:ESA:ESE. The experimental negative peak depth is best reproduced for an ESA redshift of $\Delta = 70$ meV. This fit also captures the location of the nodal line.

Figure 3.12 shows the projections onto ω_τ and ω_t for the experimental and simulated 2D spectra from Fig. 3.11 with the new adjusted weights of 1:(1/2):(1/64) for GSB:ESA:ESE and $\Delta = 70$ meV. The ω_τ projection shows qualitative agreement, but the experimental data has Fourier transform noise that is determined to be random by comparison to other 2D spectra projections at different relaxation times acquired on the same day (see below). The SRPP (ω_t projection) shows good agreement in both peak amplitudes and positions. The improved agreement in 2D spectra and the SRPP with the adjusted weights suggests that there is a large parameter space of weights and redshifts to be explored for determining the ESA redshift accurately. Nevertheless, the inhomogeneity is still represented by the same nodal line slope.

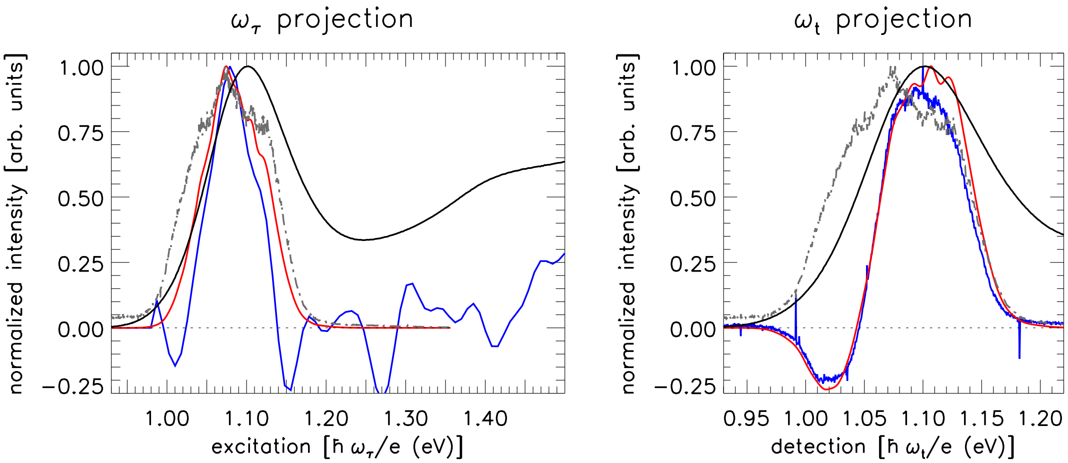

Figure 3.12: Projection onto ω_τ (left) and ω_t (right) axes for experimental and simulated 2D spectra with weights of 1:(1/2):(1/64) for GSB:ESA:ESE and $\Delta = 70$ meV. In both figures, the black solid line shows the linear absorption spectrum for the QDs, grey dash-dotted line shows the pulse spectrum, and blue and red lines show the projections of the experimental and simulated 2D spectra, respectively. The ω_τ projection shows an extended range to show the Fourier transform noise.

All of the simulated 2D spectra have a broader range along the excitation frequency axis than the experimental 2D spectrum. This can be attributed to Fourier noise. Figure 3.13 shows multiple ω_τ projections of 2D spectra taken on the same day at different T and shows that the negative regions immediately adjacent to the positive peak along the excitation frequency axis of the same magnitude as Fourier noise at higher excitation frequencies where no signal should appear and the projection is not reproducible. This indicates that the simulations reproduce the experimental 2D spectrum to within noise.

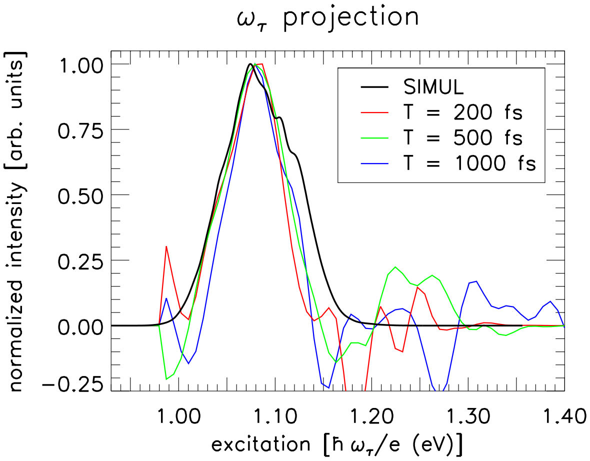

Figure 3.13: Multiple experimental ω_τ projections of 2D spectra at different T. The ω_τ projections show the level of Fourier noise both around the main peak and frequencies above 1.2 eV, where the pulse spectrum vanishes.

3.4.4 The Bi-exciton Binding Energy

The magnitude of the bi-exciton binding energy for the doubly excited $1S_e$-$1S_h$ electron-hole pair remains uncertain but the values reported for PbSe are 6 meV for 6.8 nm diameter QDs [61], 19 meV for 5 nm diameter QDs [47], and 9 meV for 4.5 nm diameter QDs [57]. The most common method by which these values are determined is through a transient absorption spectrum. For small bi-exciton binding energy, the SRPP signal will result in a quasi-derivative lineshape that pushes the peak maxima and minima apart and leads to ambiguities in determining the ESA redshift. Our analysis here using 2D spectroscopy measures the static inhomogeneity of the sample, which serves as an additional constraint in determining the ESA redshift. Assuming that the ESA redshift is purely from the bi-exciton binding energy, our simulations that agree best with the experimental data indicate Δ_{XX} between 20 – 140 meV for 3.62 nm diameter PbSe QDs. The large range of values is because of the uncertainty in the individual weights of GSB, ESA, and ESE. Even with this large uncertainty, the results presented here suggest that the ESA redshift is larger than previously reported values determined from transient absorption spectra for PbSe QDs with similar sizes [47][57].

3.5 Conclusion

We have demonstrated the application of 2D spectroscopy to extract the homogeneous linewidth and the static inhomogeneous linewidth for a QD sample. For this particular PbSe QD sample, the standard deviation of the homogeneous linewidth was determined to be $\sim 34 \mp 2$ meV ($\sim 80 \mp 5$ meV FWHM) and the static inhomogeneity was determined to have a standard deviation of $\sim 36 \pm 2$ meV ($\sim 85 \pm 5$ meV FWHM). The nodal line slope method of determining the homogeneous linewidth directly probes the absorption at the bandgap of individual QDs and depends very little on their photoluminescence, which may have additional line broadening contributions from fine structure. The disagreement between the bandgap inhomogeneity obtained using multiple sizing curves from the size distribution from TEM images and the optical inhomogeneity in this analysis remains an intriguing question. As discussed in the Appendix, the TEM size and size distribution analysis used for the sizing curves contain steps that blur the image. This could lead to systematic errors. As shown in the HRTEM images of our PbSe QD sample, the shapes of the QDs are irregular. It is not clear however, that the energy bandgap distribution arises only from the size distribution. These might differ if the growth process of the nanocrystals favors more energetically stable structures over uniform sizes. However, it is not yet established that the bandgap distribution calculated from the TEM size distribution is accurate enough to compare to the energy bandgap distribtuion from 2D spectra.

In addition by separating the inhomogeneous broadening, 2D spectroscopy can be a more accurate method of determining quantities such as the excited state absorption redshift. The relation between the excited state absorption to the bi-exciton binding energy needs to be explored further and more carefully. Applying absolute signal size measurements [62] to 2D spectroscopy might help to elucidate these quantities by experimentally determining the signal weights so that these parameters are constrained.

3.6 Acknowledgments

We thank Justin C. Johnson (NREL) for measuring the photoluminescence spectrum for our sample. Low-resolution TEM images were obtained at the Electron Microscopy Laboratory at the Colorado School of Mines with the assistance of Gary Zito and John Chandler. High-resolution TEM images were obtained at the CAMCOR High Resolution and Analytical Facility at the University of Oregon with the assistance of Josh Razink and Kurt Langworthy.

3.7 Appendix

3.7.1 Sample synthesis and preparation

The sample of lead selenide (PbSe) nanocrystals with a bandgap of 1.108 eV and a 145 meV FWHM of the first absorption peak was synthesized from lead (II) oleate and tri-n-octylphosphine selenide (TOPSe) in octadecene-1, following the hot injection procedure reported by the Colvin group [25] with a modification in the synthesis procedure. The modification consists of adding a small amount of diphenylphosphine (DPP) to the selenium precursor before injection, thus adapting the findings of the groups of Bawendi [26] and Krauss [27] who showed that secondary phosphines are responsible for the nucleation of nanocrystals and improve the precursor conversion yields. Synthesis of PbSe nanocrystals was performed under an inert atmosphere of argon on a Schlenk line.

Briefly, the procedure can be summarized as follows. First, a stock solution of TOPSe (~1.06 M) in tri-n-octylphosphine (TOP) was prepared by dissolving 3.671 g of elemental selenium (Se) in 44 ml of TOP inside the argon-filled glovebox (MBraun Unilab workstation, $\leqslant$0.1 ppm H_2O, $\leqslant$0.1-4.6 ppm O_2 levels) under stirring overnight. Next, the lead (II) oleate stock solution was prepared by reacting lead (II) oxide (PbO, 2.8 g) and oleic acid (8 ml) in octadecene-1 (42 ml) at 100 °C under vacuum on a Schlenk line. The cloudy red-brown suspension of PbO gradually turned clear light yellow after ~1 hour at 100 °C, indicating complete reaction of PbO with oleic acid to form lead (II) oleate. For the synthesis of PbSe nanocrystals, 14 g of lead (II) oleate stock solution was placed inside a 3-neck 25 ml round bottom flask equipped with a magnetic stirring bar and heated up to the injection temperature of 107 °C under vacuum. After the injection temperature was reached, the reaction flask was filled with argon, followed by three cycles of placing it under vacuum and refilling it with argon. After the last refill with argon, the flask was left at the injection temperature for 10-15 minutes while the selenium precursor solution was prepared inside the glovebox. To prepare the selenium precursor solution, 6 ml of the TOPSe stock solution were mixed with 100 μL of DPP inside a 10 ml disposable syringe equipped with an 18G stainless steel needle. Shortly after the selenium precursor solution was prepared, it was swiftly injected into the lead (II) oleate reaction mixture. Upon injection of the selenium precursor, reaction mixture remained clear light yellow for a few seconds and gradually turned clear dark black-brown during the ~90 second total reaction time. At ~90 seconds after selenium precursor injection, the reaction was quenched by transferring the flask into an ice-filled water bath while maintaining the stirring. Half an hour later, the flask with a cold and solidified reaction mixture was transferred inside the glovebox for extraction of PbSe nanocrystals by washing. Washing was performed using degassed ethanol as a "non-solvent" [63] to precipitate nanocrystals from the reaction mixture and hexane as the solvent for re-dissolution. After the unreacted precursors and ocatadecene-1 were washed from the nanocrystals, the nanocrystals were dried under vacuum and stored inside glass vials wrapped in aluminum foil inside the glovebox. For spectroscopic experiments, PbSe nanocrystals were dissolved in anhydrous tetrachloroethylene and filtered through a 0.2 μm PTFE syringe filter.

Non-linear optical experiments on the sample of PbSe nanocrystals were performed using a commercial 200 μm pathlength Starna flow cell (48-Q-0.2) modified with air-tight valves at the ends of each flow tube to minimize the exposure of the sample to air during data collection. Each valve consists of three parts: stopper with an external thread, perfluoroelastomer o-ring, and a nut with an internal thread and a gland to house the o-ring. Radial seals around the ends of each flow tube were formed by crushing the o-ring against the walls of the flow tube as the stopper was tightened in the nut. Filling and sealing the cell were done inside the glovebox.

3.7.2 Size determination from TEM images

The TEM image processing procedure was adapted from Weidman *et al.* [41] and utilizes the ImageJ software (version 1.47) [64]. The procedures are illustrated in Fig. 3.14. The magnifications used for acquiring the TEM images were 80,000X and 110,000X, which corresponds to a resolution of approximately 0.135 nm and 0.1 nm per pixel, respectively. Each TEM image was taken at a different location on the microscope grid, and contains 150-400 nanocrystals, depending on the magnification and coverage. A total of 1512 nanocrystals were measured to obtain the size distribution data.

Image processing and size analysis were performed in three steps: (1) the original image was processed by applying a built-in "FFT filter" [65][66], (2) the processed image is converted into a binary image, and (3) automatic particle analysis of the binary image is performed. Ref. [41] describes varying the parameters for the DoG filter and binary image threshold to obtain particle outlines that are judged to be best by eye. This analysis is shown here so that the results are comparable to prior work and can be used in sizing curves. The "FFT filter" is a DoG filter, which suppresses both low and high spatial frequencies, with a different parameter for each. The DoG processing steps are detailed in Ref. [66]. The labels for these parameters on the ImageJ software are minimum feature and maximum feature size; these were set at 1 nm and 40 nm. The DoG filter with a minimum feature size of 1 nm blurs the image, but helps remove grainy features of the background from the amorphous carbon on the TEM copper grid support. This improves the distinction of the particle edges when converting into a binary image (see step 2). After exploring the parameters of the DoG filter, the minimum feature set to 1 nm had the best result in identifying the particle edges, as verified by visual inspection of the particle contours identified by the software when overlapped with the unprocessed TEM image (Fig. 3.14f). The value of the maximum feature size was chosen following the example by Weidman *et al.* [41] and its effect on the particle edge identification was tested in the same way as for the minimum feature size. In step (2), the processed image is converted into a binary (black and white) image using the default routine of the threshold tool. The default routine for the threshold tool in ImageJ was also used for size distribution analysis of PbS and PbSe QDs in previous reports [42]. The particle analysis in step (3) enumerates all the particles, draws outlines around particles, determines the area, and determines the major and minor radii for each particle in the image. Finally by manual inspection of every particle analyzed in each TEM image, artifacts which are too small or too large to be nanoparticles, and particles which have been truncated at the edges are removed from the statistics. For comparison to prior sizing curves, which assume spherical particles, the areas from the particle analysis are used to determine the diameter, which yields a size distribution of 3.62 ± 0.4 nm. The size distribution assuming spherical particles is shown in Fig. 3.15. Throughout our analysis, nanocrystals appeared to have irregular shapes when inspected at higher resolutions. Therefore the average diameter calculated from the distribution of the areas of the nanocrystals is a rough approximation, while major and minor diameters determined for an elliptical shape by the ImageJ routine represent a more accurate approximation to the nanocrystal projections in the TEM images. The major and minor axes of the TEM projections were determined through the same procedure to be 4.15 ± 0.52 nm and 3.13 ± 0.42 nm, respectively.

Figure 3.16 shows the calculated inhomogeneous energy bandgap distribution using multiple reported sizing curves for PbSe QDs. This also assumes that the particles are spherical, which is not what is observed through TEM images. The energy bandgap distribution calculated from the static size distribution are always wider than the linear absorption spectrum shown in black. Moreels *et al.* [29] shows the closest agreement of linewidths, but this linewidth does not leave any room for the homogeneous linewidth. Figure 3.17 shows the calculated energy bandgaps using the minor diameter assuming ellipsoidal particles.

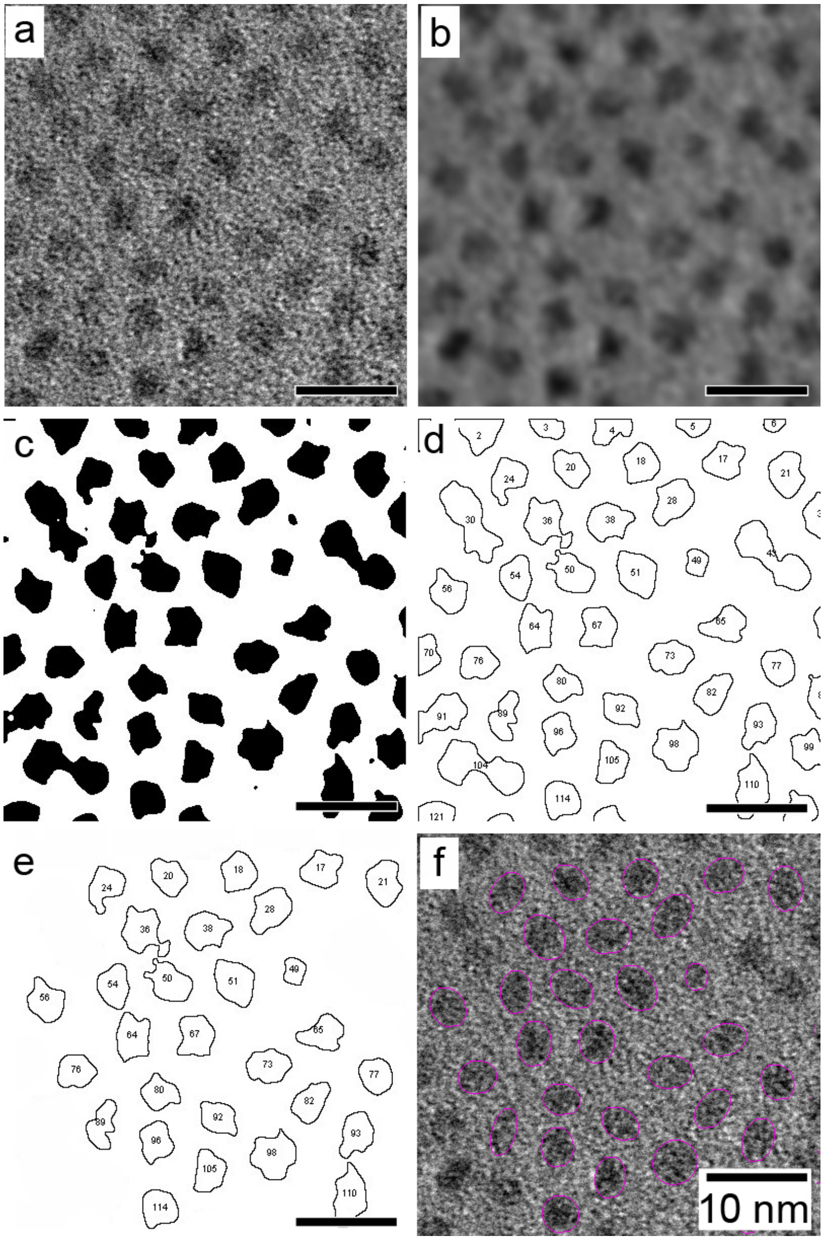

Figure 3.14: Steps in procedure for size analysis from TEM images. All the panels have dimensions of 40 × 40 nm. Panel (a) shows the raw TEM image of the particles. Panel (b) shows the TEM image after the Fourier filter used to reduce background noise. The minimum and maximum features were set to 1 nm and 40 nm, respectively. Panel (c) shows the binary image obtained by using the automatic threshold tool. Panel (d) shows the result of the particle analysis procedure where each particle is enumerated and contours are drawn. The particle analysis determines the area and the major and minor axes, which are used for size statistics. Panel (e) shows the removal of artifacts, done manually, to avoid counting particles that are truncated, too big, or too small. The purple outlines around particles in panel (f) show the final quality check that all the particles were properly accounted for.

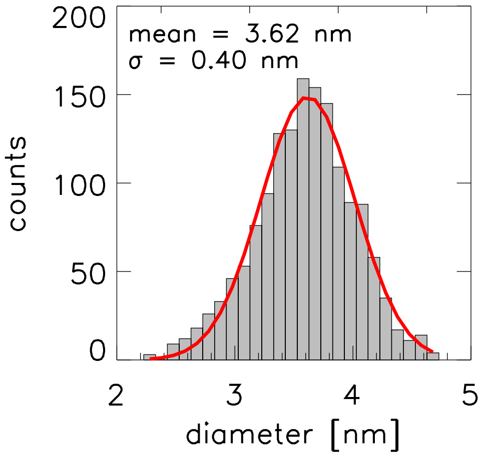

Figure 3.15: 1D size distribution determined from TEM images with 1512 particles sampled. For comparison to prior sizing curves, the nominal diameter of each particle was calculated for the area of each particle by assuming a spherical shape. With this assumption, the fitted average particle diameter is 3.62 ± 0.4 nm. A fit to ellipsoidal shapes yield a short axis diameter and long axis diameter of 3.13 ± 0.42 nm and 4.15 ± 0.52 nm, respectively.

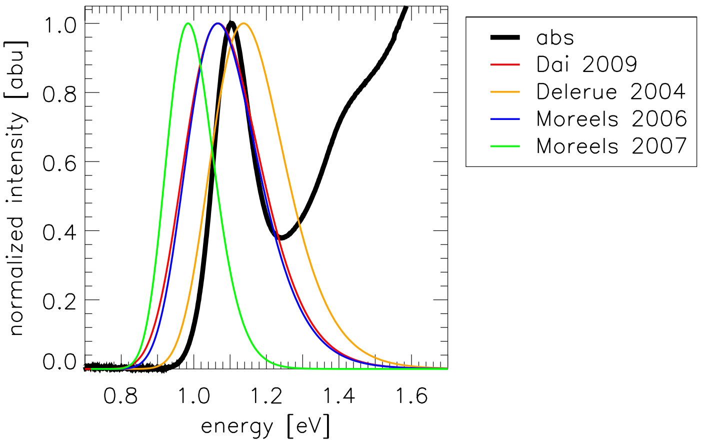

Figure 3.16: Inhomogeneous energy bandgap distribution using calculated multiple sizing curves for PbSe QDs and assuming a spherical shape. The black solid line shows the linear absorption spectrum and the colored lines show calculated energy bandgap distributions. All the energy bandgap distributions from the inhomogeneous spherical particle fit to TEM images are wider than the linear absorption spectrum. The closest width is the green curve (Moreels *et al.* [29]), which has a FWHM of ∼153 meV compared to the experimental FWHM of ∼145 meV.

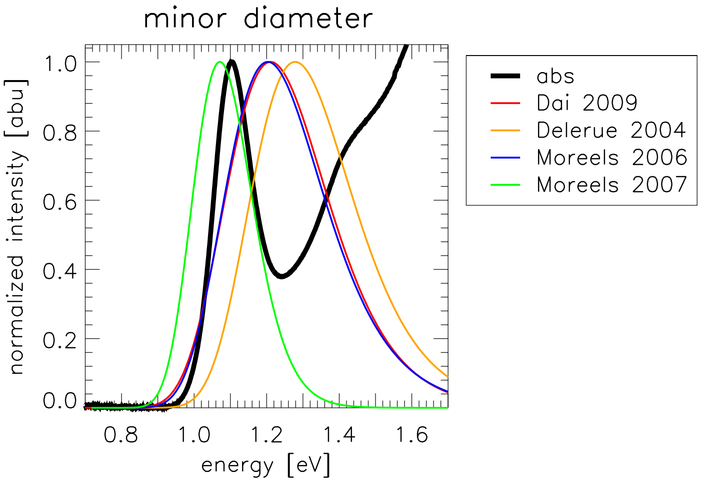

Figure 3.17: Inhomogeneous energy bandgap distribution calculated from the minor ellipsoidal axis distribution using multiple sizing curves for PbSe QDs.

3.7.3 Deconvolution procedure

Assuming a static size distribution for the QDs, which results in different energy bandgaps, the linear absorption spectrum is a convolution of the homogeneous linewidth of a single QD with the size distribution. This expression can be written as,

$$g_{abs}^{tot}(\omega) \approx \int_{-\infty}^{\infty} p(\omega_{eg}) g_{abs}^{homo}(\omega - \omega_{eg})\, d\omega_{eg} \tag{3.9}$$

where $g_{abs}^{tot}(\omega)$ is the total absorption lineshape measured by the linear absorption spectrum, $g_{abs}^{homo}(\omega - \omega_{eg})$ is the absorption lineshape of a single QD with a bandgap of ω_{eg}, and $p(\omega_{eg})$ is the inhomogeneous QD bandgap probability distribution. Deconvolution is accomplished by dividing the Fourier transform of the total absorption lineshape in the conjugate (time) domain by the Fourier transform of the inhomogeneous probability distribution. The numerical method of deconvolving the absorption lineshape consists of four main steps: (i) preparation of the linear absorption spectrum in the frequency domain, (ii) inverse Fourier transformation, (iii) division in the time domain with necessary filtering, and finally (iv)

Fourier transformation back into the frequency domain.

The linear absorption spectra for QDs have a monotonic rise at higher photon energies where the spectra become bulk-like. This is a problem for a Fourier transform because the spectrum is not band-limited. For this reason, the rising part of the absorption spectrum is multiplied to zero using a hyperbolic tangent filter, while making sure that the newly created peak from the filter is broader than the $1S_e$-$1S_h$ absorption peak. Figure 3.18 shows the filtered linear absorption spectrum on a wavelength axis (this filtering is accomplished in the wavelength domain). The pulse spectrum used for the experiment only overlaps with the $1S_e$-$1S_h$ absorption peak. Thus, the filtering at high energies will not affect the 2D lineshape that is simulated. After hyperbolic tangent filtering of the rise, the linear absorption spectrum is Fourier interpolated onto an even frequency axis from the even wavelength (nm) axis it was collected on. As a function of frequency, the $1S_e$-$1S_h$ exciton absorption peak is approximately four times narrower than the peak created by filtering the rise. This results in the $1S_e$-$1S_h$ absorption peak decay lasting ∼4× longer in the time domain, which makes it easier to position the time domain filter in the second step. After an inverse Fourier transform, the resulting signal in the time domain can be represented as,

$$\hat{g}_{abs}^{tot}(t) = \hat{g}_{abs}^{homo}(t) \cdot \hat{p}(t) = \mathscr{F}^{-1}[g_{abs}^{tot}(\omega)], \tag{3.10}$$

where $\hat{g}_{abs}^{tot}(t)$ is the inverse Fourier transform of the total absorption lineshape, $\hat{g}_{abs}^{homo}$ is the inverse Fourier transform of the bandgap dependent homogeneous lineshape [$g_{abs}^{homo}(\omega)$ in Eqn. 3.9] of a single QD, and $\hat{p}(t)$ is the inverse Fourier transform of the inhomogeneous bandgap distribution function [$p(\omega_{eg})$ in Eqn. 3.9]. In the time domain, $\hat{g}_{abs}^{tot}(t)$ is a product of $\hat{g}_{abs}^{homo}(t)$ and $\hat{p}(t)$. Thus, the inhomogeneity can be divided out of $\hat{g}_{abs}^{tot}$ to recover $\hat{g}_{abs}^{homo}$, but this requires an additional numerical filtering to avoid noise generated blow-ups at long times when $\hat{p}(t)$ is near zero. For simplicity, we assume $p(t)$ to be a Gaussian function. The linear absorption signal in time is shown with the Gaussian function in time used to deconvolve the spectrum in figure 3.19. When dividing $\hat{g}_{abs}^{tot}(t)$ by the Gaussian inhomogeneity, signals diverge at large delays when the Gaussian approaches zero. For this reason, an additional hyperbolic tangent filter is applied after deconvolution to filter out this noise from deconvolution. The width and rise/fall of this hyperbolic tangent filter are set so that the signal, $\hat{g}_{abs}^{homo}(t)$, is not also filtered. Figure 3.20 shows the signals in time domain with and without the filter.

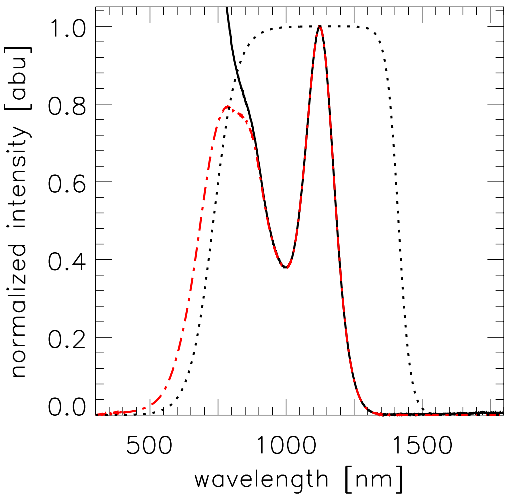

Figure 3.18: Filtering the linear absorption spectrum to prepare for Fourier transform. The solid black line shows the measured linear absorption spectrum. The dotted black line shows the hyperbolic tangent filter used for filtering out the exponential rise at high energies. The dash-dotted red line shows the resulting spectrum used for the deconvolution procedure.

Finally, the resulting signal, $\hat{g}_{abs}^{homo}(t)$, is Fourier transformed back to the frequency domain to yield the homogeneous absorption spectrum of a single QD,

$$g_{abs}^{homo}(\omega) = \mathscr{F}[\hat{g}_{abs}^{homo}(t)]. \tag{3.11}$$

This homogeneous lineshape is shown in figure 3.21 and it is used to simulate the 2D spectrum at long relaxation time. The width of the Gaussian inhomogeneity used in this deconvolution is varied so that the resulting calculated 2D spectra match the nodal line tilt shown in the

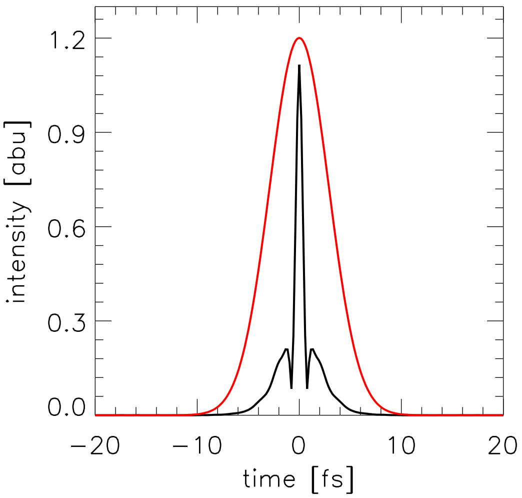

Figure 3.19: Absolute value Fourier transform of the frequency domain absorption lineshape (black) multiplied by a factor of 8 with the Fourier transform of the Gaussian inhomogeneity (red). The Gaussian inhomogeneous function shown in the figure is normalized in the frequency domain and has a frequency standard deviation of 0.055 rad/fs (36 meV).

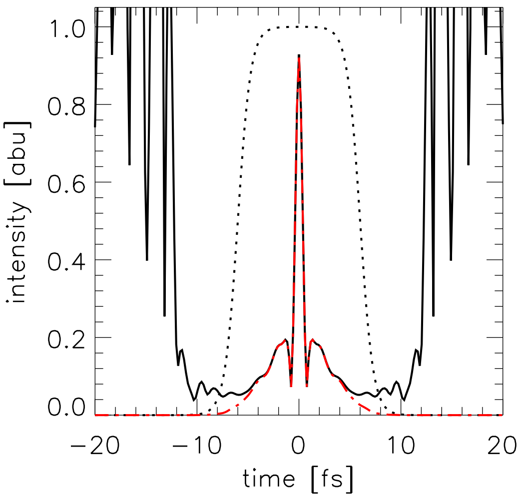

Figure 3.20: Division by the inhomogeneity in the conjugate domain for deconvolution. The solid black line shows the raw deconvolved data after the division by the Gaussian inhomogeneity multiplied by a factor of 8, which diverges when the Gaussian function approaches zero. The hyperbolic tangent filter used to filter the diverging signal is shown as a dotted line. The dash-dotted red line is the resulting deconvolved data in time, which is the Fourier transform of the homogeneous lineshape of a single QD multiplied by a factor of 8.

experimental 2D spectrum in order to determine the optical inhomogeneity.

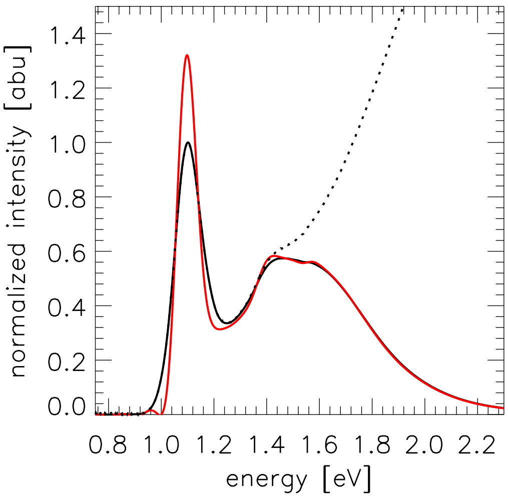

Figure 3.21: Deconvolved absorption lineshape used for simulating the 2D spectrum at long relaxation time. The dotted line shows the absorption lineshape, including the monotonic rise. The black line shows the original normalized total linear absorption spectrum after multiplication to remove the high energy absorption. The red line shows the deconvolved, area-normalized absorption lineshape.

Figure 3.22 shows the comparison between the original filtered absorption lineshape and the retrieved absorption lineshape when convolving the Gaussian inhomogeneity with the deconvolved absorption lineshape. There is less than 3% error in the absorption spectrum when convolving the deconvolved absortion lineshape with the Gaussian inhomogeneity. This error may arise from the hyperbolic tangent filter used in the time domain to reduce divergence from dividing by the wings of the Fourier transform of the Gaussian inhomogeneity.

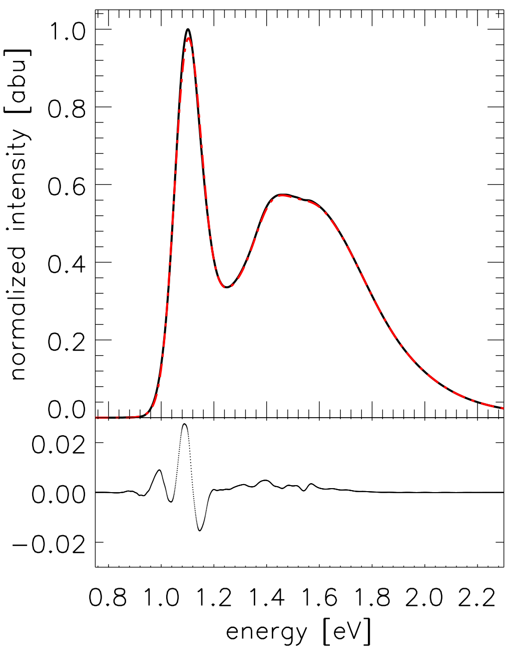

Figure 3.22: Deconvolution check by convolving with the Gaussian inhomogeneity. The top panel shows the original filtered absorption lineshape (solid black line) and the convolved absorption lineshape (red dash-dotted line). The bottom panel shows the difference between the two lineshapes. There is less than 3% error, which may arise from the hyperbolic tangent filter used in the time domain.

3.7.4 Simulations of ellipsoidal projections of QDs

As mentioned earlier, the QDs in the TEM images could not be fit well by assuming spherical dots. Most people [28][29][30][41][42][43] report a single size of the QDs with a distribution, assuming spherical particles. The procedures for determining the size distribution are often not well documented in journal articles, though the analysis of references [41] and [42] are notable exceptions. Inspection of the TEM images suggests that the particles are irregular. Assuming that the particles are ellipsoidal, the surface obeys

$$\frac{x^2}{a^2} + \frac{y^2}{b^2} + \frac{z^2}{c^2} = 1, \tag{3.12}$$

where a, b, and c are the radii along the principal axes. We simulate the 2D shadow projection distribution for an ensemble of ellipsoids by uniformly sampling the particle orientation using the algorithm of references [45] and [46]. Figure 3.23 shows the comparison between two simulation results and the experimental data. The major and minor axis projections were determined from TEM images to be 4.15 ± 0.52 nm and 3.13 ± 0.42 nm, respectively. The experimentally determined major-minor projection correlation is closer to the simulation results for prolate ellipsoids ($a = b < c$). The most noticeable difference between these alternatives is that the minor diameter never is the long axis for prolate ellipsoids.

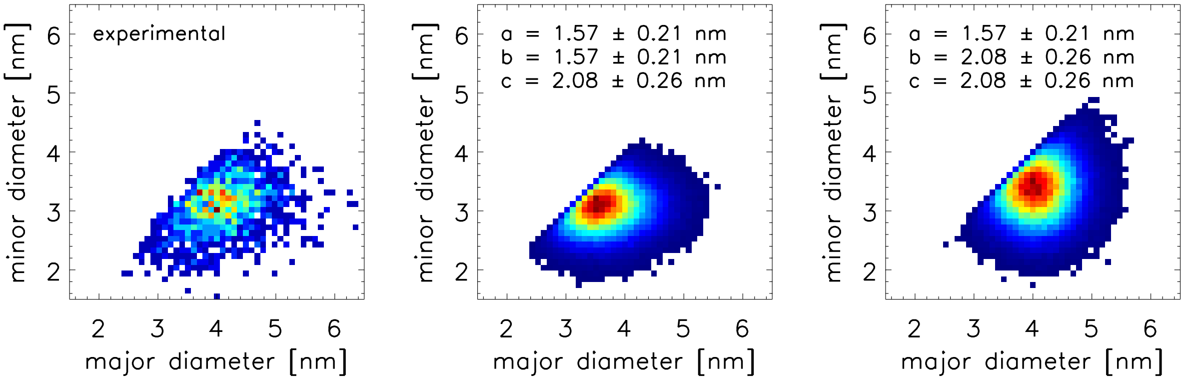

Figure 3.23: Major and minor diameter correlation determined from TEM images and simulations of ellipsoid projections with different major and minor axes. The simulation consists of projecting an ellipsoid with different major and minor axes sampled uniformly 100,000 times. The left panel shows the experimental results obtained from TEM images of 1512 particles, the middle and right panels show simulations for uniform orientation sampling of prolate and oblate ellipsoids, respectively.

References

[1] A. J. Nozik, "Quantum dot solar cells," Physica E 14, 115-120 (2002).

[2] G. H. Carey, A. L. Abdelhady, Z. Ning, S. M. Thon, O. M. Bakr, and E. H. Sargent, "Colloidal Quantum Dot Solar Cells," Chem. Rev., Article ASAP (2015).

[3] C. V. Shank and P. Becker, "Femtosecond Processes in Semiconductors. In *Spectroscopy of Nonequilibrium Electrons and Phonons*," C. V. Shank and B. P. Zakharchenya Eds. Elsivier: Amsterdamn, p. 215 (1992).

[4] B. Cho, W. K. Peters, R. J. Hill, T. L. Courtney, and D. M. Jonas, "Bulklike Hot Carrier Dynamics in Lead Sulfide Quantum Dots," Nano Lett. 10, 2498-2505 (2010).

[5] L. A. Yurs, S. B. Block, A. V. Pakoulev, R. S. Selinsky, S. Jin, and J. Wright, "Multiresonant Coherent Multidimensional Electronic Spectroscopy of Colloidal PbSe Quantum Dots," J. Phys. Chem. C 115, 22833-22844 (2011).

[6] W. A. Tisdale, K. J. Williams, B. A. Timp, D. J. Norris, E. S. Aydil, and X.-Y. Zhu, "Hot-Electron Transfer from Semiconductor Nanocrystals," Science 328, 1543-1547 (2010).

[7] J. Tang, K. W. Kemp, S. Hoogland, K. S. Jeong, H. Liu, L. Levina, M. Furukawa, X. Wang, R. Debnath, D. Cha, K. W. Chou, A. Fischer, A. Amassian, J. B. Asbury, and E. H. Sargent, "Colloidal-quantum-dot photovoltaics using atomic-ligand passivation," Nat. Mater. 10, 765-771 (2011).

[8] J. M. Pietryga, D. J. Werder, D. J. Williams, J. L. Casson, R. D. Schaller, V. I. Klimov, and J. A. Hollingsworth, "Utilizing the Lability of Lead Selenide to Produce Heterostructured Nanocrystals with Bright, Stable Infrared Emission," J. Am. Chem. Soc. 130, 4879-4885 (2008).

[9] A. N. Poddubny, M. O. Nestoklon, and S. V. Goupalov, "Anomalous suppression of valley splittings in lead salt nanocrystals without inversion center," Phys. Rev. B 86, 035324 (2012).

[10] L. Brus, "Electronic Wave Functions in Semiconductor Clusters: Experiment and Theory," J. Phys. Chem. 90, 2555-2560 (1986).

[11] D. Zhitomirsky, I. J. Kramer, A. J. Labelle, A. Fischer, R. Debnath, J. Pan, O. M. Bakr, and E. H. Sargent, "Colloidal Quantum Dot Photovoltaics: The Effect of Polydispersity," Nano Lett. 12, 1007-1012 (2012).

[12] Y. Liu, M. Gibbs, J. Puthussery, S. Gaik, R. Ihly, H. W. Hillhouse, and M. Law, "Dependence of Carrier Mobility on Nanocrystal Size and Ligand Length in PbSe Nanocrystal Solids," Nano Lett. 10, 1960-1969 (2010).

[13] Y. Shirasaki, G. J. Supran, M. G. Bawendi, and V. Bulovic, "Emergence of colloidal quantum-dot light-emitting technologies," Nature Photon. 7, 13-23 (2013).

[14] J. S. Steckel, R. Colby, W. Liu, K. Hutchinson, C. Breen, J. Ritter, and S. Coe-Sullivan, "Quantum Dot Manufacturing Requirements for the High Volume LCD Market," SID Symp. Dig. Tech. Pap. 44, 943-945 (2013).

[15] D. J. Norris, A. L. Efros, M. Rosen, and M. G. Bawendi, "Size dependence of exciton fine structure in CdSe quantum dots," Phys. Rev. B 53(24), 16347-16354 (1995).

[16] D. Segets, "Analysis of Particle Size Distributions of Quantum Dots: From Theory to Application," KONA Powder and Particle Journal (2015).

[17] D. M. Jonas, "Two-Dimensional Femtosecond Spectroscopy," Annu. Rev. Phys. Chem. 54, 435-463 (2003).

[18] J. D. Hybl, A. A. Ferro, and D. M. Jonas, "Two-dimensional Fourier transform electronic spectroscopy," J. Chem. Phys. 115(14), 6606-6622 (2001).

[19] R. Kubo, "Note on the Stochastic Theory of Resonance Absorption," J. Phys. Soc. Jpn. 9(6), 935-944 (1954).

[20] P. W. Anderson, "A Mathematical Model for the Narrowing of Spectral Lines by Exchange or Motion," J. Phys. Soc. Jpn. 9(3), 316-339 (1954).

[21] S. Park, K. Kwak, and M. D. Fayer, "Ultrafast 2D-IR vibrational echo spectroscopy: a probe of molecular dynamics," Laser Phys. Lett. 4(10), 704-718 (2007).

[22] S. T. Roberts, J. J. Loparo, and A. Tokmakoff, "Characterization of spectral diffusion from two-dimensional line shapes," J. Chem. Phys. 125, 084502 (2006).

[23] D. Karaiskaj, G. Moody, A. D. Bristow, M. E. Siemens, X. Dai, A. S. Bracker, D. Gammon, and S. T. Cundiff, "Homogeneous Linewidth Temperature Dependence of Interfacial GaAs Quantum Dots Studied with Optical 2D Fourier-Transform Spectroscopy," in CLEO: 2010 (Optical Society of America, San Jose, CA, 2010), QFD6

[24] B. Sun, R. Singh, L. A. Padilha, W. K. Bae, J. M. Pietryga, V. I. Klimov, and S. T. Cundiff, "Two Dimensional Coherent Spectroscopy of CdSe/ZnS Colloidal Quantum Dots," in CLEO:2014 (Optical Society of America, San Jose, CA, 2014), JTh2A

[25] W. W. Yu, J. C. Falkner, B. S. Shih, V. L. Colvin, "Preparation and Characterization of Monodisperse PbSe Semiconductor Nanocrystals in a Noncoordinating Solvent," Chemistry of Materials 16, 3318-3322 (2004).

[26] J. S. Steckel, B. K. H. Yen, D. C. Oertel, and M. G. Bawendi, "On the Mechanism of Lead Chalcogenide Nanocrystal Formation," J. Am. Chem. Soc. 128, 13032-13033 (2006).

[27] C. M. Evans, M. E. Evans, and T. D. Krauss, "Mysteries of TOPSe Revealed: Insights into Quantum Dot Nucleation," Journal of the American Chemical Society 132, 10973-10975 (2010).

[28] I. Moreels, Z. Hens, P. Kockaert, J. Loicq, and D. V. Thourhout, "Spectroscopy of the nonlinear refractive index of colloidal PbSe nanocrystals," Appl. Phys. Lett. 89, 193106 (2006).

[29] I. Moreels, K. Lambert, D. D. Muynck, F. Vanhaecke, D. Poelman, J. C. Martins, G. Allan, and Z. Hens, "Composition and Size-Dependent Extinction Coefficient of Colloidal PbSe Quantum Dots," Chem. Mater. 19, 6101-6106 (2007).

[30] Q. Dai, Y. Wang, X. Li, Y. Zhang, D. J. Pellegrino, M. Zhao, B. Zou, J. Seo, Y. Wang, and W. W. Yu, "Size-Dependent Composition and Molar Extinction Coefficient of PbSe Semiconductor Nanocrystals," ACS Nano 3(6), 1518-1524 (2009).

[31] J. Gao and J. C. Johnson, "Charge Trapping in Bright and Dark States of Coupled PbS Quantum Dot Films," ACS Nano 6(4), 3292-3303 (2012).

[32] D. Brida, S. Bonora, C. Manzoni, M. Marangoni, P. Villoresi, S. De Silvestri, and G. Cerullo, "Generation of 8.5-fs pulses at 1.3 μm for ultrabroadband pump-probe spectroscopy," Opt. Express 17, 12510-12515 (2009).

[33] E. Zeek, K. Maginnis, S. Backus, U. Russek, M. Murnane, G. Mourou, H. Kapteyn, and G. Vdovin, "Pulse compression by use of deformable mirrors," Opt. Lett. 24, 493-495 (1999).

[34] R. Trebino, and D. J. Kane, "Using phase retrieval to measure the intensity and phase of ultrashort pulses - frequency-resolved optical gating," J. Opt. Soc. Am. A 10, 1101-1111 (1993).

[35] M. K. Yetzbacher, T. L. Courtney, W. K. Peters, K. A. Kitney, E. R. Smith, and D. M. Jonas, "Spectral restoration for femtosecond spectral interferometry with attosecond accuracy," J. Opt. Soc. Am. B 27, 1104-1117 (2010).

[36] T. L. Courtney, S. D. Park, R. J. Hill, B. Cho, and D. M. Jonas, "Enhanced interferometric detection in two-dimensional spectroscopy with a Sagnac interferometer," Opt. Lett. 39, 513-516 (2014).

[37] S. D. Park, T. L. Courtney, D. Baranov, B. Cho, and D. M. Jonas, "Sagnac Interferometer for Two-Dimensional Spectroscopy in the Pump-Probe Geometry," *Ultrafast Phenomena XIX*, edited by K. Yamanouchi, S. Cundiff, R. Vivie-Riedle, M. Kuwata-Gonokami, and L. DiMauro (Springer, New York, 2015), p. 428.

[38] T. L. Courtney, S. D. Park, R. J. Hill, and D. M. Jonas, "Broadband, low-dispersion, Brewster's angle interferometers," (in preparation).

[39] M. Zavelani-Rossi, G. Cerullo, S. De Silvestri, L. Gallmann, N. Matuschek, G. Steinmeyer, U. Keller, G. Angelow, V. Scheuer, and T. Tschudi, "Pulse compression over a 170-THz bandwidth in the visible by use of only chirped mirrors," Opt. Lett. 26, 1155-1157 (2001).

[40] I. Kang and F. W. Wise, "Electronic structure and optical properties of PbS and PbSe quantum dots," J. Opt. Soc. Am. B 14(7), 1632-1646 (1997).

[41] M. C. Weidman, M. E. Beck, R. S. Hoffman, F. Prins, and W. A. Tisdale, "Monodisperse, Air-Stable PbS Nanocrystals *via* Precursor Stoichiometry Control," ACS Nano 8(6), 6363-6371 (2014).

[42] D. Segets, J. M. Lucas, R. N. Klupp Taylor, M. Scheele, H. Zheng, A. P. Alivisatos, and W. Peukert, "Determination of the Quantum Dot Band Gap Dependence on Particle Size from Optical Absorbance and Transmission Electron Microscopy Measurements," ACS Nano 6(10), 9021-9032 (2012).

[43] G. Allan and C. Delerue, "Confinement effects in PbSe quantum wells and nanocrystals," Phys. Rev. B 70, 245321 (2004).

[44] J. J. Peterson and T. D. Krauss, "Fluorescence Spectroscopy of Single Lead Sulfide Quantum Dots," Nano Lett. 6(3), 510-514 (2006).

[45] K. Shoemake, "Animating Rotation with Quaternion Curves," Siggraph 19(3), 245-254 (1985).

[46] K. Shoemake, "Uniform Random Rotations. In Graphics Gems III," edited by D. Kirk, Eds. Morgan Kaufmann, 124 (1995).

[47] I. Gdor, H. Sachs, A. Roitblat, D. B. Strasfeld, M. G. Bawendi, and S. Ruhman, "Exploring Exciton Relaxation and Multiexciton Generation in PbSe Nanocrystals Using Hyperspectral Near-IR Probing," ACS Nano 6(4), 3269-3277 (2012).

[48] C. A. Nelson and X.-Y. Zhu, "Reversible Surface Electron Traps in PbS Quantum Dot Solids Induced by an Order-Disorder Phase Transition in Capping Molecules," J. Am. Chem. Soc. 134, 7592-7595 (2012).

[49] J. I. Saari, E. A. Dias, D. Reifsnyder, M. M. Krause, B. R. Walsh, C. B. Murray, and P. Kambhampati, “Ultrafast Electron Trapping at the Surface of Semiconductor Nanocrystals: Excitonic and Biexcitonic Processes,” J. Phys. Chem. B 117(16), 4412-4421 (2013).

[50] S. B. Block, L. A. Yurs, A. V. Pakoulev, R. S. Selinsky, S. Jin, and J. C. Wright, “Multiresonant Multidimensional Spectroscopy of Surface-Trapped Excitons in PbSe Quantum Dots,” J. Phys. Chem. Lett. 3, 2707-2712 (2012).

[51] G. W. Hwang, D. Kim, J. M. Cordero, M. W. B. Wilson, C.-H. M. Chuang, J. C. Grossman, and M. G. Bawendi, “Identifying and Eliminating Emissive Sub-bandgap States in Thin Films of PbS Nanocrystals,” Adv. Mater. 27, 4481-4486 (2015).

[52] H. Chung, H. Choi, D. Kim, S. Jeong, and J. Kim, “Size Dependence of Excitation-Energy-Related Surface Trapping Dynamics in PbS Quantum Dots,” J. Phys. Chem. C 119, 7517-7524 (2015).

[53] D. H. Son, J. S. Wittenberg, and A. P. Alivisatos, “Multielectron Ionization of CdSe Quantum Dots in Intense Femtosecond Ultraviolet Light,” Phys. Rev. Lett. 92(12), 127406 (2004).

[54] J. T. Stewart, L. A. Padilha, M. M. Qazilbash, J. M. Pietryga, A. G. Midgett, J. M. Luther, M. C. Beard, A. J. Nozik, and V. I. Klimov, “Comparison of Carrier Multiplication Yields in PbS and PbSe Nanocrystals: The Role of Competing Energy-Loss Processes,” Nano Lett. 12, 622-628 (2012).

[55] A. G. Midgett, H. W. Hillhouse, B. K. Hughes, A. J. Nozik, and M. C. Beard, “Flowing versus Static Conditions for Measuring Multiple Exciton Generation in PbSe Quantum Dots,” J. Phys. Chem. C 114, 17486-17500 (2010).

[56] J. C. Johnson, K. A. Gerth, Q. Song, J. E. Murphy, A. J. Nozik, and G. D. Scholes, “Ultrafast Exciton Fine Structure Relaxation Dynamics in Lead Chalcogenide Nanocrystals,” Nano Lett. 8(5), 1374-1381 (2008).

[57] M. T. Trinh, M. Y. Sfeir, J. J. Choi, J. S. Owen, and X. Zhu, “A Hot Electron-Hole Pair Breaks the Symmetry of a Semiconductor Quantum Dot.” Nano Lett. (2013).

[58] G. Nair, S. M. Geyer, L.-Y. Chang, and M. G. Bawendi, “Carrier multiplication yields in PbS and PbSe nanocrystals measured by transient photoluminescence,” Phys. Rev. B 78, 125325 (2008).

[59] T. Takagahara, “Electron-Phonon Interactions and Excitonic Dephasing in Semiconductor Nanocrystals,” Phys. Rev. Lett. 71(21), 3577-3580 (1993).

[60] M. J. Fernée, P. Jensen, and H. Rubinsztein-Dunlop, “Origin of the Large Homogeneous Line Widths Obtained from Strongly Quantum Confined PbS Nanocrystals at Room Temperature,” J. Phys. Chem. C 111, 4984-4989 (2007).

[61] M. T. Trinh, A. J. Houtepen, J. M. Schins, J. Piris, and L. D. A. Siebbeles, “Nature of the Second Optical Transition in PbSe Nanocrystals,” Nano Lett. 8(7), 2112-2117 (2008).

[62] B. Cho, V. Tiwari, R. J. Hill, W. K. Peters, T. L. Courtney, A. P. Spencer, and D. M. Jonas, “Absolute Measurement of Femtosecond Pump-Probe Signal Strength,” J. Phys. Chem. A 117, 6332-6345 (2013).

[63] D. V. Talapin and C. B. Murray, “PbSe Nanocrystal Solids for n- and p-Channel Thin Film Field-Effect Transistors,” Science 310, 86-89 (2005).

[64] W. S. Rasband, ImageJ, U. S. National Institutes of Health, Bethesda, Maryland, USA, http://imagej.nih.gov/ij/, 1997-2014.

[65] J. Walter (2001) FFT-filter. Available at: http://rsb.info.nih.gov/ij/plugins/fft-filter.html

[66] G. Chinga, P. O. Johnsen, R. Dougherty, E. L. Berli, and J. Walter, “Quantification of the 3D microstructure of SC surfaces,” J. Microsc. 227, 254-265 (2007).

Chapter 4

Two-Dimensional Spectra from Cross-Phase Modulation

4.1 Introduction

Cross-phase modulation (XPM) is a non-resonant interaction between two pulses that occurs when they are temporally and spatially overlapped in a transparent medium [1]. The nonlinear interaction leads to spectral and temporal changes in both pulses. More specifically, each pulse experiences a spectral red-shift or blue-shift when overlapped with the rising or falling edge of the other pulse, respectively [2]. Through this nonlinear response, spectral broadening also occurs for a single intense pulse and this self-phase modulation (SPM) is widely used for continuum generation in optical fibers and nonlinear pulse compression [3][4]. More recently, spectrally resolved XPM traces have been used to characterize femtosecond pulses [5][6] because the XPM trace is unique to the pulse's temporal amplitude and instantaneous frequency. XPM can be used similarly to second harmonic generation and the optical Kerr effect for Frequency Resolved Optical Gating (FROG) [7]. Although XPM has been exploited for these purposes, it is deleterious in resonant third-order nonlinear spectroscopic experiments because the desired resonant signal from the absorbing sample is contaminated by non-resonant XPM from the transparent windows and solvent during pulse overlap, which makes the analysis more difficult [8]. This becomes a larger problem for absorbing samples that radiate weak signals and for shorter pulses because the XPM signal is proportional to the square of the peak intensity.

The origin of XPM is the modulation of the instantaneous phase of the pulse by the optical Kerr effect [9][10][11], in which an intense pump pulse induces a nonlinear refractive index change, $n(t) = n_0 + n_2 I(t)$, where n_0 is the linear refractive index, n_2 is the nonlinear refractive index, and $I(t)$ is the time-domain intensity of the pump pulse. This time-dependent change in refractive index causes a time-dependent shift in the instantaneous phase of the transmitted pulse that shifts its instantaneous frequency, thus affecting its spectrum. The same theory applies for SPM, but in SPM, the time-dependent refractive index change is due to the time varying envelope of the pulse itself [12][13].

Physically, we can draw a parallel between XPM and impulsive stimulated Raman scattering in transparent media. In impulsive stimulated Raman scattering, excitation of Raman-active vibrations causes the molecular electronic polarizability to oscillate at the vibrational frequency [14]. The refractive index is linearly related to the molecular polarizability, so an increase or decrease in polarizability causes an increase or decrease in the refractive index. When the electronic polarizability is rising or falling because of vibration, it causes a Raman red-shift or blue-shift, respectively, for a probe pulse. There is no change in the number of probe photons, only an exchange of higher energy photons for lower energy photons, or vice versa. In XPM, excitation drives the electronic polarization directly, and a probe experiences a red-shift or blue-shift when interacting with the matter while the electronic polarization is rising or falling, respectively. XPM is usually attributed to a nonlinearity in the refractive index arising from a non-resonant two-photon absorption [15]. For frequencies below the two-photon absorption threshold, this explains the positive sign of n_2.

Third-order nonlinear femtosecond spectroscopic techniques, such as integrated pump-probe, spectrally-resolved pump-probe, transient absorption, and two-dimensional spectroscopy are widely used to investigate the photophysical dynamics of complex systems [16][17][18]. With pulses becoming shorter in time and broader in frequency, third-order spectroscopic techniques are powerful tools to probe the coupling between excitations that are widely separated. With two-dimensional Fourier transform spectroscopy (2DFTS), it is possible to decouple the experimental frequency and time resolution in femtosecond spectroscopy [18]. The early time dynamics of the signal contains information about vibration and solvation that can separate out instantaneous frequency distributions that are inhomogeneously broadened by dynamical, environmental, and structural configurations [19]. For this reason, it will be helpful to measure the early time dynamics to uncover these quantities. However at early times, during pulse overlap, the signal can have a significant contribution from XPM [5][20].

In this chapter, we simulate the XPM signal in two-dimensional (2D) spectroscopy. We show that the XPM signal in 2D leads to cancellation effects in the projection onto the detection axis that minimize the spectrally resolved pump-probe XPM signal near zero delay and for negative delay T. As a result, the XPM signal in 2D is more complicated and crucially affects 2D lineshapes during pulse overlap, creating ambiguities in peakshape analysis at early times. As examples, the XPM signal is simulated in SRPP transients and 2D spectra for transform limited and chirped Gaussian pulses. Experimental results are compared and simulated with the pulse spectral amplitude and spectral phase retrieved through FROG. Measuring the XPM signal is very difficult with the low pulse energies required for resonant experiments because XPM originates from the third-order nonlinear response of a transparent medium. However, the results of this chapter show that the signal measured for the neat solvent used in resonant third-order experiments is consistent with XPM. the ideal approach to XPM signal contamination involves simulation of XPM generation and propagation in the absorbing sample. Finally, simulation of propagation effects in an absorbing sample suggest an improved XPM subtraction scheme for resonant SRPP experiments.

4.1.1 Theory

The XPM signal can be attributed to non-resonant two-photon absorption processes [15][21]. Far off-resonance, the XPM signal may be assumed to have a delta function impulse response [5][20][22]. As a result, the third-order nonlinear impulse response [23] can be written as

$$R^{(3)}(\tau_a, \tau_b, \tau_c) \ \propto \ n_2 \cdot \delta(\tau_a)\delta(\tau_b)\delta(\tau_c), \tag{4.1}$$

where $\delta(\tau)$ is the Dirac delta function, and τ_a, τ_b, and τ_c are pulse-labeled interaction intervals used in calculating the nonlinear polarization from the response function [19]. The usual resonant factors of i in the third-order response in Eqn. 4.1 are missing because the interactions are off-resonance. The third-order polarization induced by the three excitation pulses is given by a triple convolution with the pulse fields. Under the rotating wave approximation, this is expressed as [24],

$$\begin{aligned} P^{(3)}(k_p, t, t_a, t_b) = \int_0^\infty \int_0^\infty \int_0^\infty & \hat{R}^{(3)}(k_p, \tau_a, \tau_b, \tau_c) \\ & \cdot \hat{E}_a^*(t - t_a - \tau_a)\hat{E}_b(t - t_b - \tau_b)\hat{E}_c(t - \tau_c)\ d\tau_a d\tau_b d\tau_c + c.c., \end{aligned} \tag{4.2}$$

where $\hat{E}(t) = e(t)\exp[-i\omega t]$ is the complex electric field, $P^{(3)}$ is the third-order nonlinear polarization with wave vector $k_p = \mp k_a \pm k_b + k_c$ created by the three pulses with wave vectors k_a, k_b, and k_c at times τ_a, τ_b, and τ_c before the present, and t_a, t_b, and t_c are the experimentally controlled pulse centers for the three interacting pulses relative to the center of pulse c at $t = 0$ [19]. Signal contributions with $\omega_a = \omega_b$ are perfectly phase matched, and radiated with a signal wave-vector $k_s = k_p$ in transparent samples. When $\omega_a \neq \omega_b$, the interfacial components of k_s and k_p are equal, but unequal normal components can lead to different signal radiation directions and phase mismatch between source polarization and signal field. The short sample length and small beam-crossing angle make such effects negligible over the pulse bandwidth. For perfect phase matching, the frequency domain third-order signal field is linearly related to the frequency domain nonlinear source polarization [18]. This linear relationship is most simply expressed in the frequency domain as (Gaussian units)

$$\hat{E}_{sig}(\omega_t, t_a, t_b) = \frac{2\pi l}{n(\omega_t)c} i\omega_t \hat{P}^{(3)}(\omega_t, t_a, t_b), \tag{4.3}$$

where $n(\omega)$ is the frequency dependent index of refraction. If the index of refraction is independent of frequency over the range of $P^{(3)}$, then the time-domain signal field is proportional to the time derivative of the nonlinear source polarization.

In this experiment, the Homotime Absorptive Response Detection (HARD) 2D geometry is used, where pulses a and b travel collinearly and the signal is detected through interference with the collinear probe pulse; this is also called the pump-probe geometry. In the HARD 2D geometry, k_a and k_b have the same unit propagation vectors and as a result, the phase-matched signal radiates with the same unit propagation vector as pulse c. For this reason, the signal is detected by intrinsic interference with pulse c and the measured intensity spectrum is the square modulus of the sum of all the fields with the same wave vectors [24]:

$$\begin{aligned} \Delta I(\omega_t, t_a, t_b) = {} & |\hat{E}^{(3)}_{2D}(\omega_t, t_a, t_b) + \hat{E}^{(3)}_{ppa}(\omega_t, t_a, t_a) + \hat{E}^{(3)}_{ppb}(\omega_t, t_b, t_b) + \hat{E}^{(3)}_{ccc}(\omega_t) + \hat{E}^{(1)}_{c}(\omega_t) + \hat{E}_{c}(\omega_t)|^2 \\ & - |\hat{E}^{(3)}_{ccc}(\omega_t) + \hat{E}^{(1)}_{c}(\omega_t) + \hat{E}_{c}(\omega_t)|^2, \end{aligned} \tag{4.4}$$

where $\hat{E}^{(3)}_{2D}(\omega_t, t_a, t_b) = \hat{E}^{(3)}(\omega_t, t_a, t_b) + \hat{E}^{(3)}(\omega_t, t_b, t_a)$ is the desired 2D XPM signal field in which pulses a and b interfere in driving XPM on pulse c; $\hat{E}^{(3)}_{ppa}(\omega_t, t_a, t_a)$ and $\hat{E}^{(3)}_{ppb}(\omega_t, t_b, t_b)$ are the single-pulse XPM signal fields in which pulses a and b each separately drive XPM on pulse c, respectively; $\hat{E}^{(3)}_{ccc}(\omega_t)$ is the SPM signal from pulse c alone; and $\hat{E}^{(1)}_{c}(\omega_t)$ is the linear free induction decay from pulse c. The sum of the fields $\hat{E}^{(3)}_{ccc}(\omega_t)$, $\hat{E}^{(1)}_{c}(\omega_t)$, and $\hat{E}_c(\omega_t)$ is the transmitted probe field that interferes with the third-order signals,

$$\hat{E}_{pr} = \hat{E}^{(3)}_{ccc}(\omega_t) + \hat{E}^{(1)}_{c}(\omega_t) + \hat{E}_c(\omega_t), \tag{4.5}$$

which accounts for the SPM signal from pulse c and free induction decay phase change of pulse c upon passage through the sample.

For 2D Fourier transform spectroscopy, pulses a and b determine the excitation frequency axis and together can be regarded as the "pump". Pulse c acts as the detection pulse and can be regarded as the "probe". The excitation frequency is resolved by Fourier transforming the time delay between pulses a and b. Redefining the variables with the time delay between pulses a and b as $\tau \equiv t_b - t_a$, and the time delay between the "pump" and "probe" as $T \equiv \min(|t_a|, |t_b|)$, a 2D scan is performed by a symmetric τ scan at a fixed T. The Fourier transform with respect to τ at a given T produces the raw 2D spectrum,

$$S'_{2D}(\omega_t, \omega_\tau, T) = \int_{-\infty}^{\infty} \Delta I(\omega_t, \tau, T) \exp(i\omega_\tau \tau)\, d\tau, \tag{4.6}$$

where the prime indicates the raw 2D spectrum including all of the interference terms with the probe field. After the Fourier transform with respect to τ, the fields $\hat{E}^{(3)}_{ppa}(\omega_t, t_a, t_a)$ and $\hat{E}^{(3)}_{ppb}(\omega_t, t_a, t_a)$ in Eqn. 4.4 appear centered near $\omega_\tau = 0$ because the signals do not oscillate interferometrically with τ (they do have a width because they decay as t_a or t_b is scanned during a scan of τ). The SPM signal has no dependence on t_a or t_b and transforms to a delta function at $\omega_\tau = 0$. As a result, the desired 2D signal can be isolated in the frequency domain, where the signal appears around the pulse center frequency, $\omega_\tau = \omega_0$ [18]. Thus, we can filter the 2D spectrum to isolate the signal contribution from the desired 2D signal interfering with the probe field,

$$\Delta N_{2D}(\omega_t, t_a, t_b) \propto \frac{1}{\omega_t}[\hat{E}^{(3)}_{2D}(\omega_t, t_a, t_b)\hat{E}^*_{pr}(\omega_t) + \hat{E}^{(3)}_{2D}(\omega_t, t_a, t_b)^*\hat{E}_{pr}(\omega_t)] \tag{4.7}$$

from Eqn. 4.4. The division by ω_t is to convert energy to photon number so that $\Delta N_{2D}(\omega_t, \omega_\tau, T)$ is the resulting photon number 2D spectrum.

Using the projection-slice theorem for 2D Fourier transforms [24][25], the spectrally resolved pump-probe (SRPP) signal at a given T can be calculated by the projection of the real 2D spectrum onto the ω_t axis ($\tau = 0$ slice),

$$SRPP(\omega_t, T) = \Delta N_{pp}(\omega_t, T) \propto \frac{1}{2\pi}\int_{-\infty}^{\infty} \Delta N_{2D}(\omega_t, \omega_\tau, T)\, d\omega_\tau, \tag{4.8}$$

where $\Delta N_{pp}(\omega_t, T)$ is the experimentally detected change in photon number caused by the "pump" pulse(s).

Although both 2D and SRPP signals arise from the change in transmitted probe photon number spectrum caused by the pump, the XPM signal comes from coherent interference analogous to coherent Raman scattering during pulse overlap [24]. Using the same analogy as coherent Raman scattering, the number of photons is conserved and higher energy photons are exchanged with lower energy photons or vice versa. This coherent interference during pulse overlap results in phase changes that mix refractive signals into what is normally considered the absorptive quadrature in-phase with the probe.

4.2 Numerical Calculations of XPM

A Fortran 95/2003 program compiled using Intel Visual Fortran Compiler Professional 11.1.070 was used to calculate the signals on a 3.2 GHz Core i7 processor with 24 GB of random access memory (RAM) running 64-bit Windows 7 Professional. The grid size used for simulations was 256^3 with complex double precision (~10 seconds of computation time for calculating a set of 2D spectra at all waiting times using one pulse). The Fortran code is a modification of the code used for Ref. [26] that incorporates the delta function nonlinear response for XPM (new subroutine/function S3_nonres.f90) and complex-valued frequency domain fields for chirp (new subroutine/function pulsefiltsep_SDP.f90). The modified code has been tested by reproducing figures 2 and 7 from Ref. [26] and figure 6 from Ref. [27]. This shows that it works for an optical Bloch model, a Brownian oscillator model, for propagation effects from beam geometry, for propagation effects from sample absorption and refraction, and for chirped excitation pulses. The details of these tests are explained in the Appendix, which also includes the new and modified subroutines.

To quantify the error associated with using a discrete and finite-size grid in the calculations, convergence was estimated by comparing 2D spectra with $(256)^3$ and $(512)^3$ points in the 3D grid [26][28]. The first convergence test kept the frequency resolution the same by halving the time step size and doubling the grid size. In this test, the frequency range differs by a factor of 2, thus exposing problems associated with the finite frequency range or inadequate time resolution in sampling. At any point in the real 2D spectra, the maximum difference was less than 1% near the edges of the ω_τ range, and in the SRPP signal, the maximum difference was less than 10^{-10}. Another test kept the same time resolution and doubled the time-domain grid size. This doubles the frequency resolution to expose errors in the finite range of time-domain sampling. At any point in the real 2D spectra and SRPP, the maximum difference was less than 10^{-10}. The errors in these calculations are low because the nonlinear response is a delta function without any time-domain decay or shape in the frequency-domain lineshape function.

As a check on the numerical calculation, we can use Eqn. 4.8 with the delta function nonlinear response given in Eqn. 4.1 to simulate the spectrally resolved XPM signal and compare to the analytical solution derived for transform limited Gaussian pulses given in

Ref. [20], Eqn. 9b. Figure 4.1 compares the XPM SRPP signal calculated numerically by projecting 2D spectra to the analytical result. The analytical solution shown in the middle panel uses the same time and frequency resolution as in the numerical calculation. After dividing each trace by its global maximum, subtraction of the two results gave differences of less than ~3 × 10^{-13}, which shows good numerical accuracy and convergence. The difference oscillates with a period of ~12 fs, about three times the optical period.

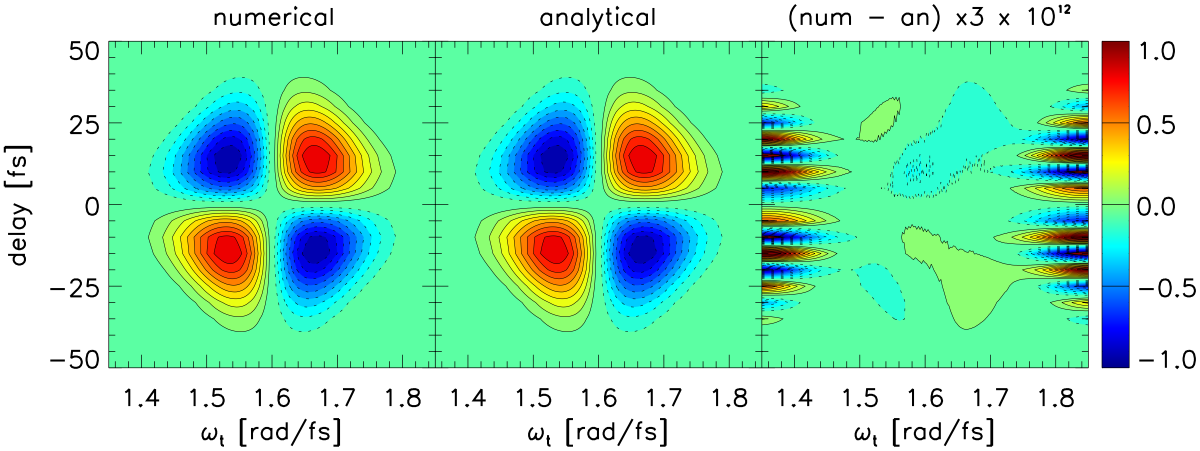

Figure 4.1: Comparison between numerical and analytical solutions for spectrally resolved XPM generated by transform limited Gaussian pulses. Transform limited Gaussian pulses centered at 1.6 rad/fs with a FWHM pulse intensity duration of 20 fs are used to simulate the spectrally resolved XPM signal. The left panel shows the numerical spectrally resolved XPM transient calculated from 2D spectra using a delta function nonlinear response and the middle panel shows the analytical solution from Ref. [20] with the same frequency and time resolution as the numerical calculation. The right panel shows the difference between the numerical and analytical results multiplied by 3 × 10^{12}.

4.2.1 XPM for Transform Limited and Chirped Gaussian Pulses

The XPM photon number spectrum in SRPP transients and 2D spectra is simulated for transform limited and chirped Gaussian pulses. Calculations have been previously reported for SRPP transients from XPM by Zhou *et al.* [20] and Yeremenko *et al.* [5]. In this section, the XPM signal for Gaussian pulses with quadratic and cubic spectral phase are shown in 2D spectra. Both signs of the chirp, positive and negative, are compared to reveal symmetry properties in SRPP transients, which are not as intuitive in 2D spectra. As will be shown below, this symmetry reflects on the symmetry of the pulses. The XPM signal in 2D spectra and SRPP transients shows complex structures, which motivates this calculation and simulation in order to subtract or simulate these signals in resonant experiments that may contain the XPM signal.

To calculate the XPM signal in 2D spectra and SRPP transients with chirped pulses, a spectral phase is added to the complex electric field in the frequency domain,

$$\hat{E}(\omega) = e(\omega) \exp\left[i\phi(\omega)\right], \tag{4.9}$$

where $e(\omega)$ is the real spectral amplitude and $\phi(\omega)$ is the spectral phase. The spectral phase of the pulse can be expanded in a Taylor series about the pulse center frequency:

$$\phi(\omega) = \phi^0(\omega_0) + \phi'(\omega - \omega_0) + \frac{1}{2}\phi''(\omega - \omega_0)^2 + \frac{1}{6}\phi'''(\omega - \omega_0)^3 + \cdots , \tag{4.10}$$

where ω_0 is the pulse center frequency, ϕ^0 and ϕ' are the zeroth- and first-order phase terms that do not affect the pulse duration (ϕ' is an overall time delay), ϕ'' is the group delay dispersion (GDD) or quadratic phase that gives rise to a time-domain linear frequency sweep, and ϕ''' is the third order dispersion (TOD) or cubic phase.

Simulation Parameters

For the simulations, the grid size used was $(256)^3$ with time steps of 5 fs. In each dimension, this corresponds to a time range from -635 to 640 fs, a frequency resolution of $\sim$0.0049 rad/fs, and a frequency range of $\sim$0.628 rad/fs from the center frequency ($\omega_0 = 1.6$ rad/fs). The Gaussian pulses used for the simulations have a 20 fs intensity FWHM, which corresponds to a spectral field envelope FWHM of $\sim$0.196 rad/fs (standard deviation of $\sim$0.08325 rad/fs). Thus, the frequency range used in the simulations extends more than 7 times the standard deviation of the Gaussian pulses in frequency, allowing the amplitude to decay to less than 10^{-13} of the peak amplitude.

Frequency and Time Marginals

The frequency and time marginals in an SRPP transient can be calculated by integrating over the time delay and detection frequency, respectively. Using $(256)^3$ and $(512)^3$ grid sizes for calculating the XPM SRPP transients yielded maximum absolute values of 10^{-14} and 10^{-15}, respectively, in both marginals. Thus, the difference from zero is attributed to a finite time resolution error. For the simulated XPM SRPP transients on the $(512)^3$ grid, both time and frequency marginals are numerically zero to within machine precision. This result indicates that the frequency and time marginals are zero regardless of chirp.

Transform Limited Gaussian Pulses

To begin with the simplest example, the XPM signal is simulated in 2D spectra and SRPP transients for transform limited symmetric Gaussian pulses. Figure 4.2 shows the connection between the XPM signal in SRPP and 2D for transform limited Gaussian pulses ($\phi(\omega) = 0$) centered at $\omega_0 = 1.6$ rad/fs with an intensity FWHM of 20 fs.

All of the 2D spectra are anti-symmetrical about the detection frequency $\omega_t = \omega_0$. An interesting feature is the large spectral range along the excitation axis, which extends well beyond the pulse spectra as a result of the signal being generated from a refractive effect. Strictly speaking, the name "excitation frequency" for ω_τ is not physically meaningful when coherence and refractive discontinuities in the response generate Fourier amplitude outside the excitation pulse spectrum. Another interesting feature of the XPM signal is how the SRPP signal is anti-symmetric with respect to the delay T, but the 2D spectra do not have symmetry with respect to T. The negative T 2D signal has an SRPP projection onto the ω_t axis that vanishes at large negative T partly through 2D cancellation; in contrast, the positive T 2D signal has smaller amplitudes than negative T, and the amplitudes vanish at large positive T so that the SRPP projection vanishes without 2D cancellation.

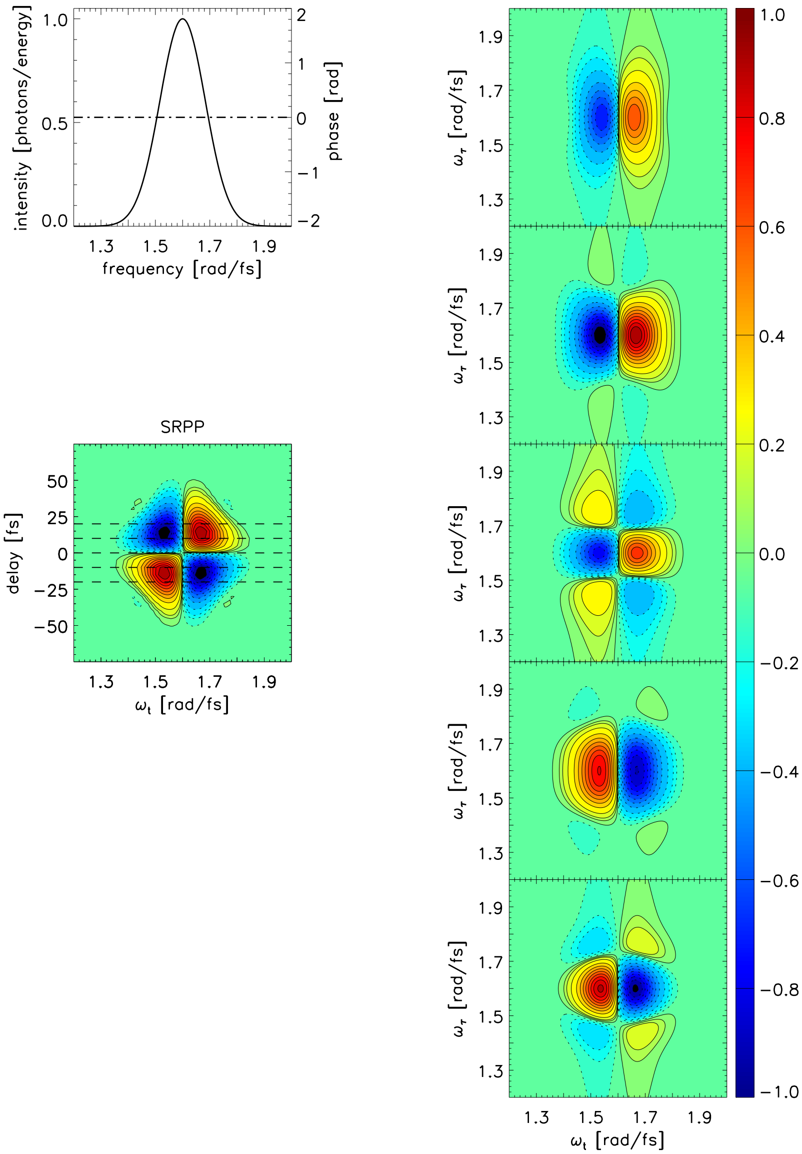

Figure 4.2: Simulated XPM for transform limited Gaussian pulses. The XPM photon number spectrum is simulated for spectrally resolved pump-probe (left) and in 2D (right column). A transform limited Gaussian pulse centered at 1.6 rad/fs with an intensity FWHM of 20 fs is shown in the panel on the top left. The spectrally resolved XPM signal is shown on the left. The horizontal dashed lines shown in the spectrally resolved XPM signal are the T delays of the 2D spectra on the right column. From top to bottom, the T delays are 20 fs, 10 fs, 0 fs, -10 fs, and -20 fs. Contours of ±1%, 3%, 5%, 10%, 20%, 30%, 40%, 50%, 60%, 70%, 80%, and 90% are shown in the panels normalized to the $T = 10$ fs spectrum. At negative delays T, the 2D spectra show more lobes that cancel the SRPP peaks, while the peaks in the 2D spectra at positive delays T simply decrease in peak amplitude. These unsymmetrical 2D spectra cause a symmetrical decay in the projection onto ω_t that gives SRPP peak amplitudes.

Another key feature in the 2D spectra of XPM is the appearance of the oppositely signed peaks from the center that gradually causes the projection onto ω_t to vanish at $T = 0$ before changing the sign of the projection onto ω_t. This feature is shown in Fig. 4.3, where the T time series of 2D XPM spectra from -5 fs to +5 fs with 2.5 fs steps show the emergence of the oppositely signed peaks at T = -5 fs. At T = -5 fs, oppositely signed peaks appear in the center and begin splitting the original peaks. The oppositely signed peaks eventually grow larger and change the sign of the projected peaks after the ω_t projection vanishes at $T = 0$.

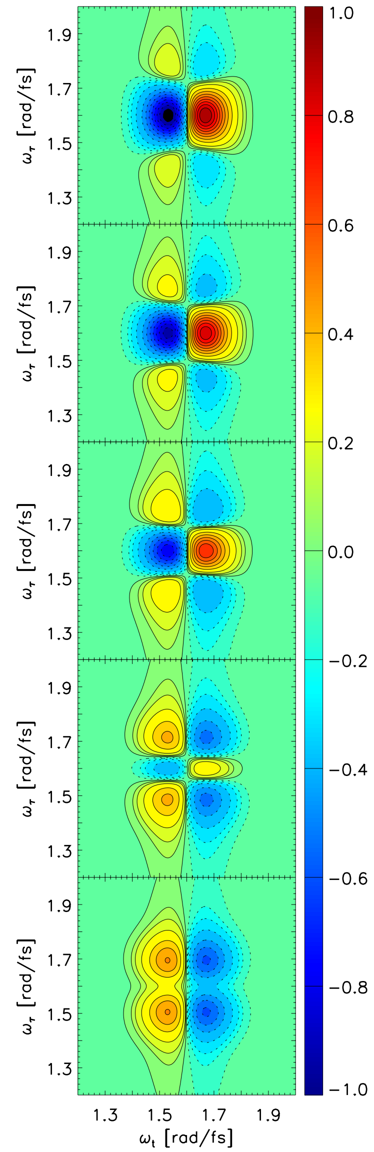

Figure 4.3: Simulated 2D XPM for transform limited Gaussian pulses showing the peak splitting at T = -5 fs and the subsequent emergence of oppositely signed peaks. Transform limited Gaussian pulses centered at 1.6 rad/fs with an intensity FWHM of 20 fs are used for simulating the 2D XPM signal. From top to bottom, the T delays are the 5 fs, 2.5 fs, 0 fs, -2.5 fs, -5 fs. Contours of ±1%, 3%, 5%, 10%, 20%, 30%, 40%, 50%, 60%, 70%, 80%, and 90% are shown in the panels, all normalized to the T = 5 fs spectrum. The T = -5 fs 2D spectrum shows a dip in the center along the excitation frequency dimension, from which oppositely signed peaks emergy as T increases.

Gaussian Pulses with a Quadratic Spectral Phase

To see how chirp affects XPM in 2D spectra, a linear chirp is added to the Gaussian pulses. Figure 4.4 shows 2D and SRPP XPM spectra for positive linearly chirped Gaussian pulses with a GDD of $\phi'' = +100$ fs^2. The quadratic phase lengthens the pulse from the transform limited intensity FWHM of 20 fs to ~24 fs by spreading the frequencies out linearly in time, with lower frequencies arriving first. The most obvious difference compared to transform limited Gaussian pulses in the SRPP transient is the loss of separate anti-symmetry with respect to reflection across $T = 0$ and the center frequency ω_0. The symmetry of the SRPP transient with respect to the product of the two reflections remains.

The SRPP XPM signal shows a tilt, which depends on the direction of the chirp [20] and is related to the instantaneous frequency of the pulse. These calculations are consistent with those reported previously by Ziegler and co-workers [20]. For comparison, Fig. 4.5 shows 2D and SRPP XPM spectra for Gaussian pulses with a GDD of ϕ'' = -100 fs^2. Comparison between Fig. 4.4 and Fig. 4.5 shows an anti-symmetry between the two linearly chirped SRPP signals from XPM upon reflection about either $T = 0$ or the center frequency ω_0.

With symmetric time and frequency pulse envelopes, 2D XPM spectra for the positive and negative linearly chirped Gaussian pulses in figures 4.4 and 4.5 are each anti-symmetrically, related to their counterpart with the same waiting time T by simultaneous reflection across the center frequency in both frequency dimensions ($\omega_t = \omega_\tau = \omega_0 = 1.6$ rad/fs).

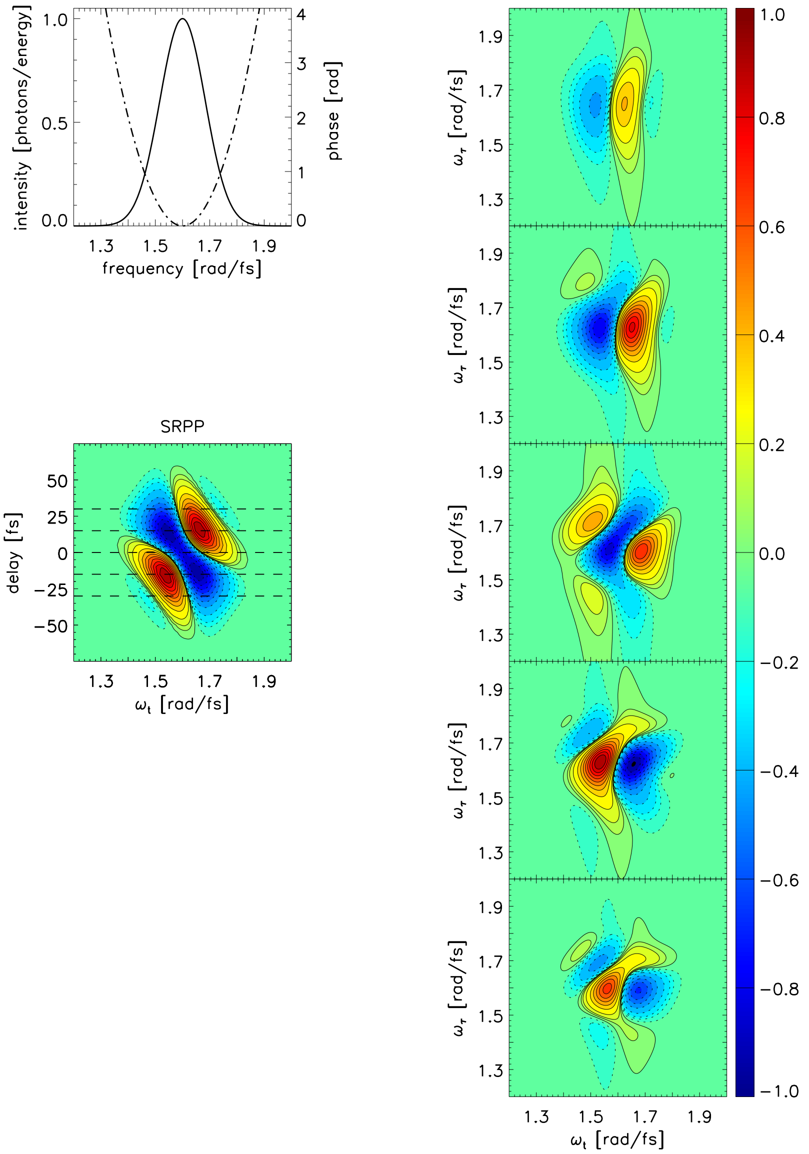

Figure 4.4: Simulated XPM for positive linearly chirped Gaussian pulses. The XPM signal is simulated for spectrally resolved pump-probe (left) and in 2D (right column). Gaussian pulses that are positive linearly chirped with a GDD of $\phi'' = +100$ fs^2, centered at 1.6 rad/fs, with a transform limited intensity FWHM of 20 fs is shown in the figure on the top left. The linear chirp lengthens the pulse intensity FWHM to ∼24 fs. The spectrally resolved XPM signal is shown on the left. The horizontal dashed lines shown in the spectrally resolved XPM signal are the T delays of the 2D spectra on the right column. From top to bottom, the T delays are 30 fs, 15 fs, 0 fs, -15 fs, and -30 fs. Contours of ±1%, 3%, 5%, 10%, 20%, 30%, 40%, 50%, 60%, 70%, 80%, and 90% are shown in the panels normalized to the T = -5 fs spectrum, which has the largest amplitude.

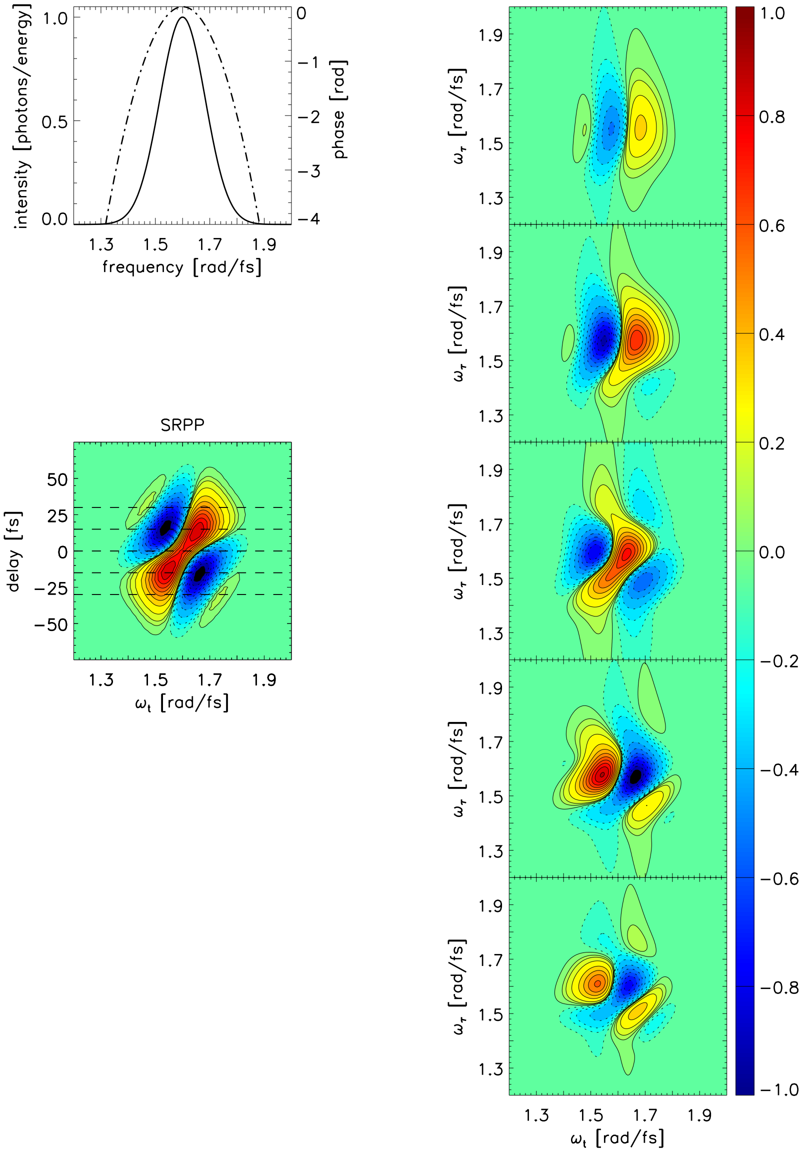

Figure 4.5: Simulated XPM for negative linearly chirped Gaussian pulses. The XPM signal is simulated for spectrally resolved pump-probe (left) and in 2D (right column). Gaussian pulses that are negative linearly chirped with a GDD of ϕ'' = -100 fs^2, centered at 1.6 rad/fs, with a transform limited intensity FWHM of 20 fs is shown in the figure on the top left. The linear chirp lengthens the pulse intensity FWHM to ∼24 fs. The spectrally resolved XPM signal is shown on the left. The horizontal dashed lines shown in the spectrally resolved XPM signal are the T delays of the 2D spectra on the right column. From top to bottom, the T delays are 30 fs, 15 fs, 0 fs, -15 fs, and -30 fs. Contours of ±1%, 3%, 5%, 10%, 20%, 30%, 40%, 50%, 60%, 70%, 80%, and 90% are shown in the panels normalized to the T = -5 fs spectrum, which as the largest amplitude.

Gaussian Pulses with a Cubic Spectral Phase

For the last example, we simulate the XPM for Gaussian pulses with a cubic spectral phase. The cubic spectral phase generates an asymmetric pulse envelope in time. As a result, we can see how the symmetry of the XPM signal is affected. Figures 4.6 and 4.7 show 2D and SRPP XPM spectra for Gaussian pulses with a positive and negative cubic phase, respectively. The Gaussian pulses are centered at 1.6 rad/fs with a TOD of $\phi''' = \pm 3000$ fs^3, which lengthens the Gaussian pulse from the transform limited 20 fs to ~24 fs and makes the pulse asymmetric in time. Each SRPP transient is anti-symmetric with respect to reflection across ω_0 (a symmetry not present for the linear chirp). Only one anti-symmetry between the positive and negative cubic phase SRPP XPM transients remains: the pair is anti-symmetric with respect to reflection about $T = 0$, the anti-symmetry between the pair with respect to reflection about the center frequency ω_0 for linear chirp is gone.

In each 2D spectrum, there is an anti-symmetry with respect to the center frequency along the detection axis, $\omega_t = \omega_0 = 1.6$ rad/fs (a symmetry not present for linear chirp). However, there is no symmetry between the 2D spectra with positive and negative cubic phase. The 2D spectra for the Gaussian pulses with positive and negative cubic phase in figures 4.6 and 4.7 are each very different from their counterpart with the same T. This may be the result of the pulse envelopes being asymmetric in time. Observations that remain true for all chirps are that the XPM 2D spectra rely on peak cancellation effects to weaken the signal in the ω_t projection at more negative T delays and the XPM 2D spectra rely on smaller amplitudes to weaken the signal without cancellation in the ω_t projection at more positive T delays.

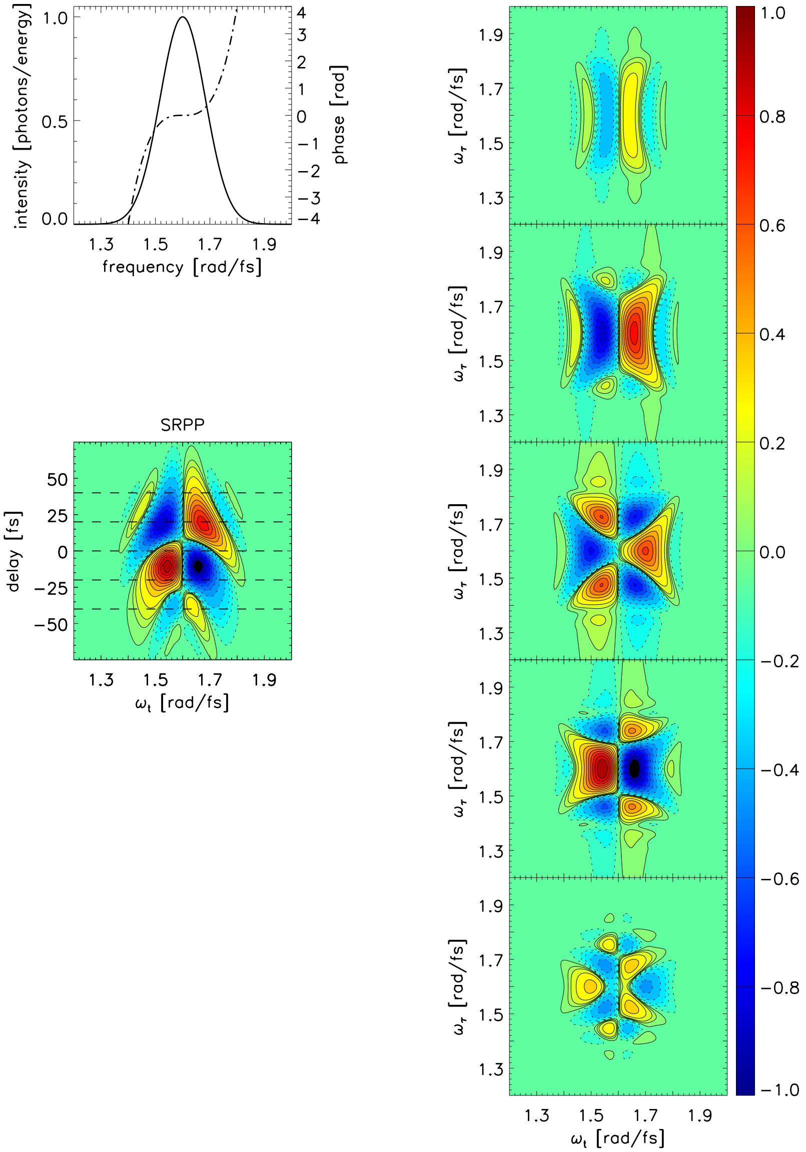

Figure 4.6: Simulated XPM for Gaussian pulses with a positive cubic phase. The XPM signal is simulated for spectrally resolved pump-probe (left) and in 2D (right column). Gaussian pulses with a TOD of $\phi''' = +3000$ fs^3, centered at 1.6 rad/fs, with a transform limited intensity FWHM of 20 fs is shown in the figure on the top left. The cubic phase lengthens the pulse intensity FWHM to ∼24 fs. The horizontal dashed lines shown in the spectrally resolved XPM signal are the T delays of the 2D spectra on the right column. From top to bottom, the T delays are 40 fs, 20 fs, 0 fs, -20 fs, and -40 fs. Contours of ±1%, 3%, 5%, 10%, 20%, 30%, 40%, 50%, 60%, 70%, 80%, and 90% are shown in the panels normalized to the T = -5 fs spectrum.

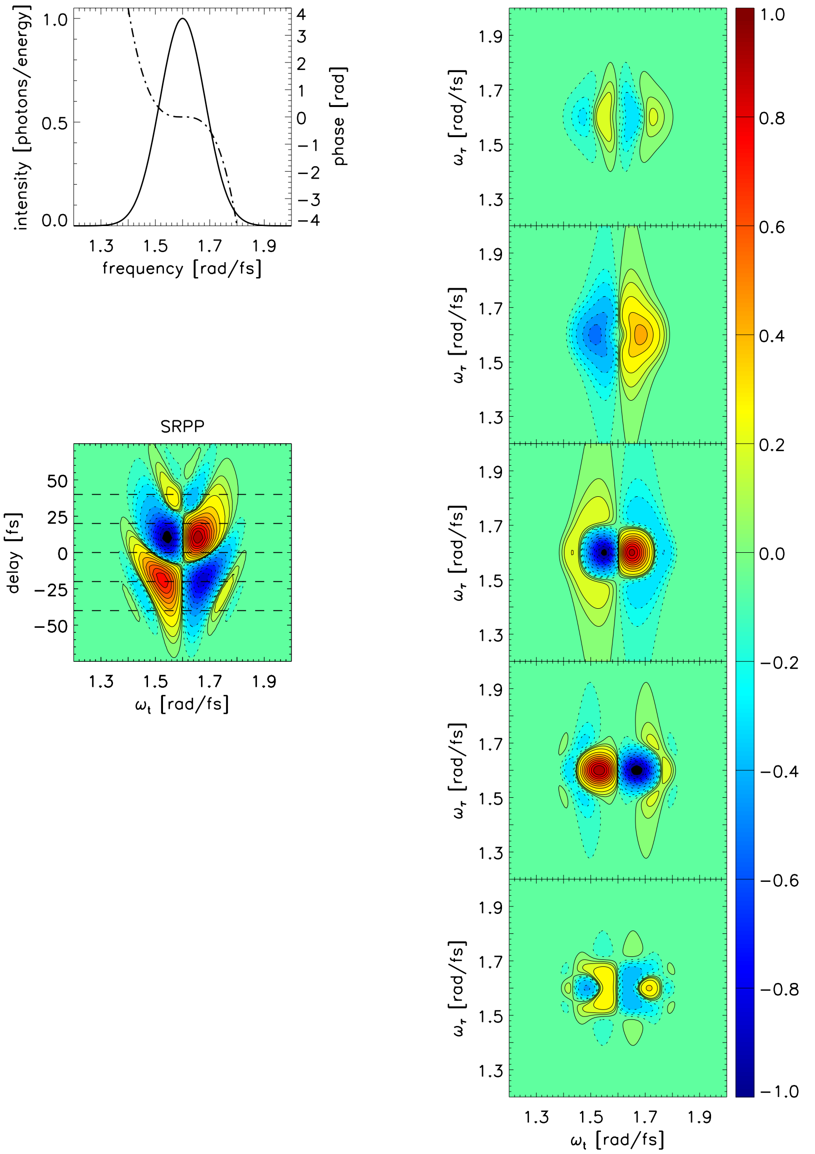

Figure 4.7: Simulated XPM for Gaussian pulses with a negative cubic phase. The XPM signal is simulated for spectrally resolved pump-probe (left) and in 2D (right column). Gaussian pulses with a TOD of $\phi''' = -3000\ \text{fs}^3$, centered at 1.6 rad/fs, with a transform limited intensity FWHM of 20 fs is shown in the figure on the top left. The cubic phase lengthens the pulse intensity FWHM to ∼24 fs. The horizontal dashed lines shown in the spectrally resolved XPM signal are the T delays of the 2D spectra on the right column. From top to bottom, the T delays are 40 fs, 20 fs, 0 fs, -20 fs, and -40 fs. Contours of ±1%, 3%, 5%, 10%, 20%, 30%, 40%, 50%, 60%, 70%, 80%, and 90% are shown in the panels normalized to the T = -5 fs spectrum.

4.3 Experimental Methods

This section describes measurements of a signal from transparent windows and solvent in SRPP and 2D spectra. Because the XPM signal is unique to the pulse spectral amplitude and spectral phase, the experimental results are compared to simulation using the retrieved spectrum and spectral phase acquired from SHG FROG. The signal has several features predicted for XPM.

Experimental Apparatus

In the experiment, a pulse train from a Ti:sapphire-pumped, short-wave infrared noncollinear optical parametric amplifier (NOPA) is directed into the pump-probe setup. The NOPA is based on the design of Cerullo and co-workers [29], and uses quasi-phase matching in a periodically poled stoichiometric lithium tantalate crystal to generate pulses over the 1 – 2 μm wavelength range with pulse energy stabilities better than 0.3% RMS. About 2 m after the deformable mirror compressor, the beam is spatially filtered by focusing with a 250 mm focal length curved mirror into a 250 μm diameter pinhole, and re-collimated by a 250 mm focal length curved mirror. Since this spatially filters the beam during adaptive pulse compression, it inhibits the optimization from introducing angular deviations that may result in spatial chirp. The pulses are compressed down to ~19 fs by a deformable mirror (OKO 30 mm 19 channel Piezoelectric Deformable Mirror) using an adaptive algorithm [29][30] to maximize the intensity of the second harmonic generation with a 20 μm thick Type I β-Barium Borate (BBO) crystal cut at 20 degrees with respect to its optical axis (Castech Inc.) at the sample position in the 2D spectrometer.

The 2D spectrometer with an all reflective design is shown in Fig. 4.8. The 2D spectrometer consists of an actively stabilized Mach-Zehnder interferometer for generating the pump pulse pair. A broadband, inconel-coated, glass window [31][32] splits the spectrometer input beam into pump and probe beams. All beam splitters in this apparatus exploit the air-glass interface Brewster's angle to prevent additional surface reflections and their interference. The pump pulse pair and probe pulse travel parallel to each other and are each vertically displaced 4 mm from the center of the concave spherical mirror (f = 125 mm) that focuses them into the sample. The pump pulse pair and probe pulse have a horizontal angle of incidence of ∼2.3° with respect to the spherical mirror's optical axis. This near retro-reflection accomodates the finite beam diameter and unusable edge of the last ∼45° mirror (a D-shaped pickoff mirror) while minimizing spherical aberrations. After the beams overlap in a common focus at the sample, a CaF_2 plano-convex lens (Eksma Optics #110-5217E, f = 125 mm at 632.8 nm) re-collimates the beams. The re-collimating lens is oriented such that the curved surface points toward the diverging beams to prevent back reflection onto the sample. After the beams are collimated, the pump pulse pair is picked off using a mirror to reflect it onto a photodiode used to measure the pump pulse pair interference. A 1D Fourier transform of the pump-pulse pair interferogram determines the interferometer phase correction for 2D spectra without any adjustable parameters. The dominant term in this phase correction is an origin shift arising from locking the interferometer near $(n+1/4)\lambda_{HeNe}$.

Two-Dimensional Spectroscopy Data Acquisition

The Brewster's angle Mach-Zehnder interferometer with inconel beam splitters creates a pump-pulse pair (pulses a and b) from the bright output with a delay, τ, roughly controlled by computerized translation stages (Newport MFA-PPD with multi-axis Newport ESP 300 controller, stepper motor, nominal 0.008 μm micro-step size). A piezoelectric transducer (Piezomechanik PCh 150/10x10/2, with a maximum displacement of ∼1 μm at ∼100 V) attached to the dihedral retroreflector in arm b of the interferometer then finely adjusts and stabilizes the delay with feedback [33][34][35] from a linearly polarized, continuous wave, red (632.8 nm wavelength) HeNe laser [Melles Griot #05-LHP-991 (currently sold as model #25-

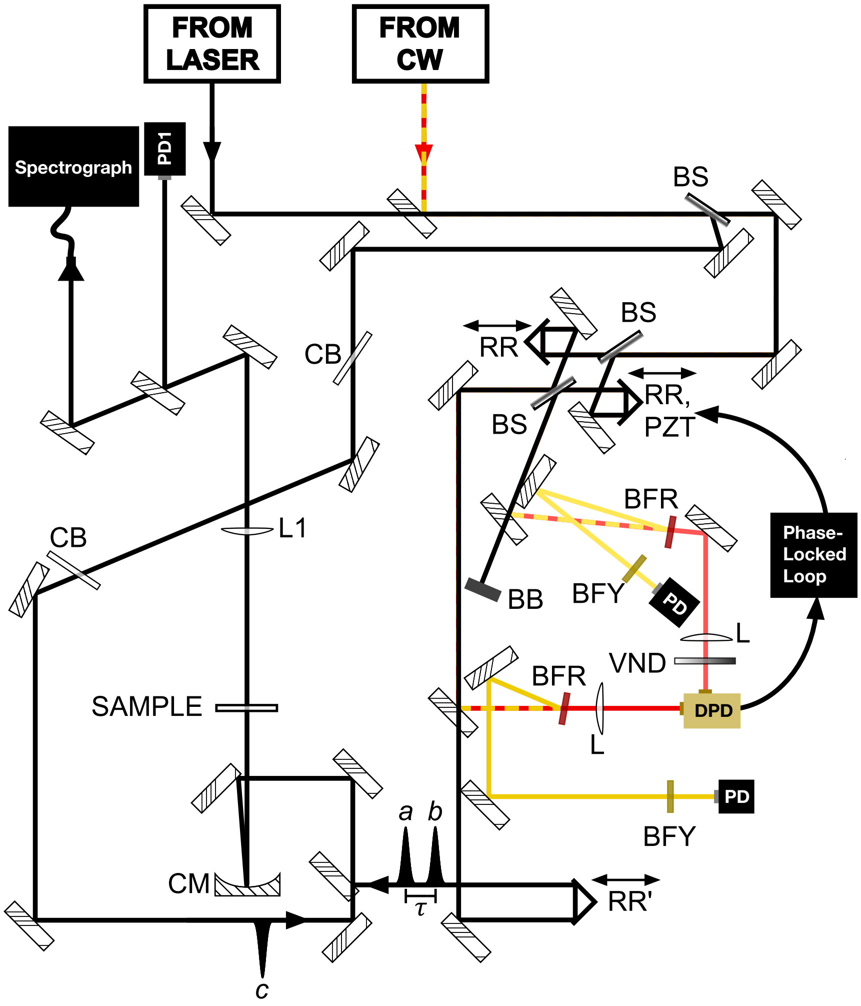

Figure 4.8: All reflective, partially collinear 2D spectrometer. Pulses a and b, separated by delay τ, exit the Mach-Zehnder interferometer's bright output. The signal and pulse c are fiber coupled to an IR spectrograph for interference detection. Each of pulses a, b, and c passes through two metallic beam splitters at oppositely signed Brewster's angles for matched dispersion and spatial compensation. Continuous wave (CW) lasers (beam paths marked with red and yellow lines) are used to stabilize the delay τ and travel a path below the pulsed laser beam. BS: inconel-coated beam splitter, CB: compensating window, CM: curved silver mirror, f = 125 mm, RR: dihedral retroreflector, RR': trihedral retroreflector, VND: variable neutral density filter, BFR: red band-pass filter (632.8 ± 5 nm), BFY: yellow band-pass filter (600 ± 5 nm), PD: photodiode for yellow CW, PD1: photodiode for pump pulse pair interference, DPD: differential photodiode for active stabilization, PZT: piezoelectric transducer, BB: beam block, L1: CaF_2 plano-convex lens for re-collimating the beams, f = 125 mm, L: plano-convex lens, f = 50 mm. Protected silver mirrors are unlabeled.

LHP-991-249), 10 mW power, ±0.5% power stability, 500:1 polarization ratio]. For maximal stability, the lock points correspond to equal red HeNe photovoltages on photodiodes monitoring the two interferometer output beams. A linearly polarized, continuous wave, yellow (594.1 nm wavelength) HeNe laser [34] (Melles-Griot #25-LYP-173-249, 2 mW power, ±0.5% power stability, 500:1 polarization ratio) provides an out-of-loop check on stabilization. The loop filter (JILA electronics shop [33], operated in the 9 dB/CPU servo mode [35] with the 9 dB corner set at 10 Hz and the PI corner, where proportional gain turns into integral gain, set to 1 kHz) was modified with a reed relay (Coto Technology 8L41-05-111) to electronically change the polarity of the locking position of the red HeNe. A 5 V high (0 V low) signal, from the output of the A/D converter (Stanford Research SR245), sets the gain setting to lock at the zero crossing of a positive (negative) slope of the red HeNe. Step scanning proceeds by fixing the PZT voltage, setting the polarity of the lock, stepping the stage, and re-locking the PZT. The double-locking (locking at both positive and negative slopes of the zero-crossing of the red HeNe in succession) procedure doubles the Nyquist frequency, which increases the measurable bandwidth in the indirectly detected frequency dimension of a 2D spectrum determined by Fourier transformation. Although the positive and negative slope data time series are each evenly spaced, the time intervals between adjacent points in the combined time series are alternatively larger and smaller than half of their common uniform time step. An interlaced Fourier transform technique is used to combine the two aliased spectra into a single spectrum with twice the bandwidth. This requires an accurate determination of the time delay between the two different time series (interferograms collected locked at the positive and negative slopes), which is measured by the phase difference between the two yellow HeNe interferograms. The details of the interlaced Fourier transform algorithm are explained in Appendix A. Previously, the Nyquist frequency was limited to ∼1.488 rad/fs (1265.8 nm) by sampling at one red HeNe cycle, which limits broadband experiments in the shortwave infrared. The double-locking interlaced Fourier transform technique extends the Nyquist frequency to ~2.976 rad/fs (632.8 nm), accessing the entire shortwave infrared region without aliasing.

Spectrally Resolved Pump-probe Data Acquisition

SRPP transients were collected in the 2D spectrometer by blocking one arm of the Mach-Zehnder interferometer. To obtain a SRPP transient, ten sets of the probe spectrum with the pump blocked and unblocked were acquired and averaged at each time delay. Two background spectra were acquired every time a spectrum was collected; the first was necessary to clear the InGaAs array detector of residual counts and the second was used for background subtraction. The order of measuring the probe spectra with and without the pump was also alternated to check for any artifacts that may arise from the detector. Spectra collected with the pump first and without the pump second did not agree with spectra collected without the pump first and with the pump second when the number of counts on each pixel exceeded 5% of the full well capacity (that is, exceeding ~3000 counts out of 65,000). For this reason, the number of photoelectrons on each pixel is restricted to less than 3% of the full well capacity (full well capacity 65,000 counts).

Fundamental Pulse Spectrum Acquisition

The fundamental pulse spectrum was recorded by coupling the light through an aspheric lens with NA = 0.25 (Thorlabs C220TMD-C, 11.0 mm focal length, 1050 – 1700 nm AR coating) into a single-mode fiber with NA = 0.14 (Thorlabs 1060XP, 980 – 1600 nm, cutoff frequency 920 ± 30 nm). The single-mode fiber output is fed into a 0.15-m Czerny-Turner spectrometer (Princeton Instruments SP-2150i, f/4) with a 150 grooves/mm grating blazed for 1.25 μm wavelength (Richardson Gratings 53-*-500R – Master No. 1107), that yields a nominal linear dispersion of 37 nm/mm on a 1024x1 pixel InGaAs array with extended wavelength sensitivity out to 2.2 μm (Princeton Instruments OMAV:1024-2.2, 25 μm pixel spacing, liquid nitrogen cooled, operated in low gain mode with a minimum well capacity of 100 Me$^-$). Ten atomic lines of Xenon (Newport #6033, Xe calibration lamp) with the wavelengths in vacuum [36][37], spanning most of the spectrograph range at the grating position (798 – 1786 nm), are fit to a second-order polynomial in pixel number for the wavelength calibration. The atomic lines used for spectrograph wavelength calibration have a FWHM of ∼3 pixels, which reflects nearly diffraction-limited spatial imaging resolution at the focal plane.

The fundamental pulse spectrum was obtained by averaging 100 spectra with a 250 ms integration time. The number of photoelectrons on each pixel is restricted to less than 3% of the full well capacity (full well capacity 65,000 counts) by attenuation with a neutral density filter in order to avoid harmonic nonlinearities previously observed in Fourier transform spectral interferometry [34]. Two successive background spectra with the pulse blocked were collected after every acquisition of the pulse spectrum; the first background is discarded because it contains residual counts due to charge persistence [38] and the second background is used for background subtraction. Previous experiments with more than two successive background spectra after the pulse spectrum found ∼1–2 residual counts on average by subtracting the second background from the first background. No residual counts above the noise floor (less than 1 count) were observed by subtracting the third background from the second background, so it was concluded that the array detector is fully cleared by the second background.

Flatfielding and Spectral Corrections

A flatfield [34][38] was recorded by using the pulse spectrum, systematically turning the grating to scan the spectrum across the InGaAs array detector, and summing the spectra. Ideally, the pulse spectrum should be scanned across the array with wavelength steps that are signficantly less than the FWHM of the narrowest feature of the spectrum. For this reason, the spectrum was scanned with a step size of 3 pixels (∼3 nm) until the spectrum runs off at the ends of the array detector. At each grating position, 6 pulse spectra were collected with 2 backgrounds taken after every pulse spectrum. The 6 pulse spectra were then separated into two data sets: one data set with the odd spectra (1,3, and 5) and another data set with the even spectra (2,4, and 6). The two data sets produced two separate flatfields, which were used to check the reproducibility of the flatfield by dividing them by each other. The division nominally equals unity over all the pixels (range of ±0.008). The flatfield was applied to each spectrum to correct for pixel-to-pixel variations in sensitivity [34][38]. The flatfield reduced the fine structure on the spectra only by a factor of 2; we suspect the imperfection in the flatfield is due to some form of nonlinear coupling between nearby pixels during charge accumulation or readout.

After flatfielding, the averaged spectrum is divided by the grating efficiency curve, provided by Richardson Gratings, and the spectral sensitivity of the InGaAs array detector, provided by Princeton Instruments. Figure 4.9 shows the necessary corrections to the raw fundamental pulse spectrum.

Sample

The sample used for this experiment was a solvent of tetrachloroethylene (TCE) inside a spinning sample cell custom built in our lab [39]. The spinning sample cell consists of an air-tight copper gasket sealed enclosure carrying a 4200 RPM, 2.5 inch diameter hard-disk drive motor and a reusable glass sandwich cell. The optical properties of the proprietary hard disk drive glass used to construct the sandwich cell are not known beyond transparency and a 8% reflection. The beams have a 1/e diameter of ∼100 μm, determined from transmission through a 75 μm pinhole, and cross at an angle of 3.7 degrees. The beams overlap throughout the sandwich cell, not only in the solvent, but also in both hard-disk drive glass windows. Thus, both hard-disk drive glass and solvent contribute to XPM. The beams do not overlap

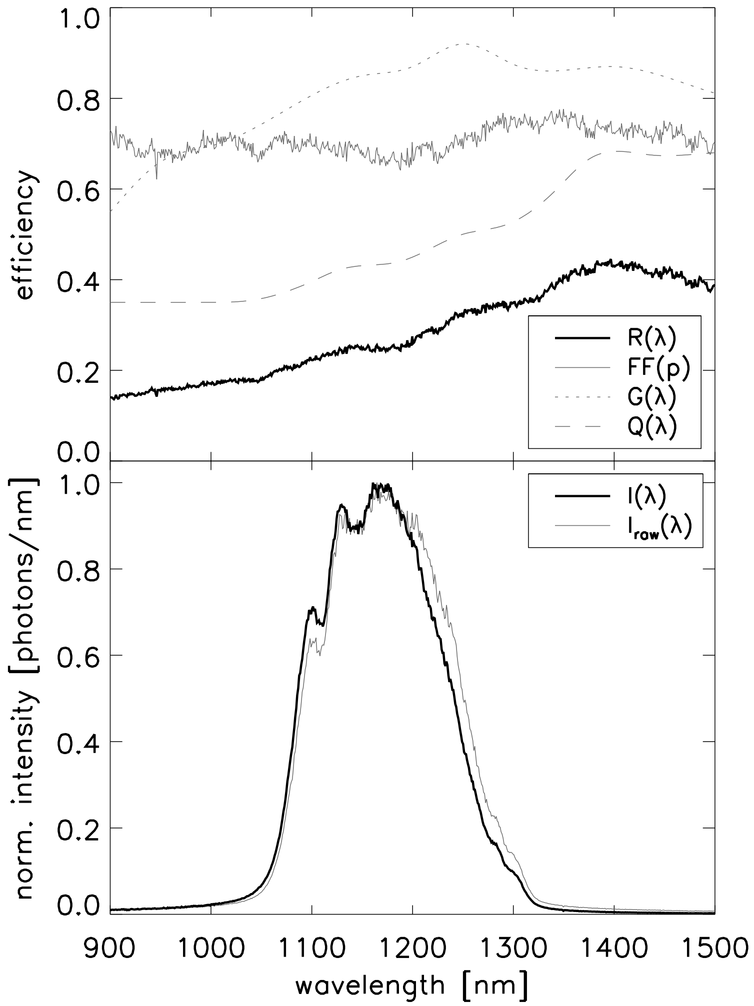

Figure 4.9: Spectral correction for InGaAs array detector. (Top panel) The total spectral correction function, $R(\lambda)$ (black solid line), is the product of the wavelength dependent grating diffraction efficiency, $G(\lambda)$ (dotted line), the wavelength dependent quantum efficiency of the array detector, $Q(\lambda)$ (dashed line), and the pixel dependent flatfield function, $FF(p)$ (grey solid line). (Bottom panel) Experimentally measured raw pulse spectrum without any correction (solid grey line) and the pulse spectrum after division by the total spectral correction, $R(\lambda)$, and re-normalization to the maximum.

in the enclosure viewports. The enclosure keeps the spinning sample cell air-free (ultra high vacuum compatible seals) with a resampling time greater than 0.9 s (due to the hard drive motor not spinning at exactly 70 Hz, or the laser not having exactly 1 kHz repetition rate, or both).

To assure the beams overlap at the sample, a 50 μm diameter pinhole mounted inside an identical glass sandwich cell is used to maximize the transmission of all the beams. There is an axial enclosure translation range of 0.005" where the transmission through the pinhole is unchanged to within a measurement uncertainty of less than 1%; the reproducibility of z-positioning is within this 0.005" range.

Determining Time Zero

The determination of time zero posed a challenge because of the absence of a resonant signal. Previously, time zero was set inside the sample by using the crossing point of symmetrical pump-probe transients, which allowed the determination of time zero to sub-femtosecond accuracy [18]. In this experiment, the SRPP XPM is used to determine the time zero. The delay at which there is a sign change is determined to be zero time delay. Because the pulses used in this experiment were near transform-limited, the time zero in the SRPP XPM is apparent compared to the signal with a chirped pulse [5]. This method of using the XPM allows the determination of the zero time delay inside the sample within ~2 fs. Methods using the autocorrelation with a BBO crystal did not give a reliable time origin, with delays displaced up to 10 fs, which might arise from the tilt of the doubling crystal.

4.3.1 Pulse Characterization using SHG FROG

Second harmonic generation (SHG) spectra were collected by free-space coupling the frequency doubled autocorrelation beam using a negative (-30 mm focal length) and positive (25.4 mm focal length) lens pair to match the numerical aperture of the Ocean Optics

USB4000 UV-VIS spectrometer (3648 active pixels, f/4). The detector wavelength axis was calibrated using 8 atomic lines of a Neon lamp (Newport #6032, Ne calibration lamp). SHG autocorrelation spectra were collected with time delays from -180 fs to +180 fs with the natural 0.9874 fs step size for the delay stage. This scan produces over 256 time delays to allow subsequent centering of 256 frequency-resolved optical gating (FROG) transients on zero time delay. The FROG retrieval program (Femtosoft version 3.2.2) requires the input FROG trace to be on a square grid with evenly spaced axes in both time and wavelength. Therefore, the obtained FROG traces are Fourier interpolated onto an even wavelength axis from 500 – 700 nm with a grid size of 256.

The agreement between the measured pulse spectrum and the fundamental pulse spectrum retrieved by FROG was used to verify the convergence of the retrieval algorithm. The fundamental pulse spectrum was measured using a single-mode fiber, which measures the spectrum that focuses at the sample position. The fundamental spectrum is corrected to a photons/wavelength intensity axis. The best agreement between the retrieved fundamental pulse spectrum and the measured pulse spectrum required that the SHG FROG trace be divided by an ω^3 factor before inputting into the FROG algorithm [40]. The ω^3 factor comes from multiplication by (1) an ω^2 dependence that follows from Maxwell's equation for the intensity of an optical signal field radiated by the source nonlinear optical polarization. (2) An ω dependence of the second harmonic intensity arising from the spatial overlap of different fundamental frequency modes [40] for the frequency dependent focusing of a collimated Gaussian beam in which the collimated beam diameter is frequency independent. Previously, others have forced agreement between the autoconvolution and the FROG frequency marginal [41] to correct for these frequency-dependent effects, frequency dependent spectrograph responses and finite phase matching bandwidths in the nonlinear optical crystal. The details of the FROG procedure are explained in the Appendix.

Figure 4.10 shows the results of the retrieval algorithm from the FROG trace. The left column shows the retrieved and experimental FROG trace on the top and bottom, respectively. The FROG error [42] for the 256x256 grid amounts to 0.0016. The figure on the right shows the experimental pulse spectrum (solid line) measured by the spectrograph, the pulse spectrum retrieved from FROG (dotted line), and the spectral phase retrieved from FROG (dash-dotted line). The algorithm retrieves a pulse width of 18.6 fs FWHM, somewhat greater than the transform limited intensity FWHM of 15.2 fs. The retrieved spectral phase has a range of 1 radian over the entire pulse spectrum. The fundamental pulse spectrum retrieved from FROG does not reproduce some details of the measured fundamental pulse spectrum (see Fig. 4.10) and obtaining this level of agreement was an experimental challenge. It is not known whether the error in retrieving the spectrum lies in the measured or retrieved spectrum - prior work in our group has found that the retrieved spectrum is a more accurate one for calculating nonlinear optical signals.

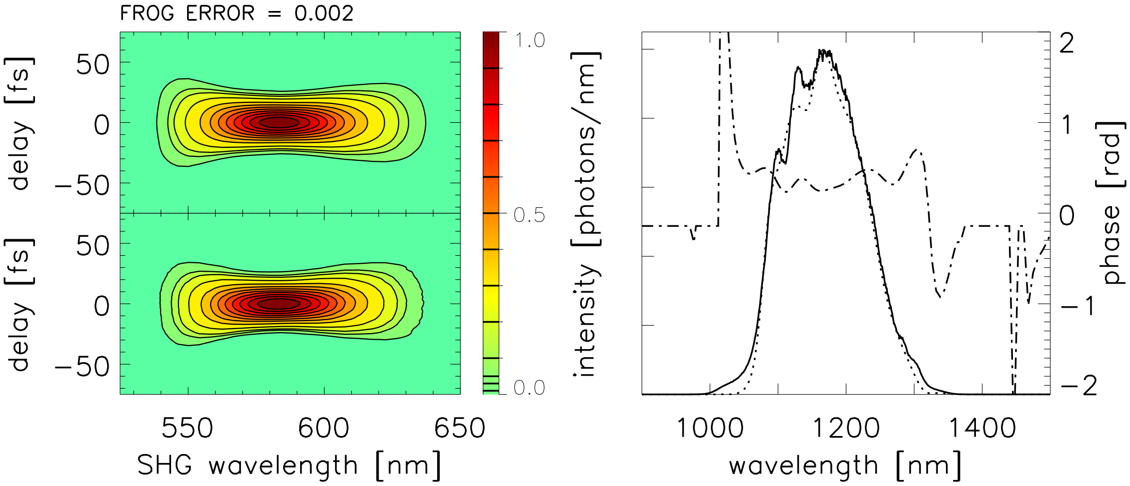

Figure 4.10: Retrieved FROG trace, spectrum, and spectral phase used for XPM experiment. Retrieved (top left) and experimental (bottom left) FROG traces with 1%, 3%, 5%, 10%, 20%, 30%, 40%, 50%, 60%, 70%, 80%, and 90% contours. Typical FROG errors were G = 0.002 on a 256×256 grid, which indicates good convergence of the FROG algorithm to the experimental data. (Right) Comparison of the experimentally measured pulse intensity spectrum (solid line) with the retrieved spectrum (dotted line) shows good agreement except that sharper features and broader wings are observed in the experimental spectrum. The retrieved spectral phase (dotted-dashed lines) shows residual uncompensated higher-order chirp.

4.4 Experimental comparison

The XPM signal in SRPP and 2D spectra is measured and compared to simulations using the pulse spectrum and spectral phase retrieved from SHG FROG. Figure 4.11 compares the experimental SRPP XPM transient on the left to the simulated SRPP XPM transient on the right. The only adjustable parameter in this comparison is the absolute signal amplitude, which is normalized in both. The signal-to-noise ratio in the experiment is 3:1. Several features of the experimental XPM SRPP transients are recovered in the simulation. For example, the connecting negative contours across $T = 0$ indicate that the pulses have a slight positive quadratic phase, consistent with the retrieved spectral phase in Fig. 4.10. The complex structure in both XPM SRPP transients also indicate a higher-order spectral phase. However, there is a discrepancy in the relative amplitudes between the peaks for positive and negative T. In particular, the experimental positive peak at negative T is ~40% too weak in comparison.

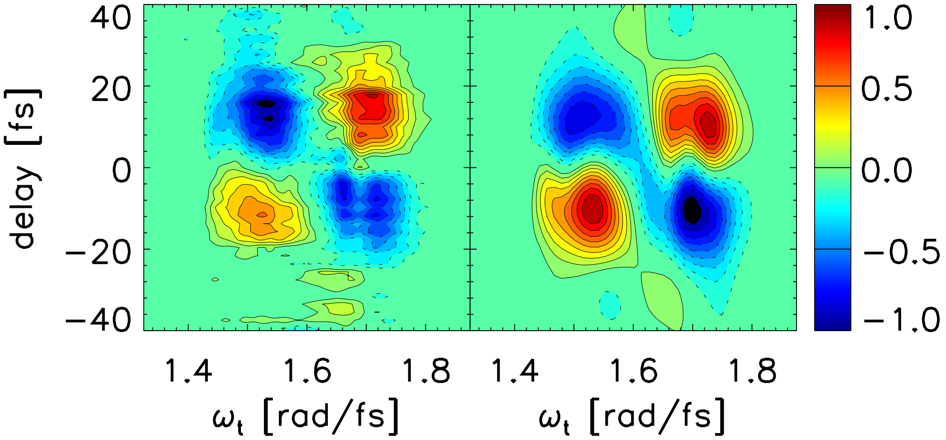

Figure 4.11: Experimental (left) and simulated (right) spectrally resolved XPM. The experimental and simulated spectrally resolved XPM signals show that the pulses are not quite transform limited, which was also determined independently from FROG. Larger distortions of the peaks near $T = 0$ also reflect the higher order phase of the pulse.

The XPM SRPP transient has interesting frequency and time marginals, which can be obtained by integrating over time delay and signal frequency, respectively. It has been stated that a non-zero time marginal indicates spectral filtering when recording the SRPP transient, and a non-zero frequency marginal indicates the optical nonlinearity is not instantaneous [5]. The theoretical zero time marginal may be physically understood as arising from the exchange of photons. XPM exchanges photons of different wavelengths but does not create or destroy photons [14]. A zero time marginal requires correct intensity axis calibration to photons. Ref. [5] does not prove or physically motivate the frequency marginal for an instantaneous response. Ziegler and co-workers [20] state that the frequency marginal only vanishes for transform limited pulses. However in our calculations for chirped pulses, including the simulations with the pulses retrieved by FROG, which have asymmetric spectra and frequency chirps, both frequency and time marginals are numerically zero.

The time and frequency marginals for the experimental SRPP XPM transient of Fig. 4.11 are shown in Fig. 4.12. The time marginal, left of Fig. 4.12, is nominally zero over the time delay scan range and does not indicate a spectral filter problem. However, the frequency marginal, right of Fig. 4.12, is not zero within measurement error. This might arise from a time step resolution or time stepping error in the delay stage. For example, the frequency marginal has a maximum amplitude of ∼0.09 when integrating the normalized XPM SRPP transient. This could have arisen from an additional (or missing) SRPP transient at the positive (or negative) time delay with signals at the 10% contour level. Such stepping errors are more important for shorter pulses. Comparing the experiment and simulation, in Fig. 4.11, this explanation requires ∼2 missing time delays near the maximum signal at T ∼ -10 fs. On the other hand, the time marginal is not affected by any time resolution or stage stepping errors because each SRPP at any given time delay integrates to zero.

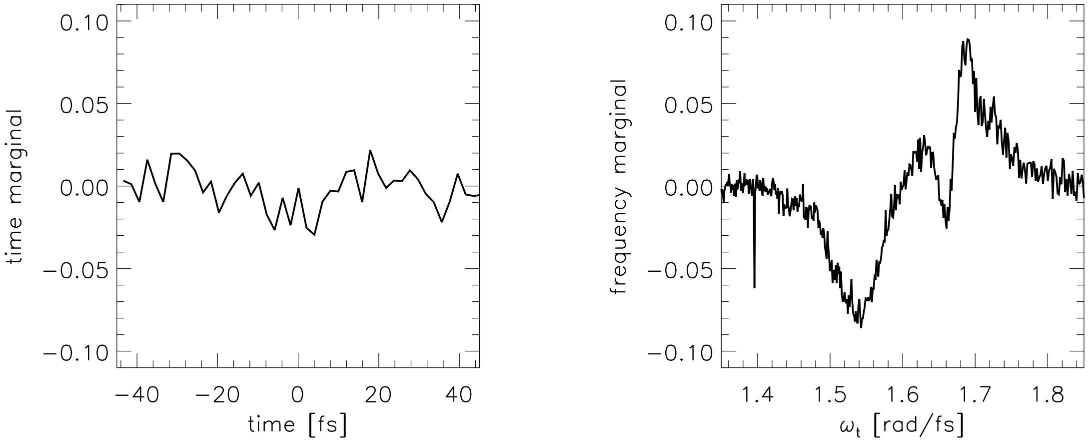

Figure 4.12: Temporal (left) and frequency (right) marginals of spectrally resolved cross phase modulation after normalizing the XPM SRPP transient.

To determine the level of experimental error in our data, another XPM SRPP transient is compared that was taken on another day. Figure 4.13 shows the XPM SRPP transient previously shown on the left and another XPM SRPP transient for comparison on the right. The XPM SRPP transient shown on the right of Fig. 4.13 was acquired with a slightly different spectrum and chirp but with the same sample cell and neat solvent. As shown on the top of the SRPP transient, the frequency marginal is again non-zero but yields a different structure than the frequency marginal of the XPM SRPP transient shown on the left of Fig. 4.13. The time marginal shown on the right of the SRPP transient is again zero within the noise level. Thus, the non-zero frequency marginal can be attributed to experimental error, possibly from time-stepping errors. Later in this chapter, we explore the effect of a non-instantaneous response on the XPM signal, which Wiersma and co-workers [5] have speculated could generate a non-zero frequency marginal.

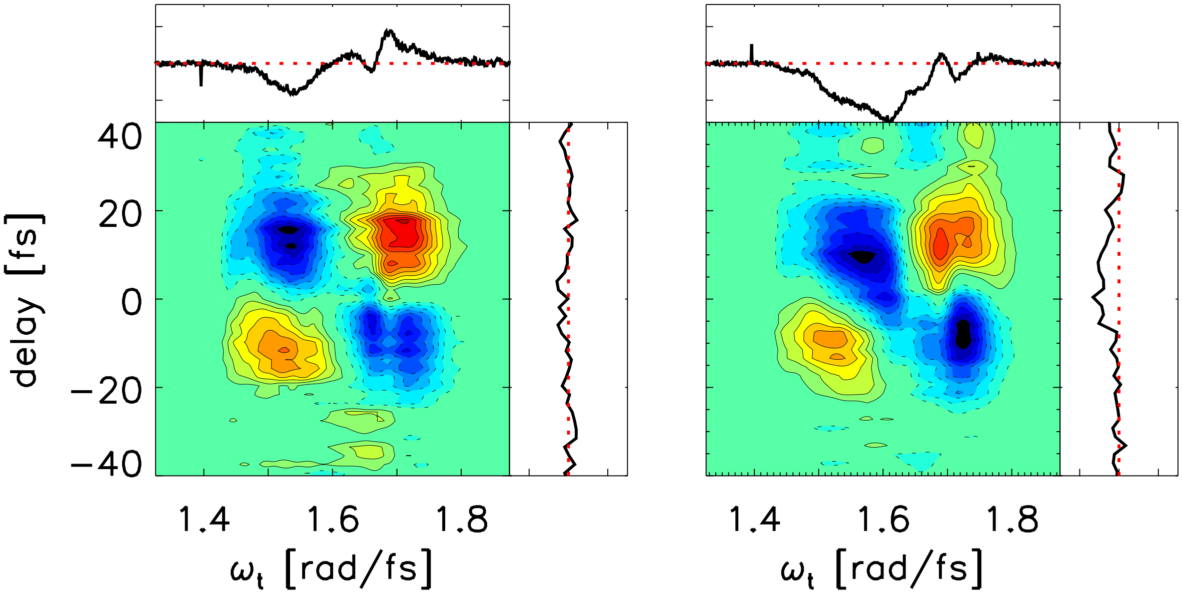

Figure 4.13: XPM SRPP transients taken on different days but on the same glass and neat solvent with similar pulse spectra and similar chirp. The XPM SRPP transient on the left is the same trace shown in Fig. 4.11. The XPM SRPP transient on the right is another trace taken on another day. The panel on top of each XPM SRPP transient shows the frequency marginal and the panel to the right of each XPM SRPP transient shows the time marginal. The horizontal and vertical red dotted lines inside the panels denote zero.

Figure 4.14 shows experimental 2D XPM spectra on the top row with simulated 2D XPM spectra on the bottom row using the amplitude and phase retrieved from FROG. Although the FROG amplitude and phase retrieval was not perfect, the qualitative features of the 2D XPM spectra are still captured. Most notably, the qualitative appearance of the oppositely signed peaks that grow and eventually change the sign of the peaks across $T = 0$ is captured in both. We attribute the quantitative disagreement between experiment and theory to time delay drifts and spectral changes during the data collection. Assuming an instantaneous response, simulations show that the 2D spectra for our pulse spectrum and duration evolve rapidly as a function of waiting time, T. For example, the calculated 2D spectra show contour changes of up to $\sim$20% for a 1 fs difference in T. This indicates a more detailed comparison with such short pulses would require the experiment be performed without such drifts in the waiting time, T. The results presented here suggest that experimentally measuring 2D XPM spectra and simulating the 2D XPM spectra with a retrieved pulse amplitude and phase is possible.

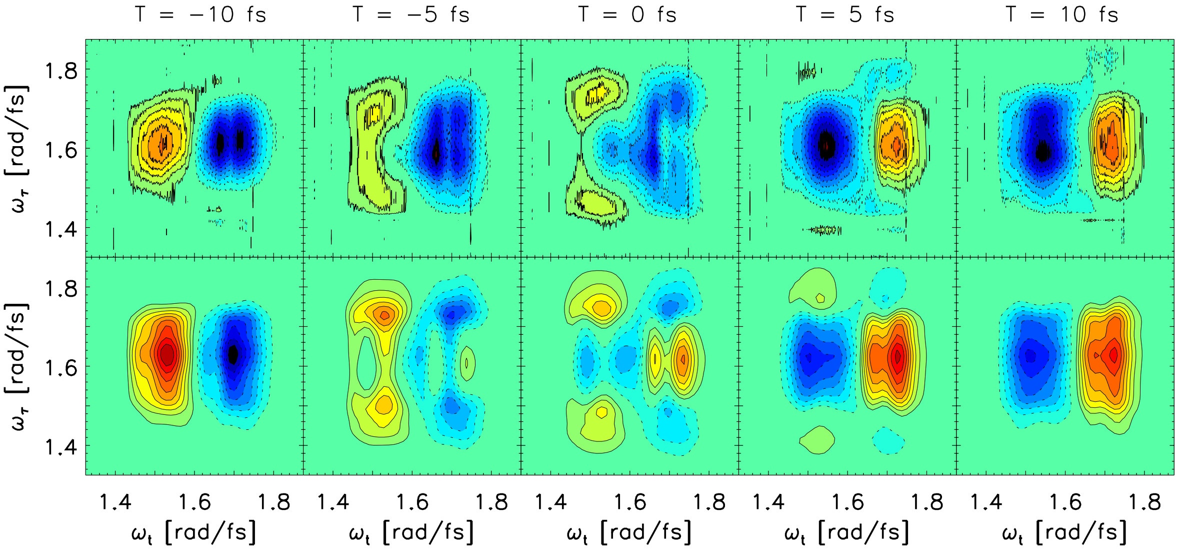

Figure 4.14: Experimental (top row) and simulated (bottom row) 2D XPM spectra. The T delays for both experimental and simulated 2D XPM spectra are shown above the figures. 10% contours are shown in all of the 2D spectra with red and blue contours indicating positive and negative signal, respectively.

4.5 Discussion

4.5.1 Propagation Effects of XPM

In this section, propagation effects for the XPM signal with an absorbing sample are simulated for SRPP transients. As mentioned previously, the XPM signal is proportional to the square of the peak intensity. For this reason, the XPM signal strength becomes more apparent and important for shorter pulses. In our experiments, XPM is an "unwanted" signal because it complicates analysis of resonant signals during pulse overlap. There have been many reports using a raw subtraction of XPM signal [8][43] to reveal the resonant signal that is of interest at early times, but it is shown here that a raw subtraction is not correct. The XPM signal with an absorbing sample is not obviously the same because some frequencies can be preferentially absorbed and new frequencies are also being generated. Furthermore, as shown in simulations, chirp complicates the SRPP XPM signal. Thus, the correct subtraction of XPM becomes particularly important for chirped pulses, for example, XPM signals are often used to measure chirp when using a white light continuum probe in transient absorption experiments [44]. For implementation of an XPM subtraction scheme, propagation effects with an absorbing sample are simulated. Transform limited Gaussian pulses with different absorbing samples are used because their XPM signals have anti-symmetry without distortions, so they show the most obvious effects of absorption on the XPM signal.

The calculation of propagation effects on XPM from an absorbing sample was done in three frequency dimensions [26][45]. In this example, only the XPM signal being generated in the sample is considered; the generation of XPM from the front and back sample cell windows is not considered. In the sample, the pulses are distorted as they propagate and the XPM signal they generate is also distorted as it propagates. Figure 4.15 shows propagation effects on XPM in SRPP for different absorbing samples with an optical density (OD) of 0.3. The top panel shows the XPM SRPP transient without any distortion from an absorbing sample

(OD = 0). As shown in the second row of Fig. 4.15, the absorption peaks (dash-dotted lines) are centered at three different frequencies with respect to the pulse spectrum (solid lines). The third row shows the calculated XPM SRPP transient for the corresponding absorbing sample. The biggest distortions are reductions in signal by 20-40%; these are largest near the absorption frequency, but significant everywhere. The most obvious distortion is the low amplitude signal before $T = 0$; the absorbing sample causes a tail at negative delays in all 3 cases. The fourth row shows the difference between the undistorted XPM SRPP transient (top figure) multiplied by a factor determined by minimizing the RMS difference between the distorted and undistorted XPM SRPP transient. The multiplication factors from left to right are 0.70, 0.69, and 0.71. With these factors, the XPM SRPP signal subtraction scheme yields 10% errors; it is not perfect due to the shape of the absorbing spectrum.

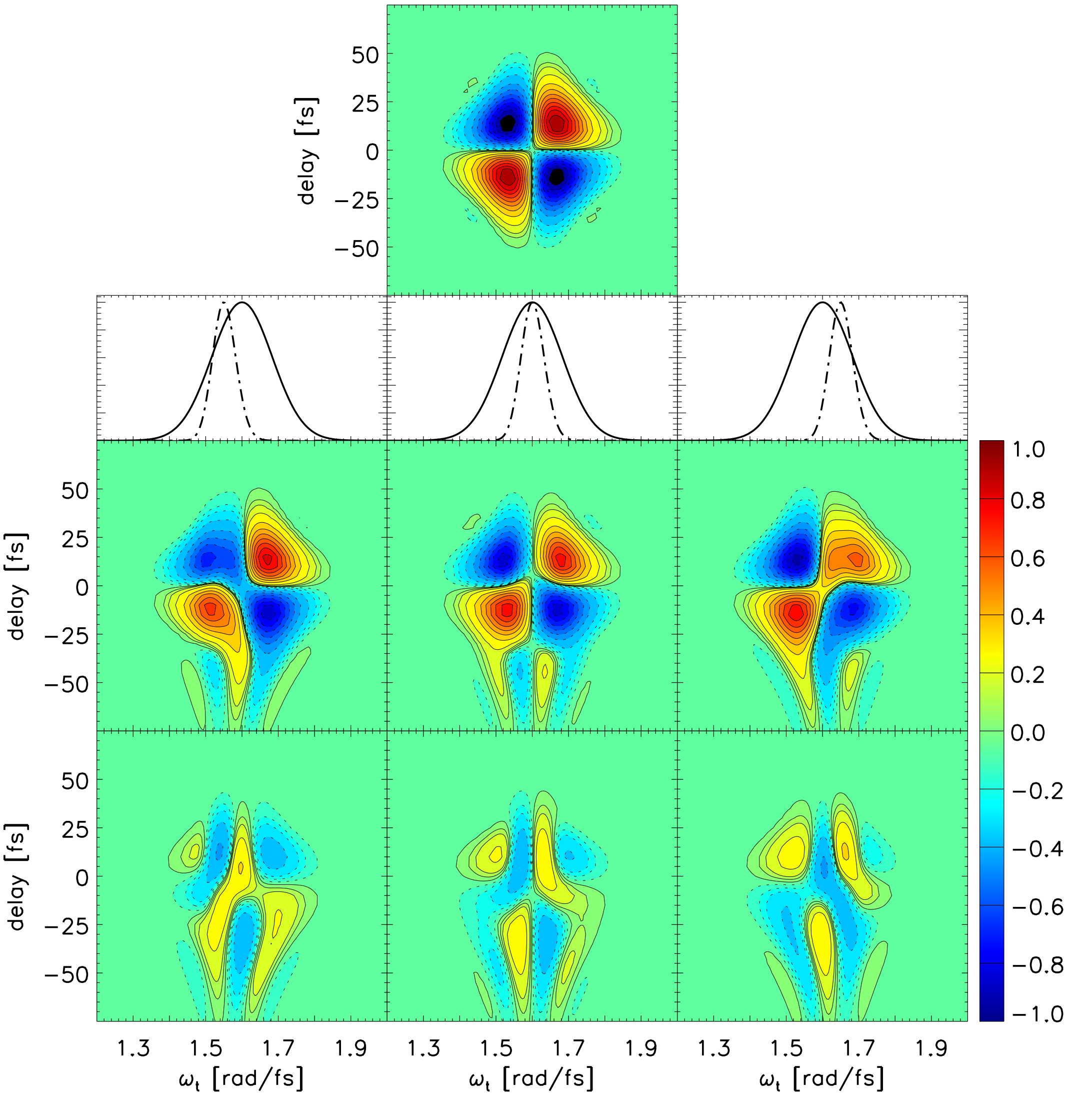

Figure 4.15: SRPP XPM propagation effects in an absorbing sample with absorption spectra centered at 3 different frequencies. The top panel shows the SRPP XPM transient without any absorption. The second row shows the pulse intensity spectrum (solid line) and the sample absorption spectra, all with a peak optical density of 0.3 (dash-dotted line). The third row shows the SRPP XPM transient with the corresponding absorbing sample. The bottom row shows the difference between the undistorted XPM transient multiplied by a factor determined minimizing the RMS difference between the distorted and undistorted XPM transient. The multiplication factors from left to right are 0.70, 0.69, and 0.71. All transients are normalized to the undistorted XPM transient (top figure). Contours of ±1%, 3%, 5%, 10%, 20%, 30%, 40%, 50%, 60%, 70%, 80%, and 90% are shown in all figures with solid/red contours indicating positive peaks and dashed/blue contours indicating negative peaks.

In addition, the absorbing sample causes non-zero time and frequency marginals in the XPM SRPP transient. This is expected because the number of photons is not conserved. Figure 4.16 shows the time and frequency marginals for the SRPP XPM for different absorbing samples. The time marginal is significant for experiments, but the calculated frequency marginal is below the signal to noise.

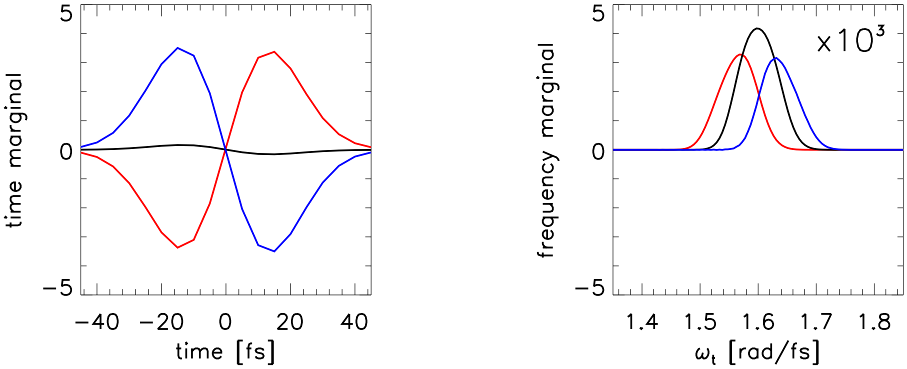

Figure 4.16: Time (left) and frequency (right) marginals after normalizing the XPM SRPP transients with different absorbing samples. In both figures, the red, black, and blue lines show the marginal for the samples absorbing at lower, center, and higher frequencies with respect to the pulse spectrum. The frequency marginals are ~1000x smaller than the time marginals and were multiplied by a factor of 10^3 to keep a common vertical axis.

The XPM propagation distortion for an absorbing sample in three frequency dimensions is a rigorous calculation for a theoretically-based subtraction scheme. For this reason, we suggest a simpler subtraction scheme using the maximum absolute value ratios between the distorted SRPP XPM and the undistorted SRPP XPM. The ratios using this method from left to right are 0.83, 0.76, and 0.84. These ratios roughly agree with the ratio of the total number of photons after (N) and before (N_0) the absorbing sample, which are 0.80, 0.74, and 0.81. Thus, a rough XPM signal subtraction scheme without simulating the propagation effect in three frequency dimensions can be written as,

$$SRPP_{sig}(\omega_t, T) \approx SRPP_{tot}(\omega_t, T) - \frac{N}{N_0} SRPP_{XPM}(\omega_t, T), \tag{4.11}$$

where T is the delay between the pump and probe pulse, N is the number of photons transmitted by the absorbing sample, N_0 is the incident number of photons, $SRPP_{tot}(\omega_t, T)$ is the total SRPP transient including both resonant signals and non-resonant solvent/window XPM, $SRPP_{XPM}(\omega_t, T)$ is the solvent/window SRPP XPM transient, and $SRPP_{sig}(\omega_t, T)$ is the desired SRPP transient without XPM. The N/N_0 factor was also calculated with different ODs from 0.1–0.5 and centering the absorption peak at different frequencies. This subtraction scheme yields 20% errors, as opposed to subtracting 100% of the SRPP XPM signal yielding 30 – 40% errors for an absorbing sample with a 0.3 OD. The quality of the subtraction depends on the OD of the absorbing sample and the shape of the absorbing spectrum.

4.5.2 Non-instantaneous Response

The XPM signal is simulated with an approximate non-instantaneous response to see the effect on the SRPP transient and 2D spectrum. As mentioned previously, Wiersma and co-workers [5] stated that a non-zero frequency marginal, which may be the case for the experimental XPM SRPP transient, indicates a non-instantaneous response. Thus, the simulation with a non-instantaneous response is explored here.

The assumption of a instantaneous (δ-function) response in time corresponds to a constant susceptibility in frequency; this is implied for non-resonant transitions [15][46]. Thus, a non-instantaneous response will have a frequency dependent susceptibility. To simulate the effect of a non-instantaneous response to first order, a constant slope in the susceptibility is used. Fourier transforming Eqn. 4.1 in frequency results in the susceptibility as a function of ω_a, ω_b, and ω_c. The third-order susceptibility with a linear slope has the form

$$R^{(3)}(\omega_a, \omega_b, \omega_c) = c + m \cdot (\omega_a + \omega_b + \omega_c), \tag{4.12}$$

where m is an arbitrary value for the slope. The constant c arises from the 3D Fourier transform of the XPM response. Eqn. 4.12 assumes the same slope as a function of the three variables. To show the effect of a linearly varying third-order susceptibility, a transform limited Gaussian pulse is used because it has an anti-symmetry with respect to time and the center frequency of 1.6 rad/fs with an instantaneous response. Figure 4.17 shows the SRPP XPM transient with $c = 0.125$ and $m = 100$. Interestingly, the anti-symmetry is conserved upon reflection about the $T = 0$ but lost upon reflection about the center frequency. The conservation of anti-symmetry in time seems analogous to the time symmetry of an autocorrelation. Figure 4.18 shows the time and frequency marginals for an instantaneous and non-instantaneous response. The above distortion from a non-instantaneous response results in a zero frequency marginal but a non-zero time marginal, which contradicts Wiersma and co-workers' statement that a non-instantaneous response results in a non-zero frequency marginal [5]. The non-instantaneous simulation here is open to question, though, because it is not based on a microscopic model with an internally consistent nonlinear response. Altering the slopes individually for ω_a, ω_b, and ω_c in Eqn. 4.12 also quantitatively showed a zero frequency marginal and a non-zero time marginal, but altered the relative intensities between the SRPP peaks at lower and higher frequencies.

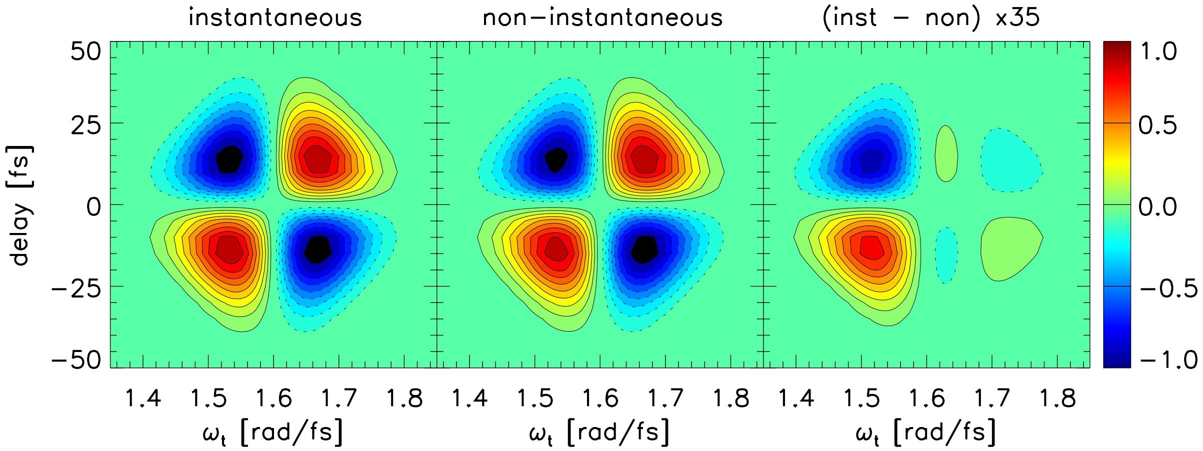

Figure 4.17: SRPP XPM transient comparison with a non-instantaneous response. The left panel shows the simulated XPM with a constant susceptibility. The middle panel shows the XPM for a susceptibility with a linear slope to simulate a non-instantaneous response to first order. The right panel shows the difference between XPM transient with an instantaneous and non-instantaneous response multiplied by a factor of 35 to show the contours. ±10% contours are shown in all figures with solid/red contours indicating positive peaks and dashed/blue contours indicating negative peaks.

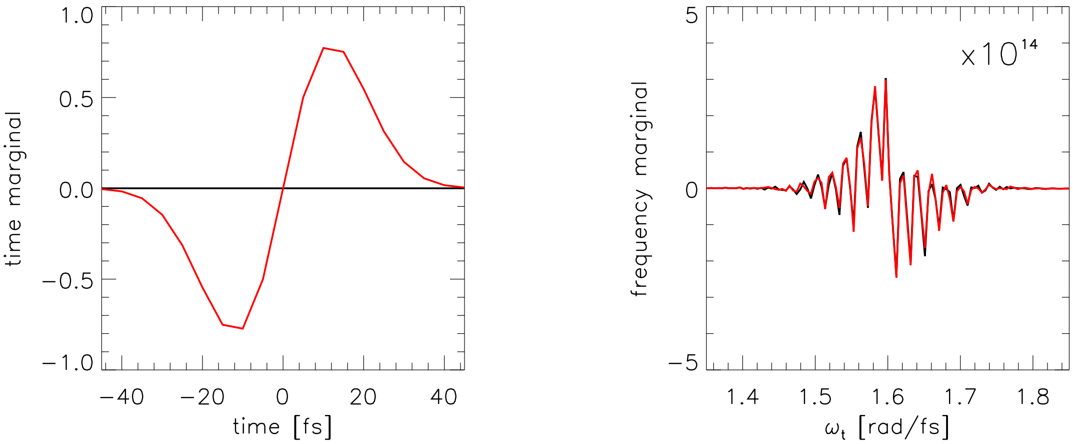

Figure 4.18: Time and frequency SRPP marginals for a non-instantaneous response. The time and frequency marginals for an instantaneous (black line) and non-instantaneous (red line) response are shown on the left and right, respectively, after normalizing the SRPP transient. The frequency marginals were multiplied by a factor of 10^{14}. The non-instantaneous response results in a non-zero time marginal and a zero frequency marginal.

Figure 4.19 shows simulated 2D XPM spectra at $T = 0$ for a transform limited Gaussian pulse, centered at 1.6 rad/fs, with the same ($m = 100$) non-instantaneous response. Similar to the SRPP XPM with a non-instantaneous response, the anti-symmetry about the center frequency on the detection axis, ω_t, is lost. The symmetry about the center frequency for the excitation axis, ω_τ, is conserved, possibly because the individual "pump" interactions from pulses a and b are complex conjugates, which results in a phase cancellation effect.

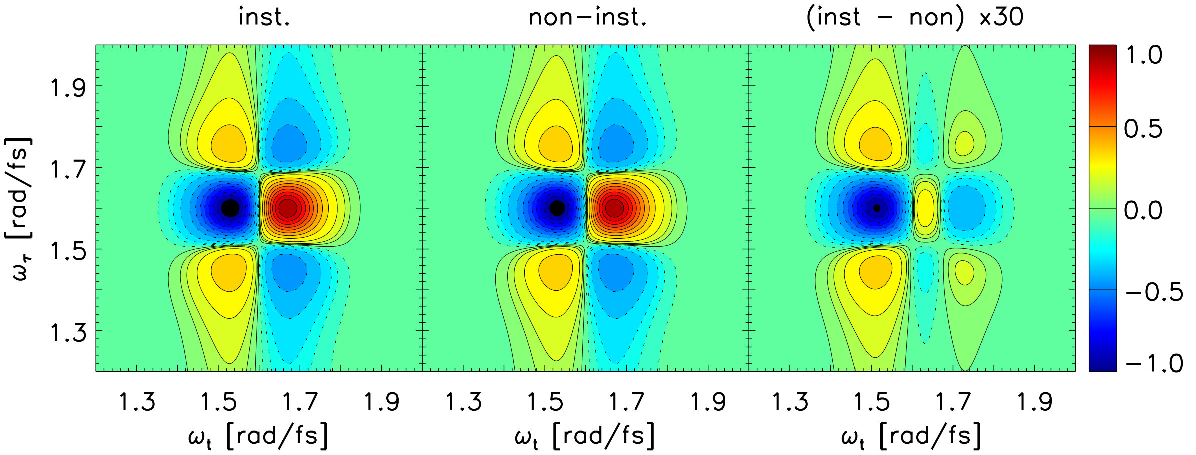

Figure 4.19: 2D XPM at $T = 0$ and comparison with a non-instantaneous response. The left and middle panels show the 2D XPM with an instantaneous and non-instantaneous response, respectively. The right panel shows the difference multiplied by a factor of 30. Contours of ± 1%, 3%, 5%, 10%, 20%, 30%, 40%, 50%, 60%, 70%, 80%, and 90% are shown in all figures with solid/red contours indicating positive peaks and dashed/blue contours indicating negative peaks.

4.6 Conclusion

The XPM signal was calculated in 2D spectra for the first time. The calculations indicate the 2D XPM spectra are more complicated with larger signals than in SRPP because there are peak cancellation effects. For the integrated pump-probe signal, XPM should result in a net zero signal for a detector with a flat spectral response (in the absence of two-photon absorption) as calculated by the zero time marginal in the SRPP XPM regardless of chirp.

The XPM signal contaminates resonant third-order signals during pulse overlap, which becomes more prominent for samples with weak signals and for shorter pulses. Especially in 2D spectra, the XPM can contribute both positive and negative features that could be misinterpreted as transient positive ground state bleaching/excited state emission and transient negative excited state absorption. This motivates the simulation of XPM in 2D spectra to uncover the desired resonant signal for peakshape analysis. This chapter shows preliminary results comparing experimental 2D XPM spectra with simulations of 2D XPM spectra using a retrieved pulse amplitude and phase from an independent measurement. However, there are rapid changes in the 2D XPM spectra as a function of the waiting time, T, so the experiment requires strict conditions for short pulses. An experiment locking the T drift to less than 1 fs during data acquisition and using a material with a known nonlinear refractive index needs to be explored in the future.

In experiments, the signal contains both XPM and the resonant signal from the absorbing sample during pulse overlap. To remove the XPM contribution from these measurements, a subtraction scheme is used involving the XPM from neat solvent and sample cell windows. Our calculations show that a simple XPM subtraction with an absorbing sample with a 0.3 OD results in 30–40% errors in the SRPP transients. Through simulations and minimizing the RMS, the lowest error using a single multiplicative factor on the undistorted XPM SRPP transient (from neat solvent and window) for subtraction has 10% errors. Thus, the

XPM propagation including absorptive and dispersive effects in three frequency dimensions is needed for an exact calculation. However, we present a rough subtraction scheme in this chapter without a rigorous calculation to result in errors down to 20% for XPM subtraction.

Finally, a first-order approximation to a non-instantaneous response was simulated in 2D and SRPP. The XPM SRPP transient with a non-instantaneous response results in a zero frequency marginal and a non-zero time marginal (i.e. the probe photon number is not conserved). A qualitatively similar non-zero time marginal is calculated for XPM generation and propagation in a medium with linear absorption on the red edge of the pulse spectrum. This result contradicts previous statements (for which no justification was given) that a non-instantaneous response yields a zero time marginal and a non-zero frequency marginal. None of the calculations reported here yield the apparent non-zero frequency marginal of the experiment. Ziegler and co-workers [20] have given a hand-waving argument that resonant two photon absorption can generate a non-zero frequency marginal. However, it seems possible that the apparently non-zero frequency marginal might result from skipped time delays.

4.7 Appendix I

To verify the Fortran program used to calculate the XPM signal, a few external checks were implemented. The cross checks consist of testing the code with propagation effects [26], which includes directional filtering effects and absorptive/dispersive distortions, and checks on the implementation of chirped pulses [27].

First, to test the code with propagation effects, results from Yetzbacher *et al.* [26] were replicated. Specifically, the free induction decay referenced 2D spectra ($\hat{S}^0_{2D}$) with directional filter effect were calculated for a pure dephasing Bloch model at increasing crossing angles, α and β [45]. These results were compared to Fig. 2 in Ref. [26] using the same parameters.

The free induction decay referenced 2D spectra ($\hat{S}^0_{2D}$) with propagation effects from sample absorption are compared to Fig. 7 from Ref. [26], a critically damped Brownian oscillator (CDBO) model with the same parameters. This CDBO model had a Stokes' shift large enough to separate absorption and emission peaks.

To test if chirp effects on the pulse were implemented correctly, calculations reported by Ogilvie and co-workers were replicated [27]. Although the agreement between SRPP XPM calculations and experiment may be regarded as qualitatively verifying that the sign of the chirp was consistently used in FROG and the XPM simulation, an external check against 2D spectra is helpful. In Ref. [27], a Brownian oscillator model with a Gaussian $M(t)$ was used for the simulations:

$$M(t) = \exp\left(\frac{-t^2}{\tau_g^2}\right), \tag{4.13}$$

where τ_g is the correlation time. The parameters stated and used were $\tau_g = 150$ fs, $\lambda/2\pi c = 45$ cm^{-1}, and T = 298 K. The pulse center frequency was not reported, but deduced to be ~440 THz by looking at the figures. The transform limited pulse intensity FWHM was 30 fs, and it was lengthened to 97 fs with a linear chirp of ±1000 fs^2; this was also verified using a separate chirp code. Figure 4.20 shows the results that replicate Fig. 6 in reference [27]. In

Ref. [27], simulations were done assuming the pump-probe (Homotime Absorptive Response Detection) geometry, where pulse c acts as the excitation pulse and the local oscillator. As a result, the 2D spectra shows the attenuated 2D spectrum [26], which is represented as $\hat{S}_{2D}^{-}$. The top row shows the simulated 2D spectra with $+1000$ fs^2, the middle row (not shown in Ref. [27]) shows the simulated 2D spectra for transform limited pulses, and the bottom row shows the simulated 2D spectra with -1000 fs^2. The axes were kept in units of THz to show a direct comparison, but the excitation and detection frequency axes are rotated to stay consistent with our convention[1] (the horizontal (vertical) axis is the detection (excitation) axis).

---

[1] The 3 frequency axis tickmark labels (435, 440, 455) are roughly evenly spaced on each axis, but numerically indicates frequency intervals that differ by a factor of 3.

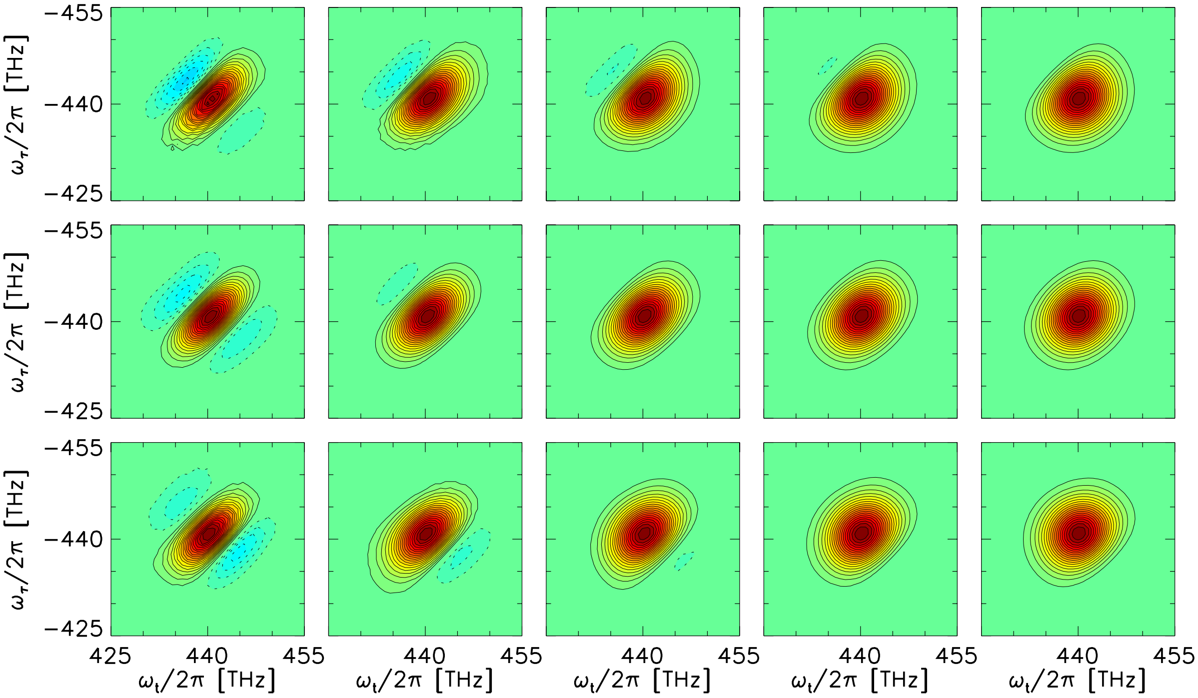

Figure 4.20: Chirp effects on 2D spectra with the $\hat{S}_{2D}^{-}$ representation. Real absorptive 2D spectra are shown for linearly chirped pump and probe pulses with a GDD of $\phi'' = +1000$ fs^2 (top row), transform limited pump and probe pulses (middle row), and linearly chirped pump and probe pulses with a GDD of ϕ'' = -1000 fs^2 (bottom row). From left to right, the 2D spectra have waiting times of $T = 0$, 30 fs, 60 fs, 90 fs, and 120 fs. Contours of ±5% are shown in all of the 2D spectra with dotted (blue) contours indicating negative amplitude and solid (red) contours indicating positive amplitude. The frequency axes in figures 2, 4, 5, 6, and 11 of Ref. [27] are all mislabeled. The range shown is evidently from 425 - 455 THz.

4.8 Appendix II: FROG Preparation and Processing Procedure

For an accurate retrieval of the experimental FROG trace using the program provided by Femtosoft Technologies©, the experimental FROG trace required a clean up procedure and a frequency dependent multiplicative factor missing in the algorithm. Although the program provided their own clean up procedures, they were not well documented so we used our own standard methods, which are explained in this section. Care was taken not to remove any signal in the clean up procedure.

The preparation of the experimental SHG FROG trace consists of the following procedures: (1) A highly averaged background subtraction. (2) Filtering the SHG FROG trace along the pixel dimension so that the spectrum properly goes to zero. (3) Fourier transforming along the pixel dimension and filtering the SHG FROG trace in quasi-time at each time delay to remove highly oscillatory noise that persists after the background subtraction. (4) Filtering the SHG FROG trace along the time delay axis so that the trace properly goes to zero. (5) Fourier transforming along the time delay axis and filtering the SHG FROG trace along this frequency axis to remove highly oscillatory noise. (6) Fourier interpolating the SHG FROG trace to fit in an even $N \times N$ grid in both time delay and wavelength. (7) Division by an ω^3 factor to fool the retrieval algorithm.

SHG autocorrelation spectra at different time delays, or SHG FROG trace, were collected by free-space coupling the frequency doubled autocorrelation beam using a negative (-30 mm focal length) and positive (25.4 mm focal length) lens pair to match the numerical aperture of an Ocean Optics USB4000 UV-VIS spectrometer (3648 active pixels, f/4). The SHG FROG trace was collected with time delays from -180 fs to +180 fs with the natural 1.333 fs step size for the delay stage (Newport MTM250PP.1). This scan produces over 256 time delays to allow subsequent centering of 256 FROG transients on zero time delay. The USB4000

UV-VIS spectrometer was calibrated in photons/nm from 178.599 nm to 887.851 nm using a pixel to wavelength calibration provided by Ocean Optics with the equation:

$$\lambda(p) = A \cdot p + B \cdot p^2 + C \cdot p^3, \tag{4.14}$$

where λ is the wavelength, p is the pixel index, and A, B and C are the provided calibration coefficients. The wavelength calibration in the spectral range of the frequency doubled autocorrelation (500 - 700 nm) was verified using the atomic lines of a Neon lamp (Newport #6032, Ne calibration lamp).

Background spectra were collected between every acquisition of the SHG autocorrelation spectra at each time delay with the same integration time of 100 ms, which were then averaged to obtain a highly averaged background spectrum and subtracted from the raw SHG FROG trace. The background subtracted FROG trace was then plotted in a two-dimensional contour map to identify the index nearest to time zero to center the SHG FROG trace with 256 time delays.

The reduced FROG trace was then filtered along the pixel dimension using a hyperbolic tangent window. This assured that the spectrum properly goes to zero at the edges and makes the FROG trace band-limited along the pixel dimension. Figure 4.21 shows the filtering of the spectrum along the pixel dimension. Care was taken not to filter out the frequency doubled autocorrelation spectrum at each time delay. The FROG trace was then Fourier transformed along the pixel dimension (into quasi-time) to clean up highly oscillatory noises that persist after the background subtraction, again utilizing a hyperbolic tangent filter. The width of the hyperbolic tangent filter in quasi-time was determined such that the artifact from the interference from the CCD array coating (~50 microns in thickness) was removed, shown in Fig. 4.22.

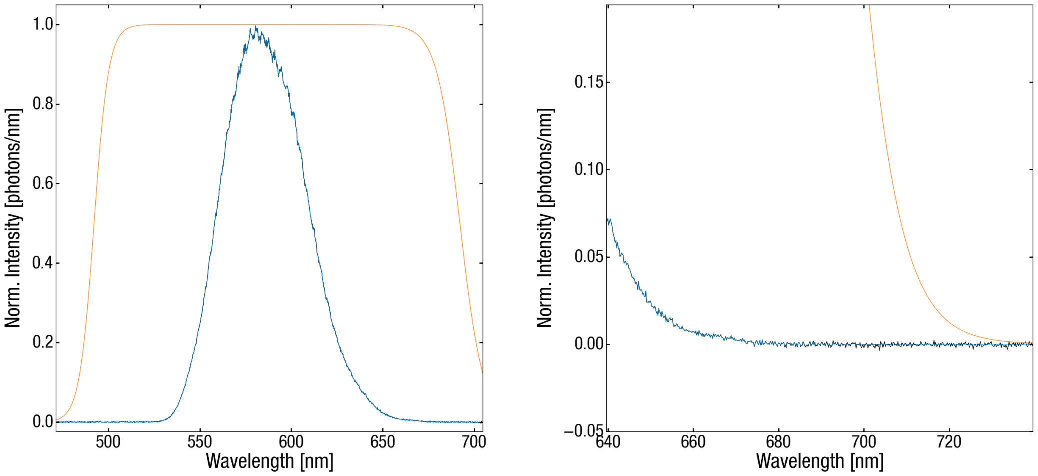

Figure 4.21: Application of hyperbolic tangent window in pixel (shown in nm here) space. The left figure shows the frequency doubled autocorrelation spectrum at one time delay (blue) and the hyperbolic tangent filter (orange). The right figure shows the same data but zoomed-in the wings to show that the spectrum is not filtered.

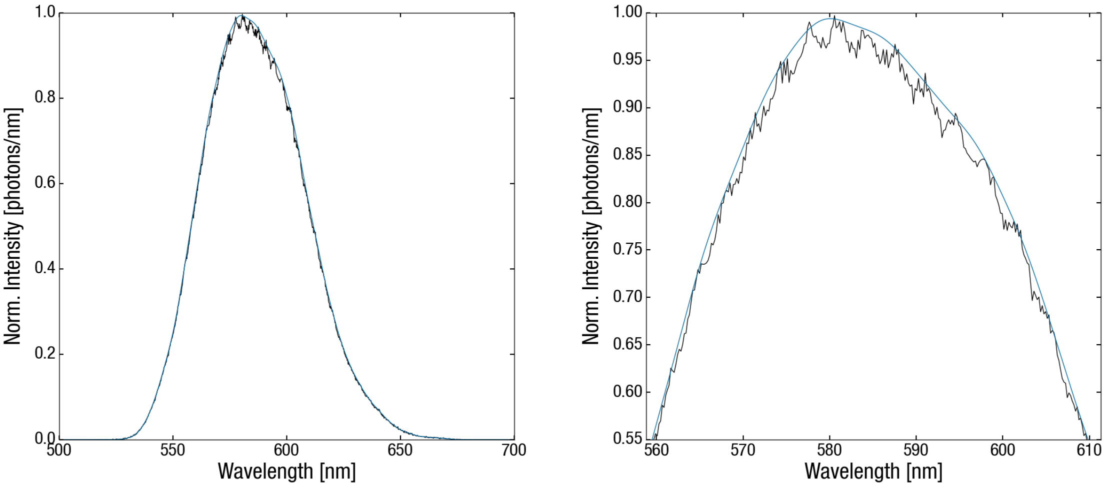

Figure 4.22: Resulting spectrum after applying a hyperbolic tangent window in quasi-time to remove highly oscillatory features. The left figure shows the raw (black) and cleaned (blue) frequency doubled spectrum. The right figure shows the same data zoomed-in to visualize the cleaned up features in the spectrum.

After inverse Fourier transforming the FROG trace back to pixel space, another hyperbolic tangent filter was applied along the time delay axis to filter out noise around the wings far outside of the pulse overlap region. After the filter along the time delay axis to assure the signal goes to zero at large time delays, the FROG trace was Fourier transformed along the time delay axis to apply the final hyperbolic tangent filter in frequency to remove highly oscillatory features along the time delay axis. Figure 4.23 shows the result of the hyperbolic tangent filtering to remove noise along the time delay axis.

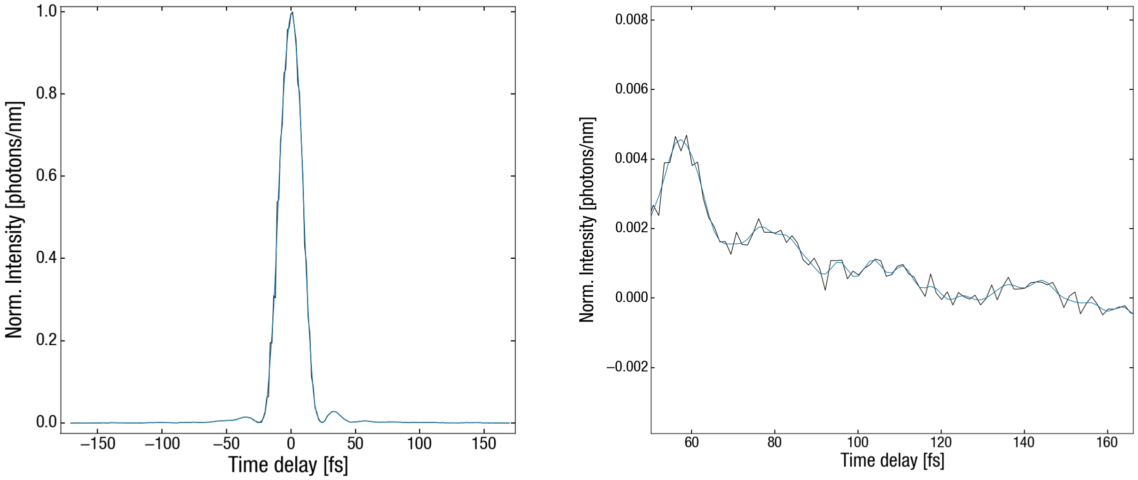

Figure 4.23: Resulting signal in time after cleaning noise along the time delay axis. The left figure shows the raw (black) and cleaned (blue) signal in time. The right figure shows the zoomed-in signal to reveal the details of the clean up.

After all of the filtering, the SHG FROG trace was interpolated to fit in a square $N \times N$ grid in time delay and wavelength for the FROG retrieval algorithm. If the input FROG trace grid size is not a square, the commercial program automatically interpolates the input FROG trace on to a square grid. Because the interpolation was also not well documented, we implemented our own interpolation. The experimental FROG trace was Fourier interpolated from evenly spaced pixels to evenly spaced wavelengths with a range from 500 nm to 700 nm on a 256 grid, which corresponds to a 0.7843 nm resolution. Figure 4.24 shows the resulting SHG FROG trace after the clean up procedure and Fourier interpolation on to a square grid evenly spaced in wavelength.

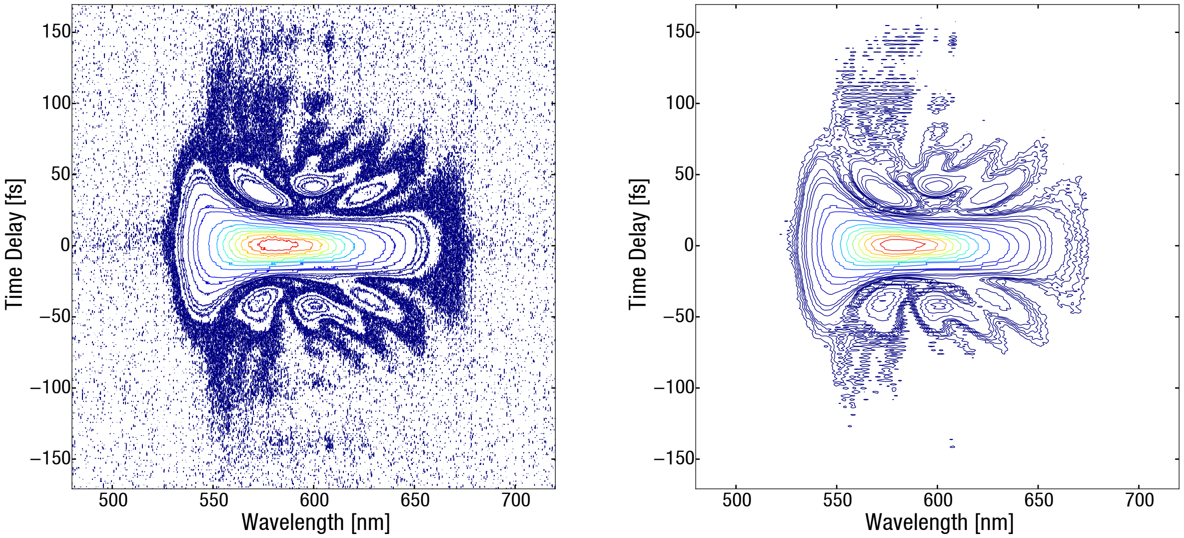

Figure 4.24: SHG FROG trace after the clean up procedure and interpolation. The left figure shows the raw SHG FROG trace before the clean up procedure and the right figure shows the resulting FROG trace after the clean up procedure and interpolation to a square grid. Contour levels of 0.1%, 0.2%, 0.3%, 0.4%, 0.5%, 1%, 1.5%, 2%, 4%, 7%, 10%, 20%, 30%, 40%, 50%, 60%, 70%, 80%, 90%, and 100% are shown in both figures.

As explained by Baltuška *et al.* [40], the standard FROG equation and algorithms do not account for the radiation dynamics of the signal or the frequency dependence of the spatial mode, which becomes important for few cycle pulses. For this reason, the prepared SHG FROG trace required a division by a power of frequency for the FROG algorithm [40]. An ω^2 dependence that follows from Maxwell's equation for the intensity of an optical signal field radiated by the source nonlinear optical polarization. The frequency dependent beam waist at the focus can contribute an additional power of ω if the waist is proportional to $1/\omega$ [40], as appropriate for focusing of a collimated Gaussian beam with a frequency independent collimated beam diameter [47]. This would be the case if the NOPA pump beam diameter was transferred to the NOPA beam in the NOPA crystal and imaged at the sample. On the other hand, if the clean-up pinhole diameter were imaged at the sample to give the same focal beam waist for all frequency, this factor of ω would not appear. There is an additional uncertainty as to whether the Ocean Optics spectrograph intensity axis is energy/nm or photons/nm [48].[2] For this reason, the FROG traces were processed with division by both ω^2 and ω^3 for comparison. Previously, methods of forcing the agreement between the autoconvolution and the FROG frequency marginal have been used by others [41] to correct for these frequency-dependent effects. Figure 4.25 shows the comparison of the FROG retrieval when inputting the experimental SHG FROG trace without any frequency dependent factors, a division by ω^2, and a division by ω^3. The results of the retrieval indicate that the division by ω^3 produces the best retrieval of the fundamental pulse spectrum from the FROG trace that measures second harmonic spectra compared to the directly measured fundamental pulse spectrum in terms of reproducing all of the spectral features of the pulse. The FROG errors of all three traces (no division, division by ω^2, and division by ω^3) were all around 0.003, but there is a better agreement in the FROG trace at 0.3% contour with

---

[2] The SHG spectrum intensity axis is either photon/nm or energy/nm, depending on who answers the phone at Ocean Optics.

the division by ω^3.

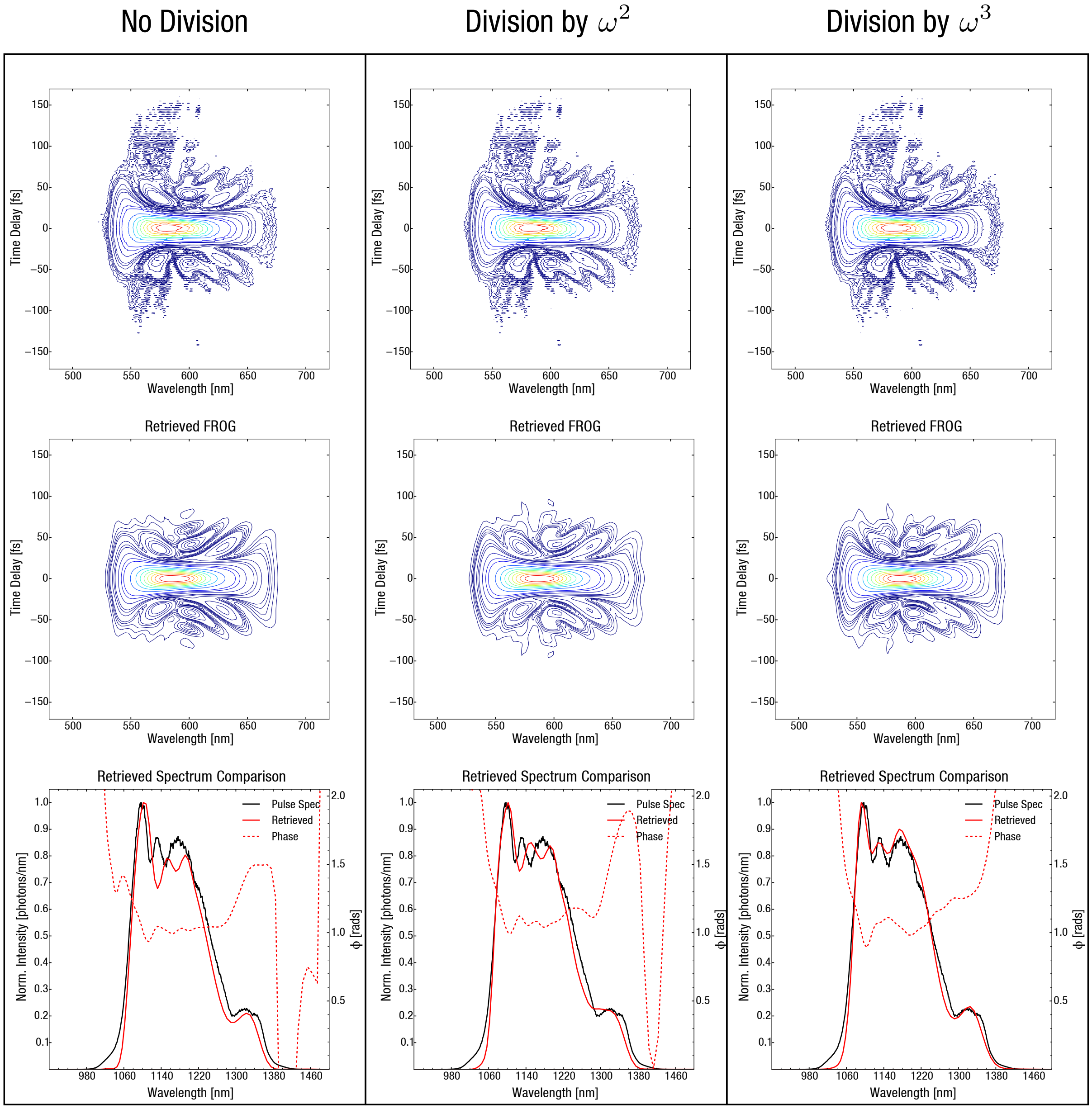

Figure 4.25: Retrieved pulse spectrum comparison with different frequency dependent factors applied to the raw SHG FROG trace. The first, second, and third column have a division by no frequency dependent factors, ω^2, and ω^3, respectively. The first row shows the experimental SHG FROG trace with the corresponding division. The second row shows the retrieved FROG trace. Contour levels of 0.1%, 0.2%, 0.3%, 0.4%, 0.5%, 1%, 1.5%, 2%, 4%, 7%, 10%, 20%, 30%, 40%, 50%, 60%, 70%, 80%, 90%, and 100%. The third row shows the measured pulse spectrum (black solid line) compared to the retrieved fundamental pulse spectrum (red solid) with the retrieved spectral phase (red dashed line).

4.9 Appendix III: Source Code

4.9.1 S3_nonres.f90

```
pure subroutine S3NRES(t,ta,tb,tc,t_inc,res)

!      !Subroutine was adapted from S3intR2.f90 to calculate
   the nonlinear
!      !response from glass by assuming a delta function
   response.
!      !- SDKP 4/13/2015

       use DPTYPE, only : DP
       use G_PARMS,only : numgt, rgoft, igoft
       use fundconst, only : imu
       implicit none


!      !INPUT/OUTPUT VARIABLES
       real(kind=DP),intent(in)::t, ta, tb, tc, t_inc
!      !t is the time at which the signal is calculated
!      !ta,tb & tc are the pulse center times
!      !(tc=0, ta<0 & tb<0) tau==(tb-ta) and T==MIN[(tc-ta),(tc
   -tb)]
!      !for 3 pulse scattering experiment
!      !t_inc is the common time increment used for t, ta, tb,
   and tc
!      !needed for conversion of times to integers for control
!      !statements

       complex(kind=DP),intent(out)::res
!      !the complex phase matched impulse response
!      !res is equal to F(t) in Gallagher Faeder & Jonas Phys.
   Rev. A


!      !INTERNAL VARIABLES (explained on first use)
       integer:: w,x,y,z
       real(kind=DP):: realr, imagr
       integer:: t1, t2, t3    !changed from real(kind=DP)
          11/19/2002
       real(kind=DP):: glass_const
```

```
!       !glass constant for nonlinear response
        glass_const = 1.0

!       !integer indices for arrays rgoft & igoft and control
    statements
        w=nint(ta/t_inc)
        x=nint(tb/t_inc)
        y=nint(tc/t_inc)
        z=nint(t/t_inc)

!       !frequencies for R
        omegaa=real(0,kind=DP)
        omegab=real(0,kind=DP)
        omegac=real(0,kind=DP)
        weg=real(0,kind=DP)


!       !causal: if ((t < tc) .or. (t < tb) .or. (t < ta)) then
        causal: if ((z < y) .or. (z < x) .or. (z < w)) then
                    res=real(0,kind=DP)
            else

            ! delta function response
            delta: if ((w == z) .and. (x == z) .and. (y == z))
               then

                    res=imu*glass_const

                    else

                    res=real(0,kind=DP)

                    end if delta

            octantboundary: if ((w==z) .and. (x==z) .and. (y==z)
               ) then
                    res=res/real(8,kind=DP)           !three
                       boundaries
                else if ((w == z) .and. (x == z)) then
                    res=res/real(4,kind=DP)           !two
                       boundaries
                else if ((x == z) .and. (y == z)) then
```

```
             res=res/real(4,kind=DP)            !two
                boundaries
         else if ((y == z) .and. (w == z)) then
             res=res/real(4,kind=DP)            !two
                boundaries
         else if (w == z) then
             res=res/real(2,kind=DP)            !one
                boundary
         else if (x == z) then
             res=res/real(2,kind=DP)            !one
                boundary
         else if (y == z) then
             res=res/real(2,kind=DP)            !one
                boundary
     end if octantboundary

 end if causal

end subroutine S3NRES
```

4.9.2 fourierinterp.f90

```
subroutine FINTERP(old_size,x_old,y_old,new_size,x_new,y_new)
!   ! FOURIER INTERPOLATION PROGRAM
!   ! REQUIRES PERFECTLY EVEN UNIT SPACING IN INCREASING ORDER
   FOR
!   ! THE INTERPOLATION TO WORK CORRECTLY. CALCULATES THE
   FOURIER
!   ! COEFFICIENTS AND PERFORMS A SLOW FOURIER TRANSFORM TO
   EXPAND
!   ! TO THE NEW AXIS.
!
!   ! INPUT:
!   ! OLD_SIZE = SIZE OF OLD AXIS
!   ! X_OLD = OLD AXIS - MUST HAVE EVEN UNIT SPACING
!   ! Y_OLD = VALUES FOR OLD AXIS
!   ! NEW_SIZE = SIZE OF NEW AXIS
!   ! X_NEW = NEW AXIS TO BE INTERPOLATED
!
!   ! OUTPUT:
!   ! Y_NEW = VALUES FOR NEW AXIS
!
!   ! CHANGELOG:
!   !
!   !
!   !
!   ! SUBROUTINE WAS CHECKED AND VERIFIED TO BE WORKING
   PROPERLY (FOR NOW..) -SDP 05062015
!
   *********************************************************************

!   ! USE MODULES
    use DPTYPE, only : DP
    use FUNDCONST, only : pi, imu
    implicit none


!   ! INPUT/OUTPUT VARIABLES
    integer, intent(in) :: old_size, new_size
    real(kind=DP),intent(in) :: x_old(1:old_size),x_new(1:
       new_size)
    complex(kind=DP),intent(in) :: y_old(1:old_size)
    real(kind=DP), intent(out) :: y_new(1:new_size)
```

```
!   ! INTERNAL VARIABLES
    integer:: M,i
    integer :: indshift
    real(kind=DP) :: xmin, xmax, dx
    complex(kind=DP) :: D(1:old_size)
    real(kind=DP),allocatable :: k(:)
    real(kind=DP) :: x_periodic(1:new_size)
    complex(kind=DP),allocatable :: coeff(:)
    complex(kind=DP) :: p(1:new_size)

!   ! BEGIN MAIN PROGRAM
   ************************************************

    call dfftcf(old_size,y_old,D)

!   ! normalize to grid size
    D = (1.0_DP/old_size)*D
!   ! shift for zero frequency to be in the center
    indshift = ceiling(old_size/2.0_DP)

!   ! old size has odd number of data points
    if (mod(old_size-1,2) == 0) then
        M = (old_size-1) / 2

        allocate(coeff(1:old_size))
        coeff = 0
        coeff = cshift(D,indshift)

        allocate(k(1:(2*M+1)))
        do i = 1,2*M+1,1
            k(i) = -M -1 + i
        end do

!   ! old size has even number of data points
    else
        M = (old_size) / 2

        allocate(coeff(1:(old_size+1)))
        coeff = 0
        coeff(1:old_size) = cshift(D,indshift)
        coeff(old_size+1) = coeff(1)
```

```
        allocate(k(1:(2*M+1)))
        do i = 1,2*M+1,1
            k(i) = -M -1 + i
        end do

    end if

    xmin = minval(x_old)
    xmax = maxval(x_old)

    dx = x_old(2) - x_old(1)

    x_periodic = 2*pi*(x_new - xmin)/ (xmax-xmin+dx)

    p = 0

    do i = 1,new_size,1
        p(i) = sum(coeff*exp(imu*k*x_periodic(i)))
    end do

    y_new = 0
    y_new = real(p, kind=DP)

end subroutine FINTERP
```

4.9.3 pulsemodule2.f90

```
     module pulsemodule

!     !module with data for spectralfilter
!     !filled by pulsewrite

       use DPTYPE, only : DP
       implicit none
       !real(kind=DP), allocatable :: pulsefilter(:)
       complex(kind=DP), allocatable :: pulsefilter(:)
       complex(kind=DP), allocatable :: gpulsea(:), gpulseb(:),
           gpulsec(:)

!      ! *** Additions made -APS 8/23/11 ***
!      ! pulsetime = intensity FWHM of pulses in fs
!      ! pulsecenter = peak of pulse spectrum in cm^-1
       real(kind=DP) :: pulsetime = 20.00d0
       !real(kind=DP) :: pulsetime = 75.0d0
       real(kind=DP) :: pulsecenter = 20000.0d0
       !real(kind=DP) :: pulsecenter = 14676.82019d0
       !real(kind=DP) :: pulsecenter = 12816.7d0
!      ! ***                             ***

       ! adding group delay for simulating chirp effects (just
          enter 0 for TL pulses)
       real(kind=DP) :: GDD = 0.0d0 ! [=] fs^2

      !real(kind=DP), parameter::pulsedur=20
      !pulse duration in fs
      !must be set <>0 for the spectral filter to be taken into
         account
      !real(kind=DP), parameter::pulsecenter=20000
      !real(kind=DP), parameter::pulsecenter=15
      !in cm-1
      !rotating wave ? w_eg=12575

      !real(kind=DP), parameter::pulsewidth=3000
      !real(kind=DP), parameter::pulsewidth=640
      !in cm-1

      !real(kind=DP), parameter::pulsewidth=905.0966799 !Field
        FWHM=Intensity FWHM*sqrt(2)
```

```
!fwhm in intensity is listed as
!604 cm^-1 from John Hybl et al JPCA 2002, 106, 7651

!real(kind=DP), parameter::pulsewidth=144.278
!144.278 fs intensity FWHM

!real(kind=DP), parameter::pulsewidth=171.5763616
!121.322 fs intensity FWHM also 121.322 cm-1 intensity
  FWHM

!real(kind=DP), parameter::pulsewidth=208.16125
!100 fs intensity FWHM

!real(kind=DP), parameter::pulsewidth=416.32249
!50 fs intensity FWHM

!real(kind=DP), parameter::pulsewidth=594.74642
!35 fs intensity FWHM

!real(kind=DP), parameter::pulsewidth=630.79165
!33 fs intensity FWHM

!real(kind=DP), parameter::pulsewidth=693.87082
!30 fs intensity FWHM

!real(kind=DP), parameter::pulsewidth=991.24403 !Field
  FWHM=Intensity FWHM*sqrt(2)
!fwhm in intensity is listed as
!21 fs from John Hybl thesis figure 5.11

!real(kind=DP), parameter::pulsewidth=1040.8062
!20 fs intensity FWHM

!real(kind=DP), parameter::pulsewidth=2081.6125
!10 fs intensity FWHM

!real(kind=DP), parameter::pulsewidth=4163.2249
!5 fs intensity FWHM

!real(kind=DP), parameter::pulsewidth=6938.7082
!3 fs intensity FWHM
```

```
!real(kind=DP), parameter::pulsewidth=20816.125
!1 fs intensity FWHM

!real(kind=DP), parameter::pulsewidth=208161.25
!0.1 fs intensity FWHM

end module pulsemodule
```

4.9.4 pulsewrite2.f90

```
        subroutine PULSEWRITE(nr,l4wm,h4wm)  !Removed pure
           attribute as well as the
                                             !parameters
                                               pulsewidth,
                                               pulsecenter, and
                                             !pulsefilter
                                                              -
                                               APS 8/23/11
!       !subroutine that fills the module PULSEMODULE used for
!       !calculation of the spectral filter due to the pulses
!
          use DPTYPE, only : DP
          use COMPLINDEX, only : xfreq
          use FUNDCONST, only : pi, c, imu
          use pulsemodule, only : pulsetime, pulsecenter,
             pulsefilter, &
          & gpulsea, gpulseb, gpulsec, GDD    ! -APS 8/23/11
          implicit none


!       !input/output variables
         integer,intent(in) :: nr
         integer,intent(in) :: l4wm,h4wm
!         real(kind=DP),intent(in) :: pulsewidth
                             ! -APS 8/23/11
!         real(kind=DP),intent(in) :: pulsecenter
                            ! -APS 8/23/11
!         real(kind=DP),intent(out):: pulsefilter(nr)
                        ! -APS 8/23/11
!       !internal variables
         integer:: i,si,sj,sk
         real(kind=DP)::  sigma,pulsec,pulsew
         real(kind=DP),allocatable::spectrum(:),gsphase(:)
         real(kind=DP) :: pulsewidth
                                               ! -APS 8/23/11


!       ! Added -APS 8/23/11
         allocate(pulsefilter(nr))
         allocate(gpulsea(nr),gpulseb(nr),gpulsec(nr))
        ! convert from intensity FWHM in fs to field FWHM in
```

```
          wavenumbers:
        pulsewidth = 4.0_DP*log(2.0_DP)/(sqrt(2.0_DP)*pulsetime
          )/(pi*c)
!      !       -APS 8/23/11

       !convert cm-1 in rad/fs
       pulsew=pulsewidth*2.0_DP*pi*c
       pulsec=pulsecenter*2.0_DP*pi*c

      allocate(spectrum(l4wm:h4wm),gsphase(l4wm:h4wm))
       spectrum=0.0_DP
       sigma=pulsew/2.0_DP/sqrt(2.0_DP*log(2.0_DP)) ! convert
          to gaussian variance
!       write(*,*)"sigma is ",sigma,"rad/fs"
       do i=l4wm,h4wm,1
        spectrum(i)=exp( -( (xfreq(i)-pulsec)**2/2/sigma**2) )
!      ! group delay chirp for gaussian pulses addition by SDP
   7/10/2015 (can add gdd and higher order terms)
        gsphase(i) = 0.5_DP*GDD*(xfreq(i)-pulsec)**2
        !gsphase(i) = 1.0/6.0_DP*30*GDD*(xfreq(i)-pulsec)**3
       end do

!      !calculate shifted indices for excitation frequencies

!      ! SDP COMMENT: only pulse a should have omega negative.
   "pulsefilter" is being
!      !              used for all pulses. this will only be
   accurate when pulse center
!      !              is equal to weg and gaussian. SHOULD
   DOUBLE CHECK -SDP 1/28/2015
       open(159,file=("gspectrum.out"),status="replace")
       do i=1,nr
       if ( (i >= 1) .and. (i <= ((nr/2)+1)) ) then
           si = -(i-1)      !minus sign because omegaa is
              negative
!      ! ADDED CORRECT INDEXING FOR PULSES B & C
           sj = i-1
           sk = i-1
       else if ( (i > ((nr/2)+1)) .and. (i <= nr) ) then
           si = -(i-1-nr)   !minus sign because omegaa is
              negative
!      ! ADDED CORRECT INDEXING FOR PULSES B & C
```

```
     sj = i-1-nr
     sk = i-1-nr
 end if

     pulsefilter(i)=spectrum(si)

     gpulsea(i) = spectrum(si)*exp(-imu*gsphase(si))
     gpulseb(i) = spectrum(sj)*exp(imu*gsphase(sj))
     gpulsec(i) = spectrum(sk)*exp(imu*gsphase(sk))
     write(159,*) xfreq(sk), spectrum(sk), gsphase(sk)
 end do

 close(159)

deallocate(spectrum,gsphase)
  end subroutine PULSEWRITE
```

4.9.5 pulsefiltsep_SDP.f90

```
subroutine PULSEFILTSEP(nr,l4wm,h4wm,speca,specb,specc, omega_t
   )

! MODULES
use DPTYPE, only : DP
use COMPLINDEX, only : xfreq
use G_PARMS, only : frogname, frog_size, signPhase
use FUNDCONST, only : pi, c, imu
use CSINT_INT
use CSVAL_INT
use CSSCV_INT

implicit none

! INPUT/OUTPUT VARIABLES
integer,intent(in) :: nr,l4wm,h4wm
complex(kind=DP),intent(out) :: speca(nr),specb(nr),specc(nr)
real(kind=DP), intent(out) :: omega_t(nr)

! ALLOCATE
real(kind=DP) :: frog_wavelength(1:2*frog_size), frog_spectrum
   (1:2*frog_size), frog_sphase(1:2*frog_size)

! output file of FROG is 2*grid size of FROG input.
! frog_wavelength = wavelength from FROG output
! frog_spectrum = spectrum from FROG output
! frog_sphase = spectral phase from FROG output
real(kind=DP) :: frog_frequency(1:2*frog_size)
real(kind=DP), allocatable :: frog_frequency_lextend(:),
   frog_frequency_extend(:)
real(kind=DP), allocatable :: frog_spectrum_lextend(:),
   frog_spectrum_extend(:)
real(kind=DP), allocatable :: frog_sphase_lextend(:),
   frog_sphase_extend(:)
real(kind=DP), allocatable :: FROG_SPECTRUM_INTERP(:),
   FROG_SPHASE_INTERP(:), FROG_GDD_SPHASE_INTERP(:)
real(kind=DP), allocatable :: FROG_FIELD_xfreq(:),
   FROG_SPHASE_xfreq(:), FROG_GDD_SPHASE_xfreq(:)

!define variables required for cubic spline
real(kind=DP), allocatable :: BREAK1(:), CSCOEFF1(:,:)
```

```
complex(kind=DP), allocatable :: frog_spectrum_extend_comp(:),
   frog_sphase_extend_comp(:)


! INTERNAL VARIABLES
integer :: i,j,si,sj,sk
integer :: ndata_new, ndata_new2, ndata_neg, ndata_pos,
   old_size
real(kind=DP) :: dfreq, specmax
integer :: n4wm

interface
      subroutine FINTERP(old_size,x_old,y_old,new_size,x_new,
         y_new)
         use DPTYPE, only : DP
         use FUNDCONST, only : pi, imu
         implicit none

      !input/output variables
        integer, intent(in) :: old_size, new_size
        real(kind=DP),intent(in) :: x_old(1:old_size),x_new(1:
           new_size)
        complex(kind=DP),intent(in) :: y_old(1:old_size)
        real(kind=DP), intent(out) :: y_new(1:new_size)
        end subroutine
end interface
!
   ===================================================================!


n4wm = h4wm - l4wm + 1

open(42,file=frogname,status="old",action="read")
    do j = 1,2*frog_size,1
        read(42,*) frog_wavelength(j),frog_spectrum(j),
           frog_sphase(j), frog_gdd_sphase(j)
    end do
close(42)

! change wavelength to frequency (rad/fs)
    do i = 1,2*frog_size,1
        frog_frequency(i) = 2.0_DP*pi*c*10**7/frog_wavelength(i
```

```
          ) ! c is in units of cm/fs
    end do

dfreq = abs(frog_frequency(2) - frog_frequency(1)) ! determine
   frequency step size
ndata_new = 2*frog_size

!       ! extend negative frequency
    if (xfreq(l4wm) < frog_frequency(1)) then
        ndata_neg = ceiling(abs((xfreq(l4wm) - frog_frequency
           (1)) / dfreq))
        ndata_new = ndata_new + ndata_neg

        allocate(frog_frequency_lextend(1:ndata_new),
           frog_spectrum_lextend(1:ndata_new),
           frog_sphase_lextend(1:ndata_new)) ! allocate size
           for left extension

        frog_spectrum_lextend = 0
        frog_sphase_lextend = 0

        frog_frequency_lextend((ndata_neg+1):ndata_new) =
           frog_frequency(1:2*frog_size)
        frog_spectrum_lextend((ndata_neg+1):ndata_new) =
           frog_spectrum(1:2*frog_size)
        frog_sphase_lextend((ndata_neg+1):ndata_new) =
           frog_sphase(1:2*frog_size)

        do i = ndata_neg,1,-1
            frog_frequency_lextend(i) = frog_frequency_lextend(
               i+1) - dfreq
        end do
    else
        allocate(frog_frequency_lextend(1:ndata_new),
           frog_spectrum_lextend(1:ndata_new),
           frog_sphase_lextend(1:ndata_new))
        frog_frequency_lextend = frog_frequency
        frog_spectrum_lextend = frog_spectrum
        frog_sphase_lextend = frog_sphase
    end if

!       ! extend positive frequency
```

```
    if (xfreq(h4wm) > frog_frequency(2*frog_size)) then
        ndata_pos = ceiling((xfreq(h4wm) - frog_frequency(2*
           frog_size)) / dfreq)
        ndata_new2 = ndata_new + ndata_pos

        allocate(frog_frequency_extend(1:ndata_new2),
           frog_spectrum_extend(1:ndata_new2),
           frog_sphase_extend(1:ndata_new2)) ! allocate size
           for right extension

        frog_spectrum_extend = 0
        frog_sphase_extend = 0

        frog_frequency_extend(1:ndata_new) =
           frog_frequency_lextend(1:ndata_new)
        frog_spectrum_extend(1:ndata_new) =
           frog_spectrum_lextend(1:ndata_new)
        frog_sphase_extend(1:ndata_new) = frog_sphase_lextend
           (1:ndata_new)

        do i = ndata_new+1,ndata_new2,1
            frog_frequency_extend(i) = frog_frequency_extend(i
               -1) + dfreq
        end do
    else
        ndata_new2 = ndata_new
        allocate(frog_frequency_extend(1:ndata_new),
           frog_spectrum_extend(1:ndata_new),frog_sphase_extend
           (1:ndata_new))

        frog_frequency_extend = frog_frequency_lextend
        frog_spectrum_extend = frog_spectrum_lextend
        frog_sphase_extend = frog_sphase_lextend

    end if
    ! checked extension of spectrum - SDP 05042015

!       ! apply jacobian
    do i = 1,ndata_new2,1
        frog_spectrum_extend(i) = frog_spectrum_extend(i) / (
           frog_frequency_extend(i)**2)
    end do
```

```
!       ! normalize spectrum
    specmax = maxval(frog_spectrum_extend)


    do i = 1,ndata_new2,1
        frog_spectrum_extend(i) = frog_spectrum_extend(i) /
           specmax
    end do

    ! needs to be complex for dfftcf
    allocate(frog_spectrum_extend_comp(1:ndata_new2),
       frog_sphase_extend_comp(1:ndata_new2))
    frog_spectrum_extend_comp = cmplx(frog_spectrum_extend,0,
       kind=DP)
    frog_sphase_extend_comp = cmplx(frog_sphase_extend,0,kind=
       DP)

!       ! fourier interpolate spectrum onto xfreq axis
    allocate(FROG_SPECTRUM_INTERP(1:n4wm),FROG_SPHASE_INTERP(1:
       n4wm))


    call FINTERP(ndata_new2,frog_frequency_extend,
       frog_spectrum_extend_comp,n4wm,xfreq,
       FROG_SPECTRUM_INTERP)
    !call FINTERP(ndata_new2,frog_frequency_extend,
       frog_sphase_extend_comp,n4wm,xfreq,FROG_SPHASE_INTERP)
    ! cubic spline phase onto xfreq axis
        allocate(BREAK1(1:ndata_new2), CSCOEFF1(1:4,1:
           ndata_new2))


        !call D_CSSCV(frog_frequency_extend,frog_sphase_extend,
            1, BREAK, CSCOEFF)
        call D_CSINT(frog_frequency_extend, frog_sphase_extend,
            BREAK1, CSCOEFF1)
!       ! interpolation worked fine - tested SDP 05052015
        do i = l4wm, h4wm, 1

        FROG_SPHASE_INTERP(i - l4wm + 1) = D_CSVAL(xfreq(i),
           BREAK1, CSCOEFF1)
```

```
        end do
!       ! put in same index as xfreq
    allocate(FROG_FIELD_xfreq(l4wm:h4wm),FROG_SPHASE_xfreq(l4wm
       :h4wm))

    do i = l4wm,h4wm,1
    ! square root for field amplitude - FROG outputs intensity
        FROG_FIELD_xfreq(i) = abs(FROG_SPECTRUM_INTERP(i - l4wm
            + 1))**0.5_DP
        if (signPhase) then
            FROG_SPHASE_xfreq(i) = FROG_SPHASE_INTERP(i - l4wm
               + 1)
        else
            FROG_SPHASE_xfreq(i) = -FROG_SPHASE_INTERP(i - l4wm
                + 1)
        end if
    end do

    do i=1,nr,1
       if ( (i >= 1) .and. (i <= ((nr/2)+1)) ) then
           si = -(i-1)       !minus sign because omegaa is
              negative
           sj = i-1
           sk = i-1
       else if ( (i > ((nr/2)+1)) .and. (i <= nr) ) then
           si = -(i-1-nr)    !minus sign because omegaa is
              negative
           sj = i-1-nr
           sk = i-1-nr
       end if

!       speca = exp( -( (xfreq(si)-pulsec)**2/2/sigma**2) )
!       speca = exp( -( (xfreq(si)-pulsec)**2/sigsq) )

        ! commented out because including frog retrieved field
        ! speca(i) = expt_pulse(si)
        ! phase here is negative with respect to pulses b & c
           because omegaa is negative - SDP 5/6/2015
        speca(i) = FROG_FIELD_xfreq(si)*exp(-imu*
           FROG_SPHASE_xfreq(si))
```

```
!       specb = exp( -( (xfreq(sj)-pulsec)**2/2/sigma**2) )
!       specb = exp( -( (xfreq(sj)-pulsec)**2/sigsq) )
        ! specb(i) = expt_pulse(sj)
        specb(i) = FROG_FIELD_xfreq(sj)*exp(imu*(
           FROG_SPHASE_xfreq(sj)))

!       specc = exp( -( (xfreq(sk)-pulsec)**2/2/sigma**2) )
!       specc = exp( -( (xfreq(sk)-pulsec)**2/sigsq) )
        ! specc(i) = expt_pulse(sk)
        specc(i) = FROG_FIELD_xfreq(sk)*exp(imu*
           FROG_SPHASE_xfreq(sk))

        omega_t(i) = xfreq(sk)
     end do



deallocate(frog_frequency_lextend,frog_frequency_extend,
   frog_spectrum_lextend,frog_spectrum_extend, &
& frog_sphase_lextend,frog_sphase_extend,FROG_SPECTRUM_INTERP,
   FROG_SPHASE_INTERP)
deallocate(FROG_FIELD_xfreq,FROG_SPHASE_xfreq)
deallocate(frog_spectrum_extend_comp,frog_sphase_extend_comp)

end subroutine PULSEFILTSEP
```

References

[1] G. P. Agrawal, “Modulation Instability Induced by Cross-Phase Modulation,” Phys. Rev. Lett. 59(8), 880-883 (1987).

[2] R. R. Alfano, P. L. Baldeck, P. P. Ho, and G. P. Agrawal, “Cross-phase modulation and induced focusing due to optical nonlinearities in optical fibers and bulk materials,” J. Opt. Soc. Am. B 6(4), 824-829 (1989).

[3] M. N. Islam, L. F. Mollenauer, R. H. Stolen, J. R. Simpson, and H. T. Shang, “Cross-phase modulation in optical fibers,” Opt. Lett. 12(8), 625-627 (1987).

[4] G. P. Agrawal, P. L. Baldeck, and R. R. Alfano, “Modulation instability induced by cross-phase modulation in optical fibers,” Phys. Rev. A 39(7), 3406-3413 (1989).

[5] S. Yeremenko, A. Baltuška, F. de Haan, M. S. Pshenichnikov, and D. A. Wiersma, “Frequency-resolved pump-probe characterization of femtosecond infrared pulses,” Opt. Lett. 27(13), 1171-1173 (2002).

[6] M. Spanner, M. Y. Ivanov, V. Kalosha, J. Hermann, D. A. Wiersma, and M. Pshenichnikov, “Tunable optimal compression of ultrabroadband pulses by cross-phase modulation,” Opt. Lett. 28(9), 749-51 (2003).

[7] R. Trebino, K. W. DeLong, D. N. Fittinghoff, J. N. Sweetser, M. A. Krumbugel, B. A. Richman, and D. J. Kane, “Measuring ultrashort laser pulses in the time-frequency domain using frequency-resolved optical gating,” Rev. Sci. Instrum. 68(9), 3277-3295 (1997).

[8] M. Lorenc, M. Ziolek, R. Naskrecki, J. Karolczak, J. Kubicki, and A. Maciejewski, “Artifacts in femtosecond transient absorption spectroscopy,” Appl. Phys. B 74, 19-27 (2002).

[9] G. Mayer and R. Gires, “The effect of an intense light beam on the index of refraction of liquids,” C. R. Acad. Sci. 258, 2039 (1963).

[10] P. D. Maker, R. W. Terhune, and C. M. Savage, “Intensity-dependent changes in the refractive index of liquids,” Phys. Rev. Lett. 12(18), 507-509 (1964).

[11] Y. R. Shen, “Electrostriction, Optical Kerr Effect and Self-focusing of Laser Beams,” Phys. Lett. 20(4), 378-380 (1966).

[12] R. Y. Chiao, E. Garmire, and C. H. Townes, “Self-trapping of Optical Beams,” Phys. Rev. Lett. 13(15), 479-482 (1964).

[13] R. G. Brewer, “Frequency Shifts in Self-focused Light,” Phys. Rev. Lett. 19(1), 8-11 (1967).

[14] Y. Yan, E. B. Gamble Jr., and K. A. Nelson, “Impulsive stimulated scattering: General importance in femtosecond laser pulse interactions with matter, and spectroscopic applications,” J. Chem. Phys. 83(11), 5391-5399 (1985).

[15] M. D. Levenson and N. Bloembergen, “Dispersion of the nonlinear optical susceptibility tensor in centrosymmetric media,” Phys. Rev. B 10(10), 4447-4464 (1974).

[16] R. B. Bernstein and A. H. Zewail, “Femtosecond real-time probing of reactions. III. Inversion to the potential from femtosecond transition-state spectroscopy experiments,” J. Chem. Phys. 90(2), 829-842 (1989).

[17] N. F. Scherer, D. M. Jonas, and G. R. Fleming, “Femtosecond wave packet and chemical reaction dynamics of iodine in solution: Tunable probe study of motion along the reaction coordinate,” J. Chem. Phys. 99(1), 153-168 (1993).

[18] J. D. Hybl, A. A. Ferro, and D. M. Jonas, “Two-dimensional Fourier transform electronic spectroscopy,” J. Chem. Phys. 115(14), 6606-6622 (2001).

[19] D. M. Jonas, “Two-Dimensional Femtosecond Spectroscopy,” Annu. Rev. Phys. Chem. 54, 425-63 (2003).

[20] J. A. Gardecki, S. Constantine, Y. Zhou, and L. D. Zieger, “Optical heterodyne detected spectrograms of ultrafast nonresonant electronic responses,” J. Opt. Soc. Am. B 17(4), 652-662 (2000).

[21] J.-L. Oudar, “Coherent Phenomena Involved in the Time-Resolved Optical Kerr Effect,” J. Quant. Electron. 19(4), 713-718 (1983).

[22] Y. Zhou, S. Constantine, J. A. Gardecki, and L. D. Ziegler, “Dispersed ultrafast nonresonant electronic responses: detuning oscillations and near resonance effects,” Chem. Phys. Lett. 314, 73-82 (1999).

[23] S. Mukamel, *Nonlinear Optical Spectroscopy* (Oxford University Press, Oxford, 1995).

[24] S. M. Gallagher Faeder and D. M. Jonas, “Two-Dimensional Electronic Correlation and Relaxation Spectra: Theory and Model Calculations,” J. Phys. Chem. A 103, 10489-10505 (1999).

[25] R. M. Mersereau and A. V. Oppenheim, “Digital Reconstruction of Multidimensional Signals from Their Projections,” Proc. IEEE 62, 1319 (1974).

[26] M. K. Yetzbacher, N. Belabas, K. A. Kitney, and D. M. Jonas, "Propagation, beam geometry, and detection distortions of peak shapes in two-dimensional Fourier transform spectra," J. Chem. Phys. 126, 044511 (2007).

[27] P. F. Tekavec, J. A. Myers, K. L. M. Lewis, F. D. Fuller, and J. P. Ogilvie, "Effects of chirp on two-dimensional Fourier transform electronic spectra," Opt. Exp. 18(11), 11015-11024 (2010).

[28] A. P. Spencer, H. Li, S. T. Cundiff, and D. M. Jonas, "Pulse Propagation Effects in Optical 2D Fourier-Transform Spectroscopy: Theory," J. Phys. Chem. A 119, 3936-3960 (2015).

[29] D. Brida, S. Bonora, C. Manzoni, M. Marangoni, P. Villoresi, S. De Silvestri, and G. Cerullo, "Generation of 8.5-fs pulses at 1.3 μm for ultrabroadband pump-probe spectroscopy," Optics Express 17(15), 12510-12515 (2009).

[30] E. Zeek, K. Maginnis, S. Backus, U. Russek, M. Murnane, G. Mourou, H. Kapteyn, and G. Vdovin, "Pulse compression by use of deformable mirrors," Optics Letters 24(7), 493-495 (1999).

[31] T. L. Courtney, S. D. Park, R. J. Hill, and D. M. Jonas, "Broadband, low-dispersion, Brewster's angle interferometers," (in preparation).

[32] M. Zavelani-Rossi, G. Cerullo, S. De Silvestri, L. Gallmann, N. Matuschek, G. Steinmeyer, U. Keller, G. Angelow, V. Scheuer, and T. Tschudi, "Pulse compression over a 170-THz bandwidth in the visible by use of only chirped mirrors," Opt. Lett. 26, 1155-1157 (2001).

[33] The JILA loop filter was designed by J. L. Hall and T. Brown.

[34] M. K. Yetzbacher, T. L. Courtney, W. K. Peters, K. A. Kitney, E. R. Smith, and D. M. Jonas, "Spectral restoration for femtosecond spectral interferometry with attosecond accuracy," J. Opt. Soc. Am. B 27(5), 1104-1117 (2010).

[35] D. J. Jones, E. O. Potma, J. X. Cheng, B. Burfeindt, Y. Pang, J. Ye, and X. S. Xie, "Synchronization of two passively mode-locked, picosecond lasers within 20 fs for coherent anti-Stokes Raman scattering microscopy," Rev. Sci. Instrum. 73, 2843-2848 (2002).

[36] The Xe vacuum wavelengths used for calibration were: 1053.074 nm, 1084.131 nm, 1174.545 nm, 1262.685 nm, 1366.021 nm, 1414.595 nm, 1473.642 nm, 1542.222 nm, 1673.273 nm, and 1733.053 nm. These values were from [37].

[37] E. B. Saloman, "Energy Levels and Observed Spectral Lines of Xenon, Xe I through Xe LIV," J. Phys. Chem. Ref. Data 33(3), 765-921 (2004).

[38] S. B. Howell, *Handbook of CCD Astronomy*, 2nd ed., Cambridge Observing Handbooks for Research Astronomers (Cambridge University Press, Cambridge, 2006).

[39] D. Baranov, R. J. Hill, S. D. Park, J. Ryu, and D. M. Jonas, “Interferometrically stable, enclosed, spinning sample cell for spectroscopic experiments on air-sensitive samples,” (in preparation).

[40] A. Baltuška, M. S. Pshenichnikov, and D. A. Wiersma, “Second-Harmonic Generation Frequency-Resolved Optical Gating in the Single-Cycle Regime,” IEEE J. Quant. Electron. 35(4), 459-478 (1999).

[41] G. Taft, A. Rundquist, M. M. Murnane, I. P. Christov, H. C. Kapteyn, K. W. Delong, D. N. Fittinghoff, M. A. Krumbügel, J. N. Sweetser, and R. Trebino, “Measurement of 10-fs Laser Pulses,” IEEE J. Sel. Topics Quantum. Electron. 2(3), 575-585 (1996).

[42] K. W. DeLong, D. N. Fittinghoff, and R. Trebino, “Practical Issues in Ultrashort- Laser-Pulse Measurement Using Frequency-Resolved Optical Gating,” IEEE J. Quant. Electron. 32(7), 1253-1264 (1996).

[43] S. Dong, D. Trivedi, S. Chakrabortty, T. Kobayashi, Y. Chan, O. V. Prezhdo, and Z.-H. Loh, “Observation of an Excitonic Quantum Coherence in CdSe Nanocrystals,” Nano Lett. ASAP (2015).

[44] I. Gdor, C. Yang, D. Yanover, H. Sachs, E. Lifshitz, and S. Ruhman, “Novel Spectral Decay Dynamics of Hot Excitons in PbSe Nanocrystals: A Tunable Femtosecond Pump-Hyperspectral Probe Study,” J. Phys. Chem. C 117, 26342-26350 (2013).

[45] N. Belabas and D. M. Jonas, “Three-dimensional view of signal propagation in femtosecond four-wave mixing with application to the boxcars geometry,” J. Opt. Soc. Am. B 22(3), 655-674 (2005).

[46] M. D. Levenson, C. Flytzanis, and N. Bloembergen, “Interference of Resonant and Nonresonant Three-Wave Mixing in Diamond,” Phys. Rev. B 6(10), 3962-3965 (1972).

[47] A. E. Siegman, *Lasers* (University Science Books, California, 1986).

[48] N. De Jesus from Ocean Optics. personal communication, April 29, 2015.

Chapter 5

The Initial Pump-Probe Polarization Anisotropy of Colloidal PbS Quantum Dots

5.1 Introduction

Bulk lead chalcogenide semiconductors have a rock salt structure and an interesting electronic structure, with their bandgap at the 4-fold degenerate (8-fold including spin) L-point of the first Brillouin zone, where $\vec{k} = (\pm\pi/a, \pm\pi/a, \pm\pi/a)$ [1]. The four L-points in the band structure are each local minima in the conduction band, and local maxima in the valence band, which are known as valleys. The electronic structure near the bandgap of their quantum dots (QDs) is more complicated than suggested by the particle in a sphere model usually used to explain quantum confinement [2][3]. Depending on nanocrystal symmetry and stoichiometry, the intervalley degeneracy may be lifted in near-spherical QDs [4]. Theoretical studies report that the electronic envelope function of the QDs is sensitive to the coupling to optical phonons [5], which affects dephasing rates. The electronic structure of

QDs is also important for Auger recombination [6][7], multiple exciton generation [8][9], and photoluminescence efficiency, where the electron and hole must align in the same valley.

Theoretical studies predicted splittings from intervalley coupling of up to 80 meV for PbSe QDs depending on the diameter, with an additional splitting to dark and bright states from electron-hole exchange interaction [10]. Two experimental papers have reported electronic splittings of the 4-fold degeneracy in lead chalcogenide QDs [11][12]. Additional theoretical studies report that the intervalley splittings of the energy levels in lead chalcogenide QDs are sensitive to the arrangement of atoms having an inversion center, stoichiometry of the QDs, and the surface passivation [4]. If correct, the predicted variation in splitting with structural details either implies nanostructures of unprecedented uniformity or casts doubt on the experimental attribution. The theoretical results imply that the confinement gives rise to a complex electronic structure, which affects both linear and non-linear spectroscopic measurements. This naturally leads to questions about how the electronic structure in QDs affects the bi-exciton states.

The pump-probe polarization anisotropy is a valuable technique for probing the electronic structure of QDs. The pump-probe polarization anisotropy is calculated from pump-probe transients recorded with a linearly polarized probe pulse that is aligned parallel and perpendicular to a linearly polarized pump pulse. The polarization anisotropy is obtained by taking the difference between parallel and perpendicular pump-probe signals and dividing by the isotropic signal. The division by the isotropic signal removes common factors, such as lifetime decay, so that the anisotropy purely reflects the changes in dipole alignment. The frequency dependent polarization anisotropy is defined as

$$r(\omega, T) = \frac{S_{\parallel}(\omega, T) - S_{\perp}(\omega, T)}{S_{\parallel}(\omega, T) + 2S_{\perp}(\omega, T)}, \tag{5.1}$$

where $S_{\parallel}(\omega, T)$ and $S_{\perp}(\omega, T)$ are the spectrally resolved pump-probe (SRPP) signals with probe polarization parallel and perpendicular with respect to the pump at a time delay T.

The anisotropy can provide structural information on the angles between transition dipoles. Coupling between valleys and and dephasing between excited states in QDs can all lead to a time dependence of the anisotropy. The rate of anisotropy decay essentially quantifies the timescale of the alignment of the transition dipole excited by the pump. Molecular rotation, electron transfer, and energy transfer can also contribute to the time dependence of the anisotropy.

If a signal is composed of several contributions S^i, with anisotropies r_i, the total signal has an average anisotropy

$$\langle r \rangle = \sum_i r_i S^i / \sum_i S^i, \tag{5.2}$$

where $S^i = (S^i_{\parallel} + 2S^i_{\perp})/3$ is the isotropic signal strength of signal i. The average anisotropy diverges to infinity if the total isotropic signal vanishes [13][14]. In an orientationally isotropic ensemble of molecules with non-degenerate transitions, the initial anisotropy should be 2/5, because the $\cos^2(\theta)$ dipolar excitation probability [15] gives rise to a 3:1 signal strength ratio between parallel and perpendicular polarization geometries. If the coupling between degenerate or quasi-degenerate transitions is weak enough such that all of the single excitations remain within the pulse bandwidth, the initial anisotropy of 2/5 is recovered in pump-probe signals from degenerate transitions [13][16]. A departure from the initial anisotropy of 2/5 for an orientationally isotropic sample with a degenerate transition has been attributed to additional excited-state absorption [17].

Theoretical calculations predict [4][10] that all of the PbS QD exciton splittings should be covered by the spectra of the pulses used for the experiments reported here. It was therefore anticipated that the initial anisotropy would contain information about the biexciton states and that the dynamics of the anisotropy would give information about the timescale of intervalley scattering, that is, the timescale for the excited transition dipole becoming randomly misaligned by exciton scattering between the 4 degenerate L-valleys after polarized excitation.

The initial anisotropy for QDs is particularly interesting because the standard dipole result of 2/5 is sometimes recovered only when both one and two electron states are considered, as will be shown in an example later in this chapter. At twice the photon energy, the one electron state for QDs corresponds to a hole deep in the valence band and an electron high in the conduction band. Hot carrier states in QDs have been reported to behave like the corresponding hot carrier states in bulk semiconductors [18]. The lowest cold excitations of bulk PbS occur at the E1 transition (~2.25 eV), which is either at Σ_5-Σ_5 along the K direction [1] or a higher lying L_6^- to L_6^- transition [1], or both. There are no obvious one-electron excited states below E1 in the bulk band structure.

Pump-probe polarization anisotropy measurements on PbSe QDs and PbSe nanorods have been previously performed by Cunningham *et al.* with ~200 fs time resolution [19]. They report that QDs have an isotropic absorption and as the aspect ratio of the nanocrystal gets larger, so that it becomes a nanorod, the absorption becomes anisotropic. They propose a geometrical interpretation of the data without considering quantum confinement effects. The pulse duration is longer than the expected intervalley scattering time. As a result, these measurements do not directly probe the polarization memory of the nanocrystal but the asymptotic anisotropy. Rosenthal *et al.* [20], using 10 fs pulses, reported initial anisotropies of 0.1 to 0.4 for CdSe QDs. The anisotropy decreased as the diameter of the QD increased and the QDs became more spherical. Rosenthal *et al.* [20] attributed the anisotropy to a change in the symmetry and degeneracy of the conduction and valence orbitals with change in QD size. The interpretation of the anisotropy, however, is incomplete, because it does not consider the different anisotropies of the ground state bleach and excited state absorption contributions to pump-probe signals, which were first treated in later work by Jonas and co-workers [21]. Rosenthal's [20] work does, however, indicate that anisotropy experiments with sufficient time resolution can probe the complex electronic structure of QDs.

In this chapter, we present broadband pump-probe polarization anisotropy results of chlorine-passivated PbS QDs using 15 fs pulses in the short-wave infrared. Our results show an anomalous initial anisotropy. We present a calculation of the anisotropy using a simple two electron in a 3D box model and an effective mass theory for the four-fold degenerate valleys. The 3D box calculation shows the possible role of hot one-electron states. The 4-valley calculation indicates that an anisotropy of 2/5 is expected unless spin-orbit or inter-valley splittings exceed the pulse spectral bandwidth.

5.2 Experimental Methods

5.2.1 Sample Synthesis and Preparation

A sample of lead sulfide (PbS) nanocrystals with a bandgap of 1.074 eV and ∼101 meV FWHM of the first absorption peak was synthesized from lead chloride and elemental sulfur in oleylamine following the hot injection procedure reported by the Tisdale group [22] with modifications in the washing procedure. Synthesis of PbS nanocrystals was performed under an atmosphere of argon on a Schlenk line. Briefly, the procedure can be summarized as follows. A saturated solution/suspension of lead (II) chloride (0.840 g) in oleylamine (7.5 ml) was prepared, in air, in a 50 ml round bottom flask equipped with a magnetic stir bar and placed under vacuum at room temperature while stirring. After 10 minutes under vacuum, the flask was refilled with argon and transferred into a hot oil bath preheated to 120 °C, stirred, and placed under vacuum again for 10 minutes. During this period, the mixture changed its appearance from cloudy white to translucent light yellow. After 10 minutes had passed, the flask was refilled with argon and heating was turned off, letting the oil bath cool down to the injection temperature of ∼92 °C. To make the nanocrystals, 2 ml of the sulfur stock solution (made by dissolving 0.060 g of elemental sulfur in 10 ml of degassed oleylamine under argon) were swiftly injected into the lead chloride and oleylamine mixture. Once the sulfur stock solution was injected, the reaction mixture turned opaque black-brown and was left for 3 minutes to let the nanocrystals grow to the desired size. At 3 minutes, the reaction was quenched by swiftly injecting 12 ml of room temperature anhydrous toluene followed by transferring the flask into an ice-filled water bath. Further post-synthetic handling and washing of synthesized nanocrystals were performed inside the argon-filled glovebox (MBraun Unilab workstation, $\leqslant$0.1 ppm H_2O, $\leqslant$0.1–1.2 ppm O_2 levels). In a departure from prior work [22], washing was performed using acetonitrile as a "non-solvent" to precipitate nanocrystals from the reaction mixture and toluene as a solvent for re-dissolution. A small amount of oleic acid was added to the solution of nanocrystals during the washing to keep them colloidally stable. Once the excess of oleylamine and unreacted lead (II) chloride were washed, the nanocrystals were dried under vacuum for an hour, dissolved in tetrachloroethylene and filtered through a 0.2 μm PTFE syringe filter prior to spectroscopic measurements.

Nonlinear optical experiments on the sample of PbS QDs were performed using a spinning sample cell that was custom built in our laboratory [23]. The spinning sample cell consists of an air-tight copper gasket sealed enclosure carrying a 4200 RPM, 2.5 inch diameter hard drive disk motor and a reusable glass sandwich cell. Inside the glovebox, the glass sandwich cell was filled with the solution of PbS QDs in tetrachloroethylene (TCE) using a mechanical pipette and sealed in the airtight enclosure. Optical density (OD) of the sample solution was adjusted to be $\sim$0.3 at 1154 nm (pathlength of the glass sandwich cell was measured to be $\sim$270 μm with $<$5% min-max internal pathlength variation). The spinning sample cell keeps the sample air-free with ultra high vacuum compatible seals and completely exchanges the sample between laser shots. The re-sampling time is 0.9 s under illumination at 1 kHz because the laser and spin frequencies, measured with a common sampling clock, have no prime factor in common at the 0.01 Hz level. Cumulative centrifugation [24] is prevented by stopping spinning every 20 minutes, allowing mixing by a gas bubble [23]. Continuous excitation of over 6 hours in an experiment showed no signs of photo-damage of the QDs, which were judged by the first exciton peak position and OD during data collection.

5.2.2 Experiment

In the experiment, a pulse train from a Ti:sapphire-pumped, short-wave infrared noncollinear optical parametric amplifier (NOPA) is directed into the pump-probe interferometer. The NOPA is based on the design of Cerullo and co-workers [25], and uses quasi-phase matching in a periodically poled stoichiometric lithium tantalate crystal (PPSLT) to generate pulses over the 1–2 μm wavelength range with pulse energy stabilities better than $\pm 0.3\%$ RMS. The pulses are compressed down to $\sim$15 fs by a deformable mirror (OKO 30 mm 19 channel Piezoelectric Deformable Mirror) using an adaptive algorithm [25][26] to maximize the intensity of the second harmonic generation (SHG) measured with the nonlinear crystal at the sample position in the pump-probe interferometer. After the deformable mirror grating compressor, the beam is spatially filtered by focusing with a 250 mm focal length curved mirror into a 250 μm pinhole, and re-collimated using a 250 mm focal length curved mirror. The transmission through the spatial filter pinhole is approximately 80%. Since this spatially filters the beam during adaptive pulse compression, it loosely constrains the optimization by penalizing angular deviations that become beam translations of spatial chirp at the pinhole. For broadband phase matching across the pulse spectrum, the nonlinear crystal is a 20 μm thick Beta Barium Borate (BBO) crystal cut at 20 degrees with respect to its optic axis for type I phase-matching.

The pump-probe interferometer and signal detection apparatus is shown in Figure 5.1. INCONEL®-coated BOROFLOAT®33 glass substrates (New Focus #5235 OD = 0.5 metallic neutral density filter, 1.1 ± 0.1 mm substrate thickness) are used as beam splitters at the Brewster's angle for the air-glass interface. A predominantly nickel and chromium alloy, INCONEL®(Special Metals Corporation) has a relatively constant and roughly equal reflectance-to-transmittance intensity ratio across the wavelength range of 500–2000 nm. Based on the refractive index [27], BOROFLOAT®33 glass has an air-glass interface Brewster's angle of 56.5 degrees in the short-wave infrared; this angle varies by 0.25 degrees over the range from 1–2 μm. The angle is set by aligning irises to bolt holes along the hypotenuse of similar right triangles (6 inches and 14 inches) defined by $\tan^{-1}(3/7) \approx 23.2^\circ$. This provides a reproducible alignment for a Brewster's angle of 56.6°. The angular deviation of reflections from the beam splitter (at worst, 3 mm error over 38.7 cm) is $\pm 0.44^\circ$; this uncertainty in beam splitter reflection angle is comparable to the range of Brewster's angles over the 0.5–2 μm wavelength range. After the trihedral retroreflectors, the pump and probe beams both travel through separate achromatic $\lambda/2$ waveplates (Thorlabs AHWP10M-1600, 0.49 - 0.51 wave retardance over 1100 - 2000 nm) followed by linear polarizers (Thorlabs LPNIR100, $>1\times10^{-5}$ extinction). Due to the unequal retardance over the range of the pulse spectrum, linear polarizers are used after the waveplates. Both pump waveplate and pump polarizer are rotated when changing the relative pump-probe polarization. A pinhole at the focus of the sample position is used to check whether that the beam focus translates when rotating the waveplate and polarizer. With an initial pulse energy of 110 ± 0.2 nJ, the transmission through a 50 μm diameter pinhole was 47.5 ± 0.2 nJ and 47.0 ± 0.2 nJ for p and s polarization, respectively. The mounts used for rotating the polarizing optics are marked with 2° increments, and interpolated to set the polarization angle reproducibly to within one degree. After the linear polarizers for the pump and probe beams, the beams have s or p polarized 90° reflections from 3 silver mirrors, a near retroreflection from the curved silver focussing mirror, and are transmitted through the sample cell windows, which include a 0.070 inch thick viewport window (MDC 450000) and a 0.635 mm thick hard drive disk glass substrate. Ideally, the polarizer should be the last optic before the sample to clean up the polarization, but this was not implemented due to space constraints in the all reflective design. Because reflection introduces a phase shift between s and p polarization, intermediate linear polarizations become elliptically polarized upon reflection and cannot be used. For this reason, special care was taken in measuring the extinction ratio after all the optics at the sample position. For s and p polarization, the extinction ratio is measured to be greater than 1000:1, limited by the detection sensitivity, immediately after a solvent blank sample. The measurement used an uncoated air-spaced glan prism calcite polarizer (Karl Lambrecht, MGTYE8, 5×10^{-6} extinction) as an analyzer placed after the solvent blank and before CM2 (Fig. 5.1) to test for any birefringence in the sample cell optics. The solvent blank includes an entrance viewport window, sandwiched sample cell with TCE solvent, and an exit viewport window.

To assure the beams overlap at the sample, a 50 μm diameter pinhole mounted inside an identical glass sandwich cell is used to maximize the transmission of both beams. Across the beam diameter, there is a range of 0.005" (= 127 μm) where the transmission through the pinhole was unchanged within measurement precision of 1%. The reproducibility of z-positioning is within this range, which was determined by measuring the total transmission after the pinhole after exchanging the sample cell enclosure and placing it back. This was particularly important because we needed to successively measure the solvent blank, after measuring the sample, for the subtraction. The pump and probe beams are separated by 12 mm before the focusing curved mirror. The Rayleigh range with a 1/e beam diameter of 82 μm is calculated to be $\sim$19 mm. With a 150 mm focal length and assuming a top hat beam, the end-to-end length of no spatial overlap is $\sim$220 mm. This indicates that the beams are well overlapped throughout the entire 270 μm sample length.

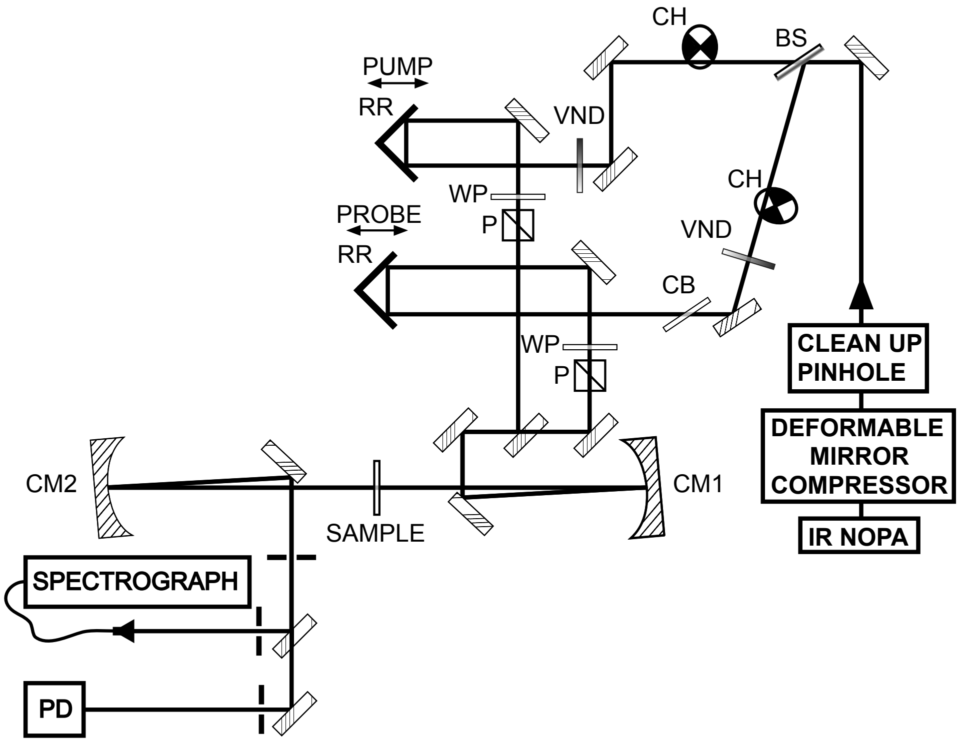

Figure 5.1: Spectrally resolved pump-probe anisotropy apparatus. An INCONEL®-coated neutral density filter set at Brewster's angle for the air-glass interface is used as a beam-splitter for our spectral range. A linear variable neutral density filter is used to adjust the power of the pump and probe for the experiment. The pump and probe each travel through separate $\lambda/2$ achromatic waveplates and linear polarizers to set the relative polarization. The polarization of the pump beam is rotated for the anisotropy experiment. The sample is placed at the focus of the curved mirrors. The extinction ratio at the sample position, after all the optics including the sample cell windows and solvent, is measured to be greater than 1000:1, limited by detection sensitivity. BS: INCONEL®-coated OD $= 0.5$ metallic neutral density filter, VND: variable neutral density filter, RR: trihedral retro-reflector, WP: $\lambda/2$ achromatic waveplate, P: linear polarizer, CB: compensating block, CM: curved mirror with radius of curvature of 300 mm, CH: optical chopper. Protected silver mirrors are unlabeled.

Excitation Probability

The pulse spectrum was tuned to simultaneously overlap with both the $1S_e{-}1S_h$ electron-hole pair absorption peak and the photoluminescence (PL) spectrum (Fig. 5.2). Pulse energies of 15 nJ and 10 nJ for the pump and probe, respectively, were used for the experiment. The 1/e beam spot size at the sample was determined by measuring the transmission through three pinholes (Lenox Laser OSS-3/8-DISC-XX). The transmission was 39% for a 50 μm diameter pinhole, 59% for a 75 μm diameter pinhole, and 66% for a 100 μm diameter pinhole. Modeling the focal spot as Gaussian, $I(r, \theta) = (1/(\pi w^2)) \exp(-r^2/w^2)$, we calculate the average 1/e diameter of roughly 82 μm. With the pulse spectrum, pulse energy, and focal spot size, the average excitation probability that the probe encounters was calculated referring to Ref. [28]. The averaged excitation probability was calculated using the following equation,

$$\langle N \rangle = \int_0^l dZ \int_0^\infty d\nu_u \; h_u(X,Y)\rho_u(\nu_u)|_{Z=0} \cdot |\sigma_{ij}(\nu_u)| \exp[-\alpha^0(\nu_u)Z], \tag{5.3}$$

where $h(X,Y)$ is the transverse spatial distribution (dimenseions, 1/area), normalized so that $\int_{-\infty}^{\infty} dX \int_{-\infty}^{\infty} dY \; h(X,Y) = 1$ (dimensions, 1/area), $\rho_u(\nu)|_{Z=0}$ is the frequency-dependent photon number distribution (dimensions, (photons/pulse)/frequency) of the pump at the front of the sample, $\sigma_{ij}(\nu)$ is the frequency-dependent absorption cross-section (dimensions, area), and α^0 is the equilibrium absorption coefficient (dimensions, 1/length). The average excitation probability is 0.12 and the peak excitation probability at the front of the sample in the center of the gaussian beam is 0.32.

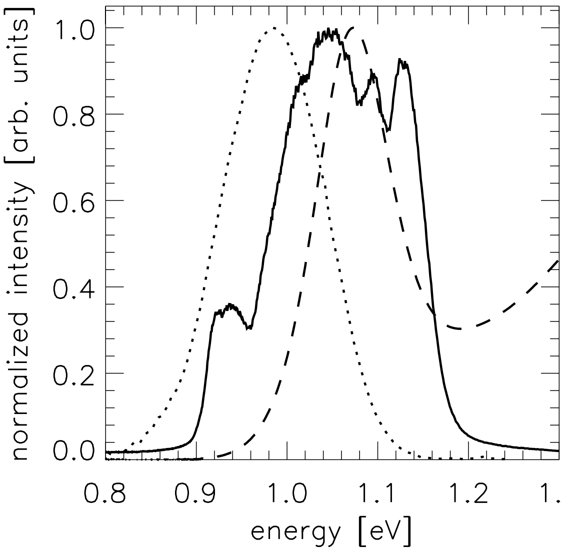

Figure 5.2: Pulse intensity spectrum and linear absorption and photoluminescence spectra of 4 nm diameter, chlorine-passivated PbS QDs. The solid line is the pulse intensity spectrum used for the experiment, which is tuned to overlap with the $1S_e - 1S_h$ electron-hole pair transition in the linear absorption spectrum (dashed line) and the photoluminescence spectrum (dotted line).

Pulse Characterization

The excitation pulse fields are measured by SHG Frequency Resolved Optical Gating (SHG FROG) [29][30] at the sample position. The agreement between the measured pulse spectrum and the fundamental pulse spectrum retrieved by FROG is used to verify the retrieval algorithm. The fundamental pulse spectrum was measured using a single-mode fiber, which ensures the spectrum that focuses at the sample position. For good agreement between the retrieved fundamental pulse spectrum and the measured pulse spectrum, the raw SHG FROG trace required a division by an ω^3 factor for the FROG algorithm [31]. The ω^3 factor comes from multiplication of (1) an ω^2 dependence that follows from Maxwell's equation from polarization radiation and (2) an ω dependence of the second harmonic intensity on the spatial overlap of the different fundamental frequency modes [31]. Previously, methods of forcing the agreement between the autoconvolution and the FROG frequency marginal has been used [32] to correct for these frequency-dependent effects.

Figure 5.3 shows the retrieved FROG trace, spectrum, and spectral phase used for the experiment. Typical FROG errors were G = 0.003 on a 256×256 grid [30], indicating a good convergence to the experimental FROG trace. The pulse intensity FWHM retrieved from FROG was 15.2 fs and the calculated transform limit FWHM was 13.8 fs. Although the pulse is nearly transform limited, the deformable mirror's curvature limits the correction for all of the higher order phase shown in Fig. 5.3C.

Determining Time Zero

The time zero between the pump and probe pulses was determined inside the sample cell using symmetrical integrated pump-probe transients. The integrated pump-probe was gated using a boxcar averager (Stanford Research Systems SR250), only using the last sample, and a lock-in amplifier (Stanford Research Systems SR830) with a 30 ms time constant. The signal is obtained ∼100 ms after completing the stage positioning and averaged 10 times

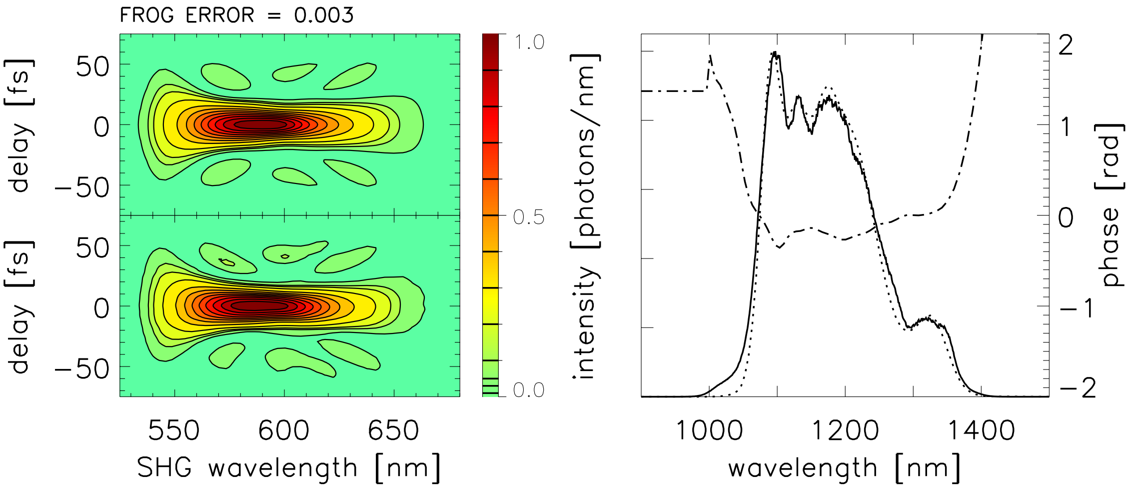

Figure 5.3: Retrieved FROG trace, spectrum, and spectral phase used for anisotropy experiment. Retrieved (top left) and experimental (bottom left) FROG traces with 1%, 3%, 5%, 10%, 20%, 30%, 40%, 50%, 60%, 70%, 80%, and 90% contours. Typical FROG errors were G = 0.003 on a 256×256 grid, which indicates good convergence of the FROG algorithm to the experimental data. (Right) Comparison of the experimentally measured pulse intensity spectrum (solid line) with the retrieved spectrum (dotted line) shows excellent agreement except on the extreme short wavelength wing. The spectral phase (dotted-dashed lines) show residual uncompensated higher-order chirp.

with ∼10 ms delay between each reading. The initial rise of the pump-probe and probe-pump scans were fit to a hyperbolic tangent and the intersection of the two curves in which the roles of the pump and probe are interchanged was determined to be time zero. This allows sub-femtosecond accuracy in the determination of time zero.

5.2.3 Data Acquisition

All spectra were recorded by coupling the light through an aspheric lens with NA = 0.15 (Thorlabs C280TMD-C) into a single-mode fiber with NA = 0.14 (Thorlabs 1060XP, 980–1600 nm, cutoff frequency 920 ± 30 nm). The single-mode fiber was fed into a 0.15-m Czerny-Turner spectrometer (Princeton Instruments SP-2150, f/4, 150 grooves/mm grating blazed for 1.25 μm wavelength, linear dispersion ∼38 nm/mm) with a 1024x1 pixel InGaAs array with extended wavelength sensitivity out to 2.2 μm (Princeton Instruments OMAV:1024-2.2, 25 μm pixel spacing, liquid nitrogen cooled, operated in low gain mode with a minimum well capacity of 100 Me^-). Ten atomic lines of Xenon (Newport #6033, Xe calibration lamp), with the wavelengths in vacuum acquired from NIST [33][34], were fit to a second-order polynomial for wavelength calibration using the following equation:

$$\lambda(p) = A \cdot \left(p - \frac{N}{2}\right)^2 + B \cdot \left(p - \frac{N}{2}\right) + C, \tag{5.4}$$

where p is the pixel number, N is the total number of pixels, and A, B, and C are the coefficients from the fit. The atomic lines used for spectrograph wavelength calibration have a FWHM of ∼3 pixels, which reflects nearly diffraction-limited spatial imaging resolution at the focal plane.

At each time delay, twenty sets of the probe spectrum with the pump blocked and unblocked were acquired and averaged. With an integration time of 250 ms, the number of photoelectrons on each pixel was restricted to less than 3% of the full well capacity ($<$ 2,000 counts out of 65,000 counts) by attenuation with a neutral density filter in order to avoid harmonic nonlinearities previously observed in Fourier transform spectral interferometry [35]. Background spectra were acquired every time a spectra was collected and were necessary to clear the InGaAs array detector of any residual counts. Spectra collected with the pump first and without the pump second did not agree with spectra collected without the pump first and with the pump second when the number of counts on each pixel exceeded 5% of the full well capacity (that is, exceeding ∼3000 counts out of 65,000). A flatfield was applied to each spectrum to correct for pixel-to-pixel variations in sensitivity [35][36]. The flatfield reduced the fine structure on the spectra by a factor of ∼2; we suspect the imperfection in the flatfielding is due to some form of nonlinear coupling between nearby pixels during charge accumulation or readout.

5.2.4 Data Analysis

At early times, just before pulse overlap, the signal is dominated by cross-phase modulation [37][38]. The cross-phase modulation (XPM) signal is proportional to the square of the peak intensity and therefore becomes more apparent with shorter pulses. Although the time resolution used for this experiment is already short, it is important to see the initial dynamics of the QDs. As a result, a subtraction scheme is used to reveal the dynamics of the PbS QDs during pulse overlap. Figure 5.4 shows the raw SRPP data for the QD solution, which has solvent and sample cell window contributions in the top row, and the XPM signal from the neat solvent and sample cell windows in the bottom row. The XPM signal can be approximately simulated assuming a delta function response, as described in the previous chapter.

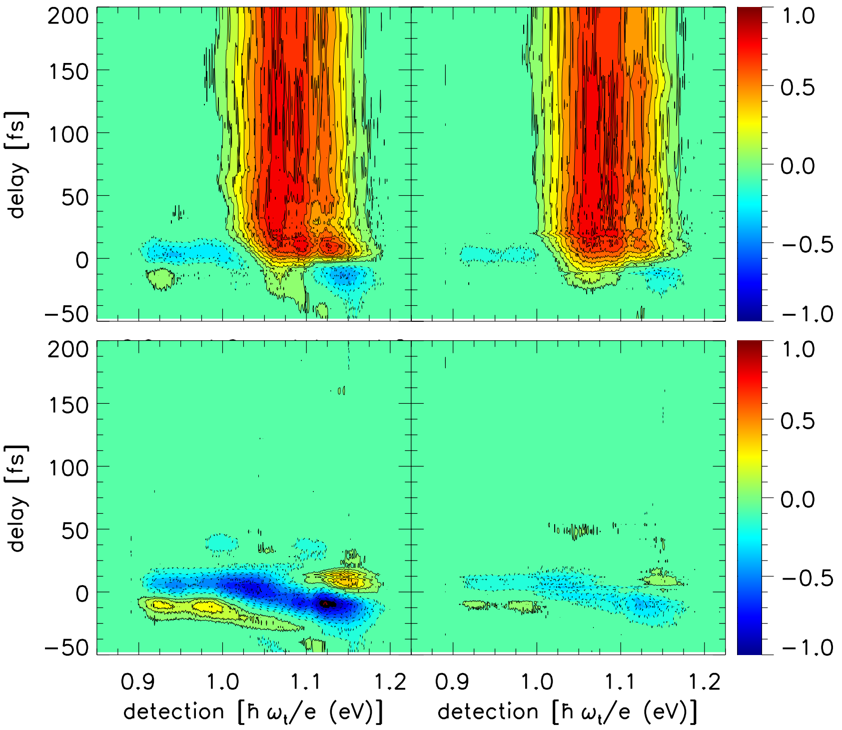

Figure 5.4: Raw SRPP signal of PbS QDs (top row)) and XPM from solvent and sample cell windows (bottom row). The left and right columns are signals measured with parallel and perpendicular polarizations, respectively. Signal during pulse overlap is dominated by the cross-phase modulation, so a subtraction scheme is used to isolate the signal from the PbS QDs.

XPM Simulation with Propagation Effects

The time and frequency marginal of the XPM SRPP transient can be calculated by integrating over the frequency and time axis, respectively. In the previous chapter, simulations for an instantaneous response found that both marginals were zero. The excitation pulses used in this experiment have larger spectral bandwidths than the pulses from the previous chapter. In addition, the XPM SRPP transient signal from neat solvent and sample cell windows in this experiment has non-zero frequency and time marginals. Figure 5.5 shows the time and frequency marginals of the XPM SRPP transient. The time marginal shows a non-zero negative peak centered at zero and the frequency marginal is also negative with features that resemble the excitation pulse spectrum. The non-zero time marginal indicates that the number of photons is not conserved. Gardecki *et al.* [38] stated that in the presence of two-photon absorption, a multiplicative phase factor causes the detected signal to become a mixture of both in-phase and $\pi/2$ out-of-phase responses. They also state that the frequency marginal of the $\pi/2$ out-of-phase response is proportional to the probe pulse spectrum, as observed in our measurement. Their use of a single frequency independent phase factor implicitly assumes the pulse spectral bandwidth is narrow compared to the two-photon resonance. Because the material of the sample cell windows is proprietary, the non-zero time and frequency marginals might arise from two-photon absorption. Multiple XPM SRPP transient measurements on different days with pulses that have similar spectral bandwidths also yielded non-zero frequency and time marginals with the same features. Thus, in order to simulate the XPM SRPP transient in this experiment, a complex phase factor, $\exp(i\theta)$, was used to obtain agreement between simulations and the experimental XPM SRPP transient. Using Eqn. 8c of Ref. [38] for the simulation produced the best agreement with $\theta = \pi/15$. As a result, the XPM SRPP transient in this experiment was simulated with the independently retrieved pulse spectrum and spectral phase plus this one adjustable parameter.

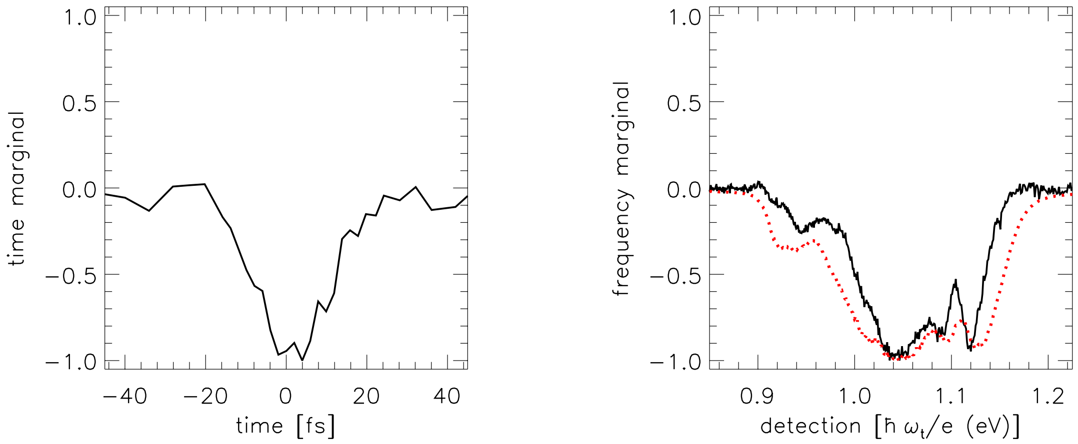

Figure 5.5: Normalized experimental XPM time and frequency marginals. The left figure shows a non-zero time marginal from the XPM SRPP transient with a negative peak centered at zero. The right figure shows a non-zero negative frequency marginal (black solid line) that resembles the excitation pulses (red dotted line) used in the experiment.

Figure 5.6 shows the comparison between the experimentally measured and simulated XPM signal with the complex phase factor. The XPM trace was simulated using the phase and amplitude retrieved from FROG. To account for pulse attenuation from absorption by the QDs, the XPM was calculated including absorptive and dispersive propagation effects. The calculation treats three regions: (i) in the front window, XPM signal is generated by undistorted pulses and then distorted by propagation through the sample; (ii) in the sample, the pulses are distorted as they propagate and the XPM signal they generate is also distorted as it propagates; (iii) in the back window, the excitation pulses are distorted by propagation through the sample before they generate the XPM signal. The nonlinear index of refraction is assumed to be the same for the glass and solvent. The XPM signals computed with and without the attenuation from the QDs differ. Scaling the unattenuated XPM by a multiplicative factor of $\sim$0.531 gives the lowest RMS difference between the two. With this factor, the subtraction has contours at the $\sim$10% level of the unattenuated XPM signal. The XPM signal propagation within an absorbing sample can only be calculated exactly in three frequency dimensions [39][40], so this crude XPM multiplication and subtraction scheme will not be exact. Figure 5.7 compares the calculated SRPP XPM signal with and without the attenuation.

After applying the multiplicative factor and subtracting the attenuated solvent signal, the SRPP signal of the QDs is revealed. The resulting SRPP signal for both parallel and perpendicular polarization geometries are shown in Fig. 5.8.

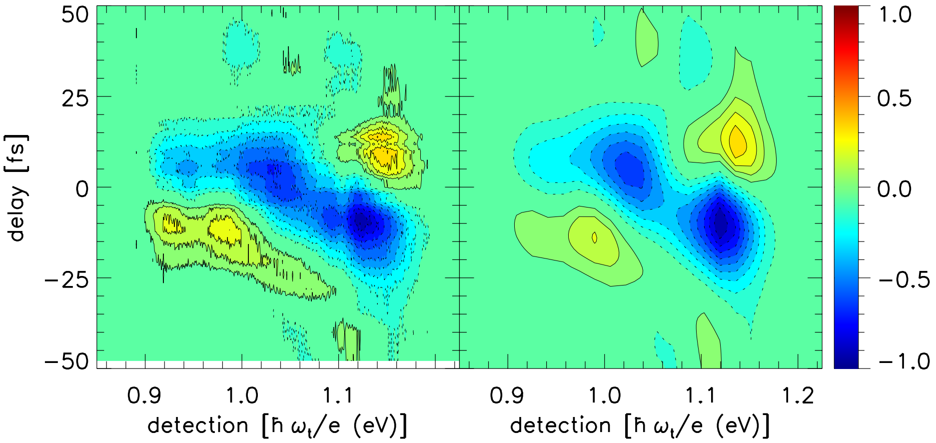

Figure 5.6: Experimental (left) and simulated (right) SRPP XPM from sample windows and neat solvent. The XPM signal was simulated with the retrieved pulse spectrum and spectral phase from FROG. The simulation shows agreement with the measured XPM to within 10%.

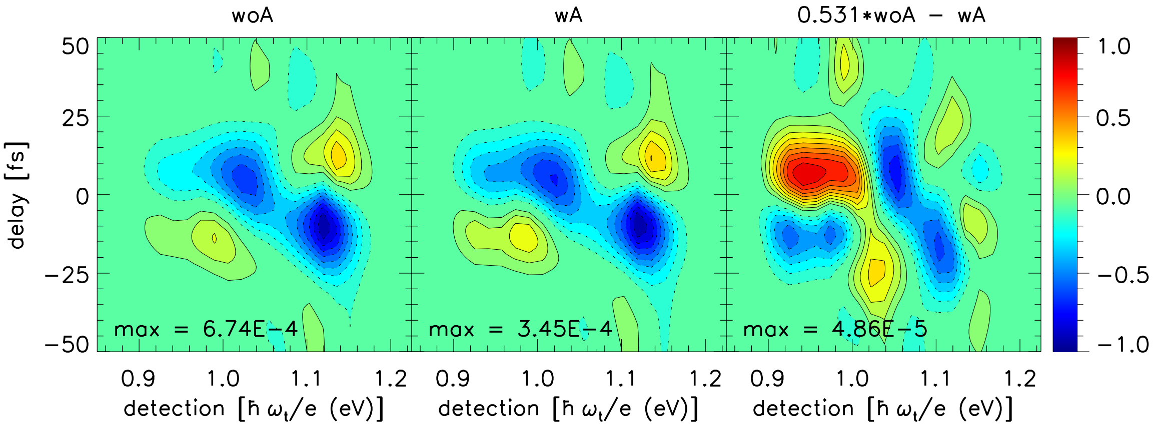

Figure 5.7: Simulated propagation effects of the XPM signal with the QD sample. The spectrum on the left shows the XPM signal without any attenuation, labeled woA. The spectrum in the middle shows the XPM signal accounting for the attenuation by the QD sample, labeled wA. The simulation consists of three separate interfaces for the signal attenuation: the XPM signal generated in the front glass window and attenuated throughout the sample pathlength, the XPM signal generated in the sample pathlength while being attenuated temporally dispersed, and finally the pulse is attenuated and dispersed before the XPM signal is generated at the back glass window. The spectrum on the right shows the difference between the signal without attenuation multiplied by a factor and with attenuation. The factor, 0.531, was determined by the lowest RMS. All spectra have 10% contours and are self normalized to the maximum absolute value to show the shape of the signal. The maximum absolute values for each spectrum are displayed in the spectra.

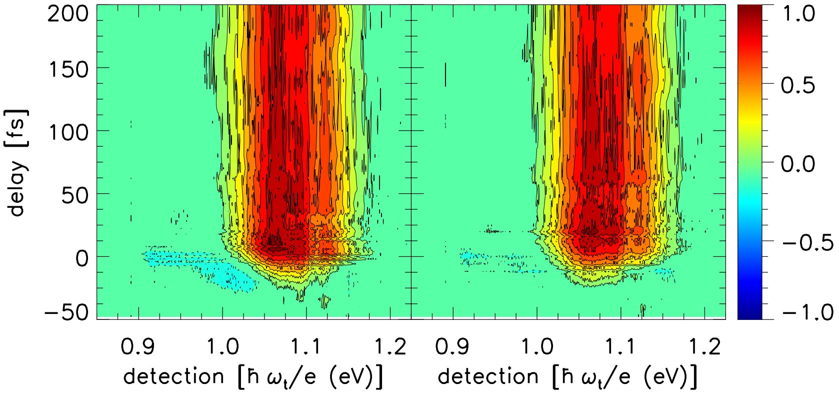

Figure 5.8: SRPP signal of PbS QDs after subtracting solvent signal.

Linear Absorption Measurements

To validate the robustness of exchanging the two samples cells, one containing PbS QDs and the other containing the TCE solvent, the linear absorption spectrum was obtained during the experiment. The linear absorption spectrum was calculated from the transmitted pulse intensity spectra with the sample and solvent. Figure 5.9 shows the retrieved linear spectrum from our experiment with the linear absorption spectrum measured with a CARY 5000. The shape of the linear absorption spectrum is retrieved where the pulse spectrum overlaps. However, the OD measured using the femtosecond pulse is 0.29 ± 0.005 and the OD measured using the CARY 5000 was 0.329. On another day, the retrieved OD with the same pulse power and spectrum differed by ∼0.05. The discrepancy is attributed to the reproducibility of exchanging sample cells. Sample cell positioning was the largest source of error in the measurement of optical density on commercial absorption spectrometers as recently as 2007 [41].

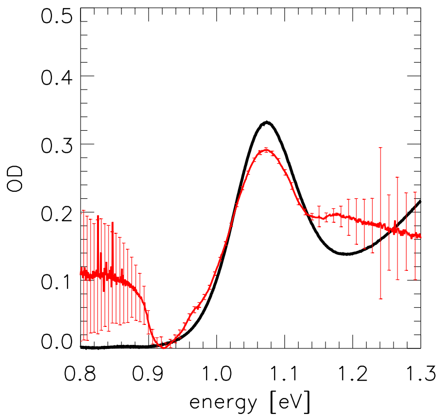

Figure 5.9: Absorption spectrum recovered during the SRPP measurement with femtosecond pulses. The black solid line shows the linear absorption spectrum measured by a CARY 5000 and the red solid line shows the linear absorption spectrum with error bars from the transmitted pulse intensities with the sample and solvent. The error is attributable to imprecision in swapping the spinning sample cell and blank. This error does not occur in pump-probe transients.

XPM Anisotropy

The SRPP XPM signal from solvent/glass was detected with both parallel and perpendicular polarization geometries with respect to the pump pulse. Thus, the anisotropy of the XPM signal can be calculated using Eqn. 5.1. Figure 5.10 shows the anisotropy as a function of frequency taken at different time delays from the XPM SRPP transients. The anisotropy of the XPM where there is signal is $\sim 2/5$, which is consistent with previous reports on the signal strength ratio of 3:1 in XPM with parallel and perpendicular polarization geometries [42][43]. For each delay, the anisotropy diverges in regions where there is no XPM signal. This measurement serves as a check on the polarized measurements between parallel and perpendicular polarization geometries.

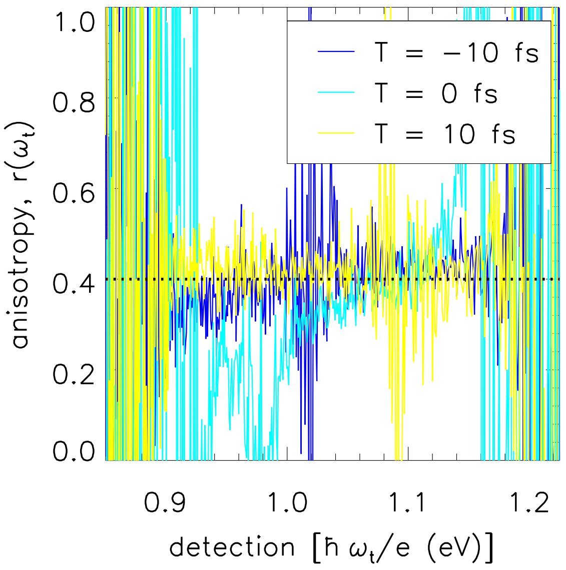

Figure 5.10: Anisotropy of glass from cross phase modulation. The XPM signal strength has the expected 3 to 1 ratio between parallel and perpendicular polarization geometries, which results in an anisotropy of 2/5. For each delay, the anisotropy diverges around sign changes in the XPM.

5.2.5 Experimental Results

After the subtraction of XPM, the parallel and perpendicular polarization geometry SRPP transients for the PbS QDs are revealed. The top row of figure 5.11 shows the SRPP trace for PbS QDs for parallel and perpendicular polarization geometries after subtracting a 0.531 multiple of the experimental XPM signal from neat solvent/glass. The bottom panel in figure 5.11 shows the signal near the bandgap (1.074 eV), shown as the vertical dashed black line in the SRPP transient, and the anisotropy calculated using Eqn. 5.1. Our result shows a nominally zero anisotropy, but may be compatible with a small initial anisotropy of up to ∼0.1. The initial anisotropy needs to be carefully considered because it can arise from an imperfect XPM subtraction or errors in time delay.

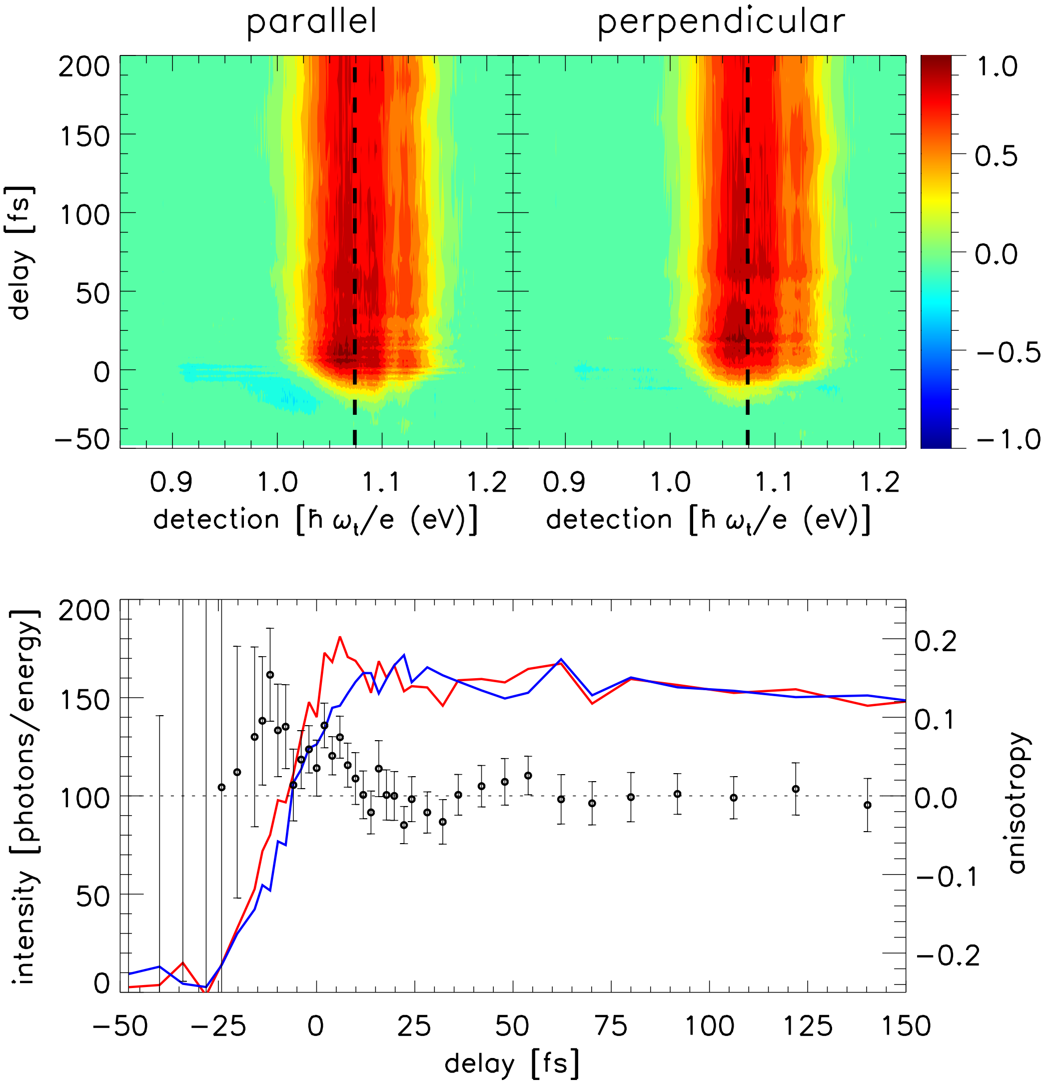

Figure 5.11: PbS anisotropy at the bandgap. The top row shows the SRPP signal for the PbS QDs after the solvent subtraction with the parallel (left) and perpendicular (right) polarization geometries. The bottom figure shows the slice near the bandgap (1.074 eV), shown as the black vertical dashed line in the figures on the top row, for the parallel (red) and perpendicular (blue) polarization geometries. The black circles shows the calculated anisotropy with error bars from laser fluctuations as a function of time delay. The anisotropy diverges where there is no signal.

Figure 5.12 shows the anisotropy as a function of the detection frequency in energy at different time delays, T. The black dashed line in Fig. 5.12 shows the linear absorption spectrum. The anisotropy diverges where there is no signal, which is all outside of the first absorption $(1S_e - 1S_h)$ peak. This indicates two possibilities: either a near zero bi-exciton binding energy for the excited state absorption spectrum so that it lies on top of the ground state absorption spectrum, or a very large bi-exciton binding energy for the excited state absorption spectrum so that it lies outside of the laser bandwidth. In addition, the anisotropy as a function of the detection energy shows that there is no contribution from the red-shifted PL spectrum. This is consistent with the hypothesis that the red-shifted PL signal arises from lower fine structure states with long radiative liftimes. Such states would not be populated immediately after excitation and would have low stimulated emission cross sections [44][45]. Again, the initial anisotropy is less than 0.1 and zero within error after 10 fs.

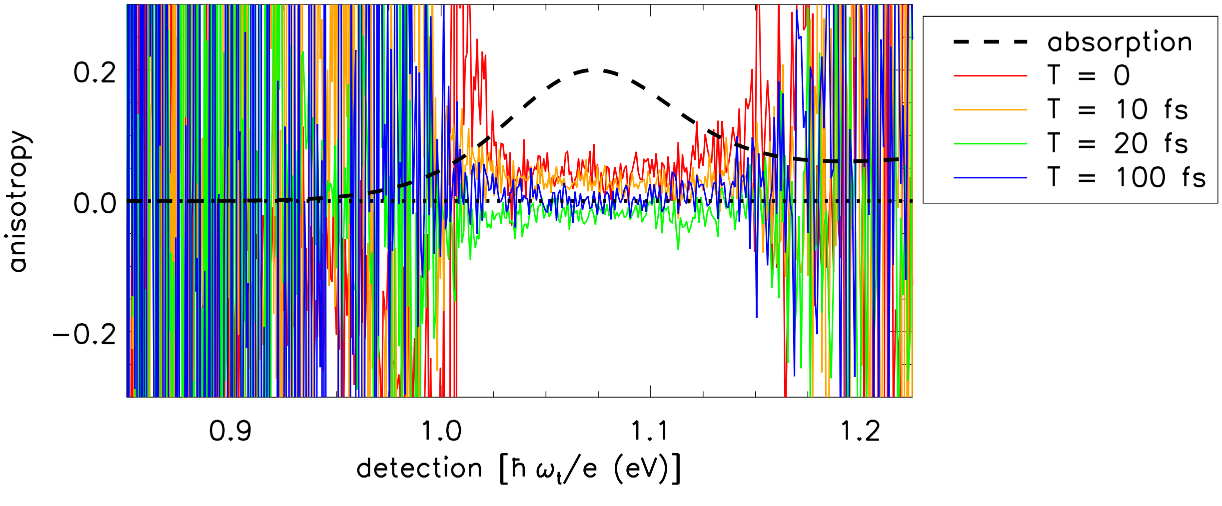

Figure 5.12: PbS anisotropy as a function of the detection frequency in energy at variable T delays. The black dashed line represents the linear absorption spectrum and the black dotted line denotes zero. The different colors show the anisotropy at different delays and labeled in the legend.

To estimate the error of an imperfect XPM subtraction, Fig. 5.13 shows the anisotropy with multiplying factors of 0, 0.4, 0.53 (least RMS through simulations), and 0.6 for the unattenuated XPM signal used for subtraction. The anisotropy without any XPM subtraction (factor of 0) is initially negative, which means that the perpendicular pump-probe signal is larger than the parallel pump-probe signal. This is due to the XPM signal being predominantly negative around $T = 0$ (from the linear chirp) with the parallel polarization geometry being 3 times larger than the XPM signal strength with the perpendicular polarization geometry. Figure 5.13 shows that the anisotropy during pulse overlap has possible errors of <0.04 from imperfect XPM signal subtraction. The region after the pulse overlap, ~10 fs, does not show any change in the near zero anisotropy.

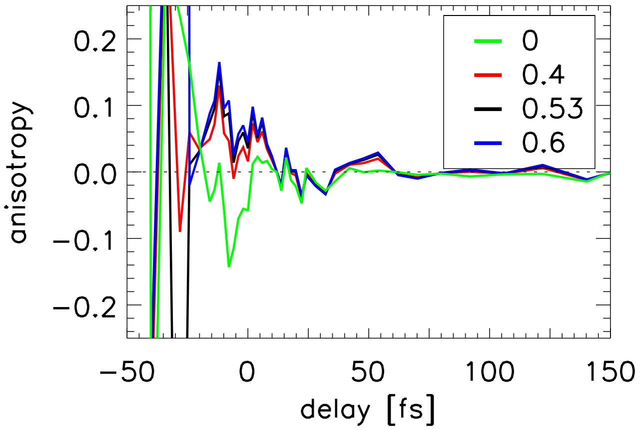

Figure 5.13: Anisotropy with different multiplication factors for XPM signal subtraction. The green, red, black, and blue lines show the anisotropy after the subtraction of the unattenuated XPM signal with a multiplicative factor of 0, 0.4, 0.53, and 0.6, respectively.

To estimate the error from time delay errors, the data set of the perpendicular polarization geometry pump-probe signal was shifted up to 2 data points in each direction to calculate the anisotropy; this corresponds to a shift in time with the range from -4 to 4 fs. Figure 5.14 shows the anisotropy after shifting the the perpendicular signal in time. The time delay error in the anisotropy is roughly ∼0.05 at zero delay and ∼0.025 at later time. Although the anisotropy retrieved from the XPM signal showed that those two traces do not have such a large time delay error, it is useful to know how the anisotropy could be affected by worse-case time delay errors in the experiment.

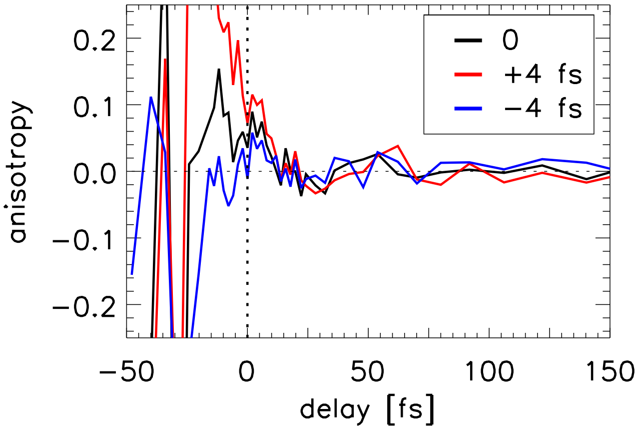

Figure 5.14: Time delay errors in the anisotropy by shifting perpendicular signal in time. The black line shows the anisotropy without any shift in time. The red and blue lines show the anisotropy shifting the perpendicular signal +4 fs and -4 fs in time, respectively.

The fastest dephasing time allowed by the width of the first exciton peak with a FWHM of ∼101 meV is ∼11 fs, meaning the initial dynamics should have been captured with the time resolution in the experiment. This anomaly suggests that the electronic structure of PbS QDs at the bandgap is more complicated than predicted by theoretical calculations [20][46] or that doubly excited states are not as simply related to single excitations. For this reason, the initial anisotropy is calculated based on simple models of a particle in a 3D box and an effective mass approximation.

5.3 Calculations

The initial anisotropy reveals information about the accessible states and the signal contributions from them. The departure from the expected anisotropy of 2/5 gives information about either a lifting of the degeneracy of the excited state absorption to the doubly-excited states. There are two kinds of doubly-excited states: two different electrons that are each singly excited (a "doubly excited state" in the language of configuration interaction) and a single electron that is doubly excited (a "singly excited state" in the language of configuration interaction). More specifically in QDs, the doubly excited single electron corresponds to either an electron in the conduction band being promoted to a higher lying conduction band (a hot electron) or to an electron from a deep valence band being promoted to fill the valence band hole (a hot hole). To model the initial anisotropy, we begin with a two-electron in a 3-dimensional box model and then a QD model with the effective mass approximation. These calculations assume that all transitions are coherently excited and that no population transfer between states has taken place. These assumptions, appropriate for no relaxation ($T = 0$), are opposite to the complete relaxation assumptions used for long relaxation times T in Chapter 3.

5.3.1 Two-electron in a 3D box model

QDs are considered to be zero-dimensional, that is, confined in all three dimensions. For this reason, as a zero-order approximation, a particle in a 3D confined box will be filled with two electrons to model the pump-probe polarization anisotropy of the PbS QDs with an octahedral (O_h) point group symmetry [47]. The total symmetry of the ground state is A_{1g}, with two electrons in the highest occupied molecular orbital (HOMO) ($n_x = n_y = n_z = 1$) with a_{1g} orbital symmetry. The lowest unoccupied molecular orbital (LUMO) has t_{1u} symmetry with degenerate components t_{1ux} ($n_x = 2, n_y = 1, n_z = 1$), t_{1uy} ($n_x = 1, n_y =$

$2, n_z = 1)$, and t_{1uz} $(n_x = 1, n_y = 1, n_z = 2)$. The t_{2g} doubly excited orbital is also triply degenerate with components t_{2gxy} $(n_x = 2, n_y = 2, n_z = 1)$, t_{2gxz} $(n_x = 2, n_y = 1, n_z = 2)$, and t_{2gyz} $(n_x = 1, n_y = 2, n_z = 2)$. States with one electron in the a_{1g} symmetry orbital $(n_x = 1, n_y = 1, n_z = 1)$ and one in the t_{2g} orbital have total symmetry T_{2g} and an energy roughly twice that of the first singly excited state. The doubly excited $(t_{1u})^2$ electron configuration leads to three different symmetry singlet states: non-degenerate A_{1g}, doubly degenerate E_g, and triply degenerate T_{2g}, all at roughly the same energy as the T_{2g} symmetry state with electron configuration $(a_{1g})(t_{2g})$. Based on Hund's rules, A_{1g} has the highest energy of the states arising from the $(t_{1u})^2$ configuration in the absence of configuration interaction. A set of coordinate wave functions that are symmetric under electron permutation (omitting the common anti-symmetric singlet spin wave function) is

$$|0A_{1g}\rangle = |a_{1g}(1)\rangle|a_{1g}(2)\rangle, \tag{5.5a}$$

$$|1T_{1ux}\rangle = (|a_{1g}(1)\rangle|t_{1ux}(2)\rangle + |t_{1ux}(1)\rangle|a_{1g}(2)\rangle)/\sqrt{2}, \tag{5.5b}$$

$$|1T_{1uy}\rangle = (|a_{1g}(1)\rangle|t_{1uy}(2)\rangle + |t_{1uy}(1)\rangle|a_{1g}(2)\rangle)/\sqrt{2}, \tag{5.5c}$$

$$|1T_{1uz}\rangle = (|a_{1g}(1)\rangle|t_{1uz}(2)\rangle + |t_{1uz}(1)\rangle|a_{1g}(2)\rangle)/\sqrt{2}, \tag{5.5d}$$

$$|2A_{1g}\rangle = (|t_{1ux}(1)\rangle|t_{1ux}(2)\rangle + |t_{1uy}(1)\rangle|t_{1uy}(2)\rangle + |t_{1uz}(1)\rangle|t_{1uz}(2)\rangle)/\sqrt{3}, \tag{5.5e}$$

$$|2E_{g(2z^2-x^2-y^2)}\rangle = (2|t_{1uz}(1)\rangle|t_{1uz}(2)\rangle - |t_{1ux}(1)\rangle|t_{1ux}(2)\rangle - |t_{1uy}(1)\rangle|t_{1uy}(2)\rangle)/\sqrt{6}, \tag{5.5f}$$

$$|2E_{g(x^2-y^2)}\rangle = (|t_{1ux}(1)\rangle|t_{1ux}(2)\rangle - |t_{1uy}(1)\rangle|t_{1uy}(2)\rangle)/\sqrt{2}, \tag{5.5g}$$

$$|2T_{2gxy}\rangle = (|t_{1ux}(1)\rangle|t_{1ux}(2)\rangle + |t_{1uy}(1)\rangle|t_{1uy}(2)\rangle)/\sqrt{2}, \tag{5.5h}$$

$$|2T_{2gxz}\rangle = (|t_{1ux}(1)\rangle|t_{1ux}(2)\rangle + |t_{1uz}(1)\rangle|t_{1uz}(2)\rangle)/\sqrt{2}, \tag{5.5i}$$

$$|2T_{2gyz}\rangle = (|t_{1uy}(1)\rangle|t_{1uy}(2)\rangle + |t_{1uz}(1)\rangle|t_{1uz}(2)\rangle)/\sqrt{2}, \tag{5.5j}$$

$$|2'T_{2gxy}\rangle = (|a_{1g}(1)\rangle|t_{2gxy}(2)\rangle + |t_{2gxy}(1)\rangle|a_{1g}(2)\rangle)/\sqrt{2}, \tag{5.5k}$$

$$|2'T_{2gxz}\rangle = (|a_{1g}(1)\rangle|t_{2gxz}(2)\rangle + |t_{2gxz}(1)\rangle|a_{1g}(2)\rangle)/\sqrt{2}, \tag{5.5l}$$

$$|2'T_{2gyz}\rangle = (|a_{1g}(1)\rangle|t_{2gyz}(2)\rangle + |t_{2gyz}(1)\rangle|a_{1g}(2)\rangle)/\sqrt{2}, \tag{5.5m}$$

where prefixes 0, 1, and 2 indicate excitation energy and the electrons are labeled (1) and (2). The prime in the $2'T_{2g}$ is used to differentiate the doubly excited single electron. Using the character table for the O_h point group, the non-zero one electron matrix elements from the ground state, A_{1g}, to the triply degenerate singly excited state, T_{1u}, are

$$\vec{\mu}_{0x} = \langle t_{1ux}|\hat{\boldsymbol{\mu}}|a_{1g}\rangle = \mu\hat{x}, \tag{5.6a}$$

$$\vec{\mu}_{0y} = \langle t_{1uy}|\hat{\boldsymbol{\mu}}|a_{1g}\rangle = \mu\hat{y}, \tag{5.6b}$$

$$\vec{\mu}_{0z} = \langle t_{1uz}|\hat{\boldsymbol{\mu}}|a_{1g}\rangle = \mu\hat{z}. \tag{5.6c}$$

Each electron from the singly excited t_{1ux}, t_{1uy}, and t_{1uz} states has a dipole allowed transition to two out of the three degenerate T_{2g} doubly excited states (t_{2gxy}, t_{2xz}, and t_{2gyz}). The t_{1ux} and t_{1uy} singly excited states both have dipole allowed transitions to the t_{2gxy} doubly excited state,

$$\vec{\mu}_{2x} = \langle t_{2gxy}|\hat{\boldsymbol{\mu}}|t_{1ux}\rangle = \mu\hat{y}, \tag{5.7a}$$

$$\vec{\mu}_{2y} = \langle t_{2gxy}|\hat{\boldsymbol{\mu}}|t_{1uy}\rangle = \mu\hat{x}. \tag{5.7b}$$

The t_{1ux} and t_{1uz} singly excited states both have dipole allowed transitions to the t_{2gxz} doubly excited state,

$$\vec{\mu}_{2x} = \langle t_{2gxz}|\hat{\boldsymbol{\mu}}|t_{1ux}\rangle = \mu\hat{z}, \tag{5.8a}$$

$$\vec{\mu}_{2z} = \langle t_{2gxz}|\hat{\boldsymbol{\mu}}|t_{1uz}\rangle = \mu\hat{x}. \tag{5.8b}$$

The t_{1uy} and t_{1uz} singly excited states both have dipole allowed transitions to the t_{2gyz} doubly excited state,

$$\vec{\mu}_{2y} = \langle t_{2gyz}|\hat{\boldsymbol{\mu}}|t_{1uy}\rangle = \mu\hat{z}, \tag{5.9a}$$

$$\vec{\mu}_{2z} = \langle t_{2gyz}|\hat{\boldsymbol{\mu}}|t_{1uz}\rangle = \mu\hat{y}. \tag{5.9b}$$

In Eqns. 5.6-5.9, $\hat{\boldsymbol{\mu}}$ is the dipole moment operator, μ is the common magnitude of all of the transition dipole matrix elements, and $\hat{x}$, $\hat{y}$, and $\hat{z}$ are the unit vectors along the molecular x, y, and z axes. The dipole allowed one electron matrix elements are illustrated in Fig. 5.15.

Using Eqn. 5.5 and Eqns. 5.6-5.9, the non-zero two-electron transition dipoles and dipole strengths ($S_{ab} = \vec{\mu}_{ab} \cdot \vec{\mu}_{ab}$) can be calculated:

$$\langle 0A_{1g}|\hat{\boldsymbol{\mu}}|1T_{1ux}\rangle = \sqrt{2}\hat{x} \qquad (S = 2), \tag{5.10a}$$

$$\langle 0A_{1g}|\hat{\boldsymbol{\mu}}|1T_{1uy}\rangle = \sqrt{2}\hat{y} \qquad (S = 2), \tag{5.10b}$$

$$\langle 0A_{1g}|\hat{\boldsymbol{\mu}}|1T_{1uz}\rangle = \sqrt{2}\hat{z} \qquad (S = 2), \tag{5.10c}$$

$$\langle 1T_{1ux}|\hat{\boldsymbol{\mu}}|2A_{1g}\rangle = \frac{\sqrt{2}}{\sqrt{3}}\hat{x} \qquad (S = 2/3), \tag{5.10d}$$

$$\langle 1T_{1uy}|\hat{\boldsymbol{\mu}}|2A_{1g}\rangle = \frac{\sqrt{2}}{\sqrt{3}}\hat{y} \qquad (S = 2/3), \tag{5.10e}$$

$$\langle 1T_{1uz}|\hat{\boldsymbol{\mu}}|2A_{1g}\rangle = \frac{\sqrt{2}}{\sqrt{3}}\hat{z} \qquad (S = 2/3), \tag{5.10f}$$

$$\langle 1T_{1ux}|\hat{\boldsymbol{\mu}}|2E_{g(2z^2-x^2-y^2)}\rangle = \frac{-1}{\sqrt{3}}\hat{x} \qquad (S = 1/3), \tag{5.10g}$$

$$\langle 1T_{1uy}|\hat{\boldsymbol{\mu}}|2E_{g(2z^2-x^2-y^2)}\rangle = \frac{-1}{\sqrt{3}}\hat{y} \qquad (S = 1/3), \tag{5.10h}$$

$$\langle 1T_{1uz}|\hat{\boldsymbol{\mu}}|2E_{g(2z^2-x^2-y^2)}\rangle = \frac{2}{\sqrt{3}}\hat{z} \qquad (S = 4/3), \tag{5.10i}$$

$$\langle 1T_{1ux}|\hat{\boldsymbol{\mu}}|2E_{g(x^2-y^2)}\rangle = \hat{x} \qquad (S = 1), \tag{5.10j}$$

$$\langle 1T_{1uy}|\hat{\boldsymbol{\mu}}|2E_{g(x^2-y^2)}\rangle = -\hat{y} \qquad (S = 1), \tag{5.10k}$$

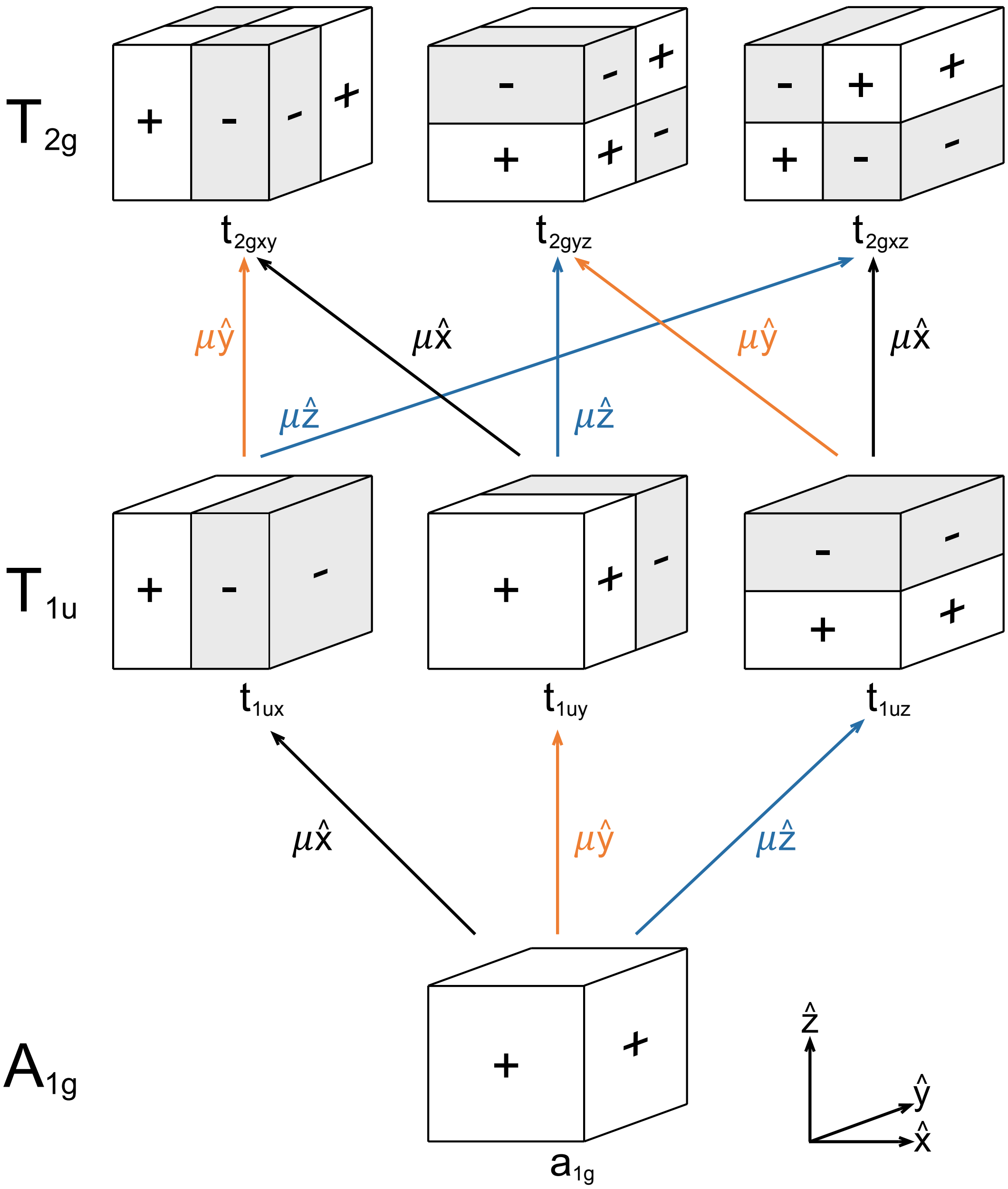

Figure 5.15: Dipole allowed transitions for a particle in a 3D box. The box at the bottom shows the ground state orbital with symmetry a_{1g}. The middle row shows the singly excited state orbitals from left to right, t_{1ux}, t_{1uy}, and t_{1uz}. The top row shows the doubly excited state orbitals from left to right, t_{2gxy}, t_{2gyz}, and t_{2gxz}. The arrows denote the dipole allowed transitions between orbitals along the molecular axes x (black), y (orange), and z (blue).

$$\langle 1T_{1ux}|\hat{\boldsymbol{\mu}}|2T_{2gxy}\rangle = \hat{y} \qquad (S=1), \tag{5.10l}$$

$$\langle 1T_{1uy}|\hat{\boldsymbol{\mu}}|2T_{2gxy}\rangle = \hat{x} \qquad (S=1), \tag{5.10m}$$

$$\langle 1T_{1ux}|\hat{\boldsymbol{\mu}}|2T_{2gxz}\rangle = \hat{z} \qquad (S=1), \tag{5.10n}$$

$$\langle 1T_{1uz}|\hat{\boldsymbol{\mu}}|2T_{2gxz}\rangle = \hat{x} \qquad (S=1), \tag{5.10o}$$

$$\langle 1T_{1uy}|\hat{\boldsymbol{\mu}}|2T_{2gyz}\rangle = \hat{z} \qquad (S=1), \tag{5.10p}$$

$$\langle 1T_{1uz}|\hat{\boldsymbol{\mu}}|2T_{2gyz}\rangle = \hat{y} \qquad (S=1), \tag{5.10q}$$

$$\langle 1T_{1ux}|\hat{\boldsymbol{\mu}}|2'T_{2gxy}\rangle = \hat{y} \qquad (S=1), \tag{5.10r}$$

$$\langle 1T_{1uy}|\hat{\boldsymbol{\mu}}|2'T_{2gxy}\rangle = \hat{x} \qquad (S=1), \tag{5.10s}$$

$$\langle 1T_{1ux}|\hat{\boldsymbol{\mu}}|2'T_{2gxz}\rangle = \hat{z} \qquad (S=1), \tag{5.10t}$$

$$\langle 1T_{1uz}|\hat{\boldsymbol{\mu}}|2'T_{2gxz}\rangle = \hat{x} \qquad (S=1), \tag{5.10u}$$

$$\langle 1T_{1uy}|\hat{\boldsymbol{\mu}}|2'T_{2gyz}\rangle = \hat{z} \qquad (S=1), \tag{5.10v}$$

$$\langle 1T_{1uz}|\hat{\boldsymbol{\mu}}|2'T_{2gyz}\rangle = \hat{y} \qquad (S=1), \tag{5.10w}$$

where common factors of μ are omitted, and S is the corresponding dipole strength.

To calculate the pump-probe signal for delta function pulses, we use diagrammatic representations of the density matrix based on energy ladder subdiagrams [13][48]. The pump-probe signal is detected as the change in transmission of the probe pulse caused by the pump pulse excitation. As a result, the contributions to the pump-probe signal consist of positive ground state bleaching (GSB), positive excited state emission (ESE), and negative excited state absorption (ESA). The corresponding 5-level system energy ladder sub-diagrams with the field interactions are shown in figures 5.16, 5.17, and 5.18 for GSB, ESE, and ESA, respectively. The number in front of the letter d represents the double sided diagram consistent with Fig. 4 in Ref. [13] and the subscript after the letter d is used to differentiate the sub-diagrams. For example, $5d_3$ is a sub-diagram of the D_5 diagram in Fig. 4 from Ref. [13].

The rules for the energy ladder sub-diagrams are explained in Ref. [13]. Briefly, each arrow indicates a perturbation by the electric field with time going from left to right. The solid (dashed) arrow indicates a perturbation acting on the ket (bra) of the density matrix. The wavy line after the three field interactions in all of the sub-diagrams represents the final coherence that generates the fourth field through free induction decay. The pump is treated to second order and represents the first two field interactions, the probe is treated to first order and represents the third field interaction, and the interference between the probe and radiation yields the pump-probe signal. Between the field-matter interactions, the propagation of density matrix element $|m\rangle\langle n|$ is represented as a Green function, $\mathbf{G}_{mn}(t)$, and in the optical Bloch limit,

$$\mathbf{G}_{mn}(t) = \theta(t)\exp\left[-\Gamma_{mn}t\right]\exp\left[-i\omega_{mn}t\right], \tag{5.11}$$

where $\theta(t)$ is the Heaviside step function, Γ_{mn} is the dephasing rate, and ω_{mn} is the Bohr frequency.

As an example, the induced dipole response to unit excitation fields for sub-diagram $5d_3$ (ESA) is expressed as

$$\begin{aligned} R^{5d_3}(t_3,t_2,t_1) = \left(\frac{1}{i\hbar}\right)^3 &\langle(\vec{\mu}_{z2}\cdot\hat{\epsilon}_{pr})(\vec{\mu}_{2x}\cdot\hat{\epsilon}_{pr})(\vec{\mu}_{x0}\cdot\hat{\epsilon}_{pu})(\vec{\mu}_{0z}\cdot\hat{\epsilon}_{pu})\rangle \\ &\times\langle\mathbf{G}_{2z}(t_3)\mathbf{G}_{xz}(t_2)\mathbf{G}_{0z}(t_1)\rho_{00}\rangle, \end{aligned} \tag{5.12}$$

where t_1, t_2, and t_3 are the time periods between the two pump interactions, second pump and first probe interaction, and the probe interaction and free induction decay, respectively. The transition dipoles between the states i and f are labeled as $\vec{\mu}_{if}$ and $\hat{\epsilon}_{pu}$ ($\hat{\epsilon}_{pr}$) is the unit vector for the pump (probe) optical electric field. Time is ordered left to right in the diagram but right to left in the response in Eqn. 5.12. The factor and sign of $\left(\frac{1}{i\hbar}\right)^3$ depends

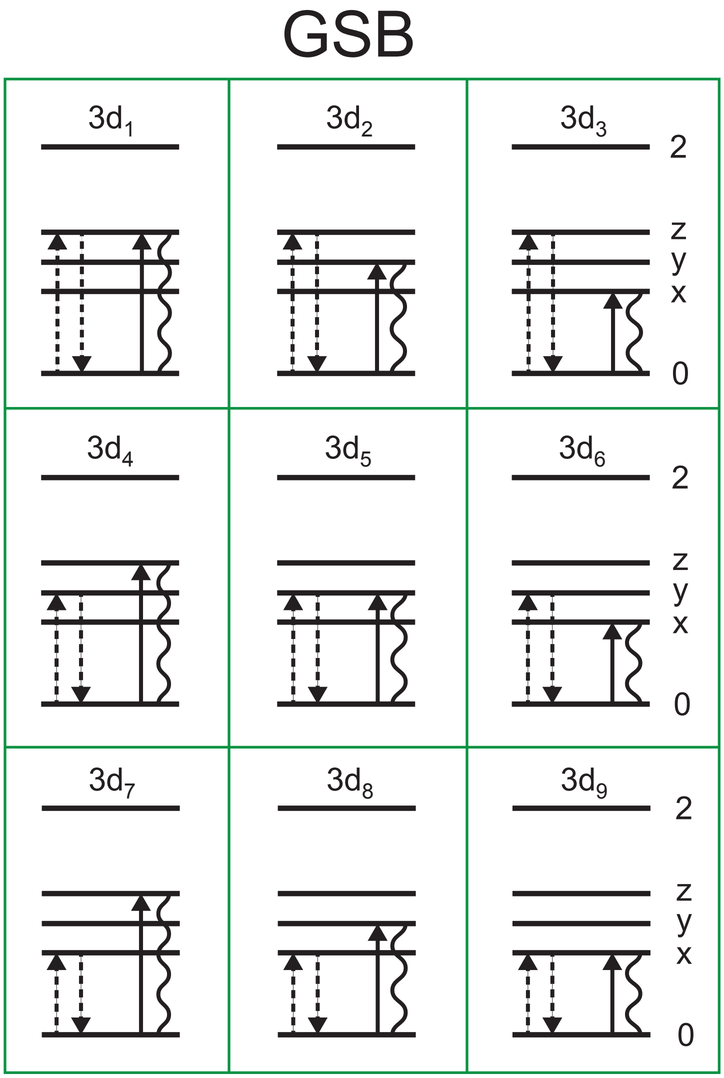

Figure 5.16: Ground state bleach energy ladder sub-diagrams for pump-probe spectroscopy on a five-level system with a nondegenerate ground state (0) and near triply degenerate singly excited states (x,y, and z). The doubly excited states (2) do not participate. The sub-diagrams each represent a term in the third-order density matrix perturbation theory. The solid and dashed arrows correspond to the field interaction on the density matrix on the ket and bra, respectively. Time increase from left to right.

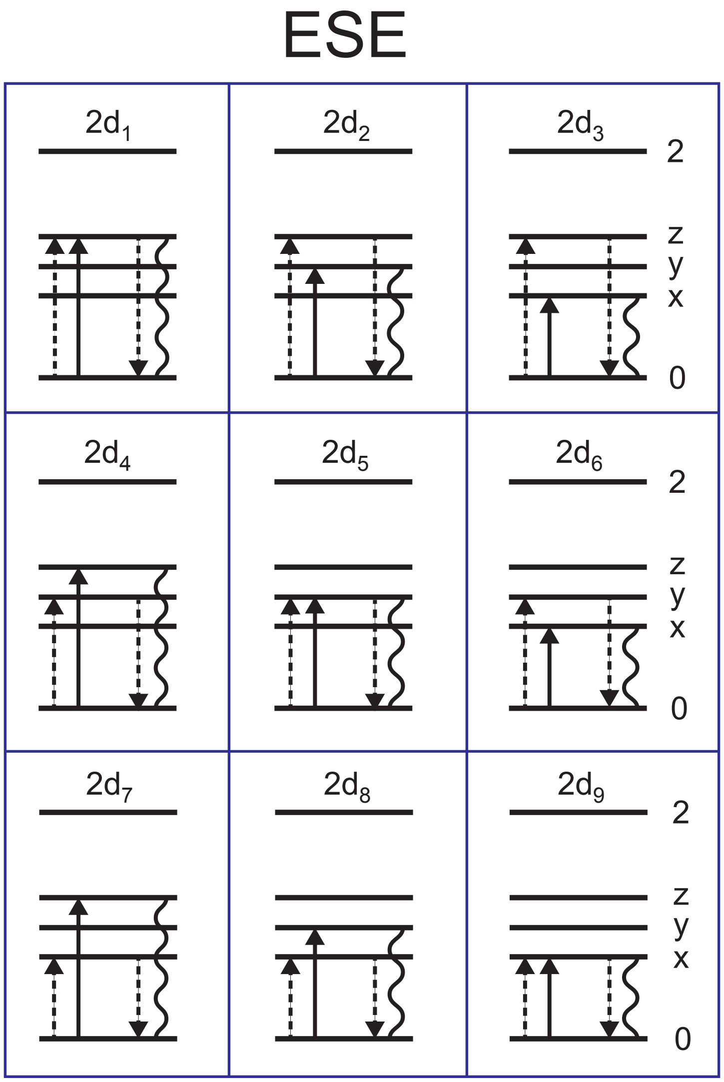

Figure 5.17: Excited state emission energy ladder sub-diagrams for pump-probe spectroscopy on a five-level system with a nondegenerate ground state (0) and near triply degenerate singly excited states (x,y, and z). The doubly excited states (2) do not participate. The sub-diagrams each represent a term in the third-order density matrix perturbation theory. The solid and dashed arrows correspond to the field interaction on the density matrix on the ket and bra, respectively. Time increase from left to right.

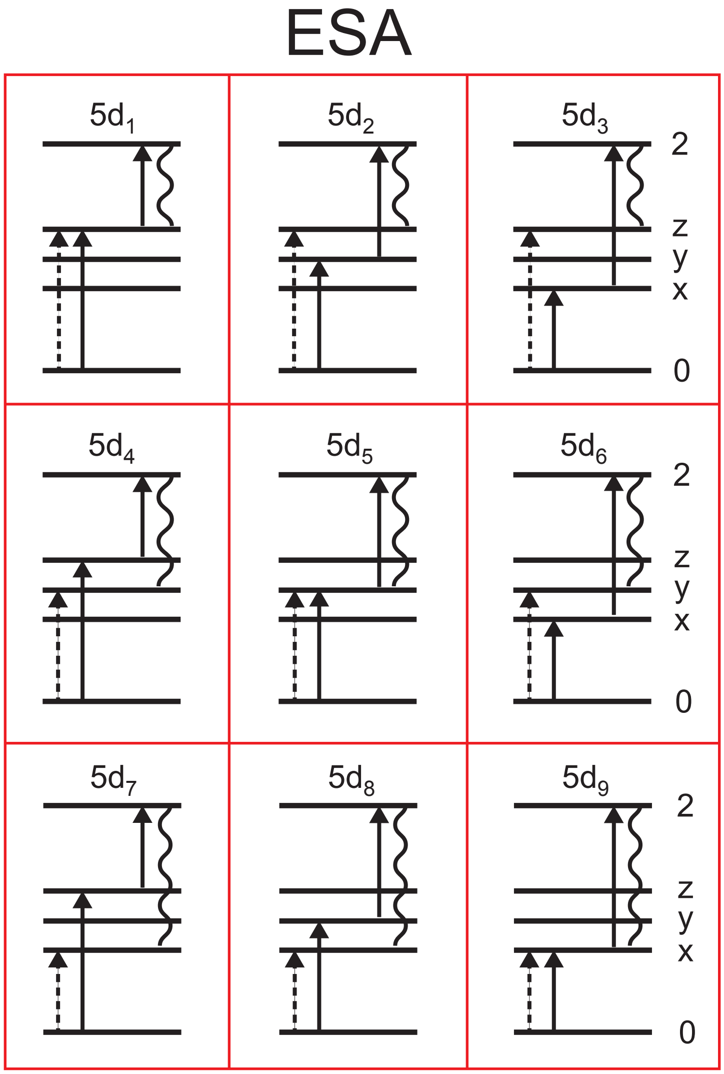

Figure 5.18: Excited state absorption energy ladder sub-diagrams for pump-probe spectroscopy on a five-level system with a nondegenerate ground state (0), nearly degenerate singly excited states (x,y, and z), and a doubly excited state (2). There is a sum over all doubly-excited states (2). Only states (2) for which the third arrow and final wavy line both have non-zero transition dipoles make a finite contribution to the sum. The sub-diagrams each represent a term in the third-order density matrix perturbation theory. The solid and dashed arrows correspond to the field interaction on the density matrix on the ket and bra, respectively. Time increase from left to right.

on the individual field interactions acting either on the bra or ket on the density matrix with an additional factor of i arising from polarization radiation. Using equations 5.10, 5.11, and 5.12, the contribution to the signal for the parallel ($\hat{Z}\hat{Z}\hat{Z}\hat{Z}$) polarization geometry for sub-diagram $5d_3$ with an A_{1g} doubly excited state symmetry can be calculated as (ignoring the common factors of μ that appears for all sub-diagrams)

$$\begin{aligned} S_{ZZZZ}^{5d_3(A_{1g})}(T) &= -\langle(\hat{Z}\cdot\frac{\sqrt{2}}{\sqrt{3}}\hat{z})(\hat{Z}\cdot\frac{\sqrt{2}}{\sqrt{3}}\hat{x})(\hat{Z}\cdot\sqrt{2}\hat{x})(\hat{Z}\cdot\sqrt{2}\hat{z})\rangle \exp\left[i\omega_{xz}T\right]\exp\left[-\Gamma_{xy}T\right] \\ &= -\frac{4}{3}\langle(\hat{Z}\cdot\hat{z})(\hat{Z}\cdot\hat{x})(\hat{Z}\cdot\hat{x})(\hat{Z}\cdot\hat{z})\rangle \exp\left[i\omega_{xz}T\right]\exp\left[-\Gamma_{xy}T\right] \end{aligned} \tag{5.13}$$

where the brackets around $\langle(\hat{Z}\cdot\hat{z})(\hat{Z}\cdot\hat{x})(\hat{Z}\cdot\hat{x})(\hat{Z}\cdot\hat{z})\rangle$ indicate an orientational average. For a randomly oriented, isotropic sample, the average can be calculated using the Euler angles [49] to relate laboratory fixed coordinates (uppercase $\hat{X}$, $\hat{Y}$, and $\hat{Z}$) and molecule fixed coordinates (lowercase $\hat{x}$, $\hat{y}$, and $\hat{z}$). The orientational average are given by Table I of Ref. [49]. The orientational average in Eqn. 5.13 is (1/15). The minus sign on the right of Eqn. 5.13 comes from the $\left(\frac{1}{i\hbar}\right)^3$ factor in Eqn. 5.12 with an additional factor of i from polarization radiation, which connects with our understanding of the signal contributing negatively because it arises from ESA (increase in absorption). With the orientational averaging, Eqn. 5.13 simplifies to

$$\begin{aligned} S_{ZZZZ}^{5d_3(A_{1g})} &= -\left(\frac{4}{3}\right)\left(\frac{1}{15}\right)\exp\left[i\omega_{xz}T\right]\exp\left[-\Gamma_{xy}T\right] \\ &= \left(\frac{-4}{45}\right)\exp\left[i\omega_{xz}T\right]\exp\left[-\Gamma_{xy}T\right]. \end{aligned} \tag{5.14}$$

Similarly, the signal for the perpendicular ($\hat{Y}\hat{Y}\hat{Z}\hat{Z}$) polarization geometry, with an orientation average of $(-1/30)$, for sub-diagram $5d_3$ with an A_{1g} doubly excited state symmetry is

$$\begin{aligned}
S^{5d_3(A_{1g})}_{YYZZ} &= -\frac{4}{3}\langle(\hat{Z}\cdot\hat{z})(\hat{Z}\cdot\hat{x})(\hat{Y}\cdot\hat{x})(\hat{Y}\cdot\hat{z})\rangle \exp\left[i\omega_{xz}T\right]\exp\left[-\Gamma_{xy}T\right] \\
&= -\left(\frac{4}{3}\right)\left(\frac{-1}{30}\right)\exp\left[i\omega_{xz}T\right]\exp\left[-\Gamma_{xy}T\right] \\
&= \left(\frac{2}{45}\right)\exp\left[i\omega_{xz}T\right]\exp\left[-\Gamma_{xy}T\right]. \qquad (5.15)
\end{aligned}$$

For these calculations, we set all $\Gamma_{nm} = 0$ and ignore any population transfer to illustrate a simple model without focusing on the role of dephasing and population exchange [13]. We will keep the signal dependence on T for the calculation and set $T = 0$ at the end to calculate the initial anisotropy.

The total pump-probe signal can be split into GSB, ESE, and ESA for each polarization geometry by adding the contributions from sub-diagrams shown in figures 5.16, 5.17, and 5.18, respectively. For the ESA contribution, we will consider all the possible symmetry allowed wave functions, A_{1g}, E_g, and T_{2g}. The possible wave functions for the doubly excited state are shown in Eqn. 5.5 with the prefix 2 (two).

For the GSB contribution (adding sub-diagrams $3d_1 - 3d_9$), the parallel and perpendicular polarization geometry signals are

$$S^{GSB}_{ZZZZ} = 4, \qquad (5.16a)$$

$$S^{GSB}_{YYZZ} = 4, \qquad (5.16b)$$

showing that the signals are isotropic ($S^{GSB}_{ZZZZ} = S^{GSB}_{YYZZ}$) and time independent because no electronic coherent superposition states are possible. The ESE contributions (adding sub-diagrams $2d_1 - 2d_9$) to the signals are

$$S^{ESE}_{ZZZZ} = 4\cdot\left[(3/5) + (2/15)\cos\left(\omega_{xy}T\right) + (2/15)\cos\left(\omega_{xz}T\right) + (2/15)\cos\left(\omega_{yz}T\right)\right], \qquad (5.17a)$$

$$S^{ESE}_{YYZZ} = 4 \cdot [(1/5) - (1/15)\cos(\omega_{xy}T) - (1/15)\cos(\omega_{xz}T) - (1/15)\cos(\omega_{yz}T)], \qquad (5.17b)$$

and can be reduced to a zero waiting time ($T = 0$) signal strength of $S^{ESE}_{ZZZZ} = 4$ and $S^{ESE}_{YYZZ} = 0$. The ESE signal at $T = 0$ is anisotropic because the excited electron is perfectly aligned to the pump laser and can only emit with the same polarization it was excited with. When the parallel ($\hat{Z}\hat{Z}\hat{Z}\hat{Z}$) and both perpendicular signals ($\hat{Y}\hat{Y}\hat{Z}\hat{Z}$ and $\hat{X}\hat{X}\hat{Z}\hat{Z}$) are added together, the total GSB signal (12) is three times stronger than the ESE signal because x, y, and z polarized transitions have all been bleached by depopulation of the ground state, but only the one actually excited can emit. The ESA contributions for A_{1g} symmetry doubly excited state are

$$S^{ESA(2A_{1g})}_{ZZZZ} = -(4/5) - (8/45)\cos(\omega_{xy}T) - (8/45)\cos(\omega_{xz}T) - (8/45)\cos(\omega_{yz}T), \qquad (5.18a)$$

$$S^{ESA(2A_{1g})}_{YYZZ} = -(4/15) + (4/45)\cos(\omega_{xy}T) + (4/45)\cos(\omega_{xz}T) + (4/45)\cos(\omega_{yz}T). \qquad (5.18b)$$

The sum of parallel and both perpendicular signals at $T = 0$ is -4/3, which is 1/3 the total ESE signal because these ESA transition dipoles are $1/\sqrt{3}$ weaker than the ESE transition dipoles. For the doubly degenerate E_g symmetry doubly excited state, the two component basis states in Eqns. 5.5f and 5.5g give

$$S^{ESA(2E_{g(2z^2-x^2-y^2)})}_{ZZZZ} = -(4/5) - (4/45)\cos(\omega_{xy}T) + (8/45)\cos(\omega_{xz}T) + (8/45)\cos(\omega_{yz}T), \qquad (5.19a)$$

$$S^{ESA(2E_{g(2z^2-x^2-y^2)})}_{YYZZ} = -(4/15) + (2/45)\cos(\omega_{xy}T) - (4/45)\cos(\omega_{xz}T) - (4/45)\cos(\omega_{yz}T), \qquad (5.19b)$$

$$S^{ESA(2E_{g(x^2-y^2)})}_{ZZZZ} = -(4/5) + (4/15)\cos(\omega_{xy}T), \qquad (5.19c)$$

$$S^{ESA(2E_{g(x^2-y^2)})}_{YYZZ} = -(4/15) - (2/15)\cos(\omega_{xy}T), \qquad (5.19d)$$

where the labels $(2z^2 - x^2 - y^2)$ and $(x^2 - y^2)$ are used to differentiate the degeneracy. Only the sum over $2E_{g(2z^2-x^2-y^2)}$ and $2E_{g(x^2-y^2)}$ is significant,

$$S_{ZZZZ}^{ESA(2E_g)} = -(8/5) + (8/45)\cos(\omega_{xy}T) + (8/45)\cos(\omega_{xz}T) + (8/45)\cos(\omega_{yz}T), \quad (5.20a)$$

$$S_{YYZZ}^{ESA(2E_g)} = -(8/15) - (4/15)\cos(\omega_{xy}T) - (4/45)\cos(\omega_{xz}T) - (4/45)\cos(\omega_{yz}T). \quad (5.20b)$$

At $T = 0$, the total (all polarizations) contribution from ESA to the E_g state is -8/3, twice that of ESA to A_{1g} because of the two-fold degeneracy. For the triply degenerate T_{2g} symmetry doubly excited state, the ESA contributions are

$$S_{ZZZZ}^{ESA(2T_{2gxy})} = -(4/15) - (4/15)\cos(\omega_{xy}T), \quad (5.21a)$$

$$S_{YYZZ}^{ESA(2T_{2gxy})} = -(8/15) + (2/15)\cos(\omega_{xy}T), \quad (5.21b)$$

$$S_{ZZZZ}^{ESA(2T_{2gxz})} = -(4/15) - (4/15)\cos(\omega_{xz}T), \quad (5.21c)$$

$$S_{YYZZ}^{ESA(2T_{2gxz})} = -(8/15) + (2/15)\cos(\omega_{xz}T), \quad (5.21d)$$

$$S_{ZZZZ}^{ESA(2T_{2gyz})} = -(4/15) - (4/15)\cos(\omega_{yz}T), \quad (5.21e)$$

$$S_{YYZZ}^{ESA(2T_{2gyz})} = -(8/15) + (2/15)\cos(\omega_{yz}T), \quad (5.21f)$$

where as in Eqn. 5.5, (xy), (xz), and (yz) are used to differentiate the degeneracy. Again, only the sum over (xy), (xz), and (yz) is significant,

$$S_{ZZZZ}^{ESA(2T_{2g})} = -(4/5) - (4/15)\cos(\omega_{xy}T) - (4/15)\cos(\omega_{xz}T) - (4/15)\cos(\omega_{yz}T), \quad (5.22a)$$

$$S_{YYZZ}^{ESA(2T_{2g})} = -(8/5) + (2/15)\cos(\omega_{xy}T) + (2/15)\cos(\omega_{xz}T) + (2/15)\cos(\omega_{yz}T). \quad (5.22b)$$

At $T = 0$, the total (all polarizations) contribution from ESA to the T_{2g} state is -4, triple that of ESA to A_{1g} because of the three-fold degeneracy.

The anisotropies at $T = 0$ with the corresponding isotropic signal strength for all of the contributions calculated using Eqn. 5.1 can be organized as:

$$r_{GSB}(T=0) = 0 \qquad (S=4), \tag{5.23a}$$

$$r_{ESE}(T=0) = 1 \qquad (S=4/3), \tag{5.23b}$$

$$r_{ESA}^{2A_{1g}}(T=0) = 1 \qquad (S=-4/9), \tag{5.23c}$$

$$r_{ESA}^{2E_g}(T=0) = 1/10 \qquad (S=-8/9), \tag{5.23d}$$

$$r_{ESA}^{2T_{2g}}(T=0) = 1/10 \qquad (S=-4/3), \tag{5.23e}$$

$$r_{ESA}^{2'T_{2g}}(T=0) = 1/10 \qquad (S=-4/3), \tag{5.23f}$$

where the prime denotes the doubly excited single electron with electron configuration $(a_{1g})(t_{2g})$. Using equation 5.2, the total anisotropy at $T = 0$ is

$$\begin{aligned} r(T=0) &= \frac{4(0) + \left(\frac{4}{3}\right)(1) + \left(-\frac{4}{9}\right)(1) + \left(-\frac{8}{9}\right)\left(\frac{1}{10}\right) + \left(-\frac{4}{3}\right)\left(\frac{1}{10}\right) + \left(-\frac{4}{3}\right)\left(\frac{1}{10}\right)}{4 + \left(\frac{4}{3}\right) + \left(-\frac{4}{9}\right) + \left(-\frac{8}{9}\right) + \left(-\frac{4}{3}\right) + \left(-\frac{4}{3}\right)} \\ &= 2/5. \end{aligned} \tag{5.24}$$

The crucial result is that when coherence and both one-electron and two-electron doubly-excited states are considered, the initial anisotropy is 2/5, the standard dipole result. A key question about QDs concerns the one-electron doubly excited states reached by excited state absorption - these hot single exciton states may play a key role in the initial anisotropy. For example, if we remove the doubly excited single electron contribution in Eqn. 5.24, the initial anisotropy is lowered,

$$\begin{aligned} r(T=0) &= \frac{4(0) + \left(\frac{4}{3}\right)(1) + \left(-\frac{4}{9}\right)(1) + \left(-\frac{8}{9}\right)\left(\frac{1}{10}\right) + \left(-\frac{4}{3}\right)\left(\frac{1}{10}\right)}{4 + \left(\frac{4}{3}\right) + \left(-\frac{4}{9}\right) + \left(-\frac{8}{9}\right) + \left(-\frac{4}{3}\right)} \\ &= 1/4. \end{aligned} \tag{5.25}$$

This yields a closer agreement to the experimental initial anisotropy but still disagrees. For this reason, we extend our calculation using an effective mass approximation at the degenerate L-points of the first Brillioun zone.

5.3.2 Initial anisotropy using an effective mass approximation

A standard approach to the electronic structure of PbS QDs uses an effective mass approximation [50][51][52]. In this model, the transition dipole vectors are aligned along the four degenerate L-points of the first Brillouin zone. This alignment can be deduced by symmetry. The crystal structure has threefold symmetry around the (1,1,1) axis, so a non-degenerate transition must have a transition dipole that points along the (1,1,1) threefold symmetry axis.

The transition dipoles between the valence and conduction bands at the four-fold degenerate L-points are expressed as:

$$\langle V_{(+++)}|\hat{\boldsymbol{\mu}}|C_{(+++)}\rangle = \hat{\boldsymbol{\mu}}_{(+++)} = \mu(+++)/\sqrt{3}, \tag{5.26a}$$

$$\langle V_{(+-+)}|\hat{\boldsymbol{\mu}}|C_{(+-+)}\rangle = \hat{\boldsymbol{\mu}}_{(+-+)} = \mu(+-+)/\sqrt{3}, \tag{5.26b}$$

$$\langle V_{(-++)}|\hat{\boldsymbol{\mu}}|C_{(-++)}\rangle = \hat{\boldsymbol{\mu}}_{(-++)} = \mu(-++)/\sqrt{3}, \tag{5.26c}$$

$$\langle V_{(--+)}|\hat{\boldsymbol{\mu}}|C_{(--+)}\rangle = \hat{\boldsymbol{\mu}}_{(--+)} = \mu(--+)/\sqrt{3}, \tag{5.26d}$$

where V and C are the valence and conduction bands, respectively, and the three symbols inside the parenthesis denote the vector from the Miller indices in reciprocal space ($(+++)$ is the Cartesian vector in the (+1,+1,+1) direction, $(+-+)$ is the Cartesian vector in the (+1,-1,+1) direction, and etc.). Because the angles between all four degenerate L-points are identical, we can generate a table for all of the orientational averages we will need in this section using Eqn. 10 from Ref. [49]. Table 5.1 lists the orientational averages with the first column showing the molecular frame transition dipoles from the L-point valleys.

Table 5.1: Orientational averages for parallel and perpendicular signals for the degenerate L-points

	$(\hat{Z}\hat{Z}\hat{Z}\hat{Z})$ $(\parallel)$	$(\hat{Y}\hat{Y}\hat{Z}\hat{Z})$ $(\perp)$
$(+++)(+++)(+++)(+++)$	(1/5)	(1/15)
$(+++)(+++)(+-+)(+-+)$	(11/135)	(17/135)
$(+++)(+-+)(+++)(+-+)$	(11/135)	(−3/135)

These orientational averages can also be calculated using the projection of the vectors onto Cartesian coordinates. If we align the $(+++)$ vector with the z-axis, another vector of the tetrahedral structure with identical angles can be expressed in terms of its projection onto the $\hat{z}$ and $\hat{x}$ coordinates. For example, $(+-+)$ can be expressed as $\left(-\frac{1}{3}\hat{z}+\frac{2\sqrt{2}}{3}\hat{x}\right)$. Thus, we can express the molecular frame $(+++)(+++)(+-+)(+-+)$ in Cartesian coordinates

$$\begin{aligned}(+++)(+++)(+-+)(+-+) &= \hat{z}\hat{z}\left(-\frac{1}{3}\hat{z}+\frac{2\sqrt{2}}{3}\hat{x}\right)\left(-\frac{1}{3}\hat{z}+\frac{2\sqrt{2}}{3}\hat{x}\right)\\ &= \frac{1}{9}\hat{z}\hat{z}\hat{z}\hat{z}+\frac{8}{9}\hat{z}\hat{z}\hat{x}\hat{x},\end{aligned} \tag{5.27}$$

and using Table I in Ref. [49], we can calculate the orientational average for the parallel signal for $\langle\hat{Z}(+++)\hat{Z}(+++)\hat{Z}(+-+)\hat{Z}(+-+)\rangle$ is

$$\begin{aligned}\langle\hat{Z}(+++)\hat{Z}(+++)\hat{Z}(+-+)\hat{Z}(+-+)\rangle &= \frac{1}{9}\langle\hat{Z}\hat{z}\hat{Z}\hat{z}\hat{Z}\hat{z}\hat{Z}\hat{z}\rangle+\frac{8}{9}\langle\hat{Z}\hat{z}\hat{Z}\hat{z}\hat{Z}\hat{x}\hat{Z}\hat{x}\rangle\\ &= \frac{1}{9}\left(\frac{1}{5}\right)+\frac{8}{9}\left(\frac{1}{15}\right)\\ &= \frac{11}{135}.\end{aligned} \tag{5.28}$$

Ground state bleach contribution

To calculate the GSB contribution to the pump-probe signal, we can refer to Fig. 5.16 but with a 4-fold degenerate singly excited state representing the 4 valleys. As shown in the sub-diagrams in Fig. 5.16, the second field interaction is dictated by the first field interaction, so we just permute the third (and fourth) field interaction over all of the 4 valleys. Because there are 4 valleys in the valence band and 4 valleys in the conduction band, there is a total of 16 sub-diagrams: 4 sub-diagrams with the same dipole-field interaction from the first and third field interactions (similar to diagrams $3d_1$, $3d_5$, and $3d_9$ in Fig. 5.16) and 12 sub-diagrams with different dipole-field interactions from the first and third field interactions (excluding diagrams similar to $3d_1$, $3d_5$, and $3d_9$ in Fig. 5.16). However, we must also consider spin, which leads to sub-sub-diagrams; for each sub-diagram, there are 4 sub-sub-diagrams. As an example, Fig. 5.19 shows the 4 sub-sub-diagrams for the sub-diagram similar to $3d_1$ in 5.16. As in the sub-diagram $3d_1$, the GSB contribution is from the same dipole-field interaction from the first and third field interactions, that is, interacting with the same valley. The sub-sub-diagrams accounts for all the permutation for each electron spin, α and β.

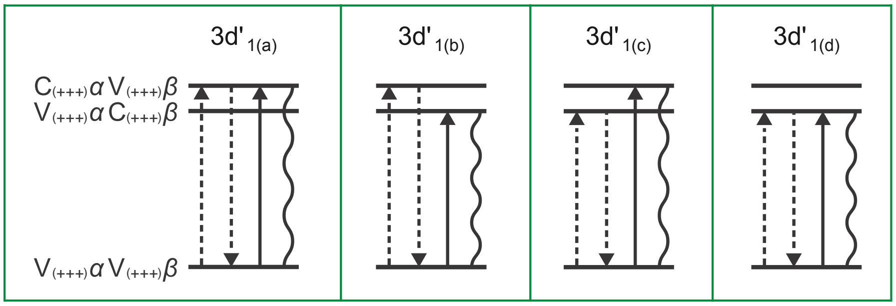

Figure 5.19: GSB sub-sub-diagrams for the $3d_1$ sub-diagram (same valley). The labeling of the sub-sub-diagrams ($3d'_{1(a)}$, $3d'_{1(b)}$, $3d'_{1(c)}$, and $3d'_{1(d)}$) are used to stay consistent with the sub-diagram $3d_1$ in Fig. 5.16. The prime is used to differentiate the sub-diagrams because they are not the same as in Fig. 5.16.

Figure 5.20 shows the 4 sub-sub-diagrams for the GSB sub-diagram similar to $3d_4$ in Fig. 5.16. As in $3d_4$, the GSB contribution is from different dipole-field interactions from the first and third field interactions, that is, interacting with different valleys. Again, there is a permutation for each electron spin and similar to Fig. 5.19 but with different valleys.

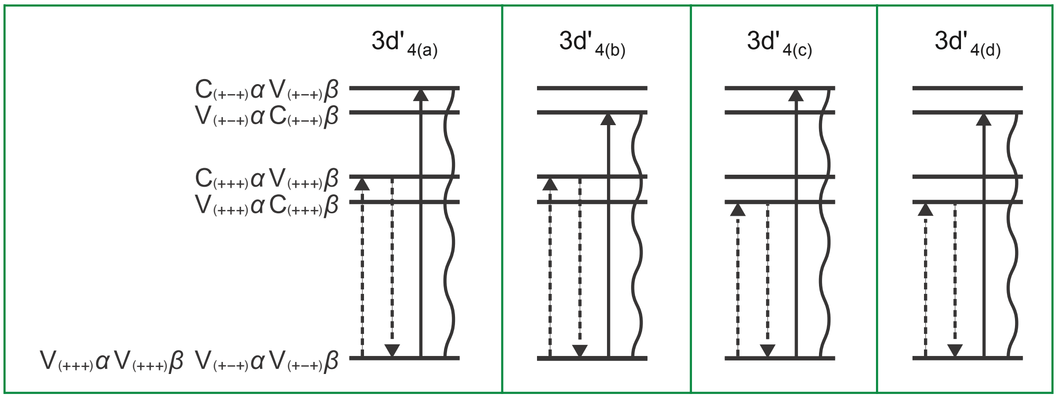

Figure 5.20: GSB sub-sub-diagrams for the $3d_4$ sub-diagram (different valleys).

For the 4 sub-diagrams from the (first and third) dipole-field interactions with the same valley, the orientational average (Table 5.1) for parallel ($\hat{Z}\hat{Z}\hat{Z}\hat{Z}$) and perpendicular ($\hat{Y}\hat{Y}\hat{Z}\hat{Z}$) polarization geometries are

$$\langle \hat{Z}(+++)\hat{Z}(+++)\hat{Z}(+++)\hat{Z}(+++)\rangle = (1/5), \tag{5.29a}$$

$$\langle \hat{Y}(+++)\hat{Y}(+++)\hat{Z}(+++)\hat{Z}(+++)\rangle = (1/15). \tag{5.29b}$$

The 12 sub-diagrams from the (first and third) dipole-field interactions with different valleys has orientational averages for parallel and perpendicular

$$\langle \hat{Z}(+++)\hat{Z}(+++)\hat{Z}(+-+)\hat{Z}(+-+)\rangle = (11/135), \tag{5.30a}$$

$$\langle \hat{Y}(+++)\hat{Y}(+++)\hat{Z}(+-+)\hat{Z}(+-+)\rangle = (17/135). \tag{5.30b}$$

The total GSB parallel signal consists of the following contributions: 4 sub-diagrams with the same valley, each with 4 sub-sub-diagrams with an orientational average of (1/5); 12 sub-diagrams with different valleys, each with 4 sub-sub-diagrams with an orientational average of (11/135). The total GSB perpendicular signal consists of the following contributions: 4 sub-diagrams with the same valley, each with 4 sub-sub-diagrams with an orientational average of (1/15); 12 sub-diagrams with different valleys, each with 4 sub-sub-diagrams with an orientational average of (17/135). Thus, the total GSB contribution to the signal can be calculated,

$$S^{GSB}_{ZZZZ} = 4 \cdot \left[4 \cdot \left(\frac{1}{5}\right) + 12 \cdot \left(\frac{11}{135}\right)\right] = \frac{64}{9}, \tag{5.31a}$$

$$S^{GSB}_{YYZZ} = 4 \cdot \left[4 \cdot \left(\frac{1}{15}\right) + 12 \cdot \left(\frac{17}{135}\right)\right] = \frac{64}{9}. \tag{5.31b}$$

When the parallel ($\hat{Z}\hat{Z}\hat{Z}\hat{Z}$) and both perpendicular signals ($\hat{Y}\hat{Y}\hat{Z}\hat{Z}$ and $\hat{X}\hat{X}\hat{Z}\hat{Z}$) are added together, the total GSB signal strength is (64/3) because of the 64 possible states including spin and the (1/3) factor from the $cos^2(\theta)$ excitation probability distribution. Similar to the particle in a 3D box in the previous section, the anisotropy for GSB is zero; the signal is isotropic.

Excited State Emission Signal

The ESE contribution to the pump-probe signal is similar to the GSB signal but the dipole moments are re-arranged leading to different orientational averages. Referring to Fig. 5.17, the third field interaction is dictated by the first field interaction and the fourth field interaction is dictated by the second field interaction. Again, there is a total of 16 sub-diagrams: 4 sub-diagrams with the first and second dipole-field interactions with the same valley (similar to figures $2d_1$, $2d_5$, and $2d_9$ in Fig. 5.17) and 12 sub-diagrams with the first and second dipole-field interactions with different valleys. Accounting for spin, each sub-diagram also has 4 sub-sub-diagrams.

For the 4 sub-diagrams from the (first and second) dipole-field interactions with the same valley, the orientational averages for parallel and perpendicular are

$$\langle \hat{Z}(+++)\hat{Z}(+++)\hat{Z}(+++)\hat{Z}(+++)\rangle = (1/5), \tag{5.32a}$$

$$\langle \hat{Y}(+++)\hat{Y}(+++)\hat{Z}(+++)\hat{Z}(+++)\rangle = (1/15). \tag{5.32b}$$

The 12 sub-diagrams from the (first and second) dipole-field interactions with different valleys, have orientational average for parallel and perpendicular

$$\langle \hat{Z}(+++)\hat{Z}(+-+)\hat{Z}(+++)\hat{Z}(+-+)\rangle = (11/135), \tag{5.33a}$$

$$\langle \hat{Y}(+++)\hat{Y}(+-+)\hat{Z}(+++)\hat{Z}(+-+)\rangle = (-3/135). \tag{5.33b}$$

The total ESE parallel signal consists of the following contributions: 4 sub-diagrams with the same valley, each with 4 sub-sub-diagrams with an orientational average of (1/5); 12 sub-diagrams with different valleys, each with 4 sub-sub-diagrams with an orientational average of (11/15). The total ESE perpendicular signal consists of the following contributions: 4 sub-diagrams with the same valley, each with 4 sub-sub-diagrams with an orientational average of (1/15); 12 sub-diagrams with different valleys, each with 4 sub-sub-diagrams with an orientational average of (-3/135). The parallel and perpendicular ESE signal contribution is

$$S_{ZZZZ}^{ESE} = 4 \cdot \left[4 \cdot \left(\frac{1}{5} \right) + 12 \cdot \left(\frac{11}{135} \right) \right] = \frac{64}{9}, \tag{5.34a}$$

$$S_{YYZZ}^{ESE} = 4 \cdot \left[4 \cdot \left(\frac{1}{15} \right) + 12 \cdot \left(\frac{-3}{135} \right) \right] = 0. \tag{5.34b}$$

The total (all polarizations) contribution from ESE is (64/9), which is 1/3 the strength of GSB. As for the particle in a 3D box, the emission is perfectly aligned to the excitation pulse, with an anisotropy of 1.

Excited State Absorption Signal

For the doubly excited states with 4 L-points, a total of 10 doubly excited state electron configurations can be optically excited: 4 configurations with the same valley (Eqns. 5.35a, 5.35e, 5.35h, and 5.35j) and 6 configurations with two different valleys (Eqns. 5.35b, 5.35c, 5.35d, 5.35f, 5.35g, 5.35i). The doubly excited states with the same valley will be labeled the doubly occupied valleys (DOV) and the doubly excited states with two different valleys will be labeled the two singly occupied valleys (TSOV).

$$(+\,+\,+)(+\,+\,+), \tag{5.35a}$$

$$(+\,+\,+)(+\,-\,+), \tag{5.35b}$$

$$(+\,+\,+)(-\,+\,+), \tag{5.35c}$$

$$(+\,+\,+)(-\,-\,+), \tag{5.35d}$$

$$(+\,-\,+)(+\,-\,+), \tag{5.35e}$$

$$(+\,-\,+)(-\,+\,+), \tag{5.35f}$$

$$(+\,-\,+)(-\,-\,+), \tag{5.35g}$$

$$(-\,+\,+)(-\,+\,+), \tag{5.35h}$$

$$(-\,+\,+)(-\,-\,+), \tag{5.35i}$$

$$(-\,-\,+)(-\,-\,+). \tag{5.35j}$$

For the DOV doubly excited states, the transition dipole moments are all the same and there is no coherence between valleys after the second dipole-field interaction. These sub-diagrams are similar to $5d_1$, $5d_5$, and $5d_9$ in Fig. 5.18 and the doubly excited configuration has only one spin state. Accounting for spin, Slater determinants should be used to form sub-sub-diagrams for each type of sub-diagram. For doubly occupied valleys, there is only one Slater determinant for the doubly excited configuration, and there are two Slater determinants for each singly excited configuration. As a result, there are 4 non-zero sub-sub-diagrams for each sub-diagram. Fig. 5.21 shows the 4 sub-sub-diagrams for the DOV sub-diagram similar to $5d_1$.

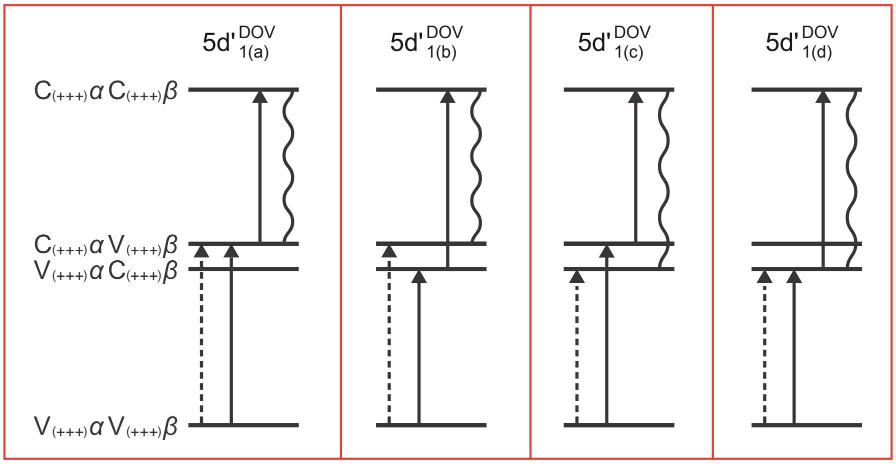

Figure 5.21: ESA sub-sub-diagrams for the $5d_1$ sub-diagram for the DOV doubly excited states. The unoccupied valence band orbital is not labeled in the doubly excited state. For the DOV doubly excited state, there is only one non-zero Slater determinant.

In summary, there are 4 DOV sub-diagrams (Eqns. 5.35a, 5.35e, 5.35h, and 5.35j), each with 4 sub-sub-diagrams. Because all 4 dipole-field interactions are with the same valley, the orientational averages for the parallel and perpendicular signal for each sub-sub-diagram is

$$\langle \hat{Z}(+++)\hat{Z}(+++)\hat{Z}(+++)\hat{Z}(+++)\rangle = (1/5), \tag{5.36a}$$

$$\langle \hat{Y}(+++)\hat{Y}(+++)\hat{Z}(+++)\hat{Z}(+++)\rangle = (1/15). \tag{5.36b}$$

As a result, the ESA contribution from the DOV is

$$S^{ESA(DOV)}_{ZZZZ} = -16 \cdot \left(\frac{1}{5}\right) = -16/5, \tag{5.37a}$$

$$S_{YYZZ}^{ESA(DOV)} = -16 \cdot \left(\frac{1}{15}\right) = -16/15. \tag{5.37b}$$

The signal is negative because ESA is an increase in absorption, lowering the overall pump-probe signal.

For two singly occupied valleys (TSOV), there are 2 sub-diagrams that populate one valley and 2 sub-diagrams that coherently excite two different valleys. These 4 sub-diagrams are similar to sub-diagrams $5d_1$, $5d_2$, $5d_4$, and $5d_5$ in Fig. 5.18, and are also shown in Fig. 5.22 with labels for the doubly excited states. The doubly excited states have two electron-hole pairs from different valleys.

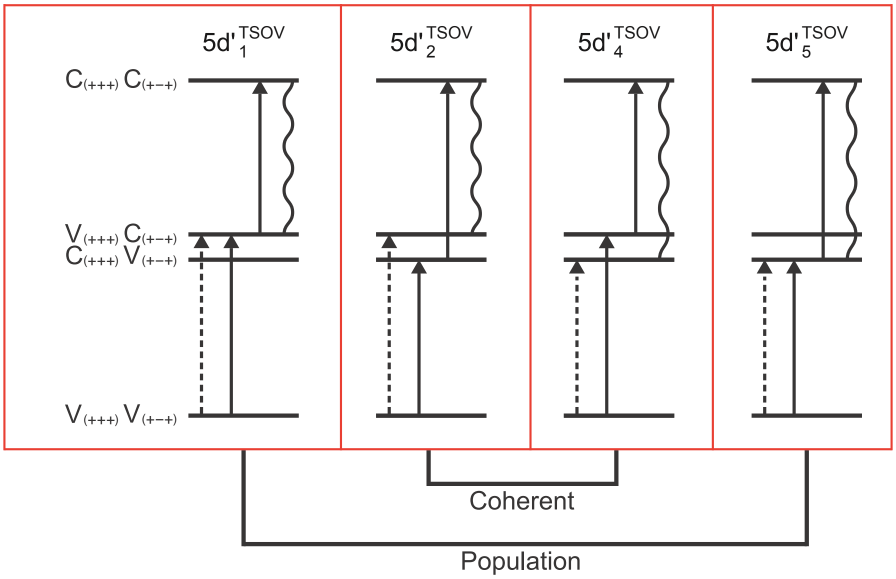

Figure 5.22: ESA sub-diagrams for TSOV doubly excited states. These sub-diagrams are labeled to stay consistent with sub-diagrams in Fig. 5.18.

Again, accounting for spin for the TSOV diagrams, the no spin-flip optical selection rule allows only 4 doubly excited Slater determinants to be reached. Graphing the selection rules for these states, it can be shown that each of the 4 doubly excited Slater determinants leads to one sub-sub-diagram for each ESA sub-diagram, so that there are 4 non-zero sub-sub-diagrams for each of the ESA sub-diagrams. As an example, Fig. 5.23 shows the 4 sub-sub-diagrams for sub-diagram $5d_1'^{TSOV}$ in Fig. 5.22 with the allowed transitions. For the sub-sub-diagrams for $5d_1'^{TSOV}$, there are two non-zero Slater determinants for each populated singly excited state because the second electron-hole pair is being created from a different fully occupied valence band orbital with both electron spins.

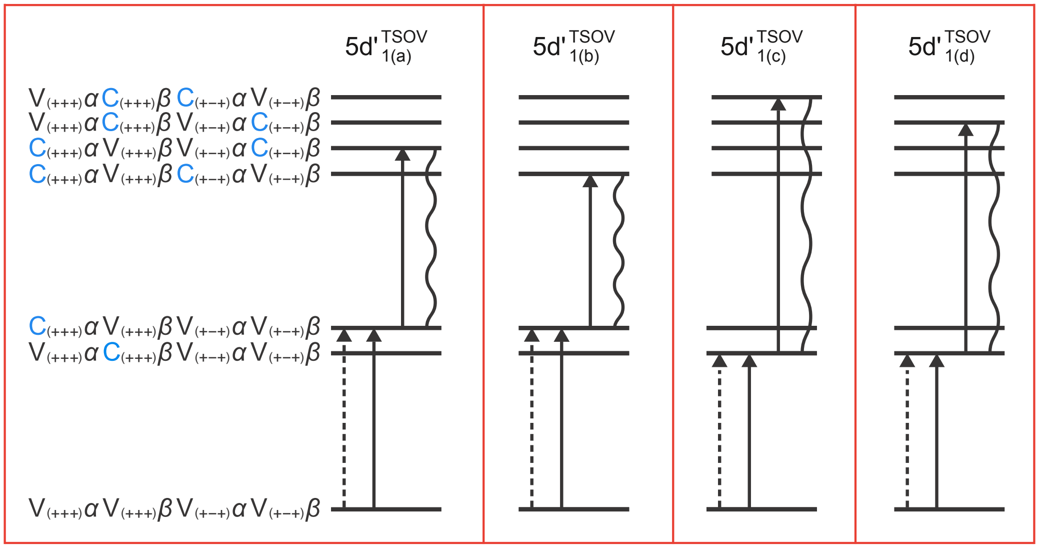

Figure 5.23: ESA sub-sub-diagrams for the ESA sub-diagram $5d_1'$ in Fig. 5.22 that populate one valley.

For the sub-diagrams that populate one valley, the first and second dipole-field interactions are with the same valley and the third and fourth dipole-field interactions are with a different valley. Thus, the orientational averages (Table 5.1) for sub-diagrams $5d_1'^{TSOV}$ and $5d_5'^{TSOV}$ in Fig. 5.22 for the parallel and perpendicular signals are

$$\langle \hat{Z}(+++)\hat{Z}(+++)\hat{Z}(+-+)\hat{Z}(+-+)\rangle = (11/135), \tag{5.38a}$$

$$\langle \hat{Y}(+++)\hat{Y}(+++)\hat{Z}(+-+)\hat{Z}(+-+)\rangle = (17/135). \tag{5.38b}$$

Because there are 6 TSOV configurations, each with 2 population (Fig. 5.22) sub-diagrams and each sub-diagram has 4 sub-sub-diagrams (Fig. 5.23), the parallel and perpendicular signals are

$$S_{ZZZZ}^{ESA(TSOV-pop)} = -6 \cdot 2 \cdot 4 \cdot \left(\frac{11}{135}\right) = -176/45, \tag{5.39a}$$

$$S_{YYZZ}^{ESA(TSOV-pop)} = -6 \cdot 2 \cdot 4 \cdot \left(\frac{17}{135}\right) = -272/45. \tag{5.39b}$$

The label $TSOV-pop$ in the superscript is to differentiate the population sub-diagrams in Fig. 5.22.

Similarly for the coherent sub-diagrams ($5d_2'^{TSOV}$ and $5d_4'^{TSOV}$ in Fig. 5.22), each sub-diagram has 4 sub-sub-diagrams because the first dipole-field interaction can excite either spin from one valley and the second dipole-field interaction can excite either spin from a different valley. Figure 5.24 shows the 4 sub-sub-diagrams for sub-diagram $5d_4'^{TSOV}$ in Fig. 5.22.

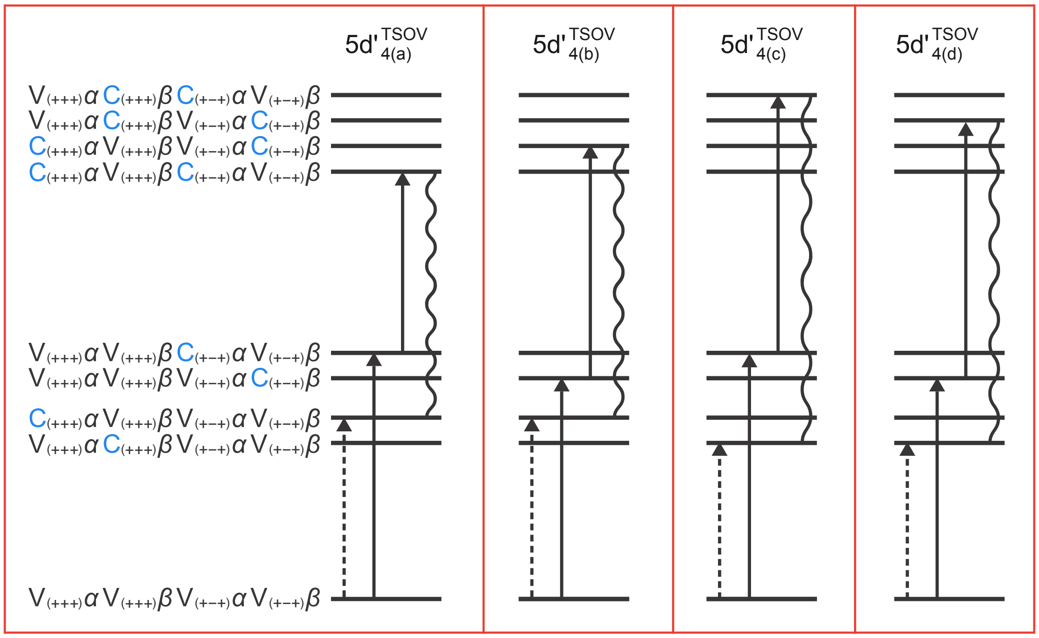

Figure 5.24: ESA sub-sub-diagrams for the ESA sub-diagram $5d_4'^{TSOV}$ in Fig. 5.22. The valence orbitals are not labeled in the doubly excited states.

For the coherent sub-diagrams, the first and third dipole-field interactions are with the same valley and the second and fourth dipole-field interactions are with a different valley. Thus, the orientational averages for each sub-sub-diagram for the parallel and perpendicular signals are

$$\langle \hat{Z}(+++)\hat{Z}(+-+)\hat{Z}(+++)\hat{Z}(+-+)\rangle = (11/135), \tag{5.40a}$$

$$\langle \hat{Y}(+++)\hat{Y}(+-+)\hat{Z}(+++)\hat{Z}(+-+)\rangle = (-3/135). \tag{5.40b}$$

There are 6 TSOV configurations, each with 2 coherent sub-diagrams (Fig. 5.22) and each sub-diagram has 4 sub-sub-diagrams (Fig. 5.24). As a result, the parallel and perpendicular signals are

$$S_{ZZZZ}^{ESA(TSOV-coh)} = -6 \cdot 2 \cdot 4 \cdot \left(\frac{11}{135}\right) = -176/135, \tag{5.41a}$$

$$S_{YYZZ}^{ESA(TSOV-coh)} = -6 \cdot 2 \cdot 4 \cdot \left(\frac{-3}{135}\right) = +16/15. \tag{5.41b}$$

The label $TSOV - coh$ in the superscript is used to differentiate the coherent sub-diagrams in Fig. 5.22.

The total ESA contribution obtained by summing Eqns. 5.37, 5.39, and 5.41 is

$$
\begin{aligned}
S_{ZZZZ}^{ESA} &= S_{ZZZZ}^{ESA(DOV)} + S_{ZZZZ}^{ESA(TSOV-pop)} + S_{ZZZZ}^{ESA(TSOV-coh)} \\
&= \frac{-16}{5} + \frac{-176}{45} + \frac{-176}{45} \\
&= \frac{-496}{45}, \qquad (5.42a) \\
S_{YYZZ}^{ESA} &= S_{YYZZ}^{ESA(DOV)} + S_{YYZZ}^{ESA(TSOV-pop)} + S_{YYZZ}^{ESA(TSOV-coh)} \\
&= \frac{-16}{15} + \frac{-272}{45} + \frac{+16}{15} \\
&= \frac{-272}{45}. \qquad (5.42b)
\end{aligned}
$$

The total (all polarizations) signal contribution from ESA is simplified to (-208/9), which is interestingly larger than the GSB signal of (64/3). However, the sum of all the signals (GSB, ESE, and ESA) is net positive.

The initial anisotropies with the corresponding isotropic signal strengths for the GSB, ESE, and ESA contributions can be organized as:

$$r_{GSB} = 0 \qquad (S = 64/9), \qquad (5.43a)$$

$$r_{ESE} = 1 \qquad (S = 64/27), \qquad (5.43b)$$

$$r_{ESA} = 14/65 \qquad (S = -208/27). \qquad (5.43c)$$

The above calculation assumes coherent excitation and no relaxation. When relaxation is complete, the signal strengths and anisotropies for this model can be calculated using the methods of Ref. [13] - all three relaxed anisotropies become zero and the relaxed isotropic signal strengths are in the same proportion as the standard weights used in Chapter 3.

Using Eqn. 5.2, the total initial anisotropy is

$$\begin{aligned} r &= \frac{\left(\frac{64}{9}\right)(0) + \left(\frac{64}{27}\right)(1) + \left(-\frac{208}{27}\right)\left(\frac{14}{65}\right)}{\left(\frac{64}{9}\right) + \left(\frac{64}{27}\right) + \left(-\frac{208}{27}\right)} \\ &= 2/5. \end{aligned} \tag{5.44}$$

The crucial result here is if each valley is an independent, uncoupled, absorber, the initial anisotropy is 2/5. Another result shown using an effective mass approximation is that an anisotropy of 2/5 can be recovered without the single electron states. Thus, it is possible that the initial anisotropy can be lowered with the inclusion of the one-electron states. The calculation in this section assumes that both valley-splitting and spin-orbit splitting of singly-excited states do not move transitions outside of the pulse spectrum. These results suggest that the 4 degenerate valleys in PbS QDs are strongly coupled or that each individual valley has strong spin-orbit coupling to split the singly-excited states outside of the pulse spectrum. Considering the bandwidth of our pulses, these values would have to be larger than ~200 meV, which is significantly greater than theoretical predictions [53].

5.4 Discussion

The electronic structure of lead chalcogenide QDs at the bandgap is not trivial, which is suggested by the departure from the initial anisotropy of 2/5 predicted by an effective mass approximation. The role of one-electron states and spin-orbit coupling in QDs must be considered. Shiang *et al.* stated that the Bloch functions and the envelope functions are mixed away from the Γ point of the Brillouin zone for finite sizes in CdSe QDs, which can be treated analogous to spin-orbit coupling [46]. With a direct bandgap at the L-point for lead chalcogenide QDs, this mixing between the Bloch functions and envelope functions might have a large effect. Another possibility to consider is the inclusion of hot one-electron states in the calculations using an effective mass approximation, which might lower the initial anisotropy. In addition to the anomalous initial anisotropy, our data shows that the anisotropy outside the pulse overlap (∼10 fs) is nominally zero, which could indicate fast scattering between symmetry related valleys in PbS QDs. This timescale is similar to a timescale of ∼30 fs previously reported for scattering between unrelated valleys in bulk $\mathrm{Al}_x\mathrm{Ga}_{1-x}\mathrm{As}$ semiconductors [54].

5.5 Conclusion

We have measured the initial anisotropy of chlorine-passivated PbS QDs at the bandgap with 15 fs pulses, which required proper subtraction of the non-resonant signal from XPM. For this subtraction, we successfully simulated the XPM signal by retrieving the spectrum and spectral phase from an independent measurement and calculated propagation effects through an absorbing sample in three frequency dimensions.

The initial anisotropy we report for PbS QDs at the bandgap is nominally zero and less than ∼0.1, which is anomalous and suggests a complicated electronic structure. We show through calculations, using a 3D particle in a box and an effective mass approximation, that the expected initial anisotropy is 2/5. Some considerations may result in a departure from the initial anisotropy of 2/5: spin-orbit coupling, intervalley coupling, and the hot one-electron states must be explored further. The spin-orbit coupling in bulk PbS [51] may be a useful guide. For considerations of spin-orbit coupling and intervalley coupling, our results suggest that one or both of these values must be larger than previous calculations indicate. The calculation of the initial anisotropy assumes these states are near degenerate. To explain the initial anisotropy, large couplings are needed to push some of these states outside of our pulse bandwidth. This suggests that the timescale of intervalley scattering between the 4 fold degenerate L-points is faster than ~20 fs.

References

[1] Y. I. Ravich, B. A. Efimova, and I. A. Smirnov, *Semiconducting Lead Chalcogenides* (Plenum Press, New York, 1970).

[2] A. L. Éfros and A. L. Éfros, “Interband absorption of light in a semiconductor sphere,” Sov. Phys. Semicond. 16(7), 772-775 (1982).

[3] L. E. Brus, “Electron-electron and electron-hole interactions in small semiconductor crystallites: The size dependence of the lowest excited electronic state,” J. Chem. Phys. 80(9), 4403-4409 (1984).

[4] A. N. Poddubny, M. O. Nestoklon, and S. V. Goupalov, “Anomalous suppression of valley splittings in lead salt nanocrystals without inversion center,” Phys. Rev. B 86, 035324 (2012).

[5] S. Nomura and T. Kobayashi, “Exciton-LO-phonon couplings in spherical semiconductor microcrystallites,” Phys. Rev. B 45(3), 1305-1316 (1992).

[6] L. Wang, M. Califano, A. Zunger, and A. Franceschetti, “Pseudopotential Theory of Auger Processes in CdSe Quantum Dots,” Phys. Rev. Lett. 91(5), 056404 (2003).

[7] H. Benisty, C. M. Sotomayor-Torres, and C. Weisbuch, “Intrinsic mechanism for the poor luminescence properties of quantum-box systems,” Phys. Rev. B 44(19), 10945-10948 (1991).

[8] A. J. Nozik, “Quantum dot solar cells,” Physica E 14, 115-120 (2002).

[9] O. E. Semonin, J. M. Luther, S. Choi, H. Chen, J. Gao, A. J. Nozik, and M. C. Beard, “Peak External Photocurrent Quantum Efficiency Exceeding 100% via MEG in a Quantum Dot Solar Cell,” Science 334, 1530-1533 (2011).

[10] J. M. An, A. Franceschetti, and A. Zunger, “The Excitonic Exchange Splitting and Radiative Lifetime in PbSe Quantum Dots,” Nano Lett. 7(7), 2129-2135 (2007).

[11] J. Bylsma, P. Dey, J. Paul, S. Hoogland, E. H. Sargent, J. M. Luther, M. C. Beard, and D. Karaiskaj, “Quantum beats due to excitonic ground-state splitting in colloidal quantum dots,” Phys. Rev. B 86, 125322 (2012).

[12] E. Harel, S. M. Rupich, R. D. Schaller, D. V. Talapin, and G. S. Engel, "Measurement of electronic splitting in PbS quantum dots by two-dimensional nonlinear spectroscopy," Phys. Rev. B 86, 075412 (2012).

[13] W. Qian and D. M. Jonas, "Role of cyclic sets of transition dipoles in the pump-probe polarization anisotropy: Application to square symmetric molecules and perpendicular chromophore pairs," J. Chem. Phys. 119(3), 1611-1622 (2003).

[14] D. M. Jonas, M. J. Lang, Y. Nagasawa, T. Joo, and G. R. Fleming, "Pump-Probe Polarization Anisotropy Study of Femtosecond Energy Transfer within the Photosynthetic Reaction Center of *Rhodobacter sphaeroides* R26," J. Phys. Chem. 100, 12660-12673 (1996).

[15] R. N. Zare, *Angular Momentum: Understanding Spatial Aspects in Physics and Chemistry* (Wiley-Interscience, New York, 1988).

[16] E. R. Smith and D. M. Jonas, "Alignment, Vibronic Level Splitting, and Coherent Coupling Effects on the Pump-Probe Polarization Anisotropy," J. Phys. Chem. A 115, 4101-4113 (2011).

[17] A. T. Yeh, C. V. Shank, J. K. McCusker, "Ultrafast Electron Localization Dynamics Following Photo-Induced Charge Transfer," Science 289, 935-938 (2000).

[18] B. Cho, W. K. Peters, R. J. Hill, T. L. Courtney, and D. M. Jonas, "Bulklike Hot Carrier Dynamics in Lead Sulfide Quantum Dots," Nano Lett. 10, 2498-2505 (2010).

[19] P. D. Cunningham, J. E. Boercker, D. Placencia, and J. G. Tischler, "Anisotropic Absorption in PbSe Nanorods," ACS Nano 8(1), 581-590 (2014).

[20] S. J. Rosenthal, A. T. Yeh, A. P. Alivisatos, and C. V. Shank, "Size Dependent Absorption Anisotropy Measurements of CdSe Nanocrystals: Symmetry Assignments for the Lowest Electronic States," *Ultrafast Phenomena X*, edited by P. F. Barbara, J. G. Fujimoto, W. H. Knox, and W. Zinth (Springer-Verlag, Berlin, 1996), p. 431.

[21] A. A. Ferro and D. M. Jonas, "Pump-probe polarization anisotropy study of doubly degenerate electronic reorientation in silicon naphthalocyanine," J. Chem. Phys. 115(14), 6281-6284 (2001).

[22] M. C. Weidman, M. E. Beck, R. S. Hoffman, F. Prins, and W. A. Tisdale, "Monodisperse, Air-Stable PbS Nanocrystals via Precursor Stoichiometry Control," ACS Nano 8, 6363-6371 (2014).

[23] D. Baranov, R. J. Hill, S. D. Park, J. Ryu, and D. M. Jonas, "Interferometrically stable, enclosed, spinning sample cell for spectroscopic experiments on air-sensitive samples," (in preparation).

[24] J. van Rijssel, V. F. D. Peters, J. D. Meeldijk, R. J. Kortschot, R. J. A. van Dijk-Moes, A. V. Petukhov, B. H. Erné, and A. P. Philipse, "Size-Dependent Second Virial Coefficients of Quantum Dots from Quantitative Cryogenic Electron Microscopy," J. Phys. Chem. B 118, 11000-11005 (2014).

[25] D. Brida, S. Bonora, C. Manzoni, M. Marangoni, P. Villoresi, S. De Silvestri, and G. Cerullo, "Generation of 8.5-fs pulses at 1.3 μm for ultrabroadband pump-probe spectroscopy," Optics Express 17(15), 12510-12515 (2009).

[26] E. Zeek, K. Maginnis, S. Backus, U. Russek, M. Murnane, G. Mourou, H. Kapteyn, and G. Vdovin, "Pulse compression by use of deformable mirrors," Optics Letters 24(7), 493-495 (1999).

[27] R. J. Schmidt, Schott Glass, "Sellmeier coefficients for BOROFLOAT 33 glass" (personal communication, Aug. 29, 2013).

[28] B. Cho, V. Tiwari, R. J. Hill, W. K. Peters, T. L. Courtney, A. P. Spencer, and D. M. Jonas, "Absolute Measurement of Femtosecond Pump-Probe Signal Strength," J. Phys. Chem. A 117, 6332-6345 (2013).

[29] R. Trebino, K. W. DeLong, D. N. Fittinghoff, J. N. Sweetser, M. A. Krumbügel, and B. A. Richman, D. J. Kane, "Measuring ultrashort laser pulses in the time-frequency domain using frequency-resolved optical gating," Rev. Sci. Instrum. 68(9), 3277-3295 (1997).

[30] K. W. DeLong, D. N. Fittinghoff, and R. Trebino, "Practical Issues in Ultrashort-Laser-Pulse Measurement Using Frequency-Resolved Optical Gating," IEEE J. Quantum Electron. 32(7), 1253-1264 (1996).

[31] A. Baltuška, M. S. Pshenichnikov, and D. A. Wiersma, "Second-Harmonic Generation Frequency-Resolved Optical Gating in the Single-Cycle Regime," IEEE J. Quant. Electron. 35(4), 459-478 (1999).

[32] G. Taft, A. Rundquist, M. M. Murnane, I. P. Christov, H. C. Kapteyn, K. W. Delong, D. N. Fittinghoff, M. A. Krumbügel, J. N. Sweetser, and R. Trebino, "Measurement of 10-fs Laser Pulses," IEEE J. Sel. Topics Quantum. Electron. 2(3), 575-585 (1996).

[33] The Xe vacuum wavelengths used for calibration were: 1053.074 nm, 1084.131 nm, 1174.545 nm, 1262.685 nm, 1366.021 nm, 1414.595 nm, 1473.642 nm, 1542.222 nm, 1673.273 nm, and 1733.053 nm. These values were from [34].

[34] E. B. Saloman, "Energy Levels and Observed Spectral Lines of Xenon, Xe I through Xe LIV," J. Phys. Chem. Ref. Data 33(3), 765-921 (2004).

[35] M. K. Yetzbacher, T. L. Courtney, W. K. Peters, K. A. Kitney, E. R. Smith, and D. M. Jonas, "Spectral restoration for femtosecond spectral interferometry with attosecond accuracy," J. Opt. Soc. Am. B 27(5), 1104-1117 (2010).

[36] S. B. Howell, *Handbook of CCD Astronomy*, 2nd ed., Cambridge Observing Handbooks for Research Astronomers (Cambridge University Press, Cambridge, 2006).

[37] S. Yeremenko, A. Baltuška, F. de Haan, M. S. Pshenichnikov, and D. A. Wiersma, "Frequency-resolved pump-probe characterization of femtosecond infrared pulses," Optics Letters 27(13), 1171-1173 (2002).

[38] J. A. Gardecki, S. Constantine, Y. Zhou, and L. D. Zieger, "Optical heterodyne detected spectrograms of ultrafast nonresonant electronic responses," J. Opt. Soc. Am. B 17(4), 652-662 (2000).

[39] N. Belabas and D. M. Jonas, "Three-dimensional view of signal propagation in femtosecond four-wave mixing with application to the boxcars geometry," J. Opt. Soc. Am. B 22(3), 655-674 (2005).

[40] M. K. Yetzbacher, N. Belabas, K. A. Kitney, and D. M. Jonas, "Propagation, beam geometry, and detection distortions of peak shapes in two-dimensional Fourier transform spectra," J. Chem. Phys. 126, 044511 (2007).

[41] J. Galbán, S. de Marcos, I. Sanz, C. Ubide, and J. Zuriarrain, "Uncertainty in modern spectrophotometers," Anal. Chem. 79(13), 4763-4767 (2007).

[42] Q. Lin and G. P. Agrawal, "Vector Theory of Cross-Phase Modulation: Role of Nonlinear Polarization Rotation," IEEE J. Quant. Electron. 40 (7), 958-964 (2014).

[43] D. C. Hutchings, J. S. Aitchison, B. S. Wherrett, G. T. Kennedy, and W. Sibbett, "Polarization dependence of ultrafast nonlinear refraction in an AlGaAs waveguide at the half-band gap," Opt. Lett. 20(9), 991-993 (1995).

[44] M. Nirmal, D. J. Norris, M. Kuno, and M. G. Bawendi, "Observation of the "Dark Exciton" in CdSe Quantum Dots," Phys. Rev. Lett. 75(20), 3728-3731 (1995).

[45] A. L. Éfros, M. Rosen, M. Kuno, M. Nirmal, D. J. Norris, and M. Bawendi, "Band-edge exciton in quantum dots of semiconductors with a degenerate valence band: Dark and bright exciton states," Phys. Rev. B 54(7), 4843-4856 (1996).

[46] J. J. Shiang, A. V. Kadavanich, R. K. Grubbs, and A. P. Alivisatos, "Symmetry of Annealed Wurtzite CdSe Nanocrystals: Assignment to the C_{3v} Point Group," J. Phys. Chem. 99, 17417-17422 (1995).

[47] F. A. Cotton, *Chemical Applications of Group Theory*, third edition (Wiley-Interscience, New York, 1990).

[48] D. Lee and A. C. Albrecht, "On Global Energy Conservation in Nonlinear Light-Matter Interaction: The Nonlinear Spectroscopies, Active and Passive," Adv. Chem. Phys. LXXXIII, 43 (1993).

[49] P. R. Monson and W. M. McClain, "Polarization Dependence of the Two-Photon Absorption of Tumbling Molecules with Application to Liquid 1-Chloronaphthalene and Benzene," J. Chem. Phys. 53(1), 29-37 (1970).

[50] I. Kang and F. W. Wise, "Electronic structure and optical properties of PbS and PbSe quantum dots," J. Opt. Soc. Am. B 14(7), 1632-1646 (1997).

[51] D. L. Mitchell and R. F. Wallis, "Theoretical Energy-Band Parameters for the Lead Salts," Phys. Rev. 151(2), 581-595 (1966).

[52] J. O. Dimmock and G. B. Wright, "Band Edge Structure of PbS, PbSe, and PbTe," Phys. Rev. 135(3A), 821-830 (1964).

[53] J. M. An, A. Franceschetti, S. V. Dudiy, and A. Zunger, "The peculiar electronic structure of PbSe quantum dots," Nano Lett. 6(12), 2728-2735 (2006).

[54] F. W. Wise, I. A. Walmsley, and C. L. Tang, "Experimental determination of hot-carrier scattering processes in $Al_xGa_{1-x}As$," Appl. Phys. Lett. 51(8), 605-607 (1987).

Appendix A

Derivation of Interlaced Fast Fourier Transform

The basic derivation follows that of Bracewell [1], but two key differences arise for the Fast Fourier Transform (FFT), and the opposite sign of i is used in the transform for compatibility with the time to frequency inverse Fourier transform in Gallagher *et al.*, Eqn. 1 [54].

The derivation begins from an adequately sampled (time) series, $f(n/2)$ with $n = 0$ to $2M - 1$ (or $n = (-M + 1)$ to $+M$).

$$\hat{F}(k) = \sum_{n=0}^{2M-1} f(n/2) \exp\left[+i2\pi k(n/2)/M\right] \tag{A.1}$$

with $k = (-M+1)$ to M, does not have any aliasing. A shifted (time) series can also generate the transform

$$\hat{F}(k) = \sum_{n=0}^{2M-1} f(n/2 + a) \exp\left[+i2\pi k(n/2 + a)/M\right]. \tag{A.2}$$

This can be written in a form that is more amenable to the FFT. The circumflex or hat reminds the reader that the (frequency) spectrum may be complex.

$$\hat{F}(k)\exp\left[-i2\pi ka/M\right] = \sum_{n=0}^{2M-1} f(n/2+a)\exp\left[+i2\pi k(n/2)/M\right]. \tag{A.3}$$

The right hand side of Eqn. A.3 is the inverse FFT of the shifted (time) series.

Aliasing enters when the sampling is half-adequate

$$^{1/2}\hat{F}_0(k) = \sum_{n=0}^{M-1} f(n)\exp\left[+i2\pi kn/M\right] \tag{A.4}$$

with $k = (-M/2) + 1$ to $M/2$.

It will be seen below that this choice of the range for k is convenient for handling the Fourier shift of interlaced frequency spectra. The left superscript 1/2 indicates half-adequate sampling, and the right subscript 0 (zero) indicates zero shift. The essence of the interlaced FFT is that the Fourier shifts of aliased contributions to the spectrum depend on their real frequencies, not their aliased frequencies.

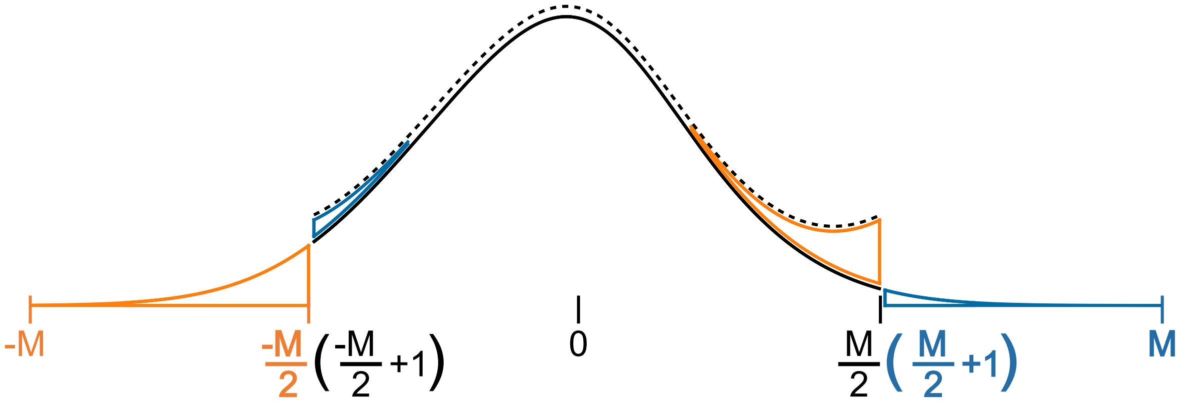

Figure A.1: How aliasing works. The blue contribution is shifted down by M. The orange contribution is shifted up by M. The sum of the aliased blue, orange, and black contributions is the dashed, aliased spectrum.

The adequately sampled spectrum has four distinct regions, and the aliased spectrum has two. The region from $k = 1$ to $k = M/2$ contains contributions from $k = -M + 1$ to $k = -M/2$. For an inverse FFT, we find the sum

$$\begin{aligned}
\hat{F}(k) + \hat{F}(k - M) &= \sum_{n=0}^{2M-1} f(n/2) \exp\left[i2\pi k(n/2)/M\right] \\
&+ \sum_{n=0}^{2M-1} f(n/2) \exp\left[i2\pi (k - M)(n/2)/M\right] \\
&= \sum_{n=0}^{2M-1} f(n/2) \exp\left[i2\pi k(n/2)/M\right](1 + \exp\left[-i2\pi(n/2)\right]) \\
&= \sum_{n=0}^{2M-1} f(n/2) \exp\left[i2\pi k(n/2)/M\right](1 + (-1)^n) \\
&= \begin{cases} 2 \cdot \displaystyle\sum_{n=0}^{2M-1} f(n/2) \exp\left[i2\pi k(n/2)/M\right] & \text{when } n \text{ is even} \\ 0 & \text{when } n \text{ is odd} \end{cases} \\
&= 2 \cdot \sum_{n=0}^{M-1} f(n) \exp\left[i2\pi kn/M\right] \\
&= 2 \cdot {}^{1/2}\hat{F}_0(k). \qquad \text{(A.5)}
\end{aligned}$$

The factor of 2 on the right hand side of Eqn. A.5 arises because the adequately sampled (time) series has twice as many points and the FFT does not account for their reduced spacing. (This is the first key difference from Bracewell [1].)

The aliased inverse FFT of the shifted (time) series is

$$^{1/2}\hat{F}_a(k) = \sum_{n=1}^{M-1} f(n + a) \exp\left[+i2\pi kn/M\right]. \qquad \text{(A.6)}$$

The inverse FFTs of the adequately sampled time series introduce the second key difference from Bracewell.

$$\hat{F}(k)\exp\left[-i2\pi ka/M\right] = \sum_{n=0}^{2M-1} f(n/2+a)\exp\left[+i2\pi k(n/2)/M\right] \tag{A.7}$$

follows from Eqn. A.2, and $k-M$ may be substituted for k on both sides of the equation

$$\hat{F}(k-M)\exp\left[-i2\pi(k-M)a/M\right] = \sum_{n=0}^{2M-1} f(n/2+a)\exp\left[+i2\pi(k-M)(n/2)/M\right]. \tag{A.8}$$

Using the same trick used to obtain Eqn. A.5, we obtain

$$\hat{F}(k)\exp\left[-i2\pi ka/M\right] + \hat{F}(k-M)\exp\left[-i2\pi(k-M)a/M\right] = 2\cdot {}^{1/2}\hat{F}_a(k), \tag{A.9}$$

for $k = 1$ to $M/2$. This can be rewritten as

$$2\cdot {}^{1/2}\hat{F}_a(k) = \Big(\hat{F}(k) + \hat{F}(k-M)\exp\left[+i2\pi a\right]\Big)\exp\left[-i2\pi ka/M\right]. \tag{A.10}$$

This differs from Bracewell [1] in the sign of i and the factor $\exp\left[-i2\pi ka/M\right]$ for the shift. (For easier applicability to the FFT, it would be convenient to replace $\text{Ш}_a f = \text{Ш}(x-a)f(x)$ with $\text{Ш} f_a = \text{Ш}(x)f(x+a)$ in Bracewell's derivation because the Fourier integral of the latter matches the FFT of the shifted time series.)

Equations A.5 and A.10 can be combined to obtain $\hat{F}(k)$ and $\hat{F}(k-M)$ from the aliased spectra ${}^{1/2}\hat{F}_0(k)$ and ${}^{1/2}\hat{F}_a(k)$ for $k = 1$ to $M/2$. Eliminating $\hat{F}(k-M)$,

$$\hat{F}(k) = \frac{2}{1-\exp\left[-i2\pi a\right]}{}^{1/2}\hat{F}_0(k) - \frac{2\exp\left[-i2\pi a\right]}{1-\exp\left[-i2\pi a\right]}{}^{1/2}\hat{F}_a(k)\exp\left[i2\pi ka/M\right], \tag{A.11}$$

for $k = 1$ to $M/2$. This can be rearranged to

$$\hat{F}(k) = (1 - i\cot(\pi a))\cdot {}^{1/2}\hat{F}_0(k) + (1 + i\cot(\pi a))\cdot {}^{1/2}\hat{F}_a(k)\exp\left[i2\pi ka/M\right]. \tag{A.12}$$

To find $\hat{F}(k-M)$, we have to recognize that the FFT repeats.

$$^{1/2}\hat{F}_0(k) = {}^{1/2}\hat{F}_0(k-M) = {}^{1/2}\hat{F}_0(k+M) \tag{A.13a}$$

$$^{1/2}\hat{F}_a(k) = {}^{1/2}\hat{F}_a(k-M) = {}^{1/2}\hat{F}_a(k+M) \tag{A.13b}$$

Using Eqn. A.5 and A.10 to eliminate $\hat{F}(k)$,

$$\begin{aligned}
\hat{F}(k-M) &= \frac{2}{1-\exp\left[i2\pi a\right]}\left[{}^{1/2}\hat{F}_0(k-M) - {}^{1/2}\hat{F}_a(k-M)\exp\left[i2\pi ka/M\right]\right] \\
&= \frac{2}{1-\exp\left[i2\pi a\right]}\left[{}^{1/2}\hat{F}_0(k-M) - \exp\left[i2\pi a\right]\cdot{}^{1/2}\hat{F}_a(k-M)\exp\left[i2\pi(k-M)a/M\right]\right] \\
&= (1+i\cot(\pi a))\cdot{}^{1/2}\hat{F}_0(k-M) \\
&+ (1-i\cot(\pi a))\cdot{}^{1/2}\hat{F}_a(k-M)\exp\left[i2\pi(k-M)a/M\right],
\end{aligned} \tag{A.14}$$

for $k = 1$ to $M/2$.

The aliased spectrum in the region from $k = -\left(\frac{M}{2}\right)+1$ to $k = 0$ contains contributions from $k = \left(\frac{M}{2}\right)+1$ to $k = M$. Analogously to Eqn. A.5, one finds

$$2\cdot{}^{1/2}\hat{F}_0(k) = \hat{F}(k) + \hat{F}(k+M) \tag{A.15}$$

and analogously to Eqn. A.10, one finds

$$2\cdot{}^{1/2}\hat{F}_a(k) = \hat{F}(k) + \exp\left[-2i\pi a\right]\hat{F}(k+M)\exp\left[-i2\pi ka/M\right] \tag{A.16}$$

for $k = -\left(\frac{M}{2}\right)+1$ to $k = 0$. Compared to Eqn. A.10, Eqn. A.16 differs in the sign of the $i2\pi a$; this arises from the different sign of the M-shift. Eqn. A.15 parallels Eqn. A.5 more closely. At the point $k = 0$, $\hat{F}(k+M) = \hat{F}(M)$, which is zero because $f(n/2)$ is adequately sampled by hypothesis. Combining Eqn. A.15 and A.16, one obtains

$$\begin{aligned}\hat{F}(k) &= (1 + i\cot(\pi a)) \cdot {}^{1/2}\hat{F}_0(k) \\ &+ (1 - i\cot(\pi a)) \cdot {}^{1/2}\hat{F}_a(k)\exp[i2\pi ka/M] \qquad \text{(A.17)}\end{aligned}$$

and

$$\begin{aligned}\hat{F}(k+M) &= (1 - i\cot(\pi a)) \cdot {}^{1/2}\hat{F}_0(k+M) \\ &+ (1 + i\cot(\pi a)) \cdot {}^{1/2}\hat{F}_a(k+M)\exp[i2\pi(k+M)a/M] \qquad \text{(A.18)}\end{aligned}$$

for $k = -\left(\frac{M}{2}\right) + 1$ to $k = 0$. Eqn. A.13 has been used in obtaining Eqn. A.18.

The set of four equations given by equations A.12, A.14, A.17, and A.18 can be combined into a single equation

$$\begin{aligned}\hat{F}(k) &= (1 - i\cot(\pi a)\,\mathrm{sgn}(k)) \cdot {}^{1/2}\hat{F}_0(k) \\ &+ (1 + i\cot(\pi a)\,\mathrm{sgn}(k)) \cdot {}^{1/2}\hat{F}_a(k)\exp[i2\pi ka/M] \qquad \text{(A.19)}\end{aligned}$$

by using the signum of sign function

$$\mathrm{sgn}(k) = \begin{cases} +1 & k > 0 \\ 0 & k = 0 \\ -1 & k < 0. \end{cases}$$

Because a is arbitrary, $\exp[i2\pi ka/M]$ does not have a cyclic behavior that would allow the actual frequencies from $k = (-M + 1)$ to 0 to be replaced by frequencies from $k = M$ to $2M - 1$. Eqn. A.19 is valid for $k = (-M + 1)$ to M. Eqn. A.19 differs from Bracewell's expression by the sign of i, a factor of 2, and the Fourier shift $\exp[i2\pi ka/M]$.

Usually the time series is input to an inverse FFT as $n = 0$ to $M - 1$ (causal signal) or as $n = 0$ to $M/2$, $-M/2 + 1$ to -1 (acausal), and the frequency spectrum is output as $k = 0$ to $M/2$, $-M/2 + 1$ to -1. With this array packing, one can, in practice, simply extend each aliased frequency spectrum by repeating it once. When this is done, the interlaced frequency index l and the aliased frequency index k correspond as:

$l = k$	$l = 0$	$k = 0$	first aliased spectrum
	$l = 1$	$k = 1$	
	$\vdots$	$\vdots$	
	$l = M/2$	$k = M/2$	
$l = k + M$	$l = M/2 + 1$	$k = -M/2 + 1$	
	$\vdots$	$\vdots$	
	$l = M - 1$	$k = -1$	
	$l = M$	$k = 0$	repeated aliased spectrum
$l = k - M$	$l = -M + 1$	$k = 1$	
	$l = -M + 2$	$k = 2$	
	$\vdots$	$\vdots$	
	$l = -M/2$	$k = M/2$	
$l = k$	$l = -M/2 + 1$	$k = -M/2 + 1$	
	$\vdots$	$\vdots$	
	$l = -1$	$k = -1$	

With this packing, Eqn. A.19 should be used with the interlaced frequency index l in place of k. The factor of 2 gives the inverse FFT the amplitude it should have for a time sampling interval corresponding to the interlaced frequency range.

References

[1] R. Bracewell, *The Fourier Transform & Its Applications*, 3rd ed., McGraw-Hill Series in Electrical and Computer Engineering (McGraw-Hill Science/Engineering/Math, New York, 1999).

[2] S. M. Gallagher, A. W. Albrecht, J. D. Hybl, B. L. Landin, B. Rajaram, and D. M. Jonas, "Heterodyne detection of the complete electric field of femtosecond four-wave mixing signals," J. Opt. Soc. Am. B 15(8), 2338 (1998).

Bibliography

[1] G. P. Agrawal, "Modulation Instability Induced by Cross-Phase Modulation," Phys. Rev. Lett. 59(8), 880-883 (1987).

[2] G. P. Agrawal, P. L. Baldeck, and R. R. Alfano, "Modulation instability induced by cross-phase modulation in optical fibers," Phys. Rev. A 39(7), 3406-3413 (1989).

[3] R. R. Alfano, P. L. Baldeck, P. P. Ho, and G. P. Agrawal, "Cross-phase modulation and induced focusing due to optical nonlinearities in optical fibers and bulk materials," J. Opt. Soc. Am. B 6(4), 824-829 (1989).

[4] G. Allan and C. Delerue, "Confinement effects in PbSe quantum wells and nanocrystals," Phys. Rev. B 70, 245321 (2004).

[5] J. M. An, A. Franceschetti, S. V. Dudiy, and A. Zunger, "The peculiar electronic structure of PbSe quantum dots," Nano Letters 6(12), 2728-2735 (2006).

[6] J. M. An, A. Franceschetti, and A. Zunger, "The Excitonic Exchange Splitting and Radiative Lifetime in PbSe Quantum Dots," Nano Lett. 7(7), 2129-2135 (2007).

[7] P. W. Anderson, "A Mathematical Model for the Narrowing of Spectral Lines by Exchange or Motion," J. Phys. Soc. Jpn. 9(3), 316-339 (1954).

[8] R. Baer and E. Rabani, "Expeditious Stochastic Calculation of Multiexciton Generation Rates in Semiconductor Nanocrystals," Nano Lett. 12, 2123-2128 (2012).

[9] M. W. Balk and G. R. Fleming, "Dependence of the coherence spike on the material dephasing time in pump-probe experiments," J. Chem. Phys. 83(9), 4300-4307 (1985).

[10] A. Baltuška, M. S. Pshenichnikov, and D. A. Wiersma, "Second-Harmonic Generation Frequency-Resolved Optical Gating in the Single-Cycle Regime," IEEE J. Quant. Electron. 35(4), 459-478 (1999).

[11] D. Baranov, R. J. Hill, S. D. Park, J. Ryu, and D. M. Jonas, "Interferometrically stable, enclosed, spinning sample cell for spectroscopic experiments on air-sensitive samples," (in preparation).

[12] P. Baum and E. Riedle, "Design and calibration of zero-additional-phase SPIDER," J. Opt. Soc. Am. B 22, 1875-1883 (2005).

[13] N. Belabas and D. M. Jonas, "Three-dimensional view of signal propagation in femtosecond four-wave mixing with application to the boxcars geometry," J. Opt. Soc. Am. B 22, 655-674 (2005).

[14] H. Benisty, C. M. Sotomayor-Torres, and C. Weisbuch, "Intrinsic mechanism for the poor luminescence properties of quantum-box systems," Phys. Rev. B 44(19), 10945-10948 (1991).

[15] R. B. Bernstein and A. H. Zewail, "Femtosecond real-time probing of reactions. III. Inversion to the potential from femtosecond transition-state spectroscopy experiments," J. Chem. Phys. 90(2), 829-842 (1989).

[16] S. B. Block, L. A. Yurs, A. V. Pakoulev, R. S. Selinsky, S. Jin, and J. C. Wright, "Multiresonant Multidimensional Spectroscopy of Surface-Trapped Excitons in PbSe Quantum Dots," J. Phys. Chem. Lett. 3, 2707-2712 (2012).

[17] R. Bracewell, *The Fourier Transform & Its Applications*, 3rd ed., McGraw-Hill Series in Electrical and Computer Engineering (McGraw-Hill Science/Engineering/Math, New York, 1999).

[18] D. Brida, S. Bonora, C. Manzoni, M. Marangoni, P. Villoresi, S. De Silvestri, and G. Cerullo, "Generation of 8.5-fs pulses at 1.3 μm for ultrabroadband pump-probe spectroscopy," Opt. Express 17, 12510-12515 (2009).

[19] R. G. Brewer, "Frequency Shifts in Self-focused Light," Phys. Rev. Lett. 19(1), 8-11 (1967).

[20] L. E. Brus, "Electron-electron and electron-hole interactions in small semiconductor crystallites: The size dependence of the lowest excited electronic state," J. Chem. Phys. 80(9), 4403-4409 (1984).

[21] L. Brus, "Electronic Wave Functions in Semiconductor Clusters: Experiment and Theory," J. Phys. Chem. 90, 2555-2560 (1986).

[22] J. Bylsma, P. Dey, J. Paul, S. Hoogland, E. H. Sargent, J. M. Luther, M. C. Beard, and D. Karaiskaj, "Quantum beats due to excitonic ground-state splitting in colloidal quantum dots," Phys. Rev. B 86, 125322 (2012).

[23] G. H. Carey, A. L. Abdelhady, Z. Ning, S. M. Thon, O. M. Bakr, and E. H. Sargent, "Colloidal Quantum Dot Solar Cells," Chem. Rev., Article ASAP (2015).

[24] E. A. Carter and J. T. Hynes, "Solvation dynamics for an ion pair in a polar solvent: Time-dependent fluorescence and photochemical charge transfer," J. Chem. Phys. 94(9), 5961-5979 (1991).

[25] W. C. W. Chan, D. J. Maxwell, X. Gao, R. E. Bailey, M. Han, and S. Nie, "Luminescent quantum dots for multiplexed biological detection and imaging," Current Opinion in Biotechnology 13, 40-46 (2002).

[26] R. Y. Chiao, E. Garmire, and C. H. Townes, "Self-trapping of Optical Beams," Phys. Rev. Lett. 13(15), 479-482 (1964).

[27] G. Chinga, P. O. Johnsen, R. Dougherty, E. L. Berli, and J. Walter, "Quantification of the 3D microstructure of SC surfaces," J. Microsc. 227, 254-265 (2007).

[28] B. Cho, W. K. Peters, R. J. Hill, T. L. Courtney, and D. M. Jonas, "Bulklike Hot Carrier Dynamics in Lead Sulfide Quantum Dots," Nano Lett. 10, 2498-2505 (2010).

[29] B. Cho, V. Tiwari, R. J. Hill, W. K. Peters, T. L. Courtney, A. P. Spencer, and D. M. Jonas, "Absolute Measurement of Femtosecond Pump-Probe Signal Strength," J. Phys. Chem. A 117, 6332-6345 (2013).

[30] H. Chung, H. Choi, D. Kim, S. Jeong, and J. Kim, "Size Dependence of Excitation-Energy-Related Surface Trapping Dynamics in PbS Quantum Dots," J. Phys. Chem. C 119, 7517-7524 (2015).

[31] F. A. Cotton, *Chemical Applications of Group Theory*, third edition (Wiley-Interscience, New York, 1990).

[32] T. L. Courtney, S. D. Park, R. J. Hill, B. Cho, and D. M. Jonas, "Enhanced interferometric detection in two-dimensional spectroscopy with a Sagnac interferometer," Opt. Lett. 39, 513- 516 (2014).

[33] T. L. Courtney, S. D. Park, R. J. Hill, and D. M. Jonas, "Broadband, low-dispersion, Brewster's angle interferometers," (in preparation).

[34] P. D. Cunningham, J. E. Boercker, D. Placencia, and J. G. Tischler, "Anisotropic Absorption in PbSe Nanorods," ACS Nano 8(1), 581-590 (2014).

[35] Q. Dai, Y. Wang, X. Li, Y. Zhang, D. J. Pellegrino, M. Zhao, B. Zou, J. Seo, Y. Wang, and W. W. Yu, "Size-Dependent Composition and Molar Extinction Coefficient of PbSe Semiconductor Nanocrystals," ACS Nano 3(6), 1518-1524 (2009).

[36] L. P. DeFlores, R. A. Nicodemus, and A. Tokmakoff, "Two-dimensional Fourier transform spectroscopy in the pump-probe geometry," Opt. Lett. 32, 2966-2968 (2007).

[37] K. W. DeLong, D. N. Fittinghoff, and R. Trebino, "Practical Issues in Ultrashort- Laser-Pulse Measurement Using Frequency-Resolved Optical Gating," IEEE J. Quant. Electron. 32(7), 1253-1264 (1996).

[38] J. O. Dimmock and G. B. Wright, "Band Edge Structure of PbS, PbSe, and PbTe," Phys. Rev. 135(3A), 821-830 (1964).

[39] S. Dobner, C. Cleff, C. Fallnich, and P. Gross, "Interferometric background reduction for femtosecond stimulated Raman scattering loss spectroscopy," J. Chem. Phys. 137, 174201 (2012).

[40] S. Dong, D. Trivedi, S. Chakrabortty, T. Kobayashi, Y. Chan, O. V. Prezhdo, and Z.-H. Loh, "Observation of an Excitonic Quantum Coherence in CdSe Nanocrystals," Nano Lett. ASAP (2015).

[41] A. L. Éfros and A. L. Éfros, "Interband absorption of light in a semiconductor sphere," Sov. Phys. Semicond. 16(7), 772-775 (1982).

[42] A. L. Éfros, M. Rosen, M. Kuno, M. Nirmal, D. J. Norris, and M. Bawendi, "Band-edge exciton in quantum dots of semiconductors with a degenerate valence band: Dark and bright exciton states," Phys. Rev. B 54(7), 4843-4856 (1996).

[43] A. O. El-Ballouli, E. Alarousu, A. Usman, J. Pan, O. M. Bakr, and O. F. Mohammed, "Real-Time Observation of Ultrafast Intraband Relaxation and Exciton Multiplication in PbS Quantum Dots," ACS Photonics 1, 285-292 (2014).

[44] R. J. Ellingson, M. C. Bear, J. C. Johnson, P. Yu, O. I. Micic, A. J. Nozik, A. Shabaev, and A. L. Efros, "Highly Efficient Multiple Exciton Generation in Colloidal PbSe and PbS Quantum Dots," Nano Lett. 5(5), 865-871 (2005).

[45] R. R. Ernst, G. Bodenhausen, and A. Wokaun, *Principles of Nuclear Magnetic Resonance in One and Two Dimensions* (Oxford Univ. Press, 1987).

[46] C. M. Evans, M. E. Evans, and T. D. Krauss, "Mysteries of TOPSe Revealed: Insights into Quantum Dot Nucleation," Journal of the American Chemical Society 132, 10973-10975 (2010).

[47] S. M. G. Faeder and D. M. Jonas, "Two-dimensional electronic correlation and relaxation spectra: Theory and model calculations," J. Phys. Chem. A 103, 10489-10505 (1999).

[48] D. A. Farrow, W. Qian, E. R. Smith, A. A. Ferro, and D. M. Jonas, "Polarized pump-probe measurements of electronic motion via a conical intersection," J. Chem. Phys. 128, 144510 (2008).

[49] M. J. Fernée, P. Jensen, and H. Rubinsztein-Dunlop, "Origin of the Large Homogeneous Line Widths Obtained from Strongly Quantum Confined PbS Nanocrystals at Room Temperature," J. Phys. Chem. C 111, 4984-4989 (2007).

[50] A. A. Ferro and D. M. Jonas, "Pump-probe polarization anisotropy study of doubly degenerate electronic reorientation in silicon naphthalocyanine," J. Chem. Phys. 115(14), 6281-6284 (2001).

[51] G. R. Fleming, *Chemical Applications of Ultrafast Spectroscopy* (Clarendon Press: Oxford, U. K., 1986).

[52] A. Franceschetti, J. M. An, and A. Zunger, "Impact Ionization Can Explain Carrier Multiplication in PbSe Quantum Dots," Nano Lett. 6(10), 2191-2195 (2006).

[53] J. Galbán, S. de Marcos, I. Sanz, C. Ubide, and J. Zuriarrain, "Uncertainty in modern spectrophotometers," Anal. Chem. 79(13), 4763-4767 (2007).

[54] S. M. Gallagher, A. W. Albrecht, J. D. Hybl, B. L. Landin, B. Rajaram, and D. M. Jonas, "Heterodyne detection of the complete electric field of femtosecond four-wave mixing signals," J. Opt. Soc. Am. B 15(8), 2338 (1998).

[55] C. Galli, K. Wynne, S. M. LeCours, M. J. Therien, and R. M. Hochstrasser, "Direct measurement of electronic dephasing using anisotropy," Chem. Phys. Lett. 206, 493-499 (1993).

[56] J. Gao and J. C. Johnson, "Charge Trapping in Bright and Dark States of Coupled PbS Quantum Dot Films," ACS Nano 6(4), 3292-3303 (2012).

[57] J. A. Gardecki, S. Constantine, Y. Zhou, and L. D. Zieger, "Optical heterodyne detected spectrograms of ultrafast nonresonant electronic responses," J. Opt. Soc. Am. B 17(4), 652-662 (2000).

[58] I. Gdor, H. Sachs, A. Roitblat, D. B. Strasfeld, M. G. Bawendi, and S. Ruhman, "Exploring Exciton Relaxation and Multiexciton Generation in PbSe Nanocrystals Using Hyperspectral Near-IR Probing," ACS Nano 6(4), 3269-3277 (2012).

[59] I. Gdor, C. Yang, D. Yanover, H. Sachs, E. Lifshitz, and S. Ruhman, "Novel Spectral Decay Dynamics of Hot Excitons in PbSe Nanocrystals: A Tunable Femtosecond Pump-Hyperspectral Probe Study," J. Phys. Chem. C 117, 26342-26350 (2013).

[60] E. M. Grumstrup, S. H. Shim, M. A. Montgomery, N. H. Damrauer, and M. T. Zanni, "Facile collection of two-dimensional electronic spectra using femtosecond pulse-shaping technology," Opt. Express 15, 16681-16689 (2007).

[61] E. Harel, A. F. Fidler, and G. S. Engel, "Real-time mapping of electronic structure with single-shot two-dimensional electronic spectroscopy," Proceedings of the Natl. Acad. Sci. USA 107, 16444-16447 (2010).

[62] E. Harel, S. M. Rupich, R. D. Schaller, D. V. Talapin, and G. S. Engel, "Measurement of electronic splitting in PbS quantum dots by two-dimensional nonlinear spectroscopy," Phys. Rev. B 86, 075412 (2012).

[63] J. Helbing and P. Hamm, "Compact implementation of Fourier transform two-dimensional IR spectroscopy without phase ambiguity," J. Opt. Soc. Am. B 28, 171-178 (2011).

[64] S. B. Howell, *Handbook of CCD Astronomy*, 2nd ed., Cambridge Observing Handbooks for Research Astronomers (Cambridge University Press, Cambridge, 2006).

[65] D. C. Hutchings, J. S. Aitchison, B. S. Wherrett, G. T. Kennedy, and W. Sibbett, "Polarization dependence of ultrafast nonlinear refraction in an AlGaAs waveguide at the half-band gap," Opt. Lett. 20(9), 991-993 (1995).

[66] G. W. Hwang, D. Kim, J. M. Cordero, M. W. B. Wilson, C.-H. M. Chuang, J. C. Grossman, and M. G. Bawendi, "Identifying and Eliminating Emissive Sub-bandgap States in Thin Films of PbS Nanocrystals," Adv. Mater. 27, 4481-4486 (2015).

[67] J. D. Hybl, A. W. Albrecht, S. M. G. Faeder, and D. M. Jonas, "Two-dimensional electronic spectroscopy," Chem. Phys. Lett. 297, 307-313 (1998).

[68] J. D. Hybl, A. A. Ferro, and D. M. Jonas, "Two-dimensional Fourier transform electronic spectroscopy," J. Chem. Phys. 115(14), 6606-6621 (2001).

[69] J. D. Hybl, Y. Christophe, and D. M. Jonas, "Peak shapes in femtosecond 2D correlation spectroscopy," Chem. Phys. 266, 295-309 (2001).

[70] M. N. Islam, L. F. Mollenauer, R. H. Stolen, J. R. Simpson, and H. T. Shang, "Cross-phase modulation in optical fibers," Opt. Lett. 12(8), 625-627 (1987).

[71] J. C. Johnson, K. A. Gerth, Q. Song, J. E. Murphy, A. J. Nozik, and G. D. Scholes, "Ultrafast Exciton Fine Structure Relaxation Dynamics in Lead Chalcogenide Nanocrystals," Nano Lett. 8(5), 1374-1381 (2008).

[72] D. M. Jonas, M. J. Lang, Y. Nagasawa, T. Joo, and G. R. Fleming, "Pump-Probe Polarization Anisotropy Study of Femtosecond Energy Transfer within the Photosynthetic Reaction Center of *Rhodobacter sphaeroides* R26," J. Phys. Chem. 100, 12660-12673 (1996).

[73] D. M. Jonas, "Two-Dimensional Femtosecond Spectroscopy," Annu. Rev. Phys. Chem. 54, 425-463 (2003).

[74] D. J. Jones, E. O. Potma, J. X. Cheng, B. Burfeindt, Y. Pang, J. Ye, and X. S. Xie, "Synchronization of two passively mode-locked, picosecond lasers within 20 fs for coherent anti-Stokes Raman scattering microscopy," Rev. Sci. Instrum. 73, 2843-2848 (2002).

[75] H. Kamisaka, S. V. Kilina, K. Yamashita, and O. V. Prezhdo, "Ultrafast Vibrationally-Induced Dephasing of Electronic Excitations in PbSe Quantum Dots," Nano Lett. 6(10), 2295-2300 (2006).

[76] I. Kang and F. W. Wise, "Electronic structure and optical properties of PbS and PbSe quantum dots," J. Opt. Soc. Am. B 14(7), 1632-1646 (1997).

[77] D. Karaiskaj, G. Moody, A. D. Bristow, M. E. Siemens, X. Dai, A. S. Bracker, D. Gammon, and S. T. Cundiff, "Homogeneous Linewidth Temperature Dependence of Interfacial GaAs Quantum Dots Studied with Optical 2D Fourier-Transform Spectroscopy," in CLEO: 2010 (Optical Society of America, San Jose, CA, 2010), QFD6

[78] B. Kopainsky, P. Qiu, W. Kaiser, B. Sens, and K. H. Drexhage, “Lifetime, photostability, and chemical-structure of IR heptamethine cyanine dyes absorbing beyond 1 μm,” Appl. Phys. B 29, 15-18 (1982).

[79] R. Kubo, “Note on the Stochastic Theory of Resonance Absorption,” J. Phys. Soc. Jpn. 9(6), 935-944 (1954).

[80] W. Kuehn, K. Reimann, M. Woerner, and T. Elsaesser, “Phase-resolved two-dimensional spectroscopy based on collinear n-wave mixing in the ultrafast time domain,” J. Chem. Phys. 130, 164503 (2009).

[81] D. Lee and A. C. Albrecht, “On Global Energy Conservation in Nonlinear Light-Matter Interaction: The Nonlinear Spectroscopies, Active and Passive,” Adv. Chem. Phys. LXXXIII, 43 (1993).

[82] M. D. Levenson, C. Flytzanis, and N. Bloembergen, “Interference of Resonant and Non-resonant Three-Wave Mixing in Diamond,” Phys. Rev. B 6(10), 3962-3965 (1972).

[83] M. D. Levenson and N. Bloembergen, “Dispersion of the nonlinear optical susceptibility tensor in centrosymmetric media,” Phys. Rev. B 10(10), 4447-4464 (1974).

[84] M. Levenson and G. Eesley, “Polarization selective optical heterodyne detection for dramatically improved sensitivity in laser spectroscopy,” Appl. Phys. A 19, 1-17 (1979).

[85] Q. Lin and G. P. Agrawal, “Vector Theory of Cross-Phase Modulation: Role of Nonlinear Polarization Rotation,” IEEE J. Quant. Electron. 40 (7), 958-964 (2014).

[86] Y. Liu, M. Gibbs, J. Puthussery, S. Gaik, R. Ihly, H. W. Hillhouse, and M. Law, “Dependence of Carrier Mobility on Nanocrystal Size and Ligand Length in PbSe Nanocrystal Solids,” Nano Lett. 10, 1960-1969 (2010).

[87] M. Lorenc, M. Ziolek, R. Naskrecki, J. Karolczak, J. Kubicki, and A. Maciejewski, “Artifacts in femtosecond transient absorption spectroscopy,” Appl. Phys. B 74, 19-27 (2002).

[88] P. D. Maker, R. W. Terhune, and C. M. Savage, “Intensity-dependent changes in the refractive index of liquids,” Phys. Rev. Lett. 12(18), 507-509 (1964).

[89] G. Mayer and R. Gires, “The effect of an intense light beam on the index of refraction of liquids,” C. R. Acad. Sci. 258, 2039 (1963).

[90] R. M. Mersereau and A. V. Oppenheim, “Digital Reconstruction of Multidimensional Signals from Their Projections,” Proc. IEEE 62, 1319 (1974).

[91] A. G. Midgett, H. W. Hillhouse, B. K. Hughes, A. J. Nozik, and M. C. Beard, “Flowing versus Static Conditions for Measuring Multiple Exciton Generation in PbSe Quantum Dots,” J. Phys. Chem. C 114, 17486-17500 (2010).

[92] K. Misawa and T. Kobayashi, "Femtosecond Sagnac interferometer for phase spectroscopy," Opt. Lett. 20, 1550-1552 (1995).

[93] D. L. Mitchell and R. F. Wallis, "Theoretical Energy-Band Parameters for the Lead Salts," Phys. Rev. 151(2), 581-595 (1966).

[94] P. R. Monson and W. M. McClain, "Polarization Dependence of the Two-Photon Absorption of Tumbling Molecules with Application to Liquid 1-Chloronaphthalene and Benzene," J. Chem. Phys. 53(1), 29-37 (1970).

[95] I. Moreels, Z. Hens, P. Kockaert, J. Loicq, and D. V. Thourhout, "Spectroscopy of the nonlinear refractive index of colloidal PbSe nanocrystals," Appl. Phys. Lett. 89, 193106 (2006).

[96] I. Moreels, K. Lambert, D. D. Muynck, F. Vanhaecke, D. Poelman, J. C. Martins, G. Allan, and Z. Hens, "Composition and Size-Dependent Extinction Coefficient of Colloidal PbSe Quantum Dots," Chem. Mater. 19, 6101-6106 (2007).

[97] J. A. Myers, K. L. M. Lewis, P. F. Tekavec, and J. P. Ogilvie, "Two-color two-dimensional Fourier transform electronic spectroscopy with a pulse-shaper," Opt. Express 16, 17420-17428 (2008).

[98] S. Mukamel, *Nonlinear Optical Spectroscopy* (Oxford University Press, Oxford, 1995).

[99] G. Nair, S. M. Geyer, L.-Y. Chang, and M. G. Bawendi, "Carrier multiplication yields in PbS and PbSe nanocrystals measured by transient photoluminescence," Phys. Rev. B 78, 125325 (2008).

[100] C. A. Nelson and X.-Y. Zhu, "Reversible Surface Electron Traps in PbS Quantum Dot Solids Induced by an Order-Disorder Phase Transition in Capping Molecules," J. Am. Chem. Soc. 134, 7592-7595 (2012).

[101] K. A. Nelson, R. Casalegno, R. J. D. Miller, and M. D. Fayer, "Laser-induced excited state and ultrasonic wave gratings: Amplitude and phase grating contributions to diffraction," J. Chem. Phys. 77(3), 1144-1152 (1985).

[102] M. Nirmal, D. J. Norris, M. Kuno, and M. G. Bawendi, "Observation of the "Dark Exciton" in CdSe Quantum Dots," Phys. Rev. Lett. 75(20), 3728-3731 (1995).

[103] S. Nomura and T. Kobayashi, "Exciton-LO-phonon couplings in spherical semiconductor microcrystallites," Phys. Rev. B 45(3), 1305-1316 (1992).

[104] D. J. Norris, A. L. Efros, M. Rosen, and M. G. Bawendi, "Size dependence of exciton fine structure in CdSe quantum dots," Phys. Rev. B 53(24), 16347-16354 (1995).

[105] A. J. Nozik, "Quantum dot solar cells," Physica E 14, 115-120 (2002).

[106] J.-L. Oudar, "Coherent Phenomena Involved in the Time-Resolved Optical Kerr Effect," J. Quant. Electron. 19(4), 713-718 (1983).

[107] E. D. Palik, *Handbook of Optical Constants of Solids* (Academic Press, 1985).

[108] S. Park, K. Kwak, and M. D. Fayer, "Ultrafast 2D-IR vibrational echo spectroscopy: a probe of molecular dynamics," Laser Phys. Lett. 4(10), 704-718 (2007).

[109] S. D. Park, T. L. Courtney, D. Baranov, B. Cho, and D. M. Jonas, "Sagnac Interferometer for Two-Dimensional Spectroscopy in the Pump-Probe Geometry," *Ultrafast Phenomena XIX*, edited by K. Yamanouchi, S. Cundiff, R. Vivie-Riedle, M. Kuwata-Gonokami, and L. DiMauro (Springer, New York, 2015), p. 428.

[110] J. J. Peterson and T. D. Krauss, "Fluorescence Spectroscopy of Single Lead Sulfide Quantum Dots," Nano Lett. 6(3), 510-514 (2006).

[111] J. M. Pietryga, D. J. Werder, D. J. Williams, J. L. Casson, R. D. Schaller, V. I. Klimov, and J. A. Hollingsworth, "Utilizing the Lability of Lead Selenide to Produce Heterostructured Nanocrystals with Bright, Stable Infrared Emission," J. Am. Chem. Soc. 130, 4879-4885 (2008).

[112] A. N. Poddubny, M. O. Nestoklon, and S. V. Goupalov, "Anomalous suppression of valley splittings in lead salt nanocrystals without inversion center," Phys. Rev. B 86, 035324 (2012)

[113] W. Qian and D. M. Jonas, "Role of cyclic sets of transition dipoles in the pump-probe polarization anisotropy: Application to square symmetric molecules and perpendicular chromophore pairs," J. Chem. Phys. 119(3), 1611-1622 (2003).

[114] W. S. Rasband, ImageJ, U. S. National Institutes of Health, Bethesda, Maryland, USA, http://imagej.nih.gov/ij/, 1997-2014.

[115] Y. I. Ravich, B. A. Efimova, and I. A. Smirnov, *Semiconducting Lead Chalcogenides* (Plenum Press, New York, 1970).

[116] S. T. Roberts, J. J. Loparo, and A. Tokmakoff, "Characterization of spectral diffusion from two-dimensional line shapes," J. Chem. Phys. 125, 084502 (2006).

[117] S. J. Rosenthal, A. T. Yeh, A. P. Alivisatos, and C. V. Shank, "Size Dependent Absorption Anisotropy Measurements of CdSe Nanocrystals: Symmetry Assignments for the Lowest Electronic States," *Ultrafast Phenomena X*, edited by P. F. Barbara, J. G. Fujimoto, W. H. Knox, and W. Zinth (Springer-Verlag, Berlin, 1996), p. 431.

[118] J. I. Saari, E. A. Dias, D. Reifsnyder, M. M. Krause, B. R. Walsh, C. B. Murray, and P. Kambhampati, "Ultrafast Electron Trapping at the Surface of Semiconductor Nanocrystals: Excitonic and Biexcitonic Processes," J. Phys. Chem. B 117(16), 4412-4421 (2013).

[119] E. B. Saloman, "Energy Levels and Observed Spectral Lines of Xenon, Xe I through Xe LIV," J. Phys. Chem. Ref. Data 33(3), 765-921 (2004).

[120] R. D. Schaller, V. M. Agranovich, and V. I. Klimov, "High-efficiency carrier multiplication through direct photogeneration of multi-excitons via virtual single-exciton states," Nat. Phys. 1, 189-194 (2005).

[121] N. F. Scherer, D. M. Jonas, and G. R. Fleming, "Femtosecond wave packet and chemical reaction dynamics of iodine in solution: Tunable probe study of motion along the reaction coordinate," J. Chem. Phys. 99(1), 153-168 (1993).

[122] R. J. Schmidt, Schott Glass, "Sellmeier coefficients for BOROFLOAT 33 glass" (personal communication, Aug. 29, 2013).

[123] D. Segets, J. M. Lucas, R. N. Klupp Taylor, M. Scheele, H. Zheng, A. P. Alivisatos, and W. Peukert, "Determination of the Quantum Dot Band Gap Dependence on Particle Size from Optical Absorbance and Transmission Electron Microscopy Measurements," ACS Nano 6(10), 9021-9032 (2012).

[124] D. Segets, "Analysis of Particle Size Distributions of Quantum Dots: From Theory to Application," KONA Powder and Particle Journal (2015).

[125] O. E. Semonin, J. C. Johnson, J. M. Luther, A. G. Midgett, A. J. Nozik, and M. C. Beard, "Absolute photoluminescence quantum yields of IR-26 dye, PbS, and PbSe quantum dots," J. Phys. Chem. Lett. 1, 2445-2450 (2010).

[126] O. E. Semonin, J. M. Luther, S. Choi, H. Chen, J. Gao, A. J. Nozik, and M. C. Beard, "Peak External Photocurrent Quantum Efficiency Exceeding 100% via MEG in a Quantum Dot Solar Cell," Science 334, 1530-1533 (2011).

[127] C. V. Shank and P. Becker, "Femtosecond Processes in Semiconductors. In *Spectroscopy of Nonequilibrium Electrons and Phonons*," C. V. Shank and B. P. Zakharchenya Eds. Elsivier: Amsterdamn, p. 215 (1992).

[128] Y. R. Shen, "Electrostriction, Optical Kerr Effect and Self-focusing of Laser Beams," Phys. Lett. 20(4), 378-380 (1966).

[129] J. J. Shiang, A. V. Kadavanich, R. K. Grubbs, and A. P. Alivisatos, "Symmetry of Annealed Wurtzite CdSe Nanocrystals: Assignment to the C_{3v} Point Group," J. Phys. Chem. 99, 17417-17422 (1995).

[130] Y. Shirasaki, G. J. Supran, M. G. Bawendi, and V. Bulovic, "Emergence of colloidal quantum-dot light-emitting technologies," Nature Photon. 7, 13-23 (2013).

[131] W. Shockley and H. J. Queisser, "Detailed Balance Limit of Efficiency of p-n Junction Solar Cells," J. App. Phys. 32, 510-519 (1961).

[132] K. Shoemake, “Animating Rotation with Quaternion Curves,” Siggraph 19(3), 245-254 (1985).

[133] K. Shoemake, “Uniform Random Rotations. In Graphics Gems III,” edited by D. Kirk, Eds. Morgan Kaufmann, 124 (1995).

[134] A. E. Siegman, *Lasers* (University Science Books, California, 1986).

[135] E. R. Smith and D. M. Jonas, “Alignment, Vibronic Level Splitting, and Coherent Coupling Effects on the Pump-Probe Polarization Anisotropy,” J. Phys. Chem. A 115, 4101-4113 (2011).

[136] D. H. Son, J. S. Wittenberg, and A. P. Alivisatos, “Multielectron Ionization of CdSe Quantum Dots in Intense Femtosecond Ultraviolet Light,” Phys. Rev. Lett. 92(12), 127406 (2004).

[137] M. Spanner, M. Y. Ivanov, V. Kalosha, J. Hermann, D. A. Wiersma, and M. Pshenichnikov, “Tunable optimal compression of ultrabroadband pulses by cross-phase modulation,” Opt. Lett. 28(9), 749-51 (2003).

[138] A. P. Spencer, H. Li, S. T. Cundiff, and D. M. Jonas, “Pulse Propagation Effects in Optical 2D Fourier-Transform Spectroscopy: Theory,” J. Phys. Chem. A 119, 3936-3960 (2015).

[139] J. S. Steckel, B. K. H. Yen, D. C. Oertel, and M. G. Bawendi, “On the Mechanism of Lead Chalcogenide Nanocrystal Formation,” J. Am. Chem. Soc. 128, 13032-13033 (2006).

[140] J. S. Steckel, R. Colby, W. Liu, K. Hutchinson, C. Breen, J. Ritter, and S. Coe-Sullivan, “Quantum Dot Manufacturing Requirements for the High Volume LCD Market,” SID Symp. Dig. Tech. Pap. 44, 943-945 (2013).

[141] W. H. Steel, *Interferometry* (Cambridge University Press, 1967).

[142] J. T. Stewart, L. A. Padilha, M. M. Qazilbash, J. M. Pietryga, A. G. Midgett, J. M. Luther, M. C. Beard, A. J. Nozik, and V. I. Klimov, “Comparison of Carrier Multiplication Yields in PbS and PbSe Nanocrystals: The Role of Competing Energy-Loss Processes,” Nano Lett. 12, 622-628 (2012).

[143] B. Sun, R. Singh, L. A. Padilha, W. K. Bae, J. M. Pietryga, V. I. Klimov, and S. T. Cundiff, “Two Dimensional Coherent Spectroscopy of CdSe/ZnS Colloidal Quantum Dots,” in CLEO:2014 (Optical Society of America, San Jose, CA, 2014), JTh2A

[144] G. Taft, A. Rundquist, M. M. Murnane, I. P. Christov, H. C. Kapteyn, K. W. Delong, D. N. Fittinghoff, M. A. Krumbügel, J. N. Sweetser, and R. Trebino, “Measurement of 10-fs Laser Pulses,” IEEE J. Sel. Topics Quantum. Electron. 2(3), 575-585 (1996).

[145] T. Takagahara, "Electron-Phonon Interactions and Excitonic Dephasing in Semiconductor Nanocrystals," Phys. Rev. Lett. 71(21), 3577-3580 (1993).

[146] J. Tang, K. W. Kemp, S. Hoogland, K. S. Jeong, H. Liu, L. Levina, M. Furukawa, X. Wang, R. Debnath, D. Cha, K. W. Chou, A. Fischer, A. Amassian, J. B. Asbury, and E. H. Sargent, "Colloidal-quantum-dot photovoltaics using atomic-ligand passivation," Nat. Mater. 10, 765-771 (2011).

[147] D. V. Talapin and C. B. Murray, "PbSe Nanocrystal Solids for n- and p-Channel Thin Film Field-Effect Transistors," Science 310, 86-89 (2005).

[148] P. E. Tekavec, J. A. Myers, K. L. M. Lewis, and J. P. Ogilvie, "Two-dimensional electronic spectroscopy with a continuum probe," Opt. Lett. 34, 1390-1392 (2009).

[149] P. F. Tekavec, J. A. Myers, K. L. M. Lewis, F. D. Fuller, and J. P. Ogilvie, "Effects of chirp on two-dimensional Fourier transform electronic spectra," Opt. Exp. 18(11), 11015-11024 (2010).

[150] W. A. Tisdale, K. J. Williams, B. A. Timp, D. J. Norris, E. S. Aydil, and X.-Y. Zhu, "Hot-Electron Transfer from Semiconductor Nanocrystals," Science 328, 1543-1547 (2010).

[151] R. Trebino and C. C. Hayden, "Antiresonant-ring transient spectroscopy," Opt. Lett. 16, 493-495 (1991).

[152] R. Trebino and D. J. Kane, "Using phase retrieval to measure the intensity and phase of ultrashort pulses - frequency-resolved optical gating," J. Opt. Soc. Am. A 10, 1101-1111 (1993).

[153] R. Trebino, K. W. DeLong, D. N. Fittinghoff, J. N. Sweetser, M. A. Krumbugel, B. A. Richman, and D. J. Kane, "Measuring ultrashort laser pulses in the time-frequency domain using frequency-resolved optical gating," Rev. Sci. Instrum. 68(9), 3277-3295 (1997).

[154] M. T. Trinh, A. J. Houtepen, J. M. Schins, J. Piris, and L. D. A. Siebbeles, "Nature of the Second Optical Transition in PbSe Nanocrystals," Nano Lett. 8(7), 2112-2117 (2008).

[155] M. T. Trinh, M. Y. Sfeir, J. J. Choi, J. S. Owen, and X. Zhu, "A Hot Electron-Hole Pair Breaks the Symmetry of a Semiconductor Quantum Dot." Nano Lett. (2013).

[156] C. H. Tseng, S. Matsika, and T. C. Weinacht, "Two-Dimensional Ultrafast Fourier Transform Spectroscopy in the Deep Ultraviolet," Opt. Express 17, 18788-18793 (2009).

[157] J. van Rijssel, V. F. D. Peters, J. D. Meeldijk, R. J. Kortschot, R. J. A. van Dijk-Moes, A. V. Petukhov, B. H. Erné, and A. P. Philipse, "Size-Dependent Second Virial Coefficients of Quantum Dots from Quantitative Cryogenic Electron Microscopy," J. Phys. Chem. B 118, 11000-11005 (2014).

[158] A. M. Walsh and R. F. Loring, "Photon echoes in a nonpolar fluid," Chem. Phys. Lett. 186(1), 77-83 (1991).

[159] L. Wang, M. Califano, A. Zunger, and A. Franceschetti, "Pseudopotential Theory of Auger Processes in CdSe Quantum Dots," Phys. Rev. Lett. 91(5), 056404 (2003).

[160] M. C. Weidman, M. E. Beck, R. S. Hoffman, F. Prins, and W. A. Tisdale, "Monodisperse, Air-Stable PbS Nanocrystals *via* Precursor Stoichiometry Control," ACS Nano 8(6), 6363-6371 (2014).

[161] F. W. Wise, I. A. Walmsley, and C. L. Tang, "Experimental determination of hot-carrier scattering processes in $\mathrm{Al}_x\mathrm{Ga}_{1-x}\mathrm{As}$," Appl. Phys. Lett. 51(8), 605-607 (1987).

[162] W. Xiong and M. T. Zanni, "Signal enhancement and background cancellation in collinear two-dimensional spectroscopies," Opt. Lett. 33, 1371-1373 (2008).

[163] S. X. Yan and H. S. Tan, "Phase cycling schemes for two-dimensional optical spectroscopy with a pump-probe beam geometry," J. Chem. Phys. 360, 110-115 (2009).

[164] Y. Yan, E. B. Gamble Jr., and K. A. Nelson, "Impulsive stimulated scattering: General importance in femtosecond laser pulse interactions with matter, and spectroscopic applications," J. Chem. Phys. 83(11), 5391-5399 (1985).

[165] A. T. Yeh, C. V. Shank, J. K. McCusker, "Ultrafast Electron Localization Dynamics Following Photo-Induced Charge Transfer," Science 289, 935-938 (2000).

[166] S. Yeremenko, A. Baltuška, F. de Haan, M. S. Pshenichnikov, and D. A. Wiersma, "Frequency-resolved pump-probe characterization of femtosecond infrared pulses," Opt. Lett. 27(13), 1171-1173 (2002).

[167] M. K. Yetzbacher, N. Belabas, K. A. Kitney, and D. M. Jonas, "Propagation, beam geometry, and detection distortions of peak shapes in two-dimensional Fourier transform spectra," J. Chem. Phys. 126, 044511 (2007).

[168] M. K. Yetzbacher, T. L. Courtney, W. K. Peters, K. A. Kitney, E. R. Smith, and D. M. Jonas, "Spectral restoration for femtosecond spectral interferometry with attosecond accuracy," J. Opt. Soc. Am. B 27, 1104-1117 (2010).

[169] W. W. Yu, J. C. Falkner, B. S. Shih, V. L. Colvin, "Preparation and Characterization of Monodisperse PbSe Semiconductor Nanocrystals in a Noncoordinating Solvent," Chemistry of Materials 16, 3318-3322 (2004).

[170] L. A. Yurs, S. B. Block, A. V. Pakoulev, R. S. Selinsky, S. Jin, and J. Wright, "Multiresonant Coherent Multidimensional Electronic Spectroscopy of Colloidal PbSe Quantum Dots," J. Phys. Chem. C 115, 22833-22844 (2011).

[171] R. N. Zare, *Angular Momentum: Understanding Spatial Aspects in Physics and Chemistry* (Wiley-Interscience, New York, 1988).

[172] M. Zavelani-Rossi, G. Cerullo, S. De Silvestri, L. Gallmann, N. Matuschek, G. Steinmeyer, U. Keller, G. Angelow, V. Scheuer, and T. Tschudi, "Pulse compression over a 170-THz bandwidth in the visible by use of only chirped mirrors," Opt. Lett. 26, 1155-1157 (2001).

[173] E. Zeek, K. Maginnis, S. Backus, U. Russek, M. Murnane, G. Mourou, H. Kapteyn, and G. Vdovin, "Pulse compression by use of deformable mirrors," Opt. Lett. 24, 493-495 (1999).

[174] D. Zhitomirsky, I. J. Kramer, A. J. Labelle, A. Fischer, R. Debnath, J. Pan, O. M. Bakr, and E. H. Sargent, "Colloidal Quantum Dot Photovoltaics: The Effect of Polydispersity," Nano Lett. 12, 1007-1012 (2012).

[175] Q. Zhong, X. Zhu, and J. T. Fourkas, "Antiresonant-ring Kerr spectroscopy," Opt. Express 15, 6561-6568 (2007).

[176] Y. Zhou, S. Constantine, J. A. Gardecki, and L. D. Ziegler, "Dispersed ultrafast nonresonant electronic responses: detuning oscillations and near resonance effects," Chem. Phys. Lett. 314, 73-82 (1999).